Università degli Studi di Padova
Center of Studies and Activities for Space - CISAS "G. Colombo"
*
Ph.D. School of **Science Technology and Measures for Space** - Cycle XXIII
Curriculum in Mechanical Measures for Engineering and Space
School Director: Ch.mo Prof. Giampiero Naletto

Modular numerical environment for the characterization of a Helicon plasma thruster

by

Yaman Güçlü

A dissertation submitted for the degree of
Philosophiæ Doctor (PhD)

Research supervisors:
Dott. Ing. Daniele Pavarin
Prof. William N. G. Hitchon

Padua, Italy - July 2011

UNIVERSITÀ
DEGLI STUDI
DI PADOVA

Sede Amministrativa: Università degli Studi di Padova
Centro Interdipartimentale di Studi ed Attività Spaziali - CISAS “G. Colombo”

SCUOLA DI DOTTORATO DI RICERCA IN: **Scienze Tecnologie e Misure Spaziali**
INDIRIZZO: **Misure Meccaniche per l’Ingegneria e lo Spazio**
CICLO: **XXIII**

AMBIENTE NUMERICO MODULARE PER LA CARATTERIZZAZIONE DI UN PROPULSORE AL PLASMA DI TIPO HELICON

Direttore della Scuola: Ch.mo Prof. Giampiero Naletto
Coordinatore d’Indirizzo: Ch.mo Prof. Stefano Debei
Supervisori: Dott. Ing. Daniele Pavarin
Prof. William N. G. Hitchon

Dottorando: Yaman Güçlü

Abstract

The Helicon Plasma Thruster is a space propulsion system composed of a Helicon plasma source, with a properly designed magnetic nozzle. It is a very attractive concept due to the expected range of specific impulse and thrust-to-weight ratio, the scalability of the design, and the simplicity of construction; moreover, it is electrode-less and has no moving parts, and hence it can be expected to have an extended lifetime.

Although Helicon plasma sources have been used for decades in laboratories for producing high density plasmas, they are not fully understood yet. In fact, despite the simple geometry, a whole range of physical phenomena take place in the source: atomic physics, fluid kinetics, electrostatics and electromagnetism must be taken into account, and they are strongly interconnected to each other.

As a result, a Helicon plasma source is a very complex system to model, and to the author's knowledge, there is no reliable set of predictive tools for the design and optimization of such a source.

This thesis work focusses on Helicon plasma sources for space propulsion applications, and more precisely, it studies the configuration proposed in the *HPH.com* project (Helicon Plasma Hydrazine. COmbined Micro), in the Seventh Framework Programme of the European Union. The plasma source under study is small (approximately 15 cm in length), and the thruster is expected to provide just about 2 mN of thrust with 50 W of electric power consumption; as such, it is intended for use in the attitude control system of micro-satellites.

In order to optimize the computational resources available, a *hybrid model* is preferred to a *monolithic model*. In the former approach, the physical system is decomposed into subsystems, and each of these is simulated by a dedicated submodel, which (ideally) would use the most appropriate level of detail.

As no extensive theory on hybrid modeling exists, part of this thesis is dedicated to the investigation of the 'best way' to construct a hybrid model. An original approach is proposed, which is based on constructing submodels which rely on many different levels of detail, instead of just 'the best one'. This approach is natural, and it is believed to provide flexibility, robustness and physical insight.

According to the ideas above, a series of increasingly complicated models have been developed. Since the detailed and self-consistent simulation of the whole plasma source falls way beyond the scope of a single PhD thesis, most of the effort has been put into understanding the *coupled dynamics of electrons and neutrals*, which has not been throughly investigated yet.

In order to assess the ionization efficiency of the source, 0D and 1D analytic models of the neutral depletion process are presented. The comparison of the two models show the regimes where a higher level of detail is necessary, and the conditions under which the 1D model asymptotically recovers the 0D solution.

Subsequently, the neutral dynamics is coupled to the electron dynamics, by means of a semi-analytic 0D model which assumes Maxwellian electrons. The solution obtained gives a first estimate of the plasma parameters in the source, so that proper ranges for the characteristic lengths and time-scales of the various physical processes are calculated. Those results are essential to the preliminary design of a *bounce averaged* electron kinetic model, which is still 0D in space, but which calculates the electron energy distribution function self-consistently with the various processes.

After that, the 0D-1V electron kinetic model is designed in detail, including the effect of electromagnetic heating and various collisional processes. Accelerated convergence to the self-consistent steady-state is obtained by means of time-scale separation, fixed-point iteration, implicit time integration with Newton's solver and variable time-step, and a reduced auxiliary model. The neutral density in the source is obtained from the aforementioned 1D analytic model.

When the necessity for a detailed kinetic model for neutrals was realized, a 3D-3V semi-Lagrangian Convected Scheme was developed, which solves the Boltzmann equation in six-dimensional phase-space, plus time. Being the first implementation of the Convected Scheme to be 3D in space, several computational problems arose, and new solutions had to be found. For this reason, a considerable part of this thesis work had to deal with a new method for implementing diffuse boundary conditions, a new injector model, a new mass-, momentum- and energy-conserving collision operator for the Bhatnagar-Gross-Krook model, and a new angular mesh. Moreover, a novel third-order positivity-preserving remapping method with low numerical diffusion was developed.

Note on the originality of this work

The bulk of this dissertation consists of completely original work. Obvious exceptions are Chapter 1, which is an introduction to the thesis work, and Chapter 2, which is a collection of bibliographic research. The models presented in the successive chapters have been developed, written, implemented, tested and run by the author, under the scientific supervision of Prof. W.N.G. Hitchon at the University of Wisconsin-Madison.

Occasionally, formulas, theories and experimental data are employed, which come from other sources. In such cases, references are given to the original work, to the best of the author's knowledge. Moreover, short reviews of the state-of-the-art are given, where appropriate for clarifying the subject under discussion; again, such reviews come with an extensive bibliography.

Sommario

Un propulsore al plasma di tipo Helicon è un sistema di propulsione spaziale composto da una sorgente Helicon e da un ugello magnetico appositamente progettato. Tale tipo di propulsore attrae molto interesse per via dell'intervallo atteso per l'impulso specifico ed il rapporto spinta-su-peso, nonché per la scalabilità del concetto e la semplicità costruttiva. Inoltre, un propulsore Helicon è privo di elettrodi e di parti in movimento, dunque ci si aspetta una lunga durata di funzionamento.

Malgrado le sorgenti Helicon siamo stata impiegate per decenni per produrre plasmi ad elevata densità, il loro funzionamento non è ancora del tutto compreso. Infatti, sebbene la geometria sia semplice, una vasta gamma di fenomeni fisici convivono all'interno della sorgente: vanno presi in considerazione la fisica atomica, la cinetica dei fluidi, l'elettrostatica e l'elettromagnetismo, e tutti questi sono strettamente interdipendenti.

La sorgente Helicon è dunque un sistema molto complesso da modellare e, a conoscenza dell'autore, non è ancora stato sviluppato un sistema di strumenti per la progettazione e l'ottimizzazione di tale tipo di sorgente.

Il lavoro svolto all'interno di questa tesi si concentra sullo studio di una sorgente Helicon da applicarsi nella propulsione spaziale e, piú precisamente, sullo studio della configurazione proposta del progetto *HPH.com* (Helicon Plasma Hydrazine. COmbined Micro), nel settimo Framework Programme dell'Unione Europea. La sorgente di plasma considerata è di piccole dimensioni (circa 15 cm in lunghezza), e ci si aspetta che il propulsore fornisca circa 2 mN di spinta a fronte di 50 W di potenza elettrica fornita. Con queste caratteristiche, il propulsore è pensato per l'utilizzo nel controllo d'assetto di micro-satelliti.

Con il fine di ottimizzare le risorse computazionali a disposizione, un *modello ibrido* risulta preferibile rispetto ad un *modello monolitico*. Secondo il primo

approccio, il sistema fisico è decomposto in sotto-sistemi, ed ognuno di essi è simulato da un sotto-modello dedicato, che (idealmente) dovrebbe utilizzare un livello di dettaglio appropriato.

Non esiste alcuna teoria esaustiva su come sviluppare modelli ibridi, e parte di questa tesi è dedicata ad investigare la 'via migliore' di costruire un modello ibrido. Viene qui proposto un approccio originale, basato sulla costruzione di sotto-modelli che si affidano a diversi livelli di dettaglio, invece che semplicemente sul miglior modello possibile. Tale approccio è naturale, e ci si aspetta che sia flessibile, robusto e che fornisca una migliore comprensione del fenomeno fisico.

Seguendo tale metodologia, è stata sviluppata una serie di modelli via via piú complessi. Poiché una simulazione dettagliata ed autoconsistente dell'intera sorgente non puó essere completata in una singola tesi di Dottorato, la maggior parte di questo lavoro si concentra sulla comprensione della dinamica accoppiata di elettroni e neutri, che in questo sistema non è mai stata approfonditamente investigata.

Per valutare l'efficienza di ionizzazione all'interno della sorgente, modelli analitici 0D e 1D del processo di deplezione dei neutri sono presentati. Il confronto dei due modelli suggerisce i regimi in cui è necessario un livello di dettaglio piú elevato, e mostra le condizioni in cui il modello 1D converge asintoticamente alla soluzione 0D.

Successivamente, la dinamica dei neutri è accoppiata alla dinamica degli elettroni, per mezzo di un modello semi-analitico 0D che assume che gli elettroni abbiano una distribuzione Maxwelliana. La soluzione ottenuta fornisce valori preliminari per i parametri di plasma all'interno della sorgente, dai quali è possibile valutare un intervallo di lunghezze caratteristiche e di scale temporali che caratterizzano i diversi processi fisici. Questi risultati sono essenziali per la progettazione preliminare di un modello cinetico per gli elettroni *mediato su un elevato numero di oscillazioni all'interno della sorgente* ("*bounce averaged*"); tale modello rimane 0D nello spazio, ma esso calcola la distribuzione energetica degli elettroni in modo autoconsistente con i vari processi.

Successivamente, un modello 0D-1V cinetico per gli elettroni è stato progettato nel dettaglio, includendo l'effetto del riscaldamento elettromagnetico e dei diversi processi collisionali. La convergenza a regime stazionario è stata accelerata attraverso la separazione delle diverse scale temporali, iterazioni di punto fisso, integrazione implicita con un solutore di Newton a passo temporale variabile, ed un modello ausiliario ridotto. La densità dei neutri nella sorgente è ottenuta dal modello analitico 1D sopra citato.

Quando si è ritenuto necessario un modello dettagliato dei neutri, è stato sviluppato un modello cinetico 3D-3V, che impiega un solutore semi-Lagrangiano chiamato *Convected Scheme*. Questo modello risolve l'equazione di Boltzmann nello spazio nelle fasi a sei dimensioni, piú il tempo. Trattandosi della prima implementazione del Convective Scheme in tre dimensioni spaziali, si sono incontrati diversi problemi di natura computazionale, per i quali è stato necessario trovare soluzioni innovative. Per questa ragione, una parte consistente di questo lavoro di tesi è stata dedicata ad implementare nuove condizioni al contorno diffusive, un nuovo modello di iniettore, una nuova mesh angolare ed un innovativo operatore collisionale per il modello di Bhatnagar-Gross-Krook che conservi esattamente massa, quantità di moto ed energia. Inoltre, è stato sviluppato un metodo innovativo di rimappatura, accurato al terzo ordine, che preserva la positività della soluzione e possiede bassa diffusione numerica.

Nota sull'originalità del lavoro

Il corpo di questa tesi è basato su lavoro completamente originale. Ovvie eccezioni sono rappresentate dal Capitolo 1, che è introduttivo al lavoro di tesi, ed il Capitolo 2, che presenta una collezione di ricerche bibliografiche. I modelli presentati nei capitoli successivi sono stati sviluppati, scritti, implementati, testati ed utilizzati dall'autore, sotto la supervisione scientifica del Prof. W.N.G. Hitchon alla University of Wisconsin-Madison.

In alcune occasioni, sono stati utilizzati formule, teorie e dati sperimentali provenienti da altri fonti. In questi casi, sono stati forniti i riferimenti ai relativi lavori originali, al meglio delle conoscenze dell'autore. Sono inoltre presenti delle brevi recensioni sullo stato dell'arte, dove appropriato per chiarificare l'argomento discusso; tali recensioni sono accompagnate da un'approfondita bibliografia.

Acknowledgments

At the end of this PhD, I am completing a 25-year journey in the Italian public educational system. It is certainly a system with many flaws, that needs renovation and investments. But it worked for me, it rewarded my merits, and it supported me financially when I could not afford being a student. And most important, every single teacher taught me something that I will carry with me for the rest of my life. I was lucky being part of this.

I want to thank my supervisor at CISAS, Dr. Daniele Pavarin, and the Faculty Board of my PhD School, for giving me the opportunity to spend abroad a substantial part of my PhD program. And I am in debt to the ECE Dept. at UW Madison for hosting me during that period.

I must express my gratitude to my supervisor at UW Madison, Prof. Nick Hitchon, for all the time he has spent in helping me out with this thesis work: the long morning discussions at the coffee shop, the many emails at any time of the day, his patience when we were in disagreement, his helpfulness whenever bureaucracy was ominous on the horizon. And I really appreciated his endless efforts in fulfilling his self-appointed and hopeless mission of teaching me how to write perfect English. Thank you for everything, Nick!

I would also like to thank Prof. James Rossmanith of the Math Dept. at UW Madison for his lessons on Numerical Methods; his suggestions were always precious, and I really appreciated his eagerness to help on any numerical issue I presented to him.

Of course, I have had a long series of computer problems. For the solution of these, I must acknowledge the valuable help of Dr. Marco Manente at CISAS, Milad Fatanejad at FLASH Center in Chicago, Matt Terry at Berkeley National Lab, Stefano Suman at WHOI in Woods Hole, and the whole group ‘The Hacker

Within' at UW Madison. I would also like to thank Stefano for his help in many other everyday problems, and for his amazing ragú.

Yes, we Italians are very picky about food, and we cannot help it, I guess. Fortunately, Faiçal created the Mediterranean Café, a 'food oasis' in Madison. Friday lunch with all our Italian and Brazilian friends was something just great. Thank you guys for the happy time we have spent together. I already miss it.

I am grateful to my family and my closest friends for all the support they have given me during the whole PhD, and particularly during the period abroad. It means a lot to me, to know that the people I love respect so deeply my decisions, even when such decisions take me so far from them.

But I cannot think of all this being possible, if not because of an extraordinary person who has always been next to me, my beloved Sara. Every day, she was the one who listened to my small difficulties, helping me finding out solutions and giving me plenty of useful suggestions. Moreover, most of my bibliographic research on Helicon plasma sources builds on Sara's previous efforts.
If I were an artist, Sara would be my inspiring Muse.

Introspection

It comes the time to say “this is it”, to stop adding paragraphs to a document that will neither be as clear, nor as extensive as I would like it to be.. and admit to myself that I did my best.

This thesis work has had a complicate evolution throughout the 3 years and a half of my PhD. Plans had to change, the title itself changed twice since the start, and I had many difficult times that made me question my capacities, my inclination, and ultimately what I wanted my future to be. But I did not give up, thanks to the support from the wonderful people around me.

And now that it is almost done, I stop and think for a second. So I realize that the most important thing I have learnt during this PhD is the incredible extent to which scientific research can be frustrating: whenever one is trying something new, there is just no way to tell how it will end up, to guess whether any interesting result will come up at all.

When I started this long journey, I thought it was the new discovery, however small, that would make me happy and give me the energy to go on. Never mind how difficult the path, because the nice part of researching is finding, of course!

It was difficult to realize that I was completely wrong, instead. With such an attitude, I had a very hard time whenever luck was not on my side: how could I be happy if nothing worked as expected? And if I am not happy, my mind is not focussed, I get easily distracted, doing a good job becomes more difficult, and ultimately the situation gets worse.

Eventually, I understood that I had to love what I was doing every day, regardless of the results I was obtaining. Because, only if I love *doing research*, and not the *result of research*, there is a chance to become a good researcher: a peaceful mind works better, and the good results come spontaneously.

Well, I cannot tell how to love doing research. But I am looking for my way to go.

Contents

List of Figures

List of Tables

Glossary

BC	Boundary Condition
BTE	Boltzmann's Transport Equation
CCSL	Cell-Centered Semi-Lagrangian
CFL	Courant-Friedrichs-Lewy
CS	Convected Scheme
DL	Double Layer
EEDF	Electron Energy Distribution Function
EM	Electro-Magnetic
FSL	Forward-trajectory Semi-Lagrangian
HDLT	Helicon Double Layer Thruster
LDLR	Local Double Logarithmic Reconstruction
LOD	Level of Detail
LTE	Local Truncation Error
LVB	Local Variation Bounded
MC	Moving Cell
MEA	Modified Equation Analysis
MOL	Method of Lines
ODE	Ordinary Differential Equation
PDE	Partial Differential Equation
RF	Radio Frequency
SL	Semi-Lagrangian
TG	Trivelpiece-Gould
TVB	Total Variation Bounded

1

Introduction

Large scale simulations of complex physical systems frequently require ’hybrid’ simulation techniques, where the hybrid consists of a coupled set of sub-models, each of which describes an aspect of the physical system.

In this document strategies are discussed for the development of a hybrid model, emphasizing the use of multiple physical levels of description of each aspect of the physical system. The importance of using descriptions of the components of the system which employ different degrees of detail is that first, testing of the models is best done by comparing the predictions of these different descriptions. Second, while detailed descriptions are essential for many purposes, such as obtaining accurate predictions, it is the simplest descriptions (once tested versus detailed models) which provide an understanding of the behavior of the system and which tend to be most effective in estimating the sensitivity of measurable quantities to other variables in the system. Third, simplified models often offer an improved interface in the hybrid between detailed models describing different aspects of the overall system. The use of simplified models in the hybrid will be described in what follows.

This approach is illustrated in application to a hybrid model of a Helicon Plasma Thruster.

Section 1.1 gives the motivation of this thesis work and it places it into a context: the configuration of the Helicon plasma source under study is described, the meaning of the term ‘characterization’ is given, and a rationale for the modularity of the numerical framework is presented.

Section 1.2 gives an outline of the various chapters of this dissertation.

1.1 Motivation and Background

1.1.1 Helicon Plasma Thruster

The Helicon plasma thruster is composed of a few basic components, as shown in Fig. 1.1:

- a gas feeding system (usually Neon, Argon, Xenon, or Nitrogen),
- a cylindrical quartz tube, open on one end,
- a Helical antenna that is wound around the tube,
- a RF power supply (usually at a frequency of 13.56 MHz),
- a system of coils (or permanent magnets) to impose a static axial magnetic field which permits the propagation of Helicon waves, when plasma is present in the source.

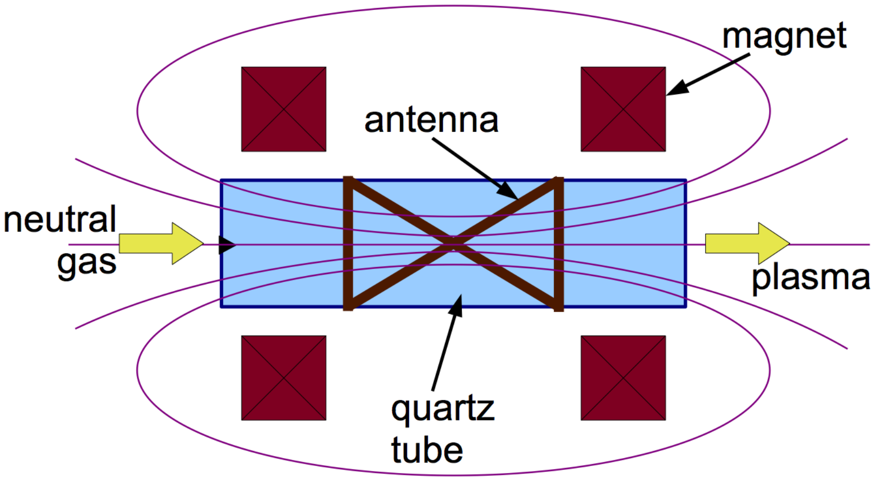

Figure 1.1: Main components of a Helicon Plasma Thruster.

The configuration under study is for the attitude control of micro-satellites, as proposed in the HPH.com project in the Seventh Framework Programme of the European Union (EU FP7). The main parameters are summarized in Table 1.1.

The physics of the Helicon Plasma Thruster is described in detail in Ch. 2. The basic working principles are outlined here:

- The electrons play a fundamental role:

Propellent:	Argon	Thrust:	2 mN
Source size:	2 x 12 cm	Exhaust velocity:	20 km/s
Total mass:	1.5 kg	Power available:	50 W

Table 1.1: Helicon Plasma Thruster: parameters of the configuration under study (HPH.com project - EU FP7).

  - the electrons are strongly magnetized, in the sense that their trajectories are helices with radius much smaller than the source radius ($r_L \ll R$), and hence they are radially confined in the source,
  - the helical antenna excites Helicon waves (i.e. confined Whistler waves), which propagate in the presence of a magnetized plasma, in a certain frequency range,
  - Electromagnetic power is coupled from the Helicon wave to the electrons (through various processes), and these can ionize the neutral gas to produce other plasma (ions + electrons);
  - the electrons are much faster then the ions (because $m_e \ll M_i$ and $T_e \gg T_i$), and hence they diffuse easily along the axis of the source,
  - to preserve charge, in steady state the electron flux equals the ion flux; for this to happen, a potential drop must exist (a *Double Layer*), which confines the electrons;

- The potential drop accelerates the ions to an energy several times $k_B T_e$, so that a *supersonic ion beam* is created, which flows out of the source through the exit section;

- The ion inertia and the divergent configuration of the magnetic field cause the electrons to detach from the magnetic field lines, so that electrons and ions are unbound and free to leave the system, and a *net Thrust* is obtained.

1.1.2 Characterization

In the context of this thesis work, the term 'characterization' basically means the determination the *propulsive parameters* of the thruster (i.e. Thrust, Specific Impulse, Propulsive Efficiency), and also to estimate an *uncertainty*, if possible, of the results. Moreover, the numerical models may be used for the *indirect measurement* of quantities that cannot be directly measured, and to provide the kind of physical insight needed to set up an *optimization* process. The use of a classical 'black box' approach is not sufficient here, because:

1. it may be necessary to determine how a certain quantity *inside the system* affects the propulsive parameters;
2. non-linear effects are often very important in plasma physics, and they are not addressed by a linear sensitivity analysis;
3. different physical processes may be involved at the same time.

Instead, a bottom-up approach is used in the thesis: the starting point is the simplest possible description that takes into account the different concurrent phenomena; somewhat drastic hypotheses are necessary, and some free parameters are introduced. Using such a model, the orders of magnitude of the important quantities are obtained, and the free parameters can be varied to get a confidence range. Usually, the estimates suggest a more complicated model, which relaxes some of the hypotheses introduced.

1.1.3 Modular Numerical Environment

The set of numerical models required for the characterization of the Helicon Plasma Thruster under study is modular both horizontally and vertically.
Horizontal modularity is required because:

- the system is conceptually decomposed into smaller problems,
- each problem is simulated in a separate numerical module.

Vertical modularity is required because:

- for each phenomenon, different models are built, which have different Level-Of-Detail (LOD);
- the most 'cost-effective' description can be sought for each problem.

When designing a modular numerical environment, it is natural to investigate the 'best' way to make modules interact. In fact, this is done in Ch. 3, where it is argued that simple models (e.g. a fitted curve, an analytic expression, etc.) may provide a flexible interface between more detailed models. According to this point of view, the driver is the sensitivity of the module with respect to the parameters passed: one should always avoid passing a parameter on which the module is highly sensitive.

1.2 Dissertation Outline

Chapter 2 presents extensive bibliographic research on the various models that have been applied to the simulation of a Helicon Plasma Thruster, and more generally to Helicon plasma sources.

Chapter 3 discusses the 'large scale simulations' of complex physical systems, which frequently require 'hybrid' simulation techniques, where the hybrid consists of a coupled set of sub-models, each of which describes an aspect of the physical system. An original approach is proposed, which emphasizes the use of multiple physical levels of description of each aspect of the physical system.

Chapter 4 shows how a simple global model can be used in the preliminary design of a hybrid model. First, 0D and 1D analytic models of the neutral depletion process are presented. Then, the neutral dynamics is coupled to the electron dynamics, by means of a semi-analytic 0D model which assumes Maxwellian electrons. The solution obtained gives a first estimate of the plasma parameters in the source, so that proper ranges for the characteristic lengths and time-scales of the various physical processes are calculated. Those results suggest a *bounce averaged* electron kinetic model, which is still 0D in space, but which calculates the electron energy distribution function (EEDF) self-consistently with the RF heating, the various collisional processes, and the hypothesis of quasi-neutrality.

Chapter 5 describes the 0D-1V electron kinetic model in detail, starting from the model equation and the experimental data, and going on to the semi-discrete formulation of the various terms (an accurate implementation is shown to conserve particle number and energy on the discrete energy mesh), resulting in a system of Ordinary Differential Equations (ODEs). Due to their different time-scales, the evolution of the electron density (which is the first moment of the EEDF) is separated from the evolution of the normalized EEDF (which is the 'shape' of the EEDF): a new ODE system, derived from the one above, describes the evolution of the normalized EEDF, while a global energy balance is used to evolve the electron density.

Chapter 6 describes a 3D-3V semi-Lagrangian Convected Scheme for the detailed kinetic modeling of neutrals. Such a scheme solves the Boltzmann equation in six-dimensional phase-space, plus time. Several novelties in the numerical model are also discussed, like a new method for implementing diffuse boundary conditions, a new injector model, a new mass-, momentum- and energy-conserving collision operator for the Bhatnagar-Gross-Krook model, and a new angular mesh. Moreover, a novel third-order positivity-preserving remapping method with low numerical diffusion is carefully described.

2

Review of Helicon Thruster Research

Although the use of Electromagnetic thrusters is widespread in modern space propulsion systems [1], the Helicon Plasma Thruster is a fairly new concept (the first prototype was built in 2002), which has not had the chance to fly yet.

For decades, Helicon plasma sources have been used in laboratories and industry for creating high density plasmas, both in the low and high pressure ranges, for a variety of applications. (According to the common jargon in the low temperature plasma community, here 'density' refers to the plasma density, while 'pressure' refers to the neutral pressure.) Accordingly, there is now a body of experience in the use of Helicon plasma sources, and a great effort has been put into modeling several of the processes that take place in a Helicon plasma source, providing considerable insight into the underlying physics.

Regardless, there is still a lack of reliable models capable of predicting and quantifying the experimental results, not just of qualitatively reproducing them after tuning; such models would require coupling self-consistently the small models, or developing dedicated multi-physics codes. Only a few attempts have been made in this sense, but none of them has addressed all of the physical processes relevant to a Helicon Plasma Thruster.

This Chapter aims at collecting information about the modeling effort that has been ongoing for the past decades, and wherever possible, it tries to relate such a research to the space propulsion application.

Section 2.1 gives an introduction to the fundamentals of rocket propulsion, and it discusses the most important *performance parameters*; *electric* rocket propulsion is presented and classified, highlighting the differences from *chemical* rocket propulsion.

Section 2.2 presents the Helicon Double Layer Thruster (HDLT) concept, its working principles and its main subsystems.

Section 2.3 reviews the mechanisms of power deposition from the Electromagnetic (EM) waves emitted by the antenna to the plasma. A simple linear theory of the normal modes of EM propagation in the plasma is discussed first, which introduces the Helicon (i.e. confined whistler waves) and Trivelpiece-Gould (quasi-electrostatic surface waves) modes. Since the basic theory based on linear (collisional) electron heating does not correctly reproduce the experimental results, a variety of other processes are discussed. Finally, a numerical code specifically designed to simulate the wave-plasma energy deposition is presented. In all these models, the plasma density profile is given.

Section 2.4 discusses the transport processes in the plasma source, i.e. the transport of particles, momentum and energy that determine the steady state profiles of electron, ion and neutral densities. A couple of simplified fluid models are presented, which are valid outside the range of applicability of ambipolar diffusion models. In all these models, the power deposition process is not taken into account.

Section 2.5 is more specific to space propulsion, as it describes the acceleration of the plasma beam through a magnetic nozzle. Both semi-analytical and numerical models are presented, which are based on different model equations, and which use the upstream plasma properties as given boundary conditions. Even though those models cannot provide a complete description of the beam acceleration, they give interesting insight into the phenomenon.

Finally, **Section 2.6** describes the attempts at building ‘complex numerical models’ of a Helicon plasma source, where the term ‘complex’ is used to indicate that different physical processes are coupled together in the same multi-physics model.

2.1 Introduction to Rocket Propulsion and Electromagnetic Thrusters

2.1.1 Performance Parameters

Thrust From the conservation of momentum, the total thrust force **T** provided by a rocket propulsion system is:

$$\mathbf{T} = \underbrace{\dot{m}\mathbf{v}}_{\text{momentum thrust}} + \underbrace{(p_E - p_a) A_E \hat{\mathbf{n}}}_{\text{pressure thrust}} = \dot{m}\mathbf{c} \tag{2.1}$$

where $\dot{m}$ is the mass flow rate, $\mathbf{v}$ is the mean (relative) velocity of the exhaust fluid, p_a and p_E are the pressure of the ambient and of the fluid at the exit of the rocket, A_E is the nozzle area at the exit (with normal unit vector $\hat{\mathbf{n}}$), and $\mathbf{c}$ is the effective exhaust velocity, i.e.

the velocity of the fluid downstream of the nozzle when it has reached the ambient pressure. For in-space conditions, $p_a = 0$. When an electric thruster is considered, the exhaust fluid is composed of charged particles (ions and electrons) plus neutral particles, and the momentum flux should really be expressed as the sum of three different contributions,

$$\dot{m}\mathbf{v} = m_e \dot{N}_e \mathbf{v}_e + M_i \dot{N}_i \mathbf{v}_i + M_0 \dot{N}_0 \mathbf{v}_0 \, , \tag{2.2}$$

where m_e, M_i and M_0 are the masses, and $\dot{N}_e$, $\dot{N}_i$ and $\dot{N}_0$ are the particle fluxes, of electrons, ions and neutrals respectively. If only singly charged positive ions exist in the system, for each ion produced in the source exactly one electron is produced, which means that $\dot{N}_e = \dot{N}_i$ in steady state. Since $m_e \ll M_i$ and $\mathbf{v}_e \approx \mathbf{v}_i$ in most cases, the contribution of electrons to the momentum thrust term is negligible for all practical purposes. Moreover the neutrals, which are a small number anyway if the source has a great efficiency, usually have an average velocity $\|\mathbf{v}_0\| \ll \|\mathbf{v}_i\|$. (There are accelerated neutrals due to the charge-exchange collisions, but these are a negligible percentage.) Hence, it can be said that *only the ions make a contribution to the momentum thrust.*

As concerns the pressure thrust, the fluid pressure is the sum of the contribution of the three species, $p_E = p_e + p_i + p_0$, and each contribution can be reasonably approximated by the ideal gas law $p_\alpha = n_\alpha K_B T_\alpha$. Since in most cases $n_e \approx n_i \gg n_0$, and $T_e \gg T_i \approx T_0$, *only the electrons give contribution to the pressure thrust.* Anyway, the electron pressure term is usually much smaller than the ion momentum term.

Specific Impulse The *total impulse* is the integral of thrust in time, as given by

$$I_{\text{tot}} = \int_{t_0}^{t_{\text{end}}} \|\mathbf{T}(t)\| \, dt \, , \tag{2.3}$$

and this thrust is created by expelling outboard the total exhaust mass

$$m_b = \int_{t_0}^{t_{\text{end}}} \dot{m}(t) \, dt \, . \tag{2.4}$$

A measure of 'how efficiently' the propellent is used for providing thrust is usually given in terms of the *average specific impulse* $\langle I_{sp} \rangle$, which is defined as the ratio of I_{tot} to the total exhaust weight (at sea level):

$$\langle I_{sp} \rangle = \frac{I_{\text{tot}}}{m_b g_0} = \frac{\int_{t_0}^{t_{\text{end}}} \|\mathbf{T}(t)\| \, dt}{g_0 \int_{t_0}^{t_{\text{end}}} \dot{m}(t) \, dt} \, [\text{s}], \tag{2.5}$$

which is given in seconds. If $\langle T\rangle$ represents the average value of $\|\mathbf{T}(t)\|$ over time, and $\langle\dot{m}\rangle$ is the average value of $\dot{m}(t)$, then (2.5) can be rewritten as

$$\langle I_{sp}\rangle = \frac{\langle T\rangle}{\langle\dot{m}\rangle g_0} \,. \tag{2.6}$$

By extension, the *instantaneous specific impulse* $I_{sp}(t)$ is defined from (2.6), using the instantaneous values of the thrust magnitude and mass-flow

$$I_{sp}(t) = \frac{T(t)}{\dot{m}(t)\, g_0} = \frac{c(t)}{g_0} \,, \tag{2.7}$$

and as such, it represents a measure of the specific kinetic energy of the exhaust flow. From (2.7) it looks clear that the *effective exhaust velocity* $c(t)$ [m/s] is a parameter completely equivalent to the specific impulse, and in fact it is often preferred to it in the Electric Propulsion community.

Efficiency The *overall efficiency* is the ratio of the jet power P_j to the input power P_{in} (i.e. the power used by the propulsion system):

$$\eta = \frac{P_j}{P_{in}} = \frac{1/2\dot{m}c^2}{P_{in}} = \frac{T^2/2\dot{m}}{P_{in}} \tag{2.8}$$

For a Helicon Plasma thruster the overall efficiency η can be given as the product of several efficiencies:

$$\eta = \eta_{RF}\eta_u\eta_p \tag{2.9}$$

$$\eta_{RF} = \frac{P_{in}}{P_{RF}}, \quad \eta_u = \frac{\dot{m}_{i\infty}}{\dot{m}}, \quad \eta_p = \frac{\dot{m}_{i\infty}u_{i\infty}^2}{2P_{in}} = \frac{T^2}{2\dot{m}_{i\infty}P_{in}} \tag{2.10}$$

where: η_{RF} is the RF generator efficiency, η_u is the propellant utilization efficiency, η_p is the propulsive efficiency, $\dot{m}_{i\infty}$ is the downstream plasma flow, $u_{i\infty} = T/\dot{m}_{i\infty}$ is the effective exhaust velocity and P_{RF} is the power given to the RF circuit.

Thus, in order to be competitive, a helicon thruster should fulfill three basic achievements:

i Good antenna coupling, in terms of transfer of the antenna wave energy into plasma internal energy, (i.e. η_{RF})

ii High ionization efficiency of the injected gas inside the chamber, (i.e η_u),

iii An efficient conversion of the plasma internal energy into directed axial kinetic energy, (i.e η_p)

2.1.2 Electric Propulsion

In-space propulsion greatly differs from boost-phase propulsion: the latter consists of taking an object from the Earth surface to orbit and is characterized by the need for a great amount of thrust to overcome the gravitational force. Thus, the boost phase rocket will be able to give an enormous thrust for a short time period. For in-space situations, on the other hand, the object in orbit or in deep space will have to execute various kinds of maneuvers and it will need a thruster able to expel propellant into the vacuum environment, where the gravitational forces are negligible, at high velocities. For chemical thrusters the thrust is due to the expansion of the heated gases in the nozzle and the limitation on the thrust they can deliver is linked to the chemical energy available between fuel and oxidant and to thermodynamical considerations. Exhaust velocities of the order of a few thousands of meters per second can be achieved. In electric thrusters, instead, the thrust is given by the acceleration of the propellent gases by means of electrical heating (and then thermodynamic expansion) or by electromagnetic forces acting directly on the particles. For chemical thrusters the energy is stored in the fuel/oxidant chemical bond and then the energy limitation is determined by the quantity of propellent on board. For electrical thrusters the energy limitation is determined by the on-board power supply, thus they can achieve high specific impulse, but low thrust.

Based on the prevalent mechanism of energy storage and conversion, electric propulsion concepts can be put into three main categories:

Electrostatic thrusters: so called because thrust is given by the electrostatic pressure. Once the propellent is ionized, the ions are accelerated alone, and the beam is then neutralized with electrons. Examples are:

- Gridded ion thruster,
- Hall-effect, also called Stationary Plasma Thruster (SPT),
- Field Emission Electric Propulsion (FEEP),
- Colloid thruster.

Electromagnetic thrusters: so called because the thrust is given by the magnetic pressure. The propellant is ionized and then all the charged particles are accelerated by the Lorentz force (or the J x B force in the MHD case). Examples are:

- Magneto-Plasma-Dynamic (MPD) thruster,
- Electrode-less plasma thruster,
- Pulsed Inductive Thruster (PIT),
- VAriable Specific Impulse Magnetoplasma Rocket (VASIMR).

Electrothermal thrusters: here the thrust is given by the kinetic pressure in general, which may be predominantly given by neutrals or by electrons. Examples are:

- Resistojet,
- DC arcjet,
- Microwave arcjet;
- Pulsed Plasma Thruster (PPT),
- Helicon Double Layer Thruster;

where the first three concepts given are somewhat closer to chemical propulsion in that the propellant, although heated electrically (for example by means of resistors or electric arcs), then expands thermodynamically and is accelerated in a conventional nozzle.

This classification is by no means exhaustive, and some concepts may fall into more than one category. Many other classifications are also possible: for example, based on the type of propellent, or on the mechanism of power deposition into the propellent fluid, or on the frequency of the electromagnetic fields (e.g. DC, pulsed, RF, Microwave).

2.2 The Helicon Double Layer Thruster (HDLT) Concept

The need for miniaturized propulsion systems for micro spacecraft together with the advances in research on Helicon plasma sources and current free Double Layers drive the interest on Helicon Plasma Thrusters, a particular type of electromagnetic thrusters. In a Helicon Plasma Thruster, the high density plasma is produced by an helical Radio Frequency antenna and it is confined by a magnetic field externally applied. The Helicon waves allow an almost full ionization of the propellant gas and deposit their energy into the plasma by heating the electrons. Ions and electrons, thus, are accelerated and ejected into free-space through a diverging magnetic field. The thermal energy of the plasma is converted into the directed kinetic energy of the supersonic beam through an ambipolar electric field, the beam is current free and there is no need of an external electrode to neutralize the exhaust.

In recent years, Charles and Boswell have reported the observation of current free Double Layers obtained in an expanding plasma created by a Helicon source [2, 3]. Their results suggest the application of this kind of thruster to in-space propulsion because of the potential high efficiency of the Helicon source and of the supersonic beam produced in the expansion zone.

The physics of this device consists of the following stages: (1) power coupling from the wave to the plasma in the source region, (2) neutral depletion and plasma dynamics in the chamber, with possibility of formation of a *current free double layer*, (3) supersonic expansion in the divergent magnetic nozzle. All these phenomena are strongly coupled to each other, and this is why the theoretical understanding and numerical modeling of a Helicon Plasma Thruster represent a big challenge. This section tries to conduct a survey of what is known up to now and what still needs to be investigated in order to make this concept of thruster feasible.

2.2.1 Helicon Plasma Source

Helicon plasma sources have a cylindrical geometry and a DC magnetic field applied along the longitudinal axis. In an Helicon plasma source the gas is first weakly ionized in the antenna region by electrostatic fields, then, when it enters a region where a DC magnetic field is induced along the longitudinal axis of the cylindrical chamber, it is further ionized by the wave-particle interaction. It is not clear how the high ionization percentages are obtained, but it is thought the ionization is aided by a wave mode conversion (from Helicon waves to Trivelpiece-Gould waves) at the boundaries or by non linear wave-particle interactions. Anyway, in the DC magnetic field zone, the Helicon waves penetrate the core of the plasma column and they are not limited by a skin depth. According to [4], Helicon sources present the following advantages over other plasma sources:

- High Density: in Argon gas the plasma density obtained with 1-2 kW of RF power has an average of $10^{19}\ m^{-3}$, which is two orders of magnitude higher than the values obtained with the usual methods;

- High Efficiency: Helicon sources produce more plasma at a given power and the density has a ‘jump’ at the transition from a RF non-resonant discharge to a Helicon wave mode;
- Low magnetic field: the imposed magnetic field aims at confining the electrons in the radial direction, but not the ions, and thus a value between 100-300 G is usually sufficient (compared with the 875 G in Electron Cyclotron Resonance ECR sources);
- No internal electrodes: the antenna lies outside the vacuum chamber and it does not release impurities in the plasma;
- Low pressure operations: non-collisional electron heating can be sufficient to sustain the discharge, thus this source can operate at a low neutral gas pressure.

This characteristics are particularly important when dealing with thrusters where the limiting power is set by weight issues and efficiency is of the greatest importance. Following from the above considerations, the Helicon Plasma Thruster has several advantages over other existing in space propulsion systems:

- The plasma jet is neutral: ions and electrons are accelerated together through a magnetic nozzle, thus there is no space charge buildup on the thruster. Instead, in Ion engines and Hall Effect thrusters only the ions are accelerated and thus these thrusters require an external cathode, susceptible to erosion, for beam neutralization.
- The magnetic radial confinement of the plasma in a Helicon Plasma Thruster minimizes wall losses and surface erosion, allowing for increased efficiency and lifetimes. This is true only in the radial direction, as concern the surface perpendicular to the axis on the side where neutrals are injected (i.e. in contact with the spacecraft), the plasma is not confined at all. This suggests the necessity to revisit the initial project with the insertion, for example, of a magnetic mirror. The low magnetic field requirement is important because low fields need low powers to be maintained and have less problems, they do not need a cooling apparatus and have few interference problems with the on-board instrumentation.
- The use of an helicon source allows the almost complete ionization of the neutral gas, i.e. the propellant, insuring a high ionization efficiency. The use of a RF antenna adds, anyway, to the complexity of the thruster’s power processing unit.

2.3 Wave Energy Deposition in the Source

2.3.1 Theory of Helicon and TG Modes

According to the usual theoretical interpretation, the waves excited in a source are the eigenvalues of a plasma column. In these terms, the first calculation was performed in 1984 by Boswell [5] for both conducting and non conducting boundaries, taking into account the electron inertia. Boswell showed that the eigenmode is a combination of a Helicon wave (electromagnetic) and a Trivelpiece Gould wave (quasi-electrostatic). However, the result agreed with the experimental data [6] only if one of these two assumptions is valid: a conducting layer arises at the interface between the quartz tube and the plasma, or there is an anomalously high rate of electron collisions. Several theoretical models have been developed which neglect electron inertia, but it is now clear that the electron inertia must be taken into account. As a matter of fact, neglecting the electron inertia causes the wave electric field parallel to the external magnetic field to vanish, corresponding to the TE (transverse electric) approximation. In this approximation, the root corresponding to the TG mode disappears [7].

The necessity for the TG root to exists appears evident when the boundary conditions are applied: the plasma is bounded by a non conducting wall, thus the radial RF current has to vanish on the surface. This is possible only for a combination of helicon and TG waves, not for a helicon wave by itself [8], thus helicon and TG waves are strongly coupled in a plasma with non conducting boundary conditions and cannot be treated with a TE approximation.

Following Shamrai in ref. [8], the typical range of frequencies for helicon waves is: $\omega_{ci} \ll \omega_{LH} < \omega \ll \omega_{ce} \ll \omega_{pe}$, and the refractive index is $n_{\parallel} = k_{\parallel} c/\omega \gg 1$ or equivalently $v_{\phi} = \omega/k_{\parallel} \gg c$. The effect of electron temperature described with by parameter $k_{\parallel} v_{the}/\omega$ is usually negligible $(k_{\parallel} c/\omega \gg 1\ )$, thus the cold plasma treatment can be applied. Also the ion motion can be neglected because the wave frequency ω is well above the lower hybrid frequency. This imposes a restriction on the external magnetic field applied: $\omega_{LH} = \omega_{pi}\sqrt{1+(\omega_{pe}/\omega_{ce})^2} \approx \sqrt{\omega_{ce}\omega_{ci}} = e/B_0\sqrt{m_e m_i} \ll \omega$, thus for the Ar plasma with wave frequency of 13.56 MHz $B_0 < 1.3$ kG = 0.13 T.

Using the Krook model to take into account the electron collisions, in the helicon frequency range, the cold plasma dispersion relation becomes:

$$\frac{k^2c^2}{\omega^2} = \frac{\omega_{pe}^2}{\omega(\omega_{ce}\cos\theta - \omega - i\nu)} \tag{2.11}$$

where ν is the collision frequency of electrons against neutrals and ions, $k^2 = k_\perp^2 + k_\parallel^2$ is the total wave number, θ is the angle between the constant magnetic field $\mathbf{B}_0 = B_0\hat{\mathbf{z}}$ and k. Note that through all this section ‘longitudinal’ (parallel) and ‘transverse’ (perpendicular) will be with respect to the direction of B_0. Here the fields have been taken to vary as $exp(-i(\omega t - \mathbf{k}\cdot\mathbf{r}))$. The solution of the dispersion relation gives the frequency:

$$\omega = \omega_{ce}\cos\theta\frac{k^2c^2}{\omega_{pe}^2 + k^2c^2}\left(1 - i\frac{\nu}{\omega_{ce}\cos\theta}\right) \tag{2.12}$$

In the limits of “long” ($k \ll \omega_{pe}/c$) and “short” ($k \gg \omega_{pe}/c$) waves, two types of waves satisfy the dispersion relation: the helicon waves

$$\omega = (\omega_{ce}\cos\theta - i\nu)\frac{k^2c^2}{\omega_{pe}^2}, \quad k \ll \omega_{pe}/c \tag{2.13}$$

and the TG waves

$$\omega = \omega_{ce}\cos\theta - i\nu, \quad k \gg \omega_{pe}/c \tag{2.14}$$

The factor c/ω_{pe} that defines the boundary for the two limits can be seen as an anomalous skin depth. When the wavelength is of the order of this skin depth, the different types of wave merge. The helicon waves are oblique whistler waves, they are long scale and weakly damped across the magnetic field, while the TG waves are quasi electrostatic waves that disappear in the limit of m_e/m_i (i.e. the TE approximation). They are short and strongly damped across the magnetic field. For a fixed ratio ω_{ce}/ω (depending on the antenna and the external magnetic field), the plasma density defines three regions for the propagation of the helicon and TG waves [9]:

$$\omega_{ce} = \frac{eB_0}{m_e} < \omega_{pe} = \sqrt{\frac{e^2n_e}{\epsilon_0 m_e}} \Longrightarrow \frac{\epsilon_0 m_e}{e^2}\omega_{ce}^2 < n_e \tag{2.15}$$

$$\Longrightarrow \left(\frac{B_0}{10^3G}\right)^2 < \frac{n_e}{10^{17}m^{-3}} \tag{2.16}$$

After defining the following quantities:

$$n_c = \frac{\epsilon_0 m_e}{e^2}\omega_{ce}^2, \quad n_{low}(k_\parallel) = n_c\frac{\omega}{\omega_{ce}}\frac{c^2k_\parallel^2}{\omega^2}, \quad n_{high}(k_\parallel) = n_c\frac{1}{4}\frac{c^2k_\parallel^2}{\omega^2} \tag{2.17}$$

The regions are:

- Propagation of both helicon and TG waves: $\omega_{ce}/\omega < (ck_{\parallel}/\omega_{pe})^{-2} < (\omega_{ce}/\omega)^2/4$, that is $n_{low} < n_e < n_{high}$. The energy absorption is maximum,

- Evanescence of helicon waves, propagation of strongly damped TG waves: $(\omega_{ce}/\omega)^2/4 < (ck_{\parallel}/\omega_{pe})^{-2}$, that is $n_e < n_{low}$.

- Evanescence of both helicon and TG waves: $(ck_{\parallel}/\omega_{pe})^{-2} < \omega_{ce}/\omega$, that is $n_e > n_{high}$.

Moreover the kinetic energy can be written in terms of the magnetic energy as [10]:

$$W_{ke} = \frac{k^2 c^2}{\omega_{pe}^2} W_B \tag{2.18}$$

This relation gives the following information, depending on the anomalous skin depth c/ω_{pe}: helicon waves have their energy concentrated in the magnetic field ($W_{ke} \ll W_B$), while the TG have energy mainly in the kinetic component ($W_{ke} \gg W_B$). Thus helicon waves are weakly damped because only a small kinetic part of their energy is accessible to be dissipated by collisions. On the other hand, the TG wave energy is concentrated in the electron motion.

In ref. [11] Degeling et al. launched in the WOMBAT large volume helicon source test waves from a small disk antenna into a pre-existent, weakly magnetized cylindrical plasma in order to investigate the conditions under which the electrostatic nature or the electromagnetic nature of the wave was dominant.

Fig. 2.1a shows the dispersion relation for whistler waves. TG modes are located on the extreme left and right, next to the dashed asymptote. The group velocity, as underlined by Stix, is always perpendicular to the k surface. For a given $k_{\parallel}$, there are two values of $k_{\perp}$: the higher $k_{\perp}$ corresponds to the TG wave and the smaller $k_{\perp}$ corresponds to the helicon wave.

Fig. 2.1b shows the surface of constant phase. Two cusp points can be observed: these points correspond to the inflection points in the helicon part of the k surface of Fig. 2.1a.

Finally, Degeling et alter observed that the transition from electrostatic (TG like) to electromagnetic (helicon like) happens at a threshold electron density n_e^*. This value decreases with magnetic field and decreases strongly with increasing collisionality.

2.3.2 Power Deposition Mechanisms

The relevant Maxwell's equations are

$$\nabla \times \mathbf{E} = -\frac{\partial \mathbf{B}}{\partial t}, \quad \nabla \times \mathbf{B} = \mu_0 \mathbf{j} + \mu_0 \frac{\partial \mathbf{D}}{\partial t} \tag{2.19}$$

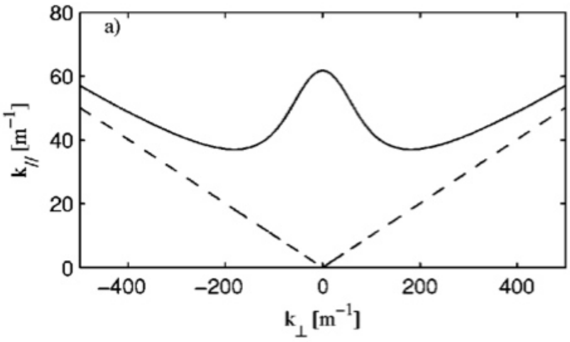

(a)

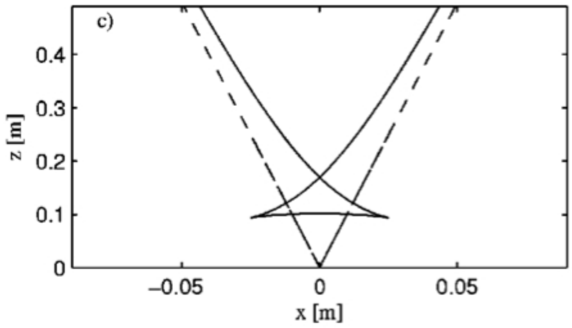

(b)

Figure 2.1: The variation of k (a) and surface of constant phase (b) with θ, for $\omega/\omega_{ce} = 0.1$ with $\omega_{pe}/\sqrt{(\omega(\omega_{ce}-\omega))} = 100$. The phase and group velocity resonance cone angles are indicated by dashed lines.

Where **j** is the external current density due to the antenna. Starting from this equations, in order to find the fields, some assumptions are to be made. The first strong assumption, made by many authors (Chen and Arnush in Refs. [7, 12, 13], Cho and Lieberman in Refs. [14–16], Shamrai and Taranov in Refs. [10] and related) is that the plasma has a uniform density. Then, the boundary conditions have to be chosen. For the plasma thruster case, the pertinent ones are: insulating boundary for a finite size plasma column, as in [10] and [14]. Chen and Arnush deal with the case of an infinitely long system, that is not pertinent to a thruster set up. Following both [10] and [14], the fields are written as a double Fourier series in azimuthal $m = \pm1, \pm3$ and longitudinal $k_\parallel = l\pi/L$ (where L is the system length and

$l = 1, 2, ...$) modes.

$$\mathbf{E} = \sum_{l,m} (\mathbf{E}_\perp(r)\sin(k_\parallel z) + E_z(r)\cos(k_\parallel z)\hat{\mathbf{z}})e^{i\phi} \tag{2.20a}$$

$$\mathbf{D} = \sum_{l,m} (\mathbf{D}_\perp(r)\sin(k_\parallel z) + D_z(r)\cos(k_\parallel z)\hat{\mathbf{z}})e^{i\phi} \tag{2.20b}$$

$$\mathbf{B} = \sum_{l,m} (\mathbf{D}_\perp(r)\cos(k_\parallel z) + B_z(r)\sin(k_\parallel z)\hat{\mathbf{z}})e^{i\phi} \tag{2.20c}$$

where the z direction is the direction of the constant magnetic field $\mathbf{B}_0 = B_0\hat{\mathbf{z}}$, and the transverse components of the fields are $\mathbf{E}_\perp(r) = E_r(r)\hat{\mathbf{r}} + E_\theta(r)\hat{\theta}$ and the phase factor $\phi = m\theta - \omega t$.The cold plasma approximation, together with the Krook model to handle collisions, allows us to relate the **E** and **D** fields using the dielectric tensor

$$\bar{\bar{\epsilon}} = \begin{bmatrix} \epsilon_{xx} & \epsilon_{xy} & 0 \\ -\epsilon_{xy} & \epsilon_{xx} & 0 \\ 0 & 0 & \epsilon_{zz} \end{bmatrix}, \tag{2.21}$$

where the elements are

$$\epsilon_{xx} = 1 + \frac{\omega_{pe}^2 (1 + i\nu/\omega)}{\omega_{ce}^2 - \omega^2 (1 + i\nu/\omega)^2} \tag{2.22a}$$

$$\epsilon_{xy} = -\frac{\omega_{pe}^2 \omega_{ce}/\omega}{\omega_{ce}^2 - \omega^2 (1 + i\nu/\omega)^2} \tag{2.22b}$$

$$\epsilon_{zz} = 1 - \frac{\omega_{pe}^2}{\omega^2 (1 + i\nu/\omega)} \tag{2.22c}$$

Accordingly, $\mathbf{D}(r) = \bar{\bar{\epsilon}} \cdot \mathbf{E}(r)$ results in

$$D_r = \epsilon_{xx}E_r + \epsilon_{xy}E_\theta \tag{2.23a}$$

$$D_\theta = -\epsilon_{xy}E_r + \epsilon_{xx}E_\theta \tag{2.23b}$$

$$D_z = \epsilon_{zz}E_z \tag{2.23c}$$

Analogously, the external current is written as:

$$\mathbf{j} = \sum_{l,m} (\mathbf{j}_\theta(r)\sin(k_\parallel z)\hat{\theta} + j_z(r)\cos(k_\parallel z)\hat{\mathbf{z}})e^{i\phi} \tag{2.24}$$

and the amplitudes of the Fourier modes of the antenna current are [17]:

$$j_\theta(r) = -i(I_a/\pi m L)\sin(k_\parallel a)\delta(r - r_0) \tag{2.25a}$$

$$j_z(r) = -i(I_a/\pi^2 l r_0)\sin(k_\parallel a)\delta(r - r_0) \tag{2.25b}$$

where $I_a \cos(\omega t)$ is the RF current carried by the single loop antenna, a is the antenna length, r_0 is the antenna radius. Up to now the different theoretical models agree, the differences start when the boundary conditions are posed.

In Shamrai Taranov [10] the helicon source is a cylindrical metal cavity of length L and radius R partially filled by a cold uniform plasma of density n and radius $r_0 < R$. The waves in the cavity are excited by a straight single-loop antenna which is located on the surface of the plasma column as in figure 2.2. Noticing that the antenna current **j** is a surface current located at $r = r_0$, they proceed in solving Maxwell's equations with $\mathbf{j} = 0$ in vacuum ($r > r_0$) and in plasma ($r < r_0$) and then joining the solutions for $r = r_0$ (i.e. on the antenna surface), where the symmetry of the antenna allows one to join the solutions for each mode separately. Once the linear response of the plasma cavity to the external RF current is found, the resonances of the cavity are found by solving the eigenvalue problem, which corresponds to solving the dispersion relation. Now, a fundamental distinction between wide and narrow vacuum gap $d = R - r_0$ is made: narrow gap corresponds to a conducting boundary, while a wide gap means that the conducting boundary is far from the antenna and the plasma column, thus an insulating boundary condition is reproduced. The condition for the wide gap results in

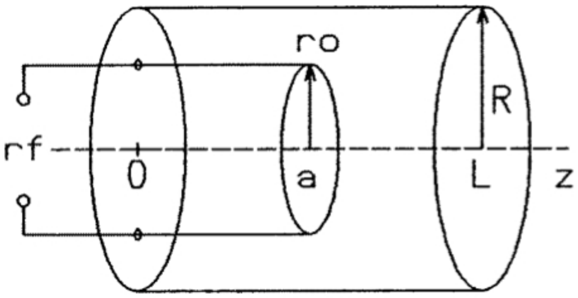

Figure 2.2: Helicon source geometry used by Shamrai and Taranov in [10]

$$d > d^* = \frac{\beta R}{2|m|}, \quad \beta = \frac{\omega_{ce}}{\omega_{pe}^2 \omega} k_\parallel^2 c^2 \,. \tag{2.26}$$

The second fundamental parameter is the strength of the external magnetic field (with fixed collision frequency) that distinguish between strongly ($B_0 > B^*$) and weakly ($B_0 < B^*$) damped TG waves.

$$B^* = \frac{m_e c}{e} \frac{\omega^2}{\nu} \frac{1}{k_\parallel r_0} \tag{2.27}$$

The relevant results of the paper can be summarized as follows:

- The antenna excites helicon modes only that are converted linearly into TG modes near the edge of the plasma column, when the gap is wide ($d > d^*$, i.e. insulating boundary).

- When looking for resonances (i.e. the amplitude of a certain mode increases sharply), all eigenmodes are hybrid, and the pure helicon resonance disappears. When $B_0 > B^*$ and the collisions are taken into account, no resonances are obtained, because of the dissipative broadening that causes the resonances of different modes to overlap and thus destroy each other.

- A helicon plasma source can manifest an *anti-resonant* regime of operation, where one of the wave contributions (Helicon or TG) is negligible. (Remember that a finite system that is forced by an external small-amplitude periodic source responds linearly with an oscillation that is a superposition of different modes; in this case, each mode is given by contributions from Helicon and TG waves.) The fundamental result found by Shamrai and Taranov is that the TG anti-resonance condition in the wide gap limit ($d > d^*$) coincides with the resonance condition for a conducting boundary: the field structure of the TG anti-resonance mode is the same as that of the eigenmode with conducting boundary.

- The TG are strongly damped and disappear in a narrow surface layer in the plasma, but when the TG waves are suppressed, due to an anti-resonance mode, the power input is directed to the helicon waves that are weakly damped and can penetrate into the bulk of the plasma, depositing their power. This explains the good agreement between the experiments (with an insulating boundary) and the calculation performed with a conducting boundary: the TG modes disappear as they did in the TE approximation.

- The collisionless Landau damping is excluded because the parallel phase velocities are high $\omega/k_\parallel \gg v_{the}$, with v_{the} the thermal velocity of the electrons.

- In conclusion, this model permits one to explain both the field profiles in the plasma bulk as being attributed to the anti-resonance TG regime and the high absorption efficiency as originating from the strong damping of the helicon waves due to their linear conversion into TG waves near the plasma edge.

Even though their derivation was based on the hypothesis of an infinitely long cylinder, Chen and Arnush confirmed in [12] that, when the electron mass is included in the analysis, the power absorption of helicon waves is mainly due to the mode conversion to TG waves at the plasma boundary, followed by a strong damping of the TG waves.

The most crucial blanks in these models are the hypothesis of uniform density and the justification of the power deposition in the core of the plasma. An explanation in response to the latter point was given using the argumentation that TG waves are in an anti-resonance regime: when the TG mode disappears, more power is deposited in the bulk plasma due to the absorption of the helicon waves only; as a result, the volume absorption is enhanced, provided the total power input is fixed. But while this gives a satisfactory explanation for the reduction of power coupled to TG waves, it remains unclear how this should relate to an increased capacity of the (almost non-collisional) Helicon waves to deposit power into the plasma.

In fact, Krämer's group claimed that, for sufficiently high densities, mode conversion is unlikely to play a role for energy dissipation and heating in the core of the plasma. In ref. [18], motivated by the observations of turbulent electrostatic fluctuations in helicon plasmas, Aliev and Krämer studied the parametric decay instabilities in the Helicon regime, in particular they investigated the parametric decay of Helicon waves into ion sound waves and TG waves, which are highly damped. They started deriving the kinetic dispersion relation in the helicon frequency range ($\omega_{ci} \ll \omega \ll \omega_{ce}$) taking into account both the ion and the electron contributions. This way they are able to take into account the non uniformity of the plasma. Then, they noticed that the linear mode conversion of electromagnetic waves is not the only mechanism for exciting longitudinal (i.e. electrostatic, TG waves) in a plasma: a non linear transformation due to the excitement of parametric instabilities may occur and explain the anomalous heating in the plasma bulk. In the long wave limit ($k_\parallel r_{Le} \ll 1$ where r_{Le} is the electron Larmor radius) the parametric decay instability excites low frequency ion sound and high frequency TG waves and the threshold for this instability, rather large in the dipole approximation, becomes lower when the finite wavenumber of the driving wave is considered: the parallel wave numbers of the driving wave and of the decay waves become comparable and the three wave parametric instability can occur. The decay of the TG waves contributes mainly in the dissipation of the Helicon wave energy: the anomalous Helicon wave absorption can be described by an *effective collision frequency*, which is sufficiently high to account for the observed strong power absorption in the plasma bulk.

More recently these results were confirmed in ref. [19]: they reported that there is a close relationship between the excitation of electrostatic fluctuations due to the parametric decay of Helicon waves into ion sound waves and TG waves, and the helicon waves absorption in the bulk of the plasma column. It is still not clear whether the majority of the RF power is actually transferred to TG waves.

The occurring of anti-resonance modes and of parametric instabilities are only two of the most recent power coupling mechanisms proposed. Borg and Kamenski [20] proposed that the dominant collisionless wave-particle interaction mechanism is the electron acceleration by the parallel component of the electric field, while the heating of electrons by wave damping is dominant in the far field. In support for this thesis, they showed that, for low values of the magnetic field, the response of the electron energy distribution near the antenna indicates a strong wave electron interaction. Landau damping has also been proposed by Chen in ref. [7] as a mechanism responsible for the efficient heating. Landau damping is responsible for trapping and acceleration of electrons by the helicon wave, in this fashion energetic primary electrons are produced and are responsible for the ionizing collisions. After these collisions, the electrons slow down and become low energy secondaries that are reaccelerated by the wave. In support of this hypothesis are, for instance, the observations by Gui and Scharer [21], who found that trapped electrons appeared as the magnetic field amplitude is increased and that the electron energy distribution displayed a bunching of particles with energies higher than the ionization potential of the gas. Other measurements by Degeling and Scharer in ref. [22] showed a good correlation between the emitted radiation and the phase velocity of the helicon wave. These observations imply that resonant electrons are trapped in the wave reference frame. Anyways, collisions have a strong effect on reducing the wave particle trapping and interaction by affecting the wave particle phase coherence and so these effects should be less pronounced at higher pressures. In fact, Chen and Blackwell [23] found that the number of phased fast electrons might not be enough to account for the majority of the ionizing collisions.

While the debate is still open about which is the main process that drives power absorption into the plasma, it is largely recognized that linear (collisional) heating alone does not give a satisfactory explanation of the experimental observations. The role of non-linear processes, in particular under and near the antenna at low electron densities, cannot be neglected.

2.3.3 Numerical Simulation of the Electromagnetic Fields

The ANTENA code Mouzouris, Scharer et al. (ref [24] and following) developed the ANTENA code to calculate the 3D electromagnetic fields due to helical RF antennas (m=0 Stix coil and a m=1 Nagoya type-III) in a 1D cylindrical hot magnetized plasma, with uniform magnetic field in the axial direction. The model also gives a profile for the radial power deposition. The inputs to the code are the plasma density and plasma temperature, which can be considered functions of the radius because their radial variation is approximated using a stratified model. Ions and electrons are assumed to have a Maxwellian velocity distribution, and the collisions are handled using a Krook collision operator. Also, the code is able to simulate Landau and collisional damping of the RF fields. The m=0 Stix coil was more efficient in coupling the power to the plasma than the m=+1 Nagoya type-III for the radial plasma profiles under study: the m=0 coil excites negligible amounts of the higher order (m>3) modes, which raise the reactance of the source and increase the edge heating effects. The m=0 coil also provides an improved directionality of the spectrum.

2.4 Transport Processes in the Source

Transport processes in a Helicon plasma source exhibit a quite complicated set of features, and this is especially true if the source is designed for space propulsion applications. There is little theory on the subject, and the zero-dimensional global models applied to common plasma sources usually employ the following procedure: if the electrons are highly collisional (that is, the frequency of electron-neutral elastic collisions is the highest frequency in the system), then it is assumed that electrons have a Maxwellian distribution, and hence they can be described by their density and temperature only. Moreover, if the ions are also collisional (that is, an ion undergoes several collisions with neutrals during its lifetime), then the charged particle transport is driven by *ambipolar diffusion*.

In this setting, the electron temperature is usually obtained from particle conservation, balancing the electron production by ionization with the electron loss at the walls (where recombination occurs); this requires knowledge of the (normalized) density profile in the source, which comes from the solution of an ambipolar diffusion equation (in simple domains, this is usually obtained by separation of variables). Once the temperature is known, the electron density is obtained from energy conservation, balancing the input power (e.g.

from the antenna, the electrodes, or a laser) with the losses by inelastic collisions, ionization, and recombination at the wall.

The following sections provide an overview of two more sophisticated semi-analytical models, which take into account the presence of a magnetic field capable of magnetizing the electrons, and which do not require ambipolar diffusion to be the predominant transport mechanism. In this regard, they will give useful insight into the physics of the Helicon plasma thruster.

2.4.1 Fruchtman's fluid model

In 2004 Fruchtman et al. [25] developed a steady-state fluid model for a two-dimensional magnetized cylindrical plasma source, and by means of that model they studied the typical configuration of a Helicon plasma source. Such a model is based on the continuity and momentum equations for electrons and ions, which are treated as two separate fluids. The main hypotheses are:

- the plasma is in steady state, it is axially-symmetric, and it is contained in a *closed cylindrical chamber*; this is not very realistic in the case of a thruster (which is open at one end);
- the magnetic field is aligned with the axial direction, and it is uniform everywhere;
- the electron fluid has a uniform temperature T_e, which is determined from a global energy balance;
- the ions are 'cold', i.e. their thermal motion is neglected ($T_i = 0$);
- the plasma is quasi-neutral (i.e. $n_i = n_e$ everywhere except in the sheaths), with boundary conditions that must match the pre-sheath requirements;
- the electron inertia is neglected, i.e. $m_e \rightarrow 0$ (hence, in principle, this model does not apply to the range $\nu_e > \omega_{lh}$);
- the neutral gas is modeled as a uniform background with given density and temperature, which is only reasonable in a weak ionization regime (not relevant to thrusters);

Following from the quasi-neutrality and the negligible electron inertia, the electric potential ϕ is determined from the electron momentum equation. This in turn gives the ambipolar electric field, which strongly influences the ion dynamics. Particular attention was paid to the modeling of ion-neutral charge-exchange collisions: they derived an approximated general form for the resulting drag force on ions, a form that retains the nonlinear drag for high ion speeds, as well as the effect of the neutral motion for low ion velocities.

Usually the variable separation technique is used within the diffusion approximation; Fruchtman et al. extended the use of a variable separation beyond the diffusion approximation to cases in which ion inertia is retained. Accordingly, the two-dimensional equilibrium was analyzed by solving two separate sets of ordinary differential equations for the axial and for the radial directions, not only in the collisional regime, but also in the collisionless regime (in which the ion inertia is dominant). The two sets of equations are decoupled except for two parameters (one of them the electron temperature) which are present in both sets. Upon imposing boundary conditions, the two parameters turn into eigenvalues of the problem, which are solved using a global energy balance.

At a subsequent step, the axial and radial profiles are solved independently. The axial model retains the full non-linear form of the ion drag force; an analytical solution shows three asymptotic regimes depending of the ion Knudsen number: collisionless, linear diffusion and nonlinear diffusion. The radial model uses a linearized drag force and neglects the effect of ion inertia; to solve for the electron cross-field transport, the equations are integrated numerically.

This model splitting is very useful for acquiring a sound understanding of the qualitative behavior of the 2D transport processes, before solving more accurate models. Moreover, this 2D model was used to interpret the experimental results, and in particular the correlation between the imposed increase of the magnetic field intensity and the observed increase in plasma density. Their results suggested that explaining such a density increase as due to better radial confinement, implies that the electron collisionality should be much larger than expected from electron-ion and electron-neutral collisions. When Bohm diffusion was assumed, good agreement between theory and experiment was found; but since the collisionality which would be required to cause Bohm diffusion is anomalously high in their case, they suggested a different explanation: *the increase in density may be due to an improvement in the plasma wave interaction with the increased magnetic field.*

Regardless, the biggest deficit in this analysis is the assumption of constant neutral density. In fact, neutral density variation plays an important role in the Helicon discharge, as measured by Denning et alter in ref. [26]: downstream of the antenna the almost complete absence of neutrals causes the plasma density to remain constant when the coupled RF power is increased. The power goes instead into the heating of the electrons.

2.4.2 Ahedo's fluid model

Ahedo in ref. [27] addresses specifically the assessment of the propulsion parameters in a Helicon plasma thruster, which is modeled as a *cylindrical chamber open at one end to vacuum*. Although specifically interested in the axial variation of the physical quantities (and ultimately with the ion speed at the exit section), Ahedo underlines the necessity of using a 2D model in order to take into account the effect of the radial density gradient on the overall transport processes. In particular, such a model handles the 2D effects caused by the expansion of the geometrical area and the divergence of the magnetic field. Following the example of Fruchtman et al. in [25], this model is based on the decoupling of the radial and axial dynamics making use of an approximate variable-separation technique; again, the electron temperature T_e is constant and is determined from a global energy balance. (It should be stressed that a reliable solution for T_e could be found only from a self consistent model of the plasma waves coupling, because the electron temperature depends heavily on the spatial distribution of the absorbed power.)

The main novelty of this model with respect to the previous one is the self-consistent inclusion of the depletion of the injected neutral gas while it diffuses along the axis of the source.

Defining the velocity as $\mathbf{u}+u_\theta\hat{\theta}$, with ($\mathbf{u}=u_z\hat{\mathbf{z}}+u_r\hat{\mathbf{r}}$), the continuity equation reads

$$\nabla\cdot(n_e\mathbf{u}_i)=\nabla\cdot(n_i\mathbf{u}_i)=-\nabla\cdot(n_n\mathbf{u}_n)=n_e n_n R_{ion}\ . \tag{2.28}$$

The momentum equation for ions and electrons along the longitudinal ($\hat{\mathbf{z}}+\hat{\mathbf{r}}$) and azimuthal directions respectively ($\hat{\theta}$):

$$m_i n_e \mathbf{u}_i\cdot\nabla\mathbf{u}_i=-en_e\nabla\phi-m_i n_i(\nu_i\mathbf{u}_i+\nu_{in}\mathbf{u}_n) \tag{2.29}$$

$$0=-T_e\nabla n_e+en_e\nabla\phi-en_eB_0u_{\theta e}\hat{\mathbf{z}}+m_en_e\left(\nu_e\mathbf{u}_e+\nu_{ei}\mathbf{u}_i+\frac{u_{\theta e}^2}{r}\hat{\mathbf{r}}\right) \tag{2.30}$$

$$m_en_e\mathbf{u}_e\cdot\nabla u_{\theta e}=en_eB_0u_{re}-m_en_e\left(\nu_e u_{\theta e}+\frac{u_{\theta e}u_{re}}{r}\right) \tag{2.31}$$

where the collision frequencies for electrons and ions are written as: $\nu_e(r,z) = \nu_{ion} + \nu_{en} + \nu_{ei}$ and $\nu_i(r,z) = \nu_{ion} + \nu_{in} + \nu_{ei} m_e / m_i$. The model takes into account the contribution from ionization $\nu_{ion} = n_n R_{ion}(T_e)$, electron-neutral collisions $\nu_{en} = n_n R_{en}(T_e)$, ion-neutral collisions $\nu_{in} = n_n R_{in}(|u_i - u_n|)$ and electron-ion collisions $\nu_{ei} = n_e R_{ei}(T_e, n_e)$. Now the radial and axial dynamics are analyzed separately. The radial model considers the dynamics of a magnetized plasma in an infinite cylinder, assuming longitudinal current ambipolarity ($\mathbf{u}_e = \mathbf{u}_i$). The main results are the following:

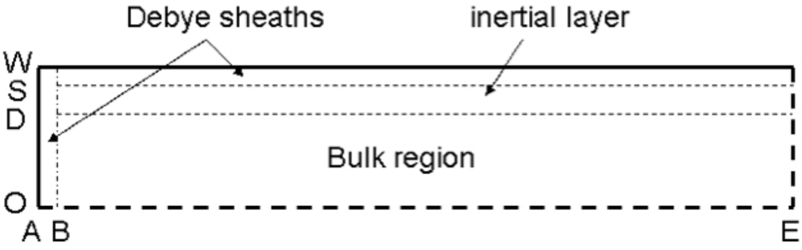

Figure 2.3: Sketch of the different plasma regions in the domain as in Ref. [27].

- in the magnetized regime, the radial quasineutral structure consists of a bulk diffusive region plus a thin inertial layer, of thickness equal to about a local electron gyroradius; the transition between the two regions occurs when the electron azimuthal velocity is of the order of the electron thermal velocity;
- the plasma pressure in the bulk region is balanced by the magnetic confinement force, whereas the electric force is much smaller;
- the ion azimuthal drift is always negligible;
- the inertial layer, where electron inertia effects are dominant, provides the correct value of the electron azimuthal energy that is later lost at the wall by the collected electrons;

As concerns the axial dynamics, a model is obtained as the radially-averaged approximation to the 2D fluid equations, in order to have z be the only independent variable. The density, for example, becomes:

$$n_e(z) = \frac{2}{R^2} \int_0^R r n_e(r,z) dr \tag{2.32}$$

where $n_e(r,z)$ comes from the radial model. The model starts from the axial fluid equations of motion and the continuity equations, and introduces a set of normalized variables. Similarly to the findings in the radial model, the i-n collisions only have a marginal role in the plasma axial dynamics and can be safely disregarded in the analysis of the axial plasma response. Nevertheless, i-n collisions can still be important for the neutral dynamics, which are not taken into account.

Finally, a global energy balance is carried out in order to determine T_e and the total ionization current in the form $I_m = e\dot{m}/m_i$, valid for singly charged ions. If lateral-wall losses can be neglected (an assumption that is reasonable because there can be very good radial confinement with only a small amount of electron azimuthal current), then, for a given absorbed power, a trade-off has to be made between the injected mass-flow and the plasma temperature, which mirrors the well-known trade-off between thrust and specific impulse.

While the radial losses are negligible for high enough values of the magnetic field intensity (higher than about 600 G), there is instead no confinement at all near the rear wall. These high losses seem to place the internal efficiency below 40%. The article, therefore, suggests a design modification: to create a magnetic mirror near the rear wall.

2.5 Plasma Acceleration in the Magnetic Nozzle

The last step is the investigation of the acceleration of a collisionless plasma jet with a large radial gradient of the plasma density.

2.5.1 Semi-analytic Fluid Models

Ahedo et Al.

In [28] Ahedo and Merino extended to two dimensions the 1D fluid model developed by Ahedo in [29]. In the nozzle of a Helicon Plasma Thruster, due to the plasma expansion, the ambipolar electric field induces a supersonic ion beam; since this beam is current free, there is no need for an external electrode to neutralize the exhaust. Ahedo [29] analyzes the influence of the formation of a Current-Free Double Layer (CFDL) in a de Laval (i.e., convergent-divergent) nozzle on the propulsion parameters. In 2009, Ahedo and Sanchez [30] presented a model of the formation of a stationary CFDL in a collisionless 3-species plasma expanding through a de Laval nozzle. There are two electrons species following the

Boltzmann relation at the temperatures T_h (hot) and T_c (cold), but the ion density is found by imposing the continuity and energy equations. More recently in 2011 [31], the same analysis was specialized to a HDLT, and the propulsive parameters were assessed.

Three species are considered, as in the older model by Sato and Miyawaki [32], but the ion properties are found as in the model by Andrews and Allen [33], where four particle groups were considered. The densities are written as:

$$\begin{cases} n_{e,h} = n_{e,h0} e^{e\phi/kT_h}, \quad n_{e,c} = n_{e,c0} e^{e\phi/kT_c} \\ n_i = \dfrac{G_i}{A}\left(\dfrac{2e\phi}{m_i}\right)^{-1/2} \end{cases} \tag{2.33}$$

where G_i is the mass flow in [1/s], the area A varies along the axis according to the convergent-divergent design of a de Laval nozzle: $A(z)/A_T = \sigma - (\sigma - 1)e^{-z^2/L^2}$, where $\sigma = A_E/A_T$, A_T is the area at the throat section, A_E is the area at the exit section. The densities and the area function are used in Poisson's equation.

The non-dimensional particle flux (in each quasineutral region) is studied as a function of the variables:

$$\bar{n}_{e,i} = \frac{n_{e,i}}{n_0}, \quad \bar{u}_i = \frac{u_i}{\sqrt{T_c/m_i}}, \quad \psi = -\frac{e\phi}{T_e}, \quad \alpha = \frac{n_{h0}}{n_0}, \quad \tau = \frac{T_h}{T_c}$$

where $n_0 = n_{h0} + n_{c0}$.

$$g(\psi) = \bar{n}_e \bar{u}_i = \sqrt{2\psi}[(1-\alpha)e^{\psi} + \alpha e^{-\psi/\tau}] \tag{2.34}$$

In the three species plasma, $g(\psi)$ presents from one to three local extrema depending on the parameters α (the density ratio of the hot electrons to the total) and τ (the ratio between the hot and the cold electron species), as reported in fig. 2.4. For $T_h > (5 + \sqrt{24}T_c \sim 9.9T_c$, two maxima appear at $-e\phi \sim T_c/2$ and $-e\phi \sim T_h/2$. For some values of $\alpha = n_{h0}/n_0$ a quasi neutral solution does not exist: in the interval $\alpha_1(\tau) < \alpha < \alpha_2\tau$ no fully quasineutral plasma expansion is possible.

The influence of the second species of electrons is shown in fig. 2.5, where the potential drop and the energy beam increase as α increases, which is expected because the energy stored in the upstream plasma increases too. But when $n_{h0}/n_0 \sim 0.46$ something happens: the potential profile has the maximum steepening and the potential value at the sonic point changes from $\sim T_c/2e$ to $\sim T_h/2e$, relative to the upstream plasma. In addition, the energy of the ion beam increases very little after this value.

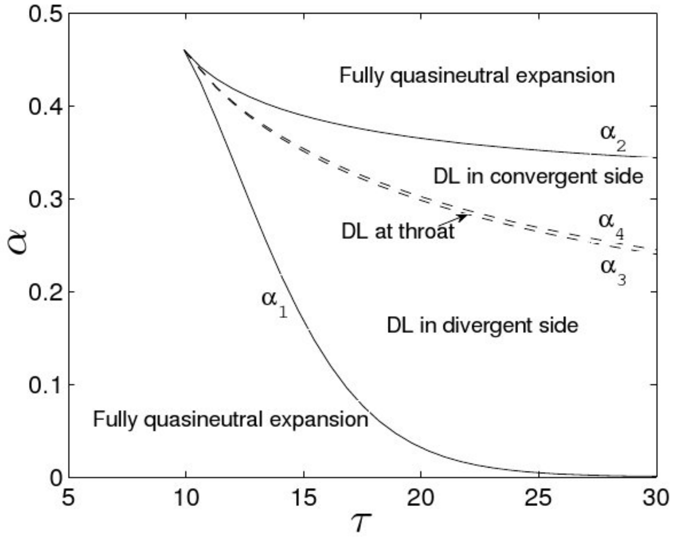

Figure 2.4: Normalized particle flux $g(\psi)$ vs hot electron normalized density α and hot to cold electrons temperature τ. Between the solid lines the DL will form: between α_1 and α_3 the DL appears in the divergent zone, while between α_4 and α_2 the DL is on the convergent side. From [29].

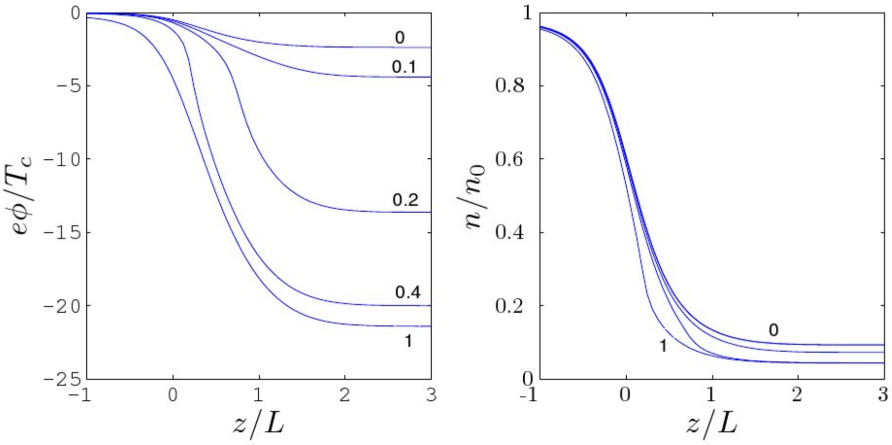

Figure 2.5: Representation of the influence of a second species of electrons: normalized potential and density vs the normalized spatial coordinate, for different values of hot electron densities. Profiles for $T_h = 9T_c$, $A_E = 3A_T$, for several $n_{h0} = n_0$. From [29].

The value of α, moreover, defines the position of the DL, but DLs have different characteristics when they are in the convergent or divergent zones. From Ahedo's analysis, the simple monotonic DL will exist only in the divergent nozzle.

The thrust and the specific impulse are:

$$T = G_i M_i u_{iE} + p_{eE} A_E, \quad I_{sp} = T/m_i G_i \tag{2.35}$$

where G_i is the ion flux, u_{iE} is the exhaust velocity and $p_e = T_h n_h + T_c n_c$ is the electron pressure. The relative dimensionless parameters are the thrust coefficient and the specific impulse coefficient (a measure of the exhaust velocity compared to the sound speed at T_{e0}):

$$c_F = \frac{F}{p_e 0 A_T}, \quad c_I = \frac{I_{sp} g_0}{\sqrt{T_{e0}/m_i}} \tag{2.36}$$

where g_0 is the gravity acceleration and all 0 values refer to upstream conditions.

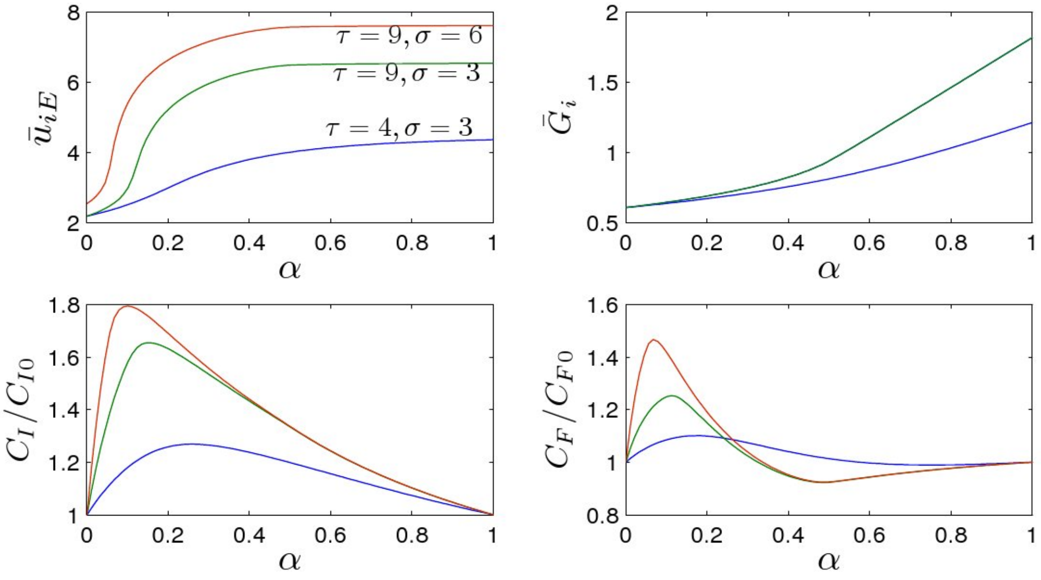

Figure 2.6: Propulsion coefficients vs hot electron normalized density α, for different hot to cold electrons temperatures τ and nozzle configurations σ. From [29].

The conclusions which can be drawn from the analysis of figure 2.6 are:

- Introducing a second species always means a gain in the specific impulse, the gain is bigger than the one due only by the increasing internal energy.
- The maximum propulsion gain can be increased either by increasing the temperature of the electrons (ref. [34]) or by increasing the magnetic field strength (i.e. the nozzle expansion area [35]).
- There are both gains and losses in c_F/c_{F0} depending on α, τ, σ.

- The DL has no role in the propulsion gains, only the presence of the hot electrons does. The DL formation is just a consequence of the expansion of the three species plasma.

When the plasma jet, at the entrance of the magnetic nozzle, is uniform, current-free, with no swirling (i.e. ion rotation) and no Hall current, the 1D model is valid for predicting the variation of the biggest part of the relevant physical quantities, however, 2D effects are more important for quantities that experience large radial variations, such as the plasma density and the ion current density.

When the focused nature of the plasma jet is taken into account, the radial structure of a plasma produced inside a cylindrical dielectric vessel of radius R with a strong applied axial magnetic field B_0, parallel to the vessel, is represented as a bulk diffusive region and two thin layers (a quasineutral inertial layer and the Debye sheaths). The main differences between the uniform and focussed jet cases are in the radial profiles of the plasma density and related magnitudes. These quantities have a big impact on the efficiency of the ion acceleration process along the nozzle: the efficiency is higher for the focussed jet case, because of the concentration of most of the plasma near the axis, where radial forces are small. As a matter of fact, the radial expansion of the plasma jet reduces the thrust efficiency.

2.5.2 Numerical Models

Winglee et al.

In [36] Winglee et al. develop 3D fluid simulations to investigate the effect of magnetic nozzles near the source and the far field characteristics of the plasma stream that expands into free space. In particular, the ability of a magnetic nozzle system to provide collimation of a plume from a plasma thruster is fundamental in increasing the propulsive efficiency that accounts for the conversion of the thermal energy in axial ion velocity. The simulations also do not include neutral interactions, since the hypothesis of collisionless expansion is reasonable when looking at the expansion of the plasma into free space. Moreover, the code does not treat the physical processes within the source region itself (i.e. plasma wave coupling and ionization), so that the plasma properties upstream the nozzle are given as a boundary condition.

It is shown that the magnetic nozzle can be very important in shaping the characteristics of a plasma plume. Most important is the result that the plasma can be guided by the magnetic nozzle without having to be strictly tied to the magnetic field lines. Successful operation of the nozzle (i.e. improved plasma efficiency through the use of the nozzle) can be achieved if the plasma enters the nozzle with a velocity less than the Alfven speed and with a low Beta (that is, the ratio of the thermal pressure to the magnetic field pressure).

Meige et al.

In [37] Meige, Boswell et al. developed an hybrid code for the simulation of a current-free DL in an expanding plasma. The ions are treated kinetically as macroparticles, while the electrons as a fluid following the Boltzmann relation: $n_e = n_0 e^{e\phi/(k_b T_e)}$, where the reference density $n_0(t)$ is found by imposing the equality of electron and ion flux at the boundaries of the domain. The model takes into account the ion-neutral charge exchange and elastic collisions; both kinds of collision are modeled taking into consideration the three-dimensional velocity of the ion that experiences the collision.

In order to achieve the steady state, the ions that leave the system are reloaded into the system with a Maxwellian distribution. The effect of the plasma expansion is simulated by removing the particles from the system at a frequency that depends on the particle position, as sketched in Fig. 2.7a.

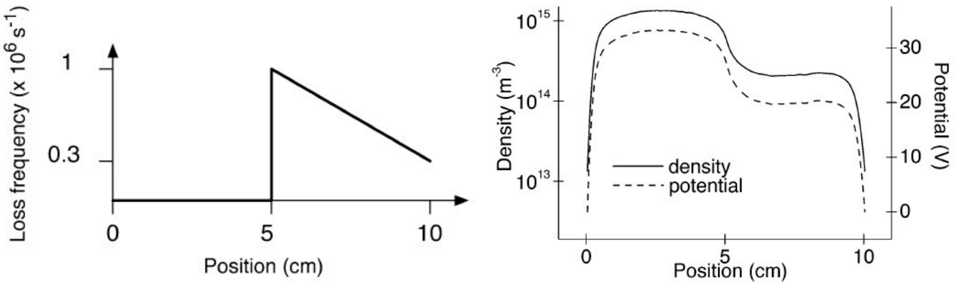

(a)

(b)

Figure 2.7: On the left: particle loss frequency vs position in the source; this allows the simulation of plasma expansion in [37]. On the right: density and potential vs position, as observed in [37]; a potential drop of 14 V over a few Debye lengths is observed, and suggests the formation of a DL.

Due to the expansion, a sharp drop in the electron density is created and, as a consequence of the resulting potential drop, a supersonic ion beam is observed downstream of the DL. A novelty presented in this paper is the way the inductive heating is simulated, without solving electromagnetic field equations. The heating is modeled by using experimental data taken from the *Chi Kung* helicon system, shown in figure 2.8,when an RF electric field E_y at $\omega/2\pi$ =10 MHz is applied in the source region in the direction normal to the z axis. The control parameter in the code is the current density amplitude J_0, which is uniform in the source region. J_0 determines the electric field amplitude and avoids electrons overheating. The heating mechanism described appears not to introduce any anomalous spatial variation of the potential, and thus is particularly suitable for the modeling of the ion acceleration in the *Chi Kung* system.

Summarizing, the relevant features of this paper are:

- The density profile determines a potential profile that shows a drop compatible with the formation of a current-free double layer. As expected, the formation of this current-free double layer is subject to the choice of the loss frequency imposed, i.e. the expansion rate, as shown in Fig. 2.8a.

- The simulation shows a high energy ion beam downstream of the DL structure.
  On the other hand, the electrons are in Boltzmann equilibrium everywhere in the system, at the same temperature.
  These results agree with some theories and are in contrast with others. In 1970 Andrews and Allen in [33] investigated the formation of a ’double sheath’ (later called DL) in an expansion zone in a gas discharge tube. The species considered in this work are four: thermal electrons, accelerated electrons, thermal ions and accelerated ions. More recently, this same procedure was followed by Lieberman in ref [38]. In that work, however, the accelerated electron distribution is considered to be near half-Maxwellian, rather than monoenergetic.
  In 1981 Perkins in [39] introduced the definition of the ‘current free double layer’ (CFDL). Perkins makes the hypothesis of the existence of a single electron species at constant temperature: the CFDL forms without the need for two different electron temperatures. Finally, in 1992 Sato and Miyawaki in [32] showed the formation of a CFDL in a two electron temperature plasma (cold downstream and hot upstream). Recently this set up has been improved by Ahedo and Sanchez in [30].
  The simulations conducted by Meige [37] seem to confirm that a single electron population in Boltzmann equilibrium is sufficient for realizing a CFDL.

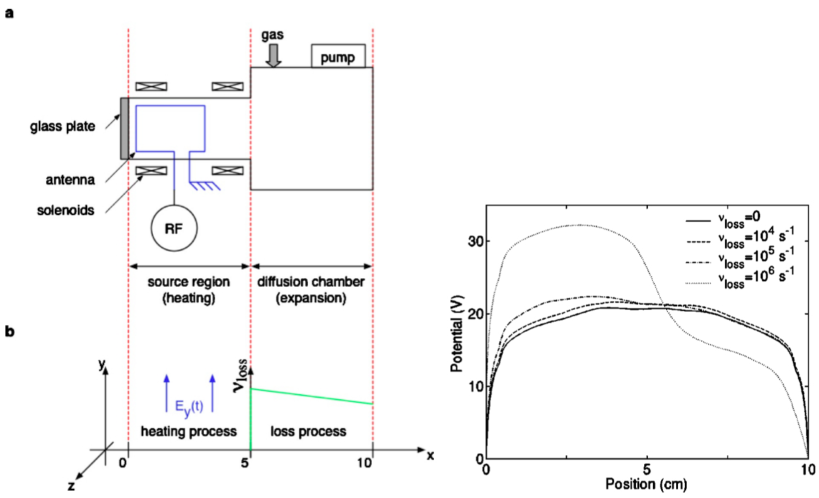

(a) **(b)**

Figure 2.8: On the left: experimental and numerical configuration used in [37]. The numerical model is 1D in space, as all calculated quantities depend on the longitudinal position in the chamber (x axis). The electron heating in the numerical model relies on experimental data from the Chi-Kung horizontal helicon system, and is due to a uniform RF electric field at 10 MHz that lies in the yz plane. The plasma expansion in the diffusion chamber is modeled with a loss process that removes charged particles at a given loss frequency.
On the right: plasma potential as a function of the axial position, obtained for the different loss frequencies, at a pressure of 1 mTorr.

This model seems to be fast and to address all the issues of the helicon thruster except the plasma detachment from the magnetic field lines. However, the electron heating reproduces specifically the experimental Chi-Kung apparatus, and thus is not suitable for the description of other systems. Moreover, PIC codes are known to have some weaknesses: to have a good statistical sample, the simulation requires a large number of particles, thus strong gradient regions, e.g. a DL, are not easily addressed.

PPDL

Very similar to the model proposed by [37] is PPDL (“Padua Plasma Double Layer”): an electrostatic hybrid code with PIC ions and Boltzmann electrons, developed by Carlsson and Manente [40]. The main novelty of PPDL is the implementation of an implicit Poisson solver, that embeds the charge conservation. This feature guarantees numerical stability for time steps longer than the electron plasma period and cell sizes larger than the Debye length.

The goal of this code is the simulation of a current free double layer in an expanding magnetic field, thus PPDL does not include an electron heating module. However, even with these limitations, the potential drop and the supersonic ion beam are observed (fig.2.9).

2.6 Complex Numerical Models

In the mechanism of the coupling of the helicon waves to the plasma, the plasma response to the energy deposition plays an important role. In fact, the plasma response is contained in the conductivity tensor that appears in the wave equation, and in the self induced electrostatic fields. Thus, power coupling and plasma dynamics are intrinsically coupled and have to be modeled in a self consistent way. The main numerical models that allow for this self consistent treatment are summarized here.

Bose et al.

Bose et al. [42] numerically simulate the wave propagation and plasma transport in a two-dimensional axisymmetric plasma. Solving the plasma transport equation together with the Maxwell equations self-consistently, they are able to study the profile of the power deposition versus the radius in a relatively high-pressure (10 mtorr) helicon discharge.

As concerns the plasma transport equations, the electron motion is assumed to be collisional and diffusive, and the ion motion is taken to be independent of the magnetic field. As concerns the wave equations, the fields and currents are split into constant and time-varying terms, where time harmonic variation is assumed. The ion response to the time-varying fields is neglected and the electrons are assumed to have a Maxwellian distribution. The antenna is considered only in an azimuthal symmetric configuration (mode m=0). Under these hypotheses the sinusoidal steady state version of Maxwell's equations, Ohm's law and the charge transport equation are integrated numerically using the semiconductor equipment modeling software (SEMS) developed at NASA Ames [43].

The self consistent model consists of two modules implemented in SEMS: the first implements the plasma transport and heating, along with the equations for the compressible gasdynamics of neutrals; the second implements Maxwell's equations in a dispersive lossy media, and is dedicated to the wave propagation and power deposition. The self-consistency between the two modules is obtained by exchanging relevant pieces of information at every time step. The power profile averaged over the RF period is obtained from

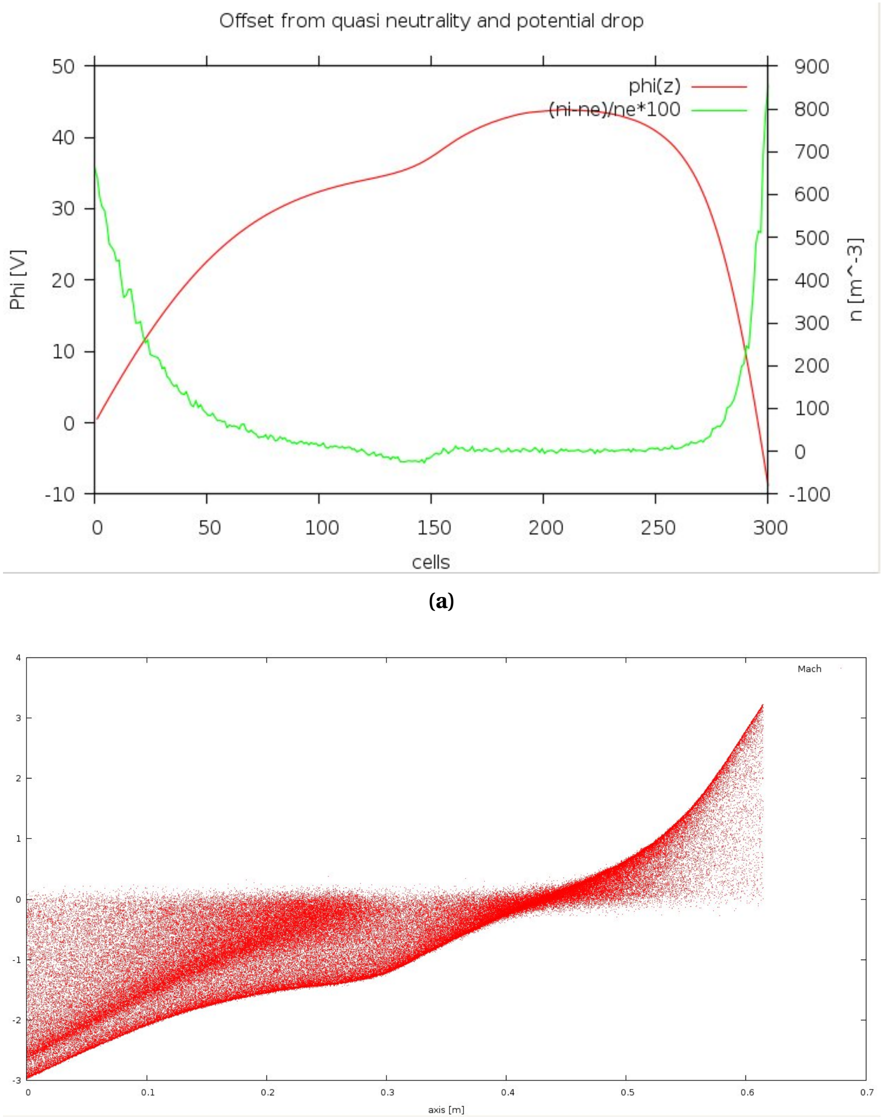

(a)

(b)

Figure 2.9: On the top: In red is potential vs position, in green relative difference between densities of ions and electrons; a deviation from quasi-neutrality can be observed corresponding to the jump in the potential profile. On the bottom: Ion Mach number vs position; the supersonic ion beam due to the acceleration in the DL is visible. The simulation is run with the following parameters: $n_0 = 10^{12}$ m^{-3}, $T_i = 0.1$ eV, $T_e = 10$ eV, according to [41]. The exit in space is located at the left of the domain, the spacecraft wall is on the right.

the wave model and it is used in the energy equation for electrons:

$$P_{ext} = \frac{1}{2}|\mathbf{J}_w^* \cdot \mathbf{E}_w|$$

$$\Downarrow$$

$$\frac{\partial}{\partial t}\left(\frac{3}{2}n_e k_B T_e\right) + \nabla \cdot \left(\frac{5}{2}n_e k_B T_e \mathbf{J}_e\right) = -\nabla \cdot \mathbf{q}_e + P_{ext} + P_{chem}$$

here $\mathbf{J}_e = n_e \mathbf{u}_e$ is the particle flux, P_{chem} is the electron energy lost or gained due to electron impact inelastic and chemical reactions, P_{ext} is the power deposition into the plasma by the antenna, $\mathbf{J}_w$ is the complex conjugate of the wave current amplitude and $\mathbf{E}_w$ is the wave electric field amplitude. In turn, the conductivity tensor σ is obtained from the plasma module from the plasma density and temperature, and it is used in the solution of the wave equation.

The results obtained for pure Argon gas at 10 mtorr pressure, flowing at 100 Atm cm^3/min, with a total discharge power deposition of 500 W, can be summarized as follows:

- the wave propagation occurs via two modes: the large wavelength helicon mode and the short wavelength TG mode. For low imposed magnetic fields ($B < 10\,\mathrm{G}$), the helicon waves are evanescent and only the TG waves can reach the plasma core. Conversely, for high values of the imposed magnetic fields ($B > 10\,\mathrm{G}$), the TG waves are strongly damped at the plasma periphery, whereas the helicon waves reach the plasma core.

- According to what was predicted by Shamrai and Taranov in [10] and [8], the radial current amplitude falls to zero near the surface, whereas the axial current has a peak. The latter current is converted into displacement current, appearing as a space charge wave (i.e. the TG mode) that rapidly drops away from the surface due to an efficient damping.

- The figure on the left of 2.10 shows the contours of the power deposition in the chamber. In the unmagnetized case, the power deposition occurs in the skin layer near the antenna coils. As the magnetic field is turned on, a volumetric power deposition is observed, even if a consistent portion of the power is still absorbed via collisional damping of the TG waves next to the surface. In the 100 G case, two power absorption peaks can be distinguished: one occurring next to the axis and the second next to the chamber wall. The first peak is due to the power deposition by the helicon waves, while the second peak is due to the damping of TG waves near the plasma periphery. Finally, at 400 G, the power profile is highly peaked near the surface, where almost all of the power deposition occurs. These results agree with the theoretical predictions made by Arnush and Chen in [12] and [13].

- The figure on the right of 2.10 shows the contours of the electron density in the chamber. As the B field is increased, the peak in the density profile moves into the larger volume chamber, away from the helicon source, because of an increased volumetric power deposition. The peak density does not significantly increase with magnetic field, as one would expect. This is because the effective plasma volume also increases.

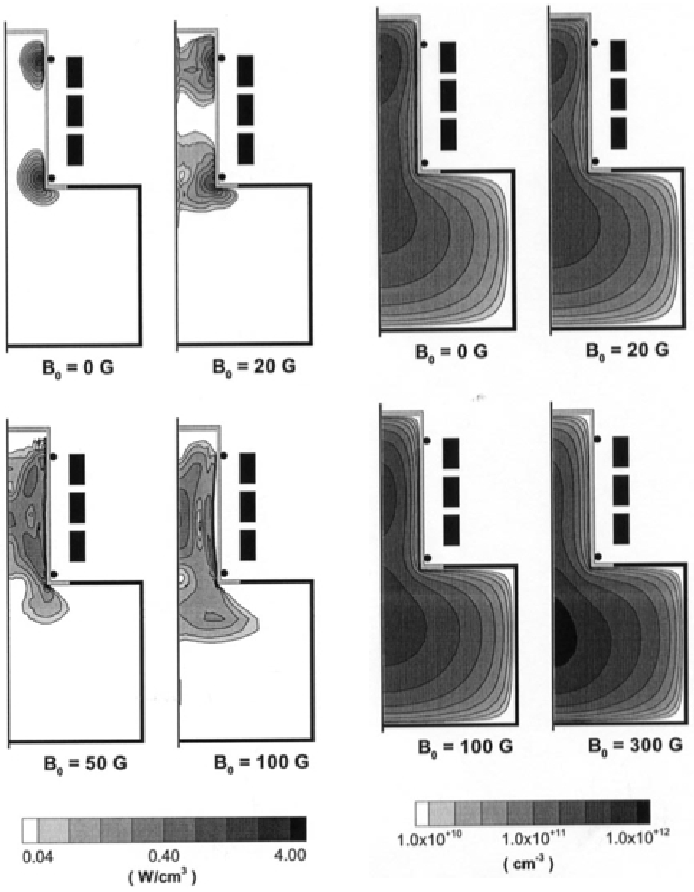

(a) **(b)**

Figure 2.10: On the left: contours of power deposition density. On the right: contours of the electron density. Simulation is for pure Argon gas at p = 10 mtorr pressure, flow rate of 100 Atm cm^3/min, and total discharge power deposition of 500 W.

The main weakness of this model is the use of a fluid approach for the plasma dynamics. The fluid approach does not describe the evolution of the electron distribution function, that is a fundamental issue in the investigation of trapping and collisionless wave-particle interactions. Moreover, this model lacks a description of the plasma acceleration in the magnetic nozzle.

Kushner et al.

In 2009, Kushner published a review paper [44] describing the Hybrid Plasma Equipment Model, which can be considered the most complete set of tools for the simulation of low temperature plasmas. This hybrid model combines different modules which address different physical phenomena; different versions of the same module use different computational algorithms, which aim to best match the operating conditions.

Indeed, this hybrid model allows one to address a wide range of physical and technological phenomena. According to [45], a proper selection of the modules should permit one to simulate a Helicon plasma source in detail. The relevant modules used in [45] are:

- **Electromagnetic Module** (**EMM**):

  This module solves the following wave equation for high frequency sinusoidal steady state, neglecting the ion current:

  $$\nabla\left(\frac{1}{\mu}\nabla\cdot\mathbf{E}\right)-\nabla\cdot\left(\frac{1}{\mu}\nabla\mathbf{E}\right)-\omega^2\epsilon\mathbf{E}=-i\omega(\mathbf{J}_a+\mathbf{j}(\mathbf{r})) \tag{2.37}$$

  here $\mathbf{J}_a$ is the antenna current density. In particular, in the implementation in [45], the EMM returns a 3D field solution for an azimuthally symmetric applied magnetic field, and the azimuthal antenna current for a m=0 mode. As input, the material properties at the boundaries are given, as well as the plasma current $\mathbf{j}(\mathbf{r})$, as a function of the position $\mathbf{r}$. (In the cases where electron heating is local, i.e. the electron energy relaxation length is much smaller than the system dimensions, a warm conductivity tensor is used to find $\mathbf{j}=\bar{\bar{\sigma}}\,\mathbf{E}$, instead.)

- **Electron Energy Transport Module (EETM)**

  This module solves the Boltzmann equation and its moments given the fields $\mathbf{E}(\mathbf{r})$, $\mathbf{B}(\mathbf{r})$ and $\mathbf{B}_{\text{static}}(\mathbf{r})$, and the species density $n_j(\mathbf{r})$. In particular, being interested in the non-local heating mechanisms, the EETM is used in the configuration that implements the Electron Monte Carlo Simulation. This module provides $\mathbf{j}(\mathbf{r})$ as a "phase derived integral of electron trajectories" [44], which contains the past history of electron acceleration by the fields $\mathbf{E}(\mathbf{r})$ and $\mathbf{B}(\mathbf{r})$.

  The outputs of this model are the electron distribution function $f_e(\varepsilon,\mathbf{r})$, the electron impact rate coefficients $k_e(\mathbf{r})$, and the source terms for electron impact processes (i.e. collision frequency per atom or molecule) $S_e(\mathbf{r})$.

- **Fluid Kinetics Poisson Module** (**FKPM**)
  Finally, the FKPM module, in the so called fully hydrodynamical version, implements the fluid equations of continuity, momentum and energy to evaluate the densities $n_j(\mathbf{r})$, the fluxes $\Gamma_j(\mathbf{r})$ and the temperatures $T_j(\mathbf{r})$ of charged particles and neutrals. Due to the tight coupling of the electrostatic fields and the densities of charged particles, this module implements the Poisson's equation to evaluate the electric potential $\phi(\mathbf{r})$ and hence the electrostatic field $\mathbf{E}_{\text{static}}(\mathbf{r})$.

The flow chart describing the information flow among the various modules is shown figure 2.11.

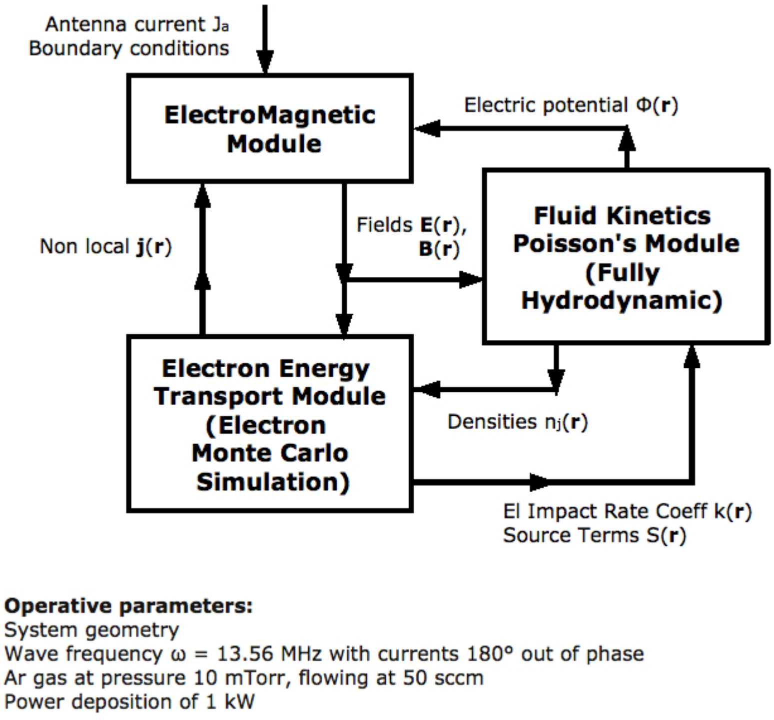

Figure 2.11: Information flow in the Hybrid Plasma Equipment model, in the implementation used for the simulation of a Helicon plasma source, as described in [45].

In [46], the objective is to investigate the coupling of electromagnetic waves to the plasma and their effects on the Electron Energy Distribution Function. In order to study the non local power deposition due to the helicon mode downstream of the antenna, the TG mode propagation is suppressed setting the term $\nabla \cdot \mathbf{E}$ to zero (i.e. quasi neutrality is imposed). The magnetic field is allowed to vary between 20 and 300 G. As a result of the self-consistent simulation, the Landau damping term accounted for at most 15% of the total collision frequency, and resulted to be most influential in the low electron density or high magnetic field regimes. Under these conditions, the increase in the effective collision frequency due to Landau damping can shift the position of the peak power deposition to higher magnetic fields, as shown in Fig. 2.12. However, the Landau damping effect has only a minimal effect on the power deposition efficiency.

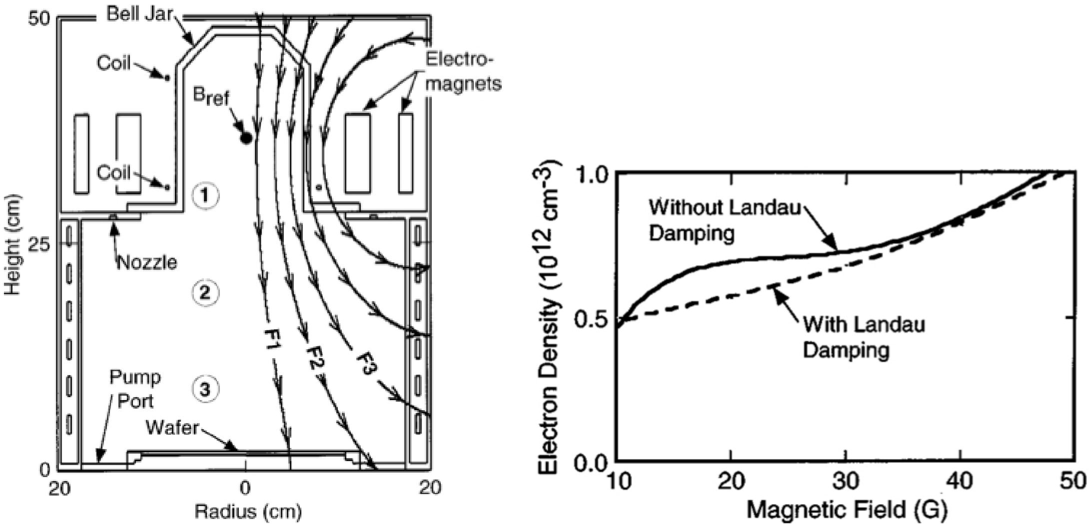

(a)

(b)

Figure 2.12: On the left: The Trikon PMT M0RI helicon source: experimental geometry used in the simulation in [46]. Simulation parameters: Argon gas at 10 mTorr, 1 kW power deposition. RF coils are operated 180° out of phase at 13.56 MHz.
On the right: on axis value of electron density as a function of static magnetic field in solenoidal geometry with and without the collisional Landau damping term.

Increasing the magnetic field, the electric field propagation progressively follows the magnetic field lines and significant power can, indeed, be deposited downstream. The tails of the EEDFs are enhanced in the downstream region, indicating some amount of electron trapping and collisionless acceleration by the axial electric field for electrons having long mean free paths.

By including the divergence term in the solution of the wave equation, the TG modes are also included in the wave equation solution. The results indicate that the effect of the TG mode is to redistribute the power deposition near the coils. The propagation of the helicon component is little affected, particularly at large magnetic fields, when the TG mode is damped: for the m= 0 excitation, the TG mode does not significantly contribute as a heating mechanism.

More recently in [47], the Electromagnetic Module was upgraded in order to account for the three dimensionality of the power coupling in the helicon source, for the $m \neq 0$ cases. As a first case, the electrostatic terms are excluded from the solution of Maxwell's equations in order to reproduce the transition from the inductive coupling to the helicon wave mode for an m = +1 plasma source. It was shown that plasma sources may have helicon-like waves but still operate in a dominantly inductively coupled mode. Secondly, the electrostatic terms are included in the solution of Maxwell's equations. The results show that the biggest fraction of the power is deposited at the periphery of the source and that the helicon damping length is shortened.

The Hybrid Plasma Equipment Model, in the configuration proposed in [47], is clearly the most complete description of the plasma evolution in a Helicon source. The model is very complicated and allows one to treat the most disparate cases, but it was not designed for the simulation of a Helicon thruster, thus a more specific version should be developed in order to address properly thruster performance.

3

Large Scale Simulations of Plasmas

In this chapter we discuss some of the issues arising as we attempt to define the most appropriate approach to modeling a complex physical system. The later chapters employ a variety of types of model, and in this chapter we lay the groundwork which determines which types of model are most effective. As we shall see, we need different types of models in different circumstances. Some of the models employed in this thesis are very detailed indeed, some are relatively simplified, and yet both are necessary to understand the system we are studying, as we shall see.

3.1 Purposes of Modeling

In Computational Physics, a useful and reliable numerical model builds upon several important features:

1. purpose for modeling;
2. selection of the important physics;
3. mathematical models;
4. numerical methods of solution;
5. code implementation;
6. testing procedure;
7. error analysis and limits of validity;
8. proper use of the code to run Numerical Experiments;

9. analysis of the results.

It should be stressed that each of the points above is related to the others, and better solutions may come up during the development process. As a result, several iterations may be necessary. Evidently, it takes a considerable effort to overcome all difficulties, especially because unspotted errors committed in any of the points above may jeopardize the whole project.

In the field of Plasma Physics, despite the amount of energy and skill devoted to developing sophisticated numerical models, these models have not led to important breakthroughs so far. There are probably many concurrent reasons why this happens, and in particular, points 1 and 2 in the list above appear to be often underestimated or overlooked. So, what are the purposes of modeling?

- theoretical investigation, i.e. verifying whether a physical theory correctly describes a specific phenomenon;
- gaining insight into complex physical phenomena;
- design and optimization;
- indirect measurement, i.e. using the model to obtain estimates about certain physical quantities that cannot be measured otherwise.

3.2 Hybrid Models

It has become common practice to employ large scale computational models consisting of several essentially unconnected pieces, in many fields of physics and elsewhere. The pieces which form the components of the overall model are typically intended to describe subsystems within an overall physical system. So, for example, in plasma physics separate models are often employed for ions, electrons and neutrals, as well as for the electromagnetic fields which the charged particles experience. There may also be separate models for external circuits, surface interactions, and so on. If all of these subsystems were described in the same level of detail (a concept that cannot be defined here) and in a seamless way, then the term ‘multiphysics model’ is perhaps the most appropriate to use. However, in addition to there being a need to include different physical subsystems, there is often motivation to separate those systems in order to simplify the computational task, and when the parts of the physical system are separated one may find that including more or less detail about the individual components is more appropriate. Then, for example, a fluid model can be used to describe the ions, but a kinetic model to describe the electrons. This combination of different types of model for different subsystems is referred to as a 'hybrid model'.

The natural questions which arise include, how should the most appropriate types of submodels be chosen? This issue is discussed in **section 3.2.1**, where the possibilities available in plasma modeling are outlined. In this section it is argued that many hybrid models use inappropriate combinations of levels of description, so that effort put into describing one subsystem is wasted because of the lack of accuracy in the description of other subsystems.

There is another issue associated with the different levels of description of physical systems that are available. It is a general opinion of the author that the testing of any large scale simulation requires the use of as many different types of calculation, employing different levels of detail, as possible. A High Level of Detail (LOD) simulation will presumably include all the physical effects considered relevant, and thus will often make use of three spatial dimensions, and so on. Unfortunately, a high-LOD simulation is computationally expensive and typically its predictions are difficult to understand, which may imply that the model is difficult to test. On the other hand, a low-LOD calculation is generally not likely to be accurate enough to provide satisfactory simulation results, but it may be straightforward to solve and to understand. As will be described later on, the comparison of these different models may be one of the rather limited set of options available for testing the components of the overall hybrid model.

Section 3.2.2 describes the iteration of the hybrid model. It is probably conventional to employ the highest-LOD submodels available, in an iteration scheme that takes a point value from submodel 1 and passes that data to submodel 2, which then is run until it finds a solution consistent with the input it was given. It then passes point data to submodel 3, and so on. A schematic of this process accompanies many papers on the subject, and consists of a number of large boxes representing the high-LOD submodels, passing information between them. It is opinion of the author that this approach is often suboptimal, and at least should be considered more carefully. An example employing a simple plasma system will be considered. Where possible, it is preferable to pass data based on a physical understanding of the likely behavior of the submodel. In other words, if it is understood that the electron behavior reflects that they have a certain temperature, then the data passed from the electron submodel should reflect that, rather than simply passing values for (say) the electron density, which is then seen to be a derived quantity which depends on the temperature and the voltage. If the information which is passed in this example is the temperature, then the other submodels can perform a much more robust iteration than if the information which is passed is the density. In some cases the above considerations will mean that low-LOD models provide a more meaningful basis for passing information between high-LOD models than the use of point data. The low-LOD model in the example will suggest the use of the temperature, to be used in the Boltzmann expression for the electron density, as a more meaningful quantity to pass than values of the electron density obtained by the electron model for a given set of point values of other quantities.

3.2.1 Levels of Description of the Physical Components of a Plasma Source

A question that arises naturally when one begins to set up a hybrid model is: *How should the appropriate level of detail (LOD) for each submodel be chosen?* One can easily define an ‘ideal approach’, which is probably very close to the following:

1. first, one should identify the quantities of interest, and define the required tolerances,
2. then, the sensitivity of each quantity with respect to various parameters should be assessed,
3. parameters on which the sensitivity is high require a high precision, and hence a high-LOD model,
4. parameters on which the sensitivity is low can be evaluated with less precision, and hence a low-LOD model suffices.

Unfortunately, point 2 in the approach above is very demanding. In fact, in order to directly evaluate those sensitivities, there are just two options:

1. obtaining the sensitivities *experimentally*; this requires one to set up an experiment with the capability of measuring the quantities of interest *and* the parameters which influence them, and to run a huge test campaign where each of those parameters is varied within a prescribed range; even if a factorial design may reduce the total number of tests, this is clearly an overkill approach;

2. obtaining the sensitivities *numerically*; this can be done if a detailed multi-physics model is already available; assuming that this is the case, and assuming that the code is fully tested and validated, such a huge campaign of simulations is extremely computationally expensive, slow, and error prone.

It should be pointed out that there is no real error underlying the 'ideal approach' proposed, but the question may be ill-posed: defining a-priori the LOD of the submodels requires more information than is usually available. As another way to put it, the detailed a-priori definition of the LOD of the submodels does not appear to be an effective procedure. In fact, most often it is the accumulated experience on the system under study that suggests the modeling approach to be employed in each subsystem.

As it is extremely common in numerical modeling, an alternative approach may rely on *iterations*: for each subsystem, different submodels should be created, which use a different LOD. Comparing the results obtained with a high-LOD and a low-LOD model, may provide an order of magnitude for the required sensitivities, or it may suggest a different subdivision into submodels, so that the process is started over again.

3.2.2 Iteration and Data Exchange in a Hybrid Model

Another fundamental question that arises early in the design of a hybrid model is: *what is the best way to exchange data between the different submodels?*

The standard approach is to *pass point values*: the data to be exchanged lie on a mesh on which two submodels (called A and B) have access, submodel A keeps a set of data D_1 constant (e.g. the electron density) while it updates another set of data D_2 (e.g. the electric field); submodel B does the exact contrary (i.e., in this example it changes the electron density while maintaining the electric field constant). There are several ways to couple submodels that exchange point values:

explicit coupling: here simply submodel A updates D_1, then B updates D_2, and so on by marching forward in time; this method can be employed in the simplest cases, by staggering in time the discrete states of the two data sets, or by employing operator splitting; it may require time-steps exceedingly small due to accuracy or stability requirements.

implicit coupling: here D_1 and D_2 are updated together, i.e. their new state is computed self-consistently; in order to do this, one of the following iterative methods are employed:

1. Picard algorithm: this is an extension of the explicit coupling, where A corrects the state of D_1, and B corrects the state of D_2, alternately, until the corrections fall below a prescribed tolerance; this method lacks of a theory for convergence, and even when it converges, it may converge too slowly or to the wrong solution;
2. Newton algorithm: this method is much more robust than the above, and it is guaranteed to converge if the first guess is sufficiently close to the solution; as a drawback, it requires the calculation of the Jacobian matrix of the coupled system, and such a matrix must be updated at each time step;
3. quasi-Newton Jacobian-free algorithm: this approach is a simplification of the Newton method, in that it uses a difference approximation for Jacobian-vector products, as occurs in iterative solvers algorithms such as GMRES; it has the advantage that the Jacobian matrix does not have to be computed explicitly.

Whatever the coupling method used, passing point values may not be the most cost-effective way to exchange data between submodels.

An alternative approach may be suggested, which uses the low-LOD versions of the submodels to exchange data between the high-LOD counterparts. The low-LOD models may be coupled with each other using one of the aforementioned standard algorithms, perhaps passing point values of the ‘most stable’ quantities; if the level of description is sufficiently low, one could even pass fitted curves or surfaces, obtaining a further speedup. Within the same subsystem, submodels at different LOD would interact with each other two-ways: from high-LOD to low-LOD, we employ *model reduction*; from low-LOD to high-LOD, we employ *extrapolation*, which should use data from the previous detailed solution.

This multi-LOD approach to hybrid modeling is believed to have several interesting characteristics:

1. it combines the advantages of the high-LOD models, which can address the relevant physics, but are computationally intensive and difficult to test, with the advantages of the low-LOD models, which are not accurate enough, but they are an agile tool to use and couple with each other, and they are easy to test against analytic results;

2. within each subsystem, different LOD models can be tested against each other;
3. coupled low-LOD models often make it possible to assess the sensitivity matrix for the relevant quantities, which is obtained from the Jacobian matrix; hence, there is better control of the errors and the uncertainties produced in the simulation;
4. if high-LOD submodels can be restarted 'smoothly' at each iteration, faster convergence and better robustness is expected, especially in steady-state problems, for two main reasons:
    (a) low-LOD submodels run much faster than their high-LOD counterparts,
    (b) the coupled low-LOD submodels effectively cut-off the high-frequency and localized phenomena that would effect the high-LOD solution.

4

The Use of a Simple Global Model in Creating a Hybrid Model

4.1 Preliminary Analytic Modeling

Characteristic quantities in cold plasmas may vary by several orders of magnitude. Hence, it is critical to make zeroth-order analytical estimates of such quantities, providing some preliminary understanding of the phenomenon at hand. Most important, a well designed analytical model can usually suggest which facet of the physics needs more insight, and it can easily be a useful guide in the set up of a more detailed model.

Section 4.1.1 discusses the effect of neutral dynamics on the plasma production in the source, and ultimately on the propulsion parameters of the thruster. In order to simplify the notation and to give sufficient generality to the results, non-dimensional parameters will be introduced where appropriate, and a relation between these parameters will be derived, which describes the most relevant physics.

Section 4.1.2 couples the neutral and electron dynamics via the simultaneous solution of three 0D global balances, providing useful order-of-magnitude estimates of the average neutral and electron density in the source, and of the electron temperature. The introduction of two free parameters permits one to determine a wide range of acceptable solutions, which will need further investigation. Characteristic mean-free-paths for the main collisional processes are then obtained, enabling the formulation of a more detailed model (Sec. 4.2).

4.1.1 Neutral Dynamics and Propellent Utilization

The most fundamental requirement of a thruster is its capacity to use all the propellent. In the case of a plasma thruster, this is equivalent to the capability of ionizing all the neutral gas that is injected into the source: ideally, no neutral molecule should escape from the source without being ionized and subsequently accelerated. Focusing on the particles that are escaping from the source through the exit section, the ratio of the number of ions to the total number of particles (flowing per unit time) is called the *ionization efficiency*:

$$\eta_{iz} = \frac{[\dot{N}_i]^{out}}{[\dot{N}_{tot}]^{out}} \,. \tag{4.1}$$

In steady-state, the definition above can be expressed as a function of the neutral gas parameters only, as

$$\eta_{iz} = 1 - \frac{[\dot{N}_g]^{out}}{[\dot{N}_g]^{in}} \,, \tag{4.2}$$

where $[\dot{N}_g]^{in}$ is the number of neutral gas molecules introduced per second into the source through the injector, and $[\dot{N}_g]^{out}$ is the number of neutral gas molecules that escape per second from the source without being ionized.

The production of plasma in the source is due to the ionization of neutral gas by electron impact. The efficiency of this process depends linearly on the product of the neutral and electron densities, and it depends non-linearly on the electron temperature (or more generally, on the average kinetic energy of the electrons; strictly the dependence is even more complex than this). A simple global balance equation can be set up for the total number of neutral particles in the source,

$$\frac{dN_g}{dt} = [\dot{N}_g]^{in} - [S_g]^{iz} + [S_g]^{rec} - [\dot{N}_g]^{out}, \tag{4.3}$$

where $[S_g]^{iz}$ is rate of production of particles per unit volume due to ionization, which can be written as

$$[S_g]^{iz} = K_{iz} \langle n_g \rangle \langle n_e \rangle V_s \,, \tag{4.4}$$

where $\langle n_g \rangle$ and $\langle n_e \rangle$ are the average densities of neutrals and electrons respectively, and V_s is the volume of the plasma source; K_{iz} is the *rate coefficient* for electron impact ionization, which depends on the ionization cross section $\sigma_{iz}(\varepsilon)$ and on the Electron Energy Distribution Function (EEDF) by means of the following integral:

$$K_{iz} = \int_0^\infty \sigma_{iz}(\varepsilon)\, v(\varepsilon)\, F(\varepsilon)\, d\varepsilon \,. \tag{4.5}$$

Here, $F(\varepsilon)$ is normalized according to $\int_0^\infty F(\varepsilon)\, d\varepsilon \equiv 1$. Being the focus of this section on the neutral dynamics, the *ionization frequency* $\nu_{iz} = K_{iz}\langle n_e \rangle$ will be used to simplify the notation.

In Eq. 4.3 the source term $[S_g]^{rec}$ reflects the creation of neutrals by means of *recombination*; many processes may lead to recombination, but for a small plasma source *wall recombination* is always the dominant effect. Wall recombination is extremely inconvenient for a thruster, as it drives a considerable amount of energy into heating the walls, and hence it causes the overall efficiency to drop. In the following treatment wall recombination will be neglected, under the assumption that the final design of any reasonable space thruster must reduce such 'wall losses' well below the level of accuracy of the analyses carried out here.

Since the gas is expanding into vacuum, it is reasonable to assume that the sonic speed is reached at the exit section. The actual value of the speed at the exit section depends on the type of thermodynamic process the gas has undergone along the source (e.g., adiabatic, isothermal, or isobaric); here it will be simply addressed as u_L to indicate the location $z = L$ along the source. Under the assumption of sonic flow, $[\dot{N}_g]^{out}$ can be expressed in terms of known quantities and Eq. 4.3 can be used to evolve the average neutral density (recall that $\langle n_g \rangle = N_g / V_s$), according to

$$V_s \frac{d\langle n_g \rangle}{dt} = [\dot{N}_g]^{in} - \nu_{iz}\langle n_g \rangle V_s - u_L \langle n_g \rangle A_s \,, \tag{4.6}$$

which has the steady state solution

$$\langle n_g \rangle = \frac{[\dot{N}_g]^{in}}{\nu_{iz} V_s + u_L A_s} \,. \tag{4.7}$$

It is easy to determine the ionization efficiency of the source predicted by this model: according to Eq. 4.2

$$\eta_{iz} = 1 - \frac{u_L \langle n_g \rangle A_s}{[\dot{N}_g]^{in}} = \frac{\nu_{iz}\langle n_g \rangle V_s}{u_L \langle n_g \rangle A_s + \nu_{iz}\langle n_g \rangle V_s} = \frac{\nu_{iz} V_s}{u_L A_s + \nu_{iz} V_s} \,, \tag{4.8}$$

an expression that can be rewritten in terms of a single non-dimensional parameter

$$\xi = \frac{\nu_{iz} V_s}{u_L A_s} \tag{4.9}$$

as

$$\eta_{iz}(\xi) = \frac{\xi}{1 + \xi} \,. \tag{4.10}$$

As expected, $\eta_{iz} \to 0$ for $\nu_{iz} \to 0$ (that is, no ionization occurs), and $\eta_{iz} \to 1$ for $\nu_{iz} \to \infty$ (i.e. all the gas is ionized before reaching the exit section).

Using Eq. 4.10, the expression for the average density (Eq. 4.7) can be manipulated to get

$$\langle n_g \rangle = \frac{[\dot{N}_g]^{in}}{\nu_{iz} V_s} \eta_{iz}(\xi) \ , \tag{4.11}$$

an expression that will be discussed later on in this section.

The 0-dimensional description presented so far does not take into account the fact that the density decreases along the source as a result of the ionization itself. In fact, the neutral density at the exit section can be considerably lower than the average density in the source, and hence the flux of particles $[\dot{N}_g]^{out}$ can be much less than what was used here. As a result, Eq. 4.10 considerably underestimates the ionization efficiency η_{iz} of the plasma source, and also the average neutral density (according to Eq. 4.11).

To overcome such limitations a more detailed description of the gas dynamics along the source is needed. As a first attempt, a 1D diffusive analytic model is presented hereafter, capable of shedding light on the phenomena that the 0D model failed to describe, and at the same time being useful for investigating what parts of the physics will need further analysis.

The average neutral density obtained from the 0D model suggests that the gas can be treated as a rarefied gas with long mean free path (i.e. the Knudsen number is > 1). This approximation gets more reasonable as the gas is ionized along the source, while it may not be sufficiently accurate in the region close to the injector. Due to the slender geometry of the source, i.e. a cylinder with L/R > 10, it is reasonable to assume that the mean axial momentum of the particles injected into the source is completely transferred to the walls after essentially all the gas has collided with the walls, that is, after the gas has travelled a few ‘mean free paths‘ along the axis. This picture suggests that the neutral particles escape from the system by performing a *random walk* along the cylinder axis, with step size of the order of the radius R. Such a random walk is naturally described by a *diffusion process*, with a diffusion coefficient

$$D_g = c\, R\, v_{g,th} \ , \tag{4.12}$$

where c is a non-dimensional constant that comes from the proper averaging of the angle of bouncing off the wall, and $v_{g,th}$ is the thermal speed of the neutrals.

Assuming that this diffusion process holds along the whole length of the source, and that D_g can be effectively treated as constant, the 1D steady-state model equation is

$$-D_g \frac{d^2 n_g}{dz^2} = -\nu_{iz} n_g \,, \tag{4.13}$$

with inflow boundary condition at $z = 0$ (non-homogeneous Neumann BC), and sonic boundary condition at $z = L$ (homogenous mixed BC):

$$\begin{cases} \dfrac{dn_g}{dz} = -\dfrac{[\dot{N}_g]^{in}}{A_s D_g} & \text{at } x = 0, \\ \dfrac{dn_g}{dz} = -\dfrac{u_L}{D_g} n_g & \text{at } x = L. \end{cases} \tag{4.14}$$

It is useful to introduce two new quantities, the *characteristic length*

$$L_c = \sqrt{\frac{D_g}{\nu_{iz}}} \tag{4.15}$$

and the *characteristic speed*

$$u_c = \sqrt{D_g \nu_{iz}} \,, \tag{4.16}$$

which permit one to define two new non-dimensional parameters:

$$\chi = \frac{u_c}{u_L} \qquad \psi = \frac{L}{L_c} \,. \tag{4.17}$$

These parameters permit the solution to Eq. 4.13 with boundary conditions (4.14) to be written in the following compact form:

$$n_g(z) = \frac{[\dot{N}_g]^{in}}{A_s u_c} \frac{e^{-z/L_c}}{1 - \alpha\beta^2} \left[1 + \alpha\, e^{-2(L-z)/L_c}\right] \tag{4.18}$$

where α and β are non-linear bounded functions of χ and ψ:

$$\alpha(\chi) = \frac{\chi - 1}{\chi + 1} \qquad \beta(\psi) = e^{-2\psi} \tag{4.19}$$

According to the definitions above, $\alpha \in [-1, 1]$ and $\beta \in [0, 1]$. Analogously to the procedure used for the 0D model, the ionization efficiency of the source can now be obtained from Eq. 4.2, observing that $[\dot{N}_g]^{out} = [\dot{N}_g]^{in}(1 - \eta)$:

$$[\dot{N}_g]^{out} = A_s u_L n_g(L) = [\dot{N}_g]^{in} \frac{\chi\beta(1+\alpha)}{1 - \alpha\beta^2} \,, \tag{4.20}$$

which gives $\left(1-\eta\right)=\left[\chi\beta\left(1+\alpha\right)\right]/\left(1-\alpha\beta^2\right)$. After some algebra it is possible to get rid of α, obtaining the final expression for η_{iz} as predicted by the 1D model:

$$\eta_{iz}\left(\chi,\psi\right) = 1-\frac{2\beta}{\chi\left(1-\beta^2\right)+\left(1+\beta^2\right)}\ . \tag{4.21}$$

It would be interesting to compare the just obtained expression for the ionization efficiency with the results from the 0D model, but unfortunately Eq. 4.10 and Eq. 4.21 make use of different non-dimensional parameters. In order to recover a unique set of variables, one should note that the product of χ and ψ gives the non-dimensional parameter ξ, which was used in the 0D analysis:

$$\chi\psi = \frac{u_c}{u_L}\frac{L}{L_c} = \frac{L}{u_L}\sqrt{\nu_{iz}D_g}\sqrt{\frac{\nu_{iz}}{D_g}} = \frac{L\nu_{iz}}{u_L} = \frac{\nu_{iz}V_s}{u_L A_s} = \xi\ . \tag{4.22}$$

At this point one might want to introduce a non-dimensional parameter ζ that is in some way ‘orthogonal’ to ξ, in order to use ξ and ζ to describe the behavior of the system, instead of χ and ψ. A good candidate for this purpose is the ratio of χ over ψ, which gives

$$\frac{\chi}{\psi} = \frac{u_c}{u_L}\frac{L_c}{L} = \frac{\sqrt{\nu_{iz}D_g}}{u_L L}\sqrt{\frac{D_g}{\nu_{iz}}} = \frac{D_g}{u_L L} = \zeta\ . \tag{4.23}$$

From Equations 4.22 and 4.23 it is easy to recover χ and ψ as functions of ξ and ζ

$$\chi = \sqrt{\xi\zeta} \qquad \psi = \sqrt{\xi/\zeta}\ , \tag{4.24}$$

and it is equally simple to rewrite the ionization efficiency in the new variables:

$$\eta_{iz}(\xi,\zeta) = 1-\frac{2\,e^{-\sqrt{\xi/\zeta}}}{\sqrt{\xi\zeta}\left(1-e^{-2\sqrt{\xi/\zeta}}\right)+\left(1+e^{-2\sqrt{\xi/\zeta}}\right)}\ . \tag{4.25}$$

As expected, in the limit of $\xi\to 0$ (that is, vanishingly small ionization frequency), the efficiency $\eta_{iz}\to 0$ as well. Similarly, $\eta_{iz}\to 1$ for $\xi\to\infty$. More interesting is the behavior of the ionization efficiency with respect to the new parameter ζ; when the diffusion coefficient is reduced (e.g. because the source has a very small radius R), the neutral particles need more time to perform the random walk along the source axis, and hence they are more likely to be ionized. In fact, Eq. 4.25 yields

$$\lim_{\zeta\to 0}\eta_{iz}(\xi,\zeta) = 1-\frac{0}{0+1} = 1\ . \tag{4.26}$$

For increasing values of the diffusion coefficient, the particles can more easily escape from the source, but the ionization efficiency does not go to zero as $\zeta \to \infty$. Instead

$$\lim_{\zeta\to\infty} \eta_{iz}(\xi,\zeta) \;=\; 1 - \frac{2}{\sqrt{\xi\zeta}\left(2\sqrt{\xi/\zeta}\right)+2} \;=\; 1 - \frac{2}{2\xi+2} \;=\; \frac{\xi}{1+\xi}\;, \tag{4.27}$$

and the expression given by Eq. 4.10 obtained from the 0D analysis is recovered. This result is not surprising, because in the limit of $\zeta \to \infty$ the density in the source becomes uniform, and hence the flux of particles escaping from the source is effectively given by $u_L \langle n_g \rangle A_s$ as in the 0D model.

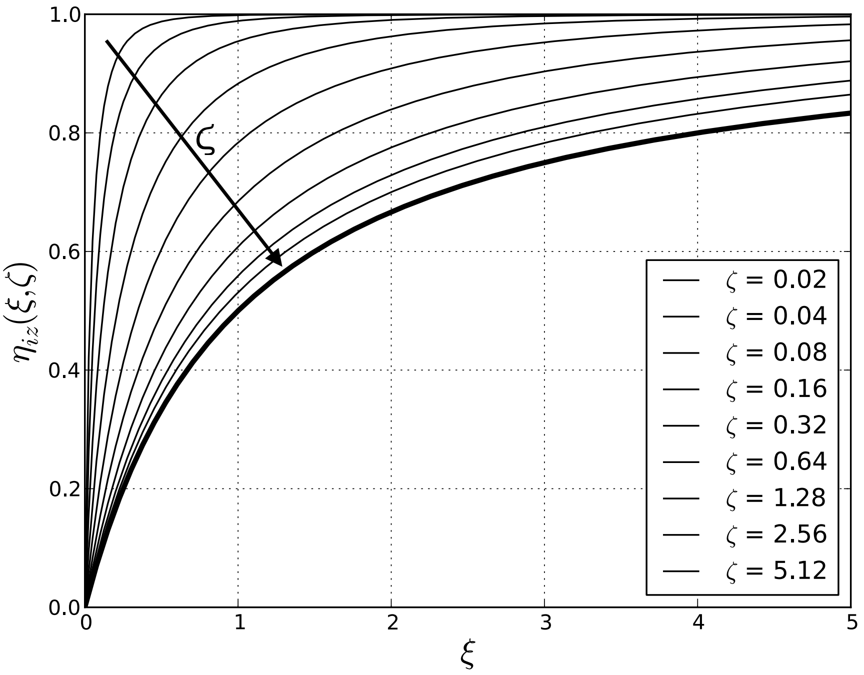

Figure 4.1: Ionization efficiency predicted by the 1D analytic model (Eq. 4.25), as a function of ξ (in abscissa) and ζ (parametric). For increasing values of ζ the 0D result (Eq. 4.10) is asymptotically recovered (thick line).

It is interesting to note that an expression for the average density similar to Eq. 4.11 can be obtained by integrating Eq. 4.18 from 0 to L, yielding

$$\langle n_g \rangle = \frac{[\dot{N}_g]^{in}}{\nu_{iz} V_s}\, \eta_{iz}(\xi,\zeta) \;. \tag{4.28}$$

4.1.2 The Coupled Dynamics of Neutrals and Electrons

The most important quantities in a cold plasma are the neutral density, the electron density and the electron mean kinetic energy. From these quantities most of the other plasma properties may be estimated. In a Helicon thruster the neutral gas is expected to be mostly ionized while flowing through the source, and hence one should solve for the average neutral density self-consistently with the electron properties. This section aims at finding the steady-state solution $(\langle n_g\rangle, \langle n_e\rangle, \langle T_e\rangle)$ to the system of three 0D global balance equations (where the whole source is the control volume): neutral particle balance, electron particle balance and electron energy balance. It is important to stress the fact that the following analyses will rely on four major hypotheses:

1. quasi-neutrality holds within the plasma source, so that there is no need to solve for the average ion density $\langle n_i\rangle \simeq \langle n_e\rangle$,
2. the normalized Electron Energy Distribution Function (EEDF) is Maxwellian,
3. wall recombination is negligible,
4. 50 W of RF power are coupled to the electrons.

The first hypothesis is based on the observation that appreciable charge separation happens in regions much smaller then the system size, with a spatial-scale of the order of a few Debye lengths. Regions of charge separation (usually sheaths, but also Double Layers) build up on the system boundaries because of the huge difference between the electron and ion diffusivities. The *potential drop* created in those regions tends to confine electrons while accelerate ions, up to the point where electron and ion fluxes are equal. Similarly, in the bulk of the plasma the equality of the electron and ion fluxes is reached because of a local *ambipolar electric field*, due to the fact that the local electron density is just slightly lower than the local ion density; from this comes the term “quasi-neutrality”. The assumption $\langle n_i\rangle \simeq \langle n_e\rangle$ necessarily holds in steady-state, but it will be also used in time-dependent calculations, by assuming that quasi-neutrality is reached on a time-scale smaller than any other transitory phenomena under study.

The second hypothesis is really only needed for making the problem manageable, so that order-of-magnitude estimates of the most important physical quantities can be obtained. In fact, a Maxwellian EEDF is completely determined by a single parameter, the electron temperature T_e. As a consequence, the rate coefficients for the various electron-neutral collisions will be functions of T_e alone (neutrals are effectively 'immobile' from the point of view of the energetic electrons). Once order-of-magnitude estimates have been obtained, they will permit one to understand whether the hypothesis of a Maxwellian EEDF was physical, and if not, they will suggest a better description of the physics.

The third hypothesis is an intrinsic requirement for a plasma thruster, because wall recombination penalizes the propulsive efficiency to the point that the feasibility of the thruster itself becomes questionable; for a Helicon plasma thruster, wall recombination mainly happens on the closed end of the cylinder, where theoretically an ion flux as large as the one on the open end could reach the wall. It is believed that the creation of a 'magnetic mirror' would permit the designer to mitigate the problem by drastically reducing the electron axial diffusivity to the back wall. Also, high neutral densities in the region just in front of the wall may help in that ion-neutral charge-exchange collisions would transfer momentum from the ion particles to the neutral particles, and from these to the back wall, increasing the net thrust delivered by the thruster. However, the usefulness of a high neutral density is not clear-cut because it would also increase the electron-neutral collisionality, reducing the effectiveness of the magnetic mirror.

The fourth hypothesis effectively decouples the following analyses from the EM power coupling chain, which involves a complex interaction between the RF power supply system, the transmission line, the antenna, and the plasma response. Broadly speaking, this is equivalent to disregarding the physics of power coupling altogether at this stage. This approach is justified in that it leaves complete freedom in the design of the most effective antenna and RF power supply, together with the proper choice of axial magnetic confinement field, once the plasma parameters are estimated with a sufficiently high confidence.

The 0D neutral particle balance reads

$$V_s \frac{d\langle n_g\rangle}{dt} = [\dot{N}_g]^{in} - \nu_{iz,g}\langle n_g\rangle V_s - n_g(L)\, u_L A_s\,, \tag{4.29}$$

where $\nu_{iz,g} = K_{iz}(T_e)\langle n_e\rangle$ is the ionization collision frequency for neutrals. It is convenient to write $n_g(L) = f_g\langle n_g\rangle$, where f_g can be regarded as a free non-dimensional parameter with values in $[0,1]$, which generalizes the standard 0D formulation (where $f_g \equiv 1$). The effect of varying f_g will be investigated once a closed form solution is obtained; at this stage, it is not clear that the introduction of f_g is useful. The steady-state solution to Eq. 4.29 is

$$\langle n_g \rangle = \frac{[\dot{N}_g]^{in}}{K_{iz}(T_e)\langle n_e \rangle V_s + f_g u_L A_s} \,. \tag{4.30}$$

The 0D electron particle balance equation is

$$V_s \frac{d\langle n_e \rangle}{dt} = \nu_{iz,e} \langle n_e \rangle V_s - n_e(L)\, u_B A_s \,, \tag{4.31}$$

where $\nu_{iz,e} = K_{iz}(T_e)\langle n_g \rangle$ is the ionization collision frequency for electrons, and $u_B(T_e)$ is the Bohm velocity, reached by the ions at the end of the quasi-neutral bulk region (here supposed to be at the exit section). The last term is to be interpreted as the loss rate to the wall, found by setting the electron loss rate equal to the ion loss rate, in the hypothesis of quasi-neutrality. Eq. 4.31 is making use of the major hypothesis of neglecting wall recombination: electrons (and ions) can only flow out of the system through the exit section. Again, it is convenient to write $n_e(L) = f_e \langle n_e \rangle$, with $f_e \leq 1$; the effect of varying f_e will be investigated using the final solution. The steady-state solution to Eq. 4.31 is

$$\langle n_g \rangle K_{iz}(T_e)\, V_s = u_B(T_e)\, f_e A_s \,, \tag{4.32}$$

where $\langle n_e \rangle$ is not present because it has been factored out. At this point, if the neutral density could be held constant somehow, Eq. 4.32 would decouple from Eq. 4.30, becoming a non-linear equation in the single variable T_e, which could be easily calculated. In fact, this is often the case for a high pressure plasma source.

The 0D electron energy balance equation is

$$\begin{aligned} V_s \frac{d\langle n_e \rangle \langle \varepsilon \rangle}{dt} &= P_a - \left(\nu_{iz,e}\varepsilon_{iz} + \sum_\alpha \nu_{ex,e}^{(\alpha)} \varepsilon_{ex}^{(\alpha)} + \nu_{el,e} \frac{2 m_e}{M_i} \langle \varepsilon \rangle \right) \langle n_e \rangle V_s \\ &\quad - n_e(L)\, u_B\, q_e \phi_w\, A_s \end{aligned} \tag{4.33}$$

where $\langle \varepsilon \rangle = 3/2 \cdot k_B T_e$ is the average electron kinetic energy, P_a is the power coupled by the RF antenna to the electron fluid, ε_{iz} is the energy loss due to an ionizing collision, $\varepsilon_{ex}^{(\alpha)}$ is the energy loss due to collisional excitation from the Ground Level to the α-th energy level, $\nu_{el,e}$ is the electron collision frequency for elastic collisions, q_e is the electron charge, and $\phi_w(T_e)$ is the confinement potential (i.e. the electrostatic barrier that must be overcome by an electron that is escaping from the plasma source). It is common practice to rewrite the terms between the parentheses in a more compact form:

$$\begin{aligned}
&\nu_{iz,e}\varepsilon_{iz} + \sum_{\alpha} \nu_{ex,e}^{(\alpha)}\varepsilon_{ex}^{(\alpha)} + \nu_{el,e}\frac{2m_e}{M_i}\langle\varepsilon\rangle = \\
&= \langle n_g\rangle K_{iz}(T_e)\left(\varepsilon_{iz} + \sum_{\alpha}\frac{K_{ex}^{(\alpha)}(T_e)}{K_{iz}(T_e)}\varepsilon_{ex}^{(\alpha)} + \frac{K_{el}(T_e)}{K_{iz}(T_e)}\frac{2m_e}{M_i}\langle\varepsilon\rangle\right) = \\
&= \langle n_g\rangle K_{iz}(T_e)\,\varepsilon_c(T_e)\ ,
\end{aligned} \tag{4.34}$$

where $\varepsilon_c(T_e)$ is the collisional energy loss per electron-ion pair created. Using Eq. 4.34 and the usual expression $n_e(L) = f_e\langle n_e\rangle$, the steady-state solution to Eq. 4.33 is

$$\langle n_e\rangle = \frac{P_a}{\langle n_g\rangle K_{iz}(T_e)\,\varepsilon_c(T_e)\,V_s + u_B(T_e)\,f_e\,q_e\,\phi_w(T_e)\,A_s}\ . \tag{4.35}$$

If Eq. 4.32 is substituted into Eq. 4.35 and then this is substituted into Eq. 4.30, after some algebra one gets

$$1 - \frac{P_a}{[\dot{N}_g]^{in}\,\left(\varepsilon_c(T_e) + q_e\phi_w(T_e)\right)} = \frac{f_g u_L A_s}{[\dot{N}_g]^{in} V_s}\cdot\frac{u_B(T_e)\,f_e A_s}{K_{iz}(T_e)} \tag{4.36}$$

which can be solved for T_e. Then, $\langle n_g\rangle$ is obtained from Eq. 4.32 and $\langle n_e\rangle$ from Eq. 4.35. The various quantities in Eq. 4.36 that depend on T_e are shown in the following figures. The only quantity that depends linearly on T_e is the confinement potential ϕ_w.

Equating the LHS and RHS of Eq. 4.36 permits one to find the electron temperature, as shown in Fig. 4.6.

Fig. 4.6 might suggest that there is more than one solution to Eq. 4.36 in the case of $f_g f_e \to 0$, and in fact there are 3 solutions for $f_g f_e < 0.001$. While it is not uncommon to have $f_e \approx 0.1$ in general, the 1D analytic model for neutrals suggests that a value of $f_g \approx 0.01$ can be obtained only for ionization efficiencies higher than 99.9 %. At a temperature $T_e < 2$ eV, this extremely high ionization efficiency requires an electron density higher than $2{\cdot}10^{21}\ m^{-3}$, orders of magnitude bigger than the density found from the solution to the three coupled balance equations. Under different operating conditions it is possible that such solutions could correspond to physical low-temperature regimes.

The steady-state values of the electron density $\langle n_e\rangle$ and neutral density $\langle n_g\rangle$ are not very sensitive to f_g (due to the extremely high ionization efficiency of the plasma source), but they are extremely sensitive to f_e, as shown in Fig. 4.7. Nevertheless, since $K_{iz}(T_e)\langle n_e\rangle\langle n_g\rangle V_s$ is the *number of ionization events per second* in the source, which is roughly equal to the number of neutral particles injected per second through the injector (due to the extremely

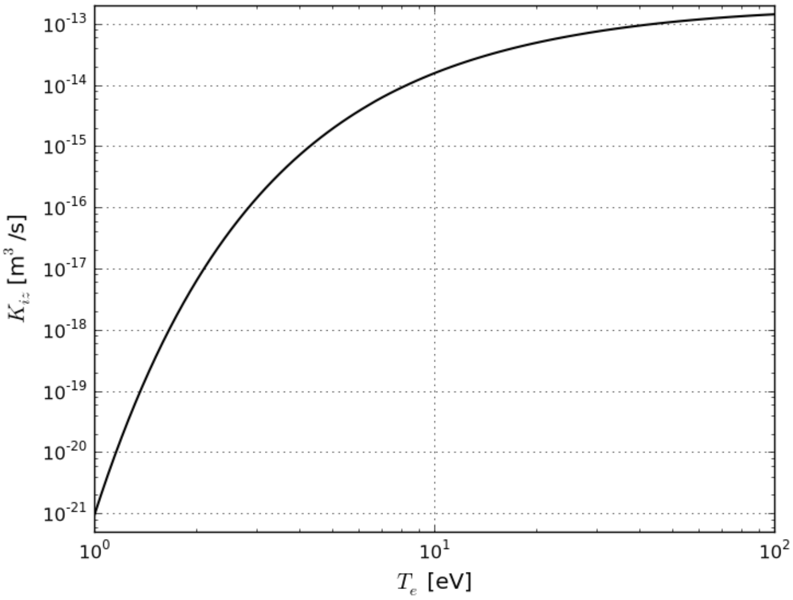

Figure 4.2: Rate coefficient for electron impact ionization in Argon gas, as a function of the electron temperature T_e.

high ionization efficiency of the source), then the product of the two densities is approximately constant, as $\langle n_e\rangle\langle n_g\rangle \approx [\dot{N}]^{in}/(K_{iz}V_s) \approx$ const.

From the point of view of electrons, the higher the neutral density, the higher the collision frequency. The highest value of the neutral density in Fig. 4.7 is $\langle n_g\rangle \simeq 1.4\cdot 10^{18}$ m^{-3}, which gives an average electron mean-free-path for elastic collisions $\langle\lambda_{el,e}\rangle \approx K_{el}\, n_g / v_{th,e} \simeq$ 9.8 m, and a mean-free-path for inelastic collisions $\langle\lambda_{in,e}\rangle \approx \left(K_{iz} + \sum_\alpha K_{ex}^{(\alpha)}\right) n_g / v_{th,e} \simeq 33$ m. Under these conditions, an average electron will bounce approximately 80 times along the axis of the source before colliding elastically with a neutral particle, and approximately every 3 elastic collisions an inelastic collision will occur. Since these mean-free-paths are obtained with the maximum possible neutral density, they can be considered a *lower bound estimate* to the real values; hence, it can be safely stated that

$$\lambda_{el,e}\, ,\, \lambda_{in,e} \gg L \tag{4.37}$$

where $L \simeq 0.12$ m is the system length.

Clearly, electrons bounce in the plasma source only if they have a kinetic energy associated with their motion along the field line lower than the confinement potential ϕ_w, i.e.

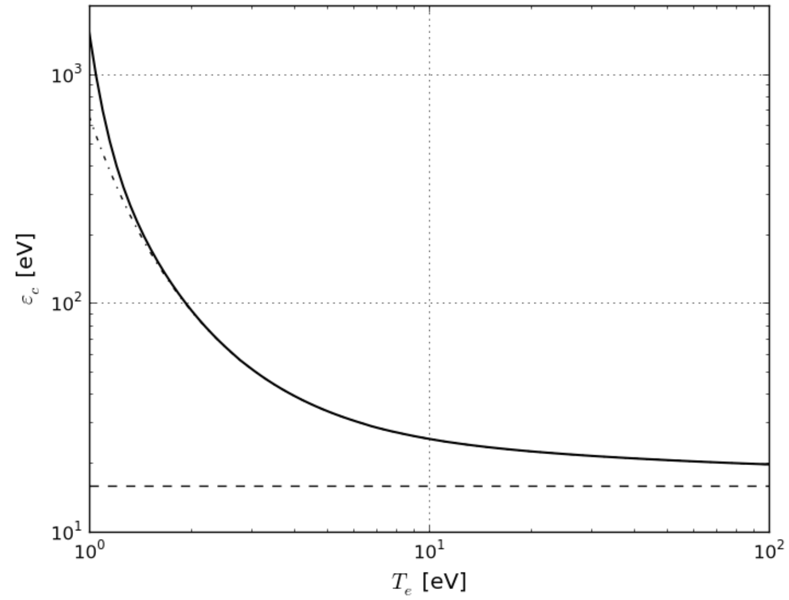

Figure 4.3: Collisional energy loss per electron-ion pair created in Argon gas, as a function of the electron temperature T_e (solid line). For comparison, the ionization energy ε_{iz} is shown by a dashed line. The dot-dashed line represents the result that would be obtained by neglecting the contribution of elastic collisions: for $T_e > 2$ eV, the energy loss in elastic collisions can be safely disregarded for all practical purposes.

only if they are *electrostatically confined* in the source. A Maxwellian EEDF decreases as $\exp\left[-\varepsilon/\left(k_B\,T_e\right)\right]$ for $\varepsilon \ll k_B\,T_e$, but still there is a number of highly energetic electrons with $\varepsilon > q_e\phi_w$, which are responsible for a non-negligible fraction of all the ionization events. Such *unconfined* electrons are usually produced in the bulk plasma and they diffuse toward the boundary, where they can escape from the source, unless they have lost their excess energy $\left(\varepsilon - q_e\phi_w\right)$; hence, they can play a role only if the chances are high that they can undergo an inelastic collision in their residence time inside the source.

In the situation at hand, for the maximum average neutral density $\langle n_g \rangle \simeq 1.4 \cdot 10^{18}$ m^{-3}, unconfined electrons have an elastic mean-free-path $\lambda_{el} \approx 1/\left[n_g\,\sigma_{el}\left(q_e\,\phi_w\right)\right] \simeq 34$ m, and an inelastic mean-free-path $\lambda_{el} \approx 1/[n_g\,\sigma_{iz}\left(q_e\,\phi_w\right) + \sum_\alpha \sigma_{ex}^{(\alpha)}\left(q_e\,\phi_w\right)] \simeq 20$ m. Clearly, unconfined electrons have an extremely small chance to undergo an inelastic collision before escaping from the system; because of this, it is perfectly reasonable to assume that the EEDF

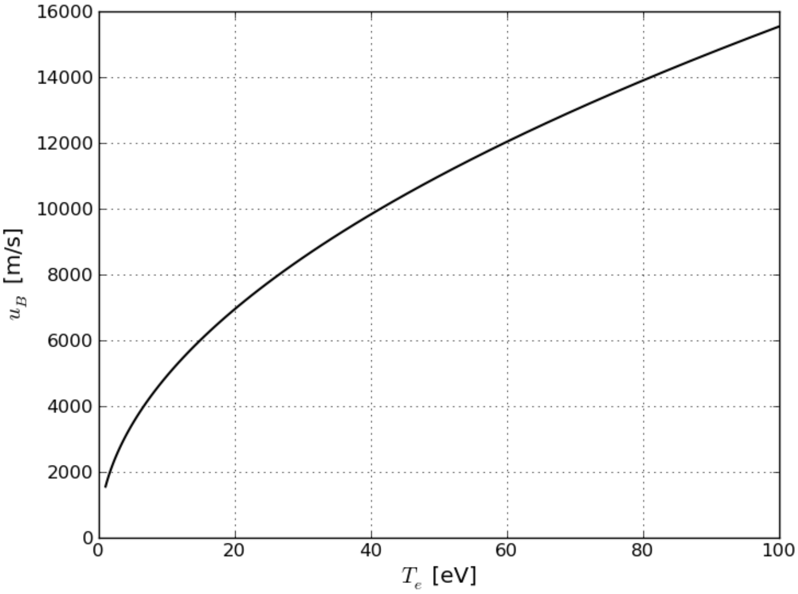

Figure 4.4: Bohm velocity in Argon gas, as a function of the electron temperature T_e.

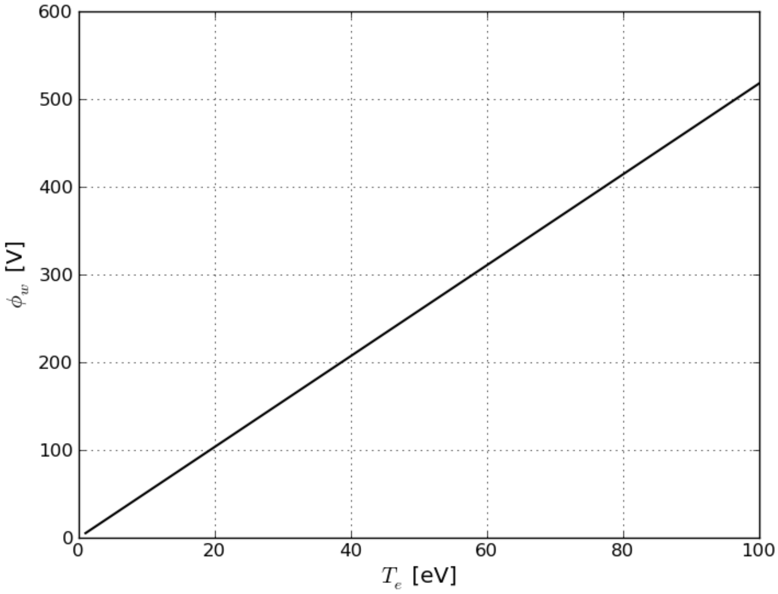

Figure 4.5: Confinement potential in Argon gas, as a function of the electron temperature T_e.

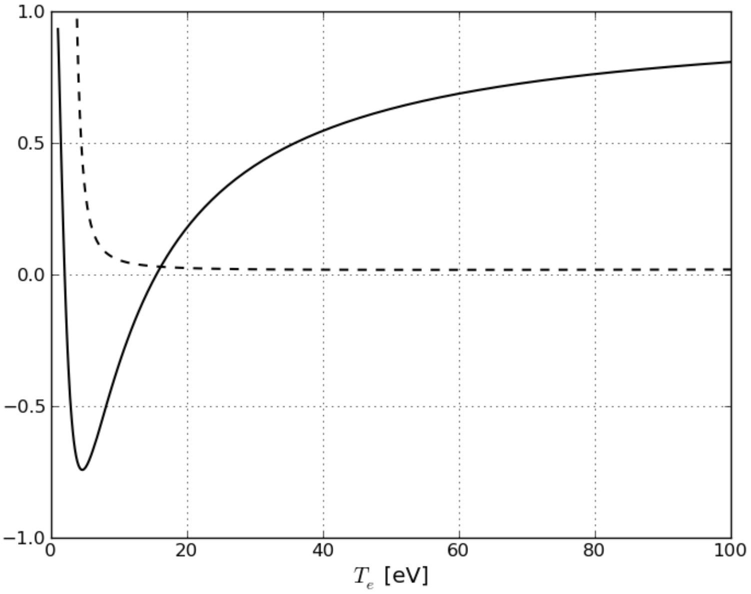

Figure 4.6: The LHS (solid line) and RHS (dashed line) of Eq. 4.36, as functions of the electron temperature, evaluated for the nominal operating parameters of the Helicon plasma thruster under analysis. The intersection of the two curves gives an equilibrium temperature of 15.8 eV. Here $f_g = f_e = 1$ was used, but T_e is not very sensitive to these parameters, at least for the operating conditions studied; in fact, if $f_g f_e \to 0$, then RHS → 0 and $T_e = 15.5$ eV is found.

is vanishingly small for energies higher than the confinement potential energy:

$$F(\varepsilon) = 0 \qquad \text{for } \varepsilon > q_e \phi_w \,. \tag{4.38}$$

Accordingly, the EEDF can be at most a *truncated* Maxwellian, and this fact already invalidates part of the analysis carried out so far. More important, it is even questionable whether the EEDF has any similarity at all to a Maxwellian distribution.

4.1.3 Ion Dynamics

An Argon atom has mass $M_{Ar} \simeq 39.948$ AMU, while an electron at rest has mass $m_e \simeq 1/1823$ AMU, which gives an ion to electron mass ratio

$$\frac{M_{Ar}}{m_e} \simeq 72\,825. \tag{4.39}$$

Several phenomena are affected by this huge mass ratio:

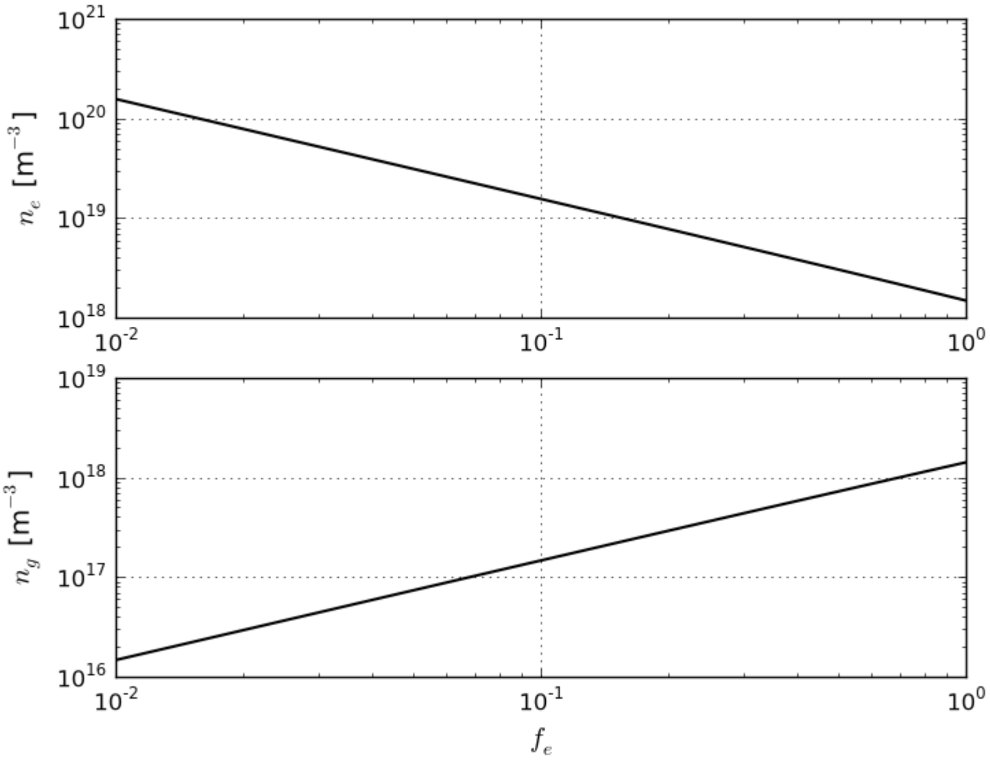

Figure 4.7: Steady state average densities of electrons and neutrals, for a wide range of values of $f_e = n_e(L)/\langle n_e \rangle$. It should be noted that $\langle n_e \rangle$ varies as $1/f_e$, and $\langle n_g \rangle$ varies as f_e; in fact the product $\langle n_e \rangle \cdot \langle n_g \rangle$ is mostly insensitive to f_e.

1. the thermal velocity of the electrons is much higher then the thermal velocity of ions, since
$$\frac{v_{th,e}}{v_{th,i}} = \sqrt{\frac{M_{Ar}}{m_e}} \sqrt{\frac{T_e}{T_i}} \simeq 270 \sqrt{\frac{T_e}{T_i}}, \tag{4.40}$$
even when ions and electrons are thermalized, i.e. $T_e = T_i$; as a consequence, electrons diffuse much faster toward the boundaries of the system;

2. when a high frequency oscillating electric field is applied ('high frequency' meaning that the oscillation frequency is higher than the total momentum transfer collision frequency), the electric current carried by electrons is (M_{Ar}/m_e) times the current carried by ions; in fact, Helicon waves couple energy primarily to electrons;

3. electron-ion Coulomb collisions are not efficient in heating the ions, because the frac-

tion of kinetic energy that is transferred from the impacting electron to the target ion is only $2m_e/M_{Ar}$ on average.

Electron-Ion collisions

According to [48], the cross-section for Coulomb collisions can be written in a general form as

$$\sigma_{1-2} = \frac{8}{\pi} b_0^2 \ln \Lambda \qquad [\mathrm{m}^2], \tag{4.41}$$

where b_0 is the impact parameter for a 90°deflection,

$$b_0 = \frac{q_1 q_2}{4\pi\epsilon_0 W_R} \qquad [\mathrm{m}], \tag{4.42}$$

and W_R is the impact energy in the center-of-mass reference frame:

$$W_R = \frac{1}{2} m_R v_R^2 \qquad [\mathrm{J}], \tag{4.43}$$

with $m_R = m_1 m_2/(m_1 + m_2)$ being the reduced mass [kg], and v_R the relative velocity [m/s]. In Eq. 4.41,

$$\Lambda = \frac{\lambda_D}{b_0}, \tag{4.44}$$

where

$$\lambda_D = \sqrt{\frac{\epsilon_0 K_B T_e}{n_e q_e^2}} \qquad [\mathrm{m}] \tag{4.45}$$

is the Debye length.

In order to understand whether electron-ion Coulomb collisions can heat the ions in the source, the collision time $\tau_{i-e} = \nu_{i-e}^{-1}$ [s] of momentum transfer for ions, due to collisions with electrons, should be compared to the typical residence time of the ions in the system, τ_i^{conf}.

τ_{i-e} is the *average time required to cumulatively deflect an ion by 90°*, by effect of Coulomb collisions with electrons. According to [49], the relation

$$\nu_{i-e} = \frac{m_e}{M_{Ar}} \nu_{e-i} \qquad [\mathrm{s}^{-1}] \tag{4.46}$$

holds, which permits one to obtain τ_{i-e} from an estimate of ν_{e-i}, as

$$\nu_{e-i} = n_e \sigma_{e-i} v_{th,e}, \tag{4.47}$$

where the quasi-neutrality relation $n_e = n_i$ was used. Eq. 4.47 is to be evaluated with the highest electron density expected in the source. Unfortunately, Section 4.1.2 showed that n_e

strongly depends on the coefficient f_e (see Fig. 4.7), which cannot be easily estimated. Prior experience in low pressure discharges suggests that $f_e \geq 0.1$, and hence the lower bound is chosen here. Using

$$\begin{cases} n_e = 2 \cdot 10^{19} \text{ m}^{-3}, \\ T_e = 15.5 \text{ eV}, \end{cases}$$

in the formulas above yields:

$$\lambda_D \simeq 6.5 \cdot 10^{-6} \text{ m}, \quad b_0 \simeq 6.2 \cdot 10^{-11} \text{ m}, \quad \ln \Lambda \simeq 12, \quad \sigma_{e-i} \simeq 1.2 \cdot 10^{-19} \text{ m}^2$$

and since $v_{th,e} \simeq 2.9 \cdot 10^6$ m/s, one gets

$$\begin{cases} \nu_{e-i} \simeq 7.0 \cdot 10^6 \text{ Hz}, \\ \nu_{i-e} \simeq 96 \text{ Hz}, \end{cases}$$

and the collision time for ion-electron Coulomb collisions is

$$\tau_{i-e} \geq 0.01 \text{ s}.$$

An upper bound to the ion residence time τ_i^{conf} is obtained by assuming that the ions travel with the thermal velocity of neutrals $v_{th,g} \approx 430$ m/s, so that

$$\tau_i^{\text{conf}} \leq \frac{L}{v_{th,g}} \approx 2.8 \cdot 10^{-4} \text{ s}.$$

From the above estimates it is clear that $\tau_i^{\text{conf}} \ll \tau_{i-e}$ is a condition that is always satisfied, and hence electron-ion Coulomb collisions do not have time to deposit energy from electrons to ions. For this reason, ions are ‘cold’ in the Helicon plasma source under study, i.e. $T_e \gg T_i \simeq T_g$.

Ion-neutral collisions

When ions are accelerated by the electrostatic E field, they deliver momentum to neutrals via charge-exchange and elastic collisions. The ion dynamics is heavily affected by those two processes, and the quantity of interest is the ratio of the ion mean-free-path to the system length, λ_{e-g}/L. According to [48], one can distinguish several regimes, in order of decreasing collisionality:

- When $\frac{\lambda_{i-g}}{L} \lesssim \frac{T_i}{T_e}$, the ion dynamics is properly described by an *ambipolar diffusion* model, where the natural ion diffusivity is enhanced by the ambipolar electric field (electrons diffuse much faster than ions, and the quasi-neutrality condition requires an electric field); the electrons transfer energy to the ions via the ambipolar E field, and the ions deliver kinetic energy to the neutrals: neutrals and ions are thermalized in the bulk, with a temperature usually considerably higher than the neutral injection temperature. In this situation the ions cannot pick up much kinetic energy in one mean-free-path, and so the impact velocity $v_i \simeq v_{th,i}$ is constant in most of the source: if the neutral density is constant as well, this leads to a constant mobility diffusion model.

- When $\frac{\lambda_{i-g}}{L} \gtrsim \frac{T_i}{T_e}$, the situation is similar to the point above, but with the difference that in one mean-free-path the ions can pick up a kinetic energy greater than the ion thermal energy: the impact velocity $v_i \simeq u_i$ and the ion dynamics can be described by a *variable mobility* ambipolar diffusion model.
- When $\frac{\lambda_{i-g}}{L} > 1$, the ions are essentially *collisionless*, and ion-neutral collisions can be disregarded altogether; this is the situation that is preferable in a Helicon plasma thruster.

According to [50], the combined effect of charge-exchange and elastic collisions between ions and neutrals can be described by a single formula that well reproduces the literature results for Argon:

$$\lambda_{i-g}\left(v_i, n_g\right) = \frac{|v_i|}{n_g \sigma_0 \sqrt{v_0^2 + v_i^2}} \qquad [\mathrm{m}] \tag{4.48}$$

where $\sigma_0 = 10^{-18}$ m^2 and $v_0 = 550$ m/s. A lower bound to λ_{i-g} is obtained for the maximum value of $n_g = 1.4 \cdot 10^{18}$ m^{-3} and a minimum velocity $v_i = v_0$, yielding $\lambda_{i-g} \geq 0.5$ m, so that ions are in the collisionless regime $\lambda_{i-g} > L$.

Ion-ion collisions

Now that ion-electron and ion-neutral elastic collisions have been ruled out, it is also important to estimate the importance of ion-ion Coulomb collisions. In fact, when the mean-free-path for such collisions is much smaller than the system dimensions, $\lambda_{i-i} \ll L$, the ion velocity distribution has time to relax towards a drift-Maxwellian; in such a situation, a fluid description of ions is most often appropriate. On the other hand, if $\lambda_{i-i} > L$, the motion of each ion is essentially uncorrelated from each other, and a kinetic treatment is necessary.

The picture just given is somewhat complicated by the fact that the Coulomb cross-section has a strongly non-linear dependence on the relative impact velocity, $\sigma_{i-i} \propto v_R^{-4}$. Ions are created with a velocity $v_i \approx v_{th,g}$, and they accelerate in the z direction due to the electrostatic E field. In proximity of the exit section, it is assumed that ions enter a very small positively charged region, the *double layer*, with an average velocity u_i equal to the Bohm velocity $u_B \gg v_{th,g}$.

Clearly, ions created in the bulk region collide with each other with a relative velocity of the order of the thermal velocity, so that $v_R \approx v_{th,g}$: due to the low impact velocity, we expect $\sigma_{i-i}^{\text{bulk}}$ to be a large cross-section. On the other hand, ions created in proximity to the exit section collide with an 'ion beam' having velocity close to the Bohm velocity, so that $v_R \approx u_B$: we expect this cross section to be $\left(v_{th,g}/u_B\right)^4 = (3T_i/T_e)^2$ times smaller than $\sigma_{i-i}^{\text{bulk}}$. Moreover, the ion production rate per unit volume is proportional to the local neutral density $n_g(z)$, which decreases exponentially along the source axis (see Section 4.1.1), so it is reasonable to assume that most ions are created in a small region close to the inlet region. For all these reasons, the residual ions produced in the rest of the source are a small fraction of the total that does not interact appreciably with the main ion beam.

For the bulk ions one gets:

$$\begin{cases} m_R = M_{Ar}/2 \\ v_R = v_{th,i} = \sqrt{\frac{3k_B T_i}{M_{Ar}}} \end{cases} \implies \sigma_{i-i}^{\text{bulk}} = \frac{8}{9\pi^3} \frac{q_i^4 \ln \Lambda}{\epsilon_0^2 (k_B T_i)^2} \tag{4.49}$$

In order to evaluate an upper bound for the mean-free-path $\lambda_{i-i}^{\text{bulk}} = 1/\left(n_i \sigma_{i-i}^{\text{bulk}}\right)$, one needs to use the lowest ion (electron) density and the highest ion temperature foreseen in the source. Using the values

$$\begin{cases} n_i = 1 \cdot 10^{18}\ \text{m}^{-3}, \\ T_i = 600\ \text{K}, \end{cases}$$

one finds that

$$\lambda_{i-i}^{\text{bulk}} \leq 2.4 \cdot 10^{-5}\ \text{m} \ll L.$$

Accordingly, the thermal ions in the bulk of the plasma source are highly collisional; hence, the ion velocity distribution function is a drifting Maxwellian.

Conclusions

Summarizing, the coupled analytic model permitted us to estimate the mean free path (or the collision frequency) for the various collisional processes of ions. In turn, those estimates yielded the following information about the ion dynamics:

1. EM fields primarily heat the electrons, and electron-ion Coulomb collisions are not effective in heating the ions; as a consequence, the ion temperature is much lower than the electron temperature, and it is expected to be close to the temperature of neutrals, i.e. $T_e \gg T_i \approx T_g$;
2. ion-neutral elastic collisions (including both the scattering and the charge-exchange events) are negligible; hence, the ions are essentially drag-free, and they can be thought of as being free-falling down the electrostatic 'potential hill';
3. ion-ion collisions are predominant in the small region where most ions are created by ionization; therefore, the ion velocity distribution is a drifting Maxwellian.

4.2 Suggested Detailed Modeling

4.2.1 Non-Maxwellian Electron Energy Distribution Function

The actual shape of the EEDF is determined by a number of concurrent phenomena:

1. *inelastic collisions*, which tend to deplete the high energy tail of the EEDF while they replenish the low energy bulk;
2. *Coulomb collisions*, which relax the EEDF toward the aforementioned truncated Maxwellian (but with $F(\varepsilon) \to 0$ as $\varepsilon \to q_e\phi_w$);
3. *RF electromagnetic heating*, which in general tends to push electrons 'smoothly' toward higher energies;
4. *balance of electron and ion fluxes*: Coulomb collisions and EM heating make hot electrons 'jump out' of the electrostatic potential that confined them, so that they can escape quickly form the source; in order to ensure quasi-neutrality, the loss-rate of electrons must equal the loss-rate of ions.

To obtain an EEDF that is consistent with these phenomena, a 'kinetic approach' is necessary: the EEDF should come from the steady state solution of the Boltzmann Equation, in the hypothesis of isotropic velocity distribution function. Hence, the problem at hand becomes 0D-1V, since $F(\varepsilon)$ lies in a one-dimensional velocity space, and the complexity of the methods involved in the numerical solution dramatically increases. Moreover, since the various phenomena depend on n_e and n_g, one should solve for the EEDF consistently with those two quantities, with a procedure similar to the Maxwellian case already described. Unfortunately, solving directly for the self-consistent steady-state $\left(n_e, n_g, F(\varepsilon)\right)$ turns out to be a difficult task; instead, integrating the equations in time has been demonstrated to be a robust procedure.

It should be pointed out that integration in time is a delicate matter, as several transitory phenomena exist, which are coupled to each other and have widely different characteristic time-scales (in mathematical jargon, this is called a "*stiff* system"):

- ambipolar relaxation (electrostatic phenomenon, steady-state sheaths are created which equalize ion and electron fluxes);
- electron energy relaxation (normalized EEDF relaxes towards its steady state, higher moments relax faster);
- particle density relaxation (production and losses of neutrals, electrons and ions mutually balance each other).

An accurate analysis of the ambipolar relaxation process would involve the simultaneous kinetic solution of the ion and electron dynamics, coupled to Poisson's equation; but this is clearly beyond the scope of the present analyses. Therefore, unless otherwise specified, it will be assumed that ambipolar relaxation has already taken place, so that the net fluxes of ions and electrons are identical.

The big issue in the solution for $F(\varepsilon)$ is the fact that ϕ_w is unknown: this means that the domain of $F(\varepsilon)$ is not completely defined. Such a problem is solved by integrating $F(\varepsilon)$ in time while keeping ϕ_w, n_e and n_g constant: once $F(\varepsilon)$ has relaxed to its 'artificial' steady-state, the electron loss rate can be evaluated. The ion loss rate is also evaluated (as it depends non-linearly on $F(\varepsilon)$), but it will not equal the electron loss rate. Hence, the same procedure is repeated for different values of ϕ_w, without changing n_e or n_g, until the electron and ion loss rates are equal: the $F(\varepsilon)$ so obtained takes self-consistently into account the 4 phenomena of interest, but it is defined for a *specific operating point* $\left(n_e, n_g\right)$. The electron and neutral densities are then integrated in time while keeping the EEDF constant, and when one of the two densities has changed by more than a prescribed relative tolerance, the EEDF is recalculated using the aforementioned procedure.

It may seem unclear which equation, particle balance or energy balance, should be used for evolving the electron density. Here, the energy balance equation is preferred because, for a fixed antenna power P_a, it admits a steady-state solution, and hence it has better stability properties when used in the iterative method just described.

4.2.2 RF heating as a random-walk process

Correctly describing the effect of the RF electromagnetic heating on the EEDF is a formidable task, which falls way beyond the scope of the present analysis. With sufficient generality it is possible to describe the RF heating as a *random walk in velocity space*, and as such it can be considered a *diffusion process*. Most likely, the Diffusion Coefficient in velocity space D_v depends on the kinetic energy, and hence an electromagnetic module would be needed, with the specific purpose of providing the profile $D_v(\varepsilon)$. Still, there would be the problem of coupling exactly 50 W to the electrons, as this was one of the immutable assumptions made at the onset of the present analysis.

If a diffusion coefficient D_v uniform in energy is used, there is no need for a dedicated electromagnetic module, and it is also extremely easy to impose $P_a = 50$ W. In fact, for each velocity component, the flux in velocity space is

$$\Gamma_v = -D_v \frac{\partial f}{\partial v} = f(v)\, \dot{v}(v)\ , \tag{4.50}$$

where $\dot{v}(v)$ is the mean rate of change of the velocity for a particle having velocity v. Accordingly, the mean rate of change of the kinetic energy of an electron with velocity v is

$$\dot{\varepsilon}(v) = \frac{d}{dt}\left(\frac{1}{2} m_e v^2\right) = m_e\, v\, \dot{v} = -m_e D_v \frac{v}{f} \frac{\partial f}{\partial v}\ , \tag{4.51}$$

from which the power coupled per electron P_e^* can be evaluated as the average value of $\dot{\varepsilon}(v)$ over the electron distribution function:

$$P_e^* = \int_{-\infty}^{+\infty} \dot{\varepsilon}(v) f(v)\, dv = -m_e D_v \int_{-\infty}^{+\infty} v \frac{\partial f}{\partial v}\, dv\ . \tag{4.52}$$

Integration by parts gives

$$\int_{-\infty}^{+\infty} v \frac{\partial f}{\partial v}\, dv = \Big[v\, f(v)\Big]_{-\infty}^{+\infty} - \int_{-\infty}^{+\infty} f(v)\, dv = 0 - 1 = -1\ , \tag{4.53}$$

so that $P_e^* = m_e D_v$. In 3D velocity space, the contribution of each of the velocity components sums up to

$$P_e^* = 3\, m_e D_v\ . \tag{4.54}$$

4.2.3 Ion Loss Rate

It may seem unclear how the ion loss rate may be estimated without using a 1D ion model coupled to the electron model. Consistently with the level of detail of the suggested detailed model (0D in space), it is argued hereafter that a semi-analytical 0D description of ions can be efficaciously employed.

Due to the very low collision frequency for elastic electron-neutral and electron-ion encounters, it is possible to use the well-known results of the *collisionless sheath theory* for planar electrostatic probes. According to such a theory, the ions enter the sheath with a mean velocity u_B, called the Bohm velocity, which in general depends on the distribution functions of ions and electrons [51]. At the sheath boundary quasi-neutrality still holds, $n_e = n_i = n_S$, so that the ion flux is

$$\Gamma_i \;=\; n_S\, u_B \qquad \left[\mathrm{m}^{-2}\,\mathrm{s}^{-1}\right]. \tag{4.55}$$

For collisionless ions, the value of the density n_S is generally obtained from a relation of the kind $n_e\,(\Phi)$, which relates the electron density $n_e(z)$ to the local potential drop $\Phi(z)$. The form of $n_e\,(\Phi)$ is related to the shape of the electron distribution function, i.e. it depends on the normalized EEDF.

In the case of a Maxwellian EEDF with temperature T_e, the *Boltzmann's relation* for electrons holds, that is

$$n_e\,(\Phi) \;=\; n_e\,(0)\,\exp\left(-\frac{q_e \Phi}{k_B T_e}\right). \tag{4.56}$$

A generalization of the last relation that holds for non-Maxwellian EEDFs is given by Amemiya [52] as

$$n_e\,(\Phi) \;=\; n_e\,(0)\left[\int_{q_e\Phi}^{q_e\Phi_w} \sqrt{1-\frac{q_e\Phi}{\varepsilon}}\,F(\varepsilon)\,d\varepsilon \;+\; \frac{1}{2}\int_{q_e\Phi_w}^{\infty} \sqrt{1-\frac{q_e\Phi}{\varepsilon}}\,F(\varepsilon)\,d\varepsilon\right], \tag{4.57}$$

where the first integral on the r.h.s. is taken over all the *confined* electrons, and the second integral is taken over all *unconfined* electrons. Confined electrons are reflected by the potential drop Φ_w and hence they give a contribution to the density that is twice the contribution given by unconfined electrons; accordingly, the pre-integral factor is 1 instead of 1/2. For a Maxwellian $F\,(\varepsilon)$, Eq. 4.57 reduces to Eq. 4.56 in the limit as $\Phi_w \to \infty$.

According to the considerations in Section 4.1.2, the EEDF is negligibly small for values of the electron kinetic energy ε higher than the confinement potential Φ_w. Therefore the contribution of the unconfined electrons to the electron density at the sheath boundary is neglected, and the following simplified relation is used,

$$n_S \;=\; \langle n_e \rangle \int_{q_e\Phi_S}^{q_e\Phi_w} \sqrt{1 - \frac{q_e\Phi_S}{\varepsilon}}\, F(\varepsilon)\, d\varepsilon, \tag{4.58}$$

where the approximation $n_e(0) \approx \langle n_e \rangle$ is introduced. In Eq. 4.58, Φ_S is related to u_B by energy conservation for ions:

$$\frac{1}{2} M_{Ar}\, u_B^2 \;=\; q_e\Phi_S \tag{4.59}$$

In order to use Eq. 4.55, it remains to relate the Bohm velocity (or equivalently, the sheath potential Φ_S) to the ion and the electron distribution functions. In [51], Baalrud and Hegna suggest a kinetic Bohm criterion based on positive-exponent velocity moments of the Boltzmann equation. In the case of $T_e \gg T_i$ and $\lambda_D \ll \lambda_i$, their criterion reduces to

$$u_{i,S} \geq u_B = \sqrt{\frac{2}{3}\frac{\langle \varepsilon \rangle}{M_{Ar}}}, \tag{4.60}$$

where $\langle \varepsilon \rangle$ is the average electron energy:

$$\langle \varepsilon \rangle \;=\; \int_0^\infty \varepsilon\, F(\varepsilon)\, d\varepsilon. \tag{4.61}$$

Equivalently, it can be stated that, in a cold collisionless plasma, the ions enter the sheath (or the double layer) with a directional kinetic energy that is one third of the average electron kinetic energy:

$$\frac{1}{2} M_{Ar}\, u_B^2 \;=\; q_e\Phi_S \;=\; \frac{\langle \varepsilon \rangle}{3} \tag{4.62}$$

It is worth pointing out that, while traveling through the sheath (or the double layer), the ions will pick up a kinetic energy corresponding to the whole confinement potential Φ_w, which is usually more than twice $\langle \varepsilon \rangle / q_e$. The power flux that goes into accelerating the ion beam is therefore $P_i^* = \Gamma_i\, q_e\, \Phi_w\ \left[\mathrm{W/m^2}\right]$.

5

Detailed Electron Model

The main purpose of the numerical model described in this chapter is to further investigate the coupled dynamics of electrons and neutrals in the source, which were preliminarily studied in Sec. 4.1.2, by relaxing the incorrect hypothesis of a Maxwellian EEDF as suggested in Sec. 4.2. The other simplifying hypotheses employed in Sec. 4.1.2 still hold, that is, quasi-neutrality, negligible wall recombination, and 50 W of RF power coupled to electrons.

Section 5.1 presents the model equation that describes the time evolution of the average Electron Energy Distribution Function in the source. The model equation is a balance equation in energy space, consisting of a Partial Differential Equation (PDE) in the independent variables ε (the electron kinetic energy) and t (time). Since the resulting model retains no information about the location of the electrons in physical space, and it only uses one dimension in velocity space (i.e., the kinetic energy), it will be referred to as a '0D-1V kinetic model'.

Section 5.2 gives a mathematical description of the role of the various collisional processes in the aforementioned balance equation. The effect of electron-electron Coulomb collisions will be described as the partial derivative with respect to energy of a properly defined *flux function*; although such a formulation appears to be *local* in energy space, it will be shown that the flux function itself is *non-local*, as it describes the effect of the interactions of electrons having different velocities. Inelastic collisions (excitation and ionization) will be described by non-local (integral) operators. The experimental data employed in the model are also shown, in the form of tables and fitted curves.

Section 5.3 presents the first important step toward the numerical solution of the electron kinetic equation: by subdividing the energy axis in small intervals $[\varepsilon_{j-1/2}, \varepsilon_{j+1/2}]$, and integrating the model PDE over each of those intervals, a set of N rate equations are obtained for the time evolution of the number n_j of electrons with energy in $[\varepsilon_{j-1/2}, \varepsilon_{j+1/2}]$;

suitable finite-difference approximations are then introduced, resulting in a linear system of N first-order Ordinary Differential Equations (ODEs), which is the *semi-discrete formulation* of the model PDE. Particular emphasis is posed on the proper formulation of each process (heating, Coulomb collisions, and inelastic collisions) in a *matrix form*, because such a form considerably simplifies the numerical implementation, and it permits one to define simple criteria for the enforcement of particle (and energy) conservation; moreover, the matrix form proves to be useful in combination with implicit time-stepping.

Section 5.4 shows how the system of ODEs is integrated in time. By means of *time-scale separation*, the evolution of the electron density is separated from the evolution of the *normalized EEDF*. Since the confinement potential Φ_w is one of the unknowns, it is assumed that the correct value of Φ_w ensures that the electron and ion fluxes going out of the system are identical. An iterative scheme is used: given Φ_w, the normalized EEDF is run to steady-state, and the two fluxes are evaluated; if their difference is bigger than a prescribed tolerance, a feedback mechanism changes Φ_w and the procedure is repeated until convergence. Once the normalized EEDF and the confinement potential are self-consistently obtained, the electron density is evolved in time by means of a 0D power balance, and the neutral density is obtained from the 1D analytic model developed in Section 4.1.1.

5.1 Theory for the 0D-1V Kinetic Description of Electrons

5.1.1 Boltzmann's Equation

In low density gases, particles spend most of their time without interacting with the surrounding fluid. Interactions happen occasionally, and they are limited to an extremely short time-scale: such impulsive events are called *collisions*. Under these conditions of 'low correlation', the *one-particle* phase-space density function $f(t, \mathbf{x}, \mathbf{v})$ satisfactorily describes the state of the system. Specializing to electrons, the function $f(t, \mathbf{x}, \mathbf{v})$ is more commonly called the 'electron distribution function', and its time evolution is described by Boltzmann's equation,

$$\frac{\partial f}{\partial t} + \mathbf{v} \cdot \frac{\partial f}{\partial \mathbf{x}} + \frac{\mathbf{F}}{m_e} \cdot \frac{\partial f}{\partial \mathbf{v}} = \left[\frac{\partial f}{\partial t} \right]_{coll}, \tag{5.1}$$

where $\mathbf{F}(t, \mathbf{x}, \mathbf{v})$ is the force field acting on a single electron having mass m_e.

The r.h.s. of Eq. 5.1 describes the effect of collisions; by definition, collisions are events during which the Boltzmann description does not attempt to follow the dynamics deterministically. Of course, such a 'collision term' would be of little interest unless it could be specified from the one-particle distribution functions f and f_t (the latter being the distribution function of the target particles). In fact, Boltzmann demonstrated that, taking into account only two-body collisions between particles that are assumed to be uncorrelated prior to the collision, the collision term can be written as a velocity-space integral over the product of f and f_t:

$$\left[\frac{\partial f}{\partial t}\right]_{coll} = \oiint B\left(\mathbf{v}-\mathbf{v}'\right)\left[f\left(t,\mathbf{x},\mathbf{v}+\mathbf{v}'\right)f_t\left(t,\mathbf{x},\mathbf{v}-\mathbf{v}'\right)-f\left(t,\mathbf{x},\mathbf{v}\right)f_t\left(t,\mathbf{x},\mathbf{v}'\right)\right]d\mathbf{v}'d\mathbf{v}\,, \tag{5.2}$$

where $B\left(\mathbf{v}-\mathbf{v}'\right)$ is the Kernel function of the collision operator, which depends on the relative velocity of the two colliding particles. The expression in Eq. 5.2 is called the *Boltzmann Collision Integral*; usually, further simplifications must be introduced in order to evaluate the integral explicitly.

5.1.2 Bounce-Averaged Kinetic Model

According to the preliminary estimates in Section 4.1, an average electron bounces at least 80 times in the source before undergoing an elastic collision with a neutral, and sufficiently energetic electrons undergo an inelastic collision only once every three elastic collisions. This is quite a typical situation for low-pressure plasma sources. As a consequence, if one wants to integrate Eq. 5.1 for several ionization collision times while resolving the full electron dynamics, the length of the simulation may easily become unmanageable.

A natural simplification is averaging the electron motion over many bounces in the potential well that is confining them in the source. This leads to a family of so-called ‘bounce-averaged’ kinetic models, which attempt to solve for the spatially-averaged electron distribution function.

Moreover, a rigorous *‘nonlocal’ approach* has been developed (see [53] and references therein), which permits one to take a spatial average directly from Eq. 5.1. Such a method usually focuses on the isotropic part of the distribution function only, and by making use of the difference between electron momentum and energy relaxation rates it reduces the independent variables from $(t,\mathbf{x},\mathbf{v})$ to $\left(t,\varepsilon^0\right)$, where $\varepsilon^0 = \varepsilon + q_e\Phi(\mathbf{x})$ is the total electron energy, the sum of the kinetic energy plus the potential energy. This way, the spatial dependence of the solution is still present, but only indirectly via the plasma potential $\Phi(\mathbf{x})$ encapsulated in ε^0. A space-averaged kinetic equation is then obtained by averaging over the volume $V\left(\varepsilon^0\right)$, which is limited by the "turning-point surface" $S\left(\varepsilon^0\right)$ where $\varepsilon^0 = q_e\Phi(\mathbf{x})$ and the electron kinetic energy vanishes. Such a procedure evidently requires knowledge of the potential spatial profile $\Phi(\mathbf{x})$, which can be obtained by additionally solving Poisson's equation together with a kinetic equation for the ions.

Instead, a simpler approach is used in the following analysis, which is less rigorous but allows for the introduction of more detail at a subsequent stage. The idea is to completely drop the dependence of the total kinetic energy of a single electron on space, or equivalently to assume that $\Phi \equiv 0$ everywhere in the source.

The collisional processes depend on the local electron kinetic energy, not on the total kinetic energy. But if one can assume that collisions happen mostly in a small spatial region where the potential is quite flat and close to its maximum, i.e. $\Phi \simeq 0$, then it is reasonable to use ε as the independent variable instead of ε^0. In fact, this is the approach used in the following analysis. (Accordingly, the terms 'energy', 'kinetic energy' and 'total energy' will be used interchangeably in this section.)

The (non-normalized) electron energy distribution function $f(\varepsilon, t)$ is defined saying that $f(\varepsilon, t)\,d\varepsilon$ is the number density of electrons having energy between ε and $\varepsilon + d\varepsilon$, at time t. As such, $f(\varepsilon, t)$ has the units of $\left[\mathrm{m}^{-3}/\mathrm{J}\right]$ and its zeroth-order moment gives the electron density

$$n_e(t) = \int_0^{\varepsilon_{max}(t)} f(\varepsilon, t)\,d\varepsilon \qquad \left[\mathrm{m}^{-3}\right] . \tag{5.3}$$

Similarly, the first-order moment of $f(\varepsilon, t)$ gives the average electron energy

$$\langle\varepsilon\rangle(t) = \frac{1}{n_e(t)} \int_0^{\varepsilon_{max}(t)} \varepsilon f(\varepsilon, t)\,d\varepsilon \qquad [\mathrm{J}] . \tag{5.4}$$

In the last two equations, $\varepsilon_{max}(t)$ is the maximum kinetic energy of trapped electrons, i.e. the energy associated with the confinement potential $\Phi_w(t)$:

$$\varepsilon_{max}(t) = q_e\Phi_w(t) \tag{5.5}$$

According to Rockwood [54], the time evolution of $f(\varepsilon, t)$ can be written in flux conservative form as

$$\frac{\partial f(\varepsilon, t)}{\partial t} = -\frac{\partial J_{RF}}{\partial\varepsilon} - \frac{\partial J_{el}}{\partial\varepsilon} - \frac{\partial J_{e-e}}{\partial\varepsilon} - \frac{\partial J_{e-i}}{\partial\varepsilon} + \sum_i S_i , \tag{5.6}$$

where each of the terms on the right-hand side describes a different process:

- J_{RF} is the particle flux in energy space driven by the applied electric field,

- J_{el} is the particle flux in energy space due to elastic collisions with neutrals,
- J_{e-e} is the particle flux in energy space due to electron-electron Coulomb collisions,
- J_{e-i} is the particle flux in energy space due to electron-ion Coulomb collisions,
- S_i are source terms due to inelastic collisional processes (excitation, deexcitation, ionization, recombination).

Elastic collisions of electrons with massive neutrals and ions are effective in isotropizing the distribution function, but have very little effect on the energy distribution; this is due to the fact that in an elastic collision the fraction of kinetic energy transferred from the electron to the massive particle is on average only $2m_e/M_{Ar} \approx 1.4 \cdot 10^{-5}$. Accordingly, in the present analysis the effects of J_{el} and J_{e-i} will be disregarded altogether.

On the other hand, Coulomb collisions between electrons may exchange kinetic energy effectively, and they have the overall effect of driving $f(\varepsilon, t)$ toward a (truncated) Maxwellian distribution. The momentum-transfer cross-section for e-e Coulomb collisions is proportional to T_e^{-2}, and it is only slightly dependent on the electron density via the logarithm of the Debye length. Accordingly, the average collision frequency for e-e Coulomb collisions is $\langle \nu_{e-e} \rangle = n_e \langle \sigma_{e-e} v_{th,e} \rangle$, and therefore

$$\langle \nu_{e-e} \rangle \propto n_e T_e^{-3/2} , \tag{5.7}$$

that is, this process is important at high electron densities and low electron temperatures. It is unclear whether Coulomb collisions really need to be included in this model, especially because a fairly high T_e is expected, according to Section 4.1.2. Nevertheless, the wide range of variability of n_e given by the same estimates, together with the effectiveness of e-e Coulomb collisions on the EEDF dynamics whenever $\langle \nu_{e-e} \rangle$ becomes comparable to other processes, suggests that it would be unsafe to neglect this phenomenon a-priori. Therefore, the numerical model will include electron-electron Coulomb collisions.

With regards to the source terms, the effect of collisional deexcitation and recombination will not be taken into account. The justification for this is in the small dimensions of the plasma source and in the very low neutral density: once produced, the excited species will either de-excite by spontaneous photon emission (transitory states) or by collisions with the walls (metastable states). In fact, there is little chance that an emitted photon may impact a neutral particle before escaping from the source (*optically thin* plasma), and there is a similarly little chance that a metastable neutral may be ionized by an electron before reaching the wall. (Penning ionization, i.e. the production of an ion after the collision of two metastable neutrals, is neglected for the same reason.) Overall, the aforementioned assumptions about inelastic collisions permit one to considerably simplify the model, as there is no need to determine the densities of the excited levels of Argon in the source.

As a consequence of the hypotheses just introduced, Eq. 5.6 can be simplified to

$$\frac{\partial f(\varepsilon,t)}{\partial t} = -\frac{\partial J_{RF}}{\partial \varepsilon} - \frac{\partial J_{e-e}}{\partial \varepsilon} + S_{ex} + S_{iz}\,, \tag{5.8}$$

where S_{ex} is the source term due to electron impact excitation, and S_{iz} is the source term due to electron impact ionization.

5.1.3 Time Evolution of the Normalized EEDF

Section 4.2 pointed out that the relaxation of the normalized Electron Energy Distribution Function (EEDF) is a process much faster than the relaxation of the electron density $n_e(t)$ towards its steady-state value $n_{e,ss}$. The normalized EEDF is simply defined as

$$F(\varepsilon,t) = \frac{1}{n_e(t)} f(\varepsilon,t) \quad \left[\mathrm{J}^{-1}\right], \tag{5.9}$$

and it has the same normalization property as a probability density function:

$$\int_0^{\varepsilon_{max}} F(\varepsilon,t)\,d\varepsilon \equiv 1\,. \tag{5.10}$$

Accordingly, $F(\varepsilon,t)$ retains no information about the actual particle number, but it only gives information about how the kinetic energy is distributed among electrons. Given $F(\varepsilon,t)$, the average kinetic energy is simply obtained as

$$\langle\varepsilon\rangle(t) = \int_0^{\varepsilon_{max}} \varepsilon F(\varepsilon,t)\,d\varepsilon\,. \tag{5.11}$$

Following the time evolution of $f(\varepsilon,t)$ is equivalent to separately following the time evolution of $F(\varepsilon,t)$ and $n_e(t)$; the latter option is in fact preferred to the direct solution of Boltzmann's Equation, for a number of reasons. The main advantage of distinguishing the dynamics of $F(\varepsilon,t)$ from the evolution of $n_e(t)$ is that it permits to accelerate the convergence to steady-state by means of a time-scale separation method, which will be described in detail in Section 5.4.

The time evolution of $n_e(t)$ is given by a 0D global balance equation (e.g. the particle number or the energy balance may be used). An equation for the time evolution of $F(\varepsilon, t)$ is obtained by differentiating Eq. 5.9 with respect to time:

$$\frac{\partial F(\varepsilon,t)}{\partial t} = \frac{1}{n_e(t)}\frac{\partial f(\varepsilon,t)}{\partial t} - \frac{1}{n_e(t)}\frac{dn_e(t)}{dt}F(\varepsilon,t)\,, \tag{5.12}$$

where $n_e(t)$ is given (it will also be assumed constant during the time integration), the instantaneous value of $\partial f/\partial t$ is evaluated using Eq. 5.8, and dn_e/dt is estimated by taking the integral over energy space of the same expression.

5.1.4 Electromagnetic Heating

The heating of electrons by interaction with the EM fields emitted by the RF antenna is modeled as a random-walk process in velocity space with a diffusion coefficient $D_v(\varepsilon, t)$ $\left[\mathrm{m}^2/\mathrm{s}^3\right]$. As such, the corresponding particle flux in energy space is

$$J_{RF}(\varepsilon,t) = 4\pi v^2\left(-D_v(\varepsilon,t)\frac{\partial f(v,t)}{\partial v}\right) \qquad \left[m^{\text{-}3}/s\right], \tag{5.13}$$

where $f(v,t)$ is the 3D velocity distribution function of electrons $\left[\mathrm{s}^3/\mathrm{m}^6\right]$, which is assumed to be isotropic and hence depends on the velocity magnitude v only. The normalization property of the isotropic $f(v,t)$ is

$$\int_0^{v_{\max}} f(v,t)\,4\pi v^2\,dv = n_e, \tag{5.14}$$

which can be compared to the normalization property of the EEDF $f(\varepsilon,t)$,

$$n_e = \int_0^{\varepsilon_{\max}} f(\varepsilon,t)d\varepsilon = \int_0^{\varepsilon_{\max}} f\left(\frac{1}{2}m_e v^2, t\right)m_e v\,dv, \tag{5.15}$$

to obtain a relation between $f(v,t)$ and $f(\varepsilon,t)$:

$$f(v,t) = \frac{m_e}{4\pi v}f(\varepsilon,t). \tag{5.16}$$

Differentiating the last equation with respect to v one gets

$$\frac{\partial f(v,t)}{\partial v} = \frac{\partial}{\partial v}\left[\frac{m_e}{4\pi v}f(\varepsilon,t)\right] = -\frac{m_e}{4\pi v^2}f(\varepsilon,t) + \frac{m_e}{4\pi v}\frac{\partial f(\varepsilon,t)}{\partial v}. \tag{5.17}$$

But

$$\frac{\partial f(\varepsilon,t)}{\partial v} = \frac{\partial f(\varepsilon,t)}{\partial \varepsilon}\frac{d\varepsilon}{dv} = \frac{\partial f(\varepsilon,t)}{\partial \varepsilon}m_e v, \tag{5.18}$$

so that

$$\frac{\partial f(v,t)}{\partial v} = -\frac{m_e}{4\pi v^2}\left[f(\varepsilon,t) - m_e v^2 \frac{\partial f(\varepsilon,t)}{\partial \varepsilon}\right]. \tag{5.19}$$

Substituting Eq. 5.19 into Eq. 5.13, and noticing that $m_e v^2 = 2\varepsilon$, one gets the following expression for the particle flux in energy space due to RF heating:

$$J_{RF}(\varepsilon,t) = 2\varepsilon m_e D_v(\varepsilon,t)\left(\frac{f(\varepsilon,t)}{2\varepsilon} - \frac{\partial f(\varepsilon,t)}{\partial \varepsilon}\right). \tag{5.20}$$

Eq. 5.20 completely describes the effect of the Electromagnetic heating on the EEDF, provided that the coefficient of diffusion in velocity space $D_v(\varepsilon,t)$ is fully characterized. Nevertheless, the detailed evaluation of $D_v(\varepsilon,t)$ is beyond the scope of this thesis work, as it would require a sophisticated EM model, which should couple the RF feeding circuit to the emitting antenna, and the antenna to the plasma response, in order to evaluate the EM fields in the plasma. Ultimately, $D_v(\varepsilon,t)$ would depend on the EEDF itself, and on external parameters like the operational frequency, the circuit impedance, the axial magnetic field, the geometry of the source, the antenna configuration, etc..

If the details of power coupling are neglected, one may easily impose 50 W of RF power coupled to electrons by assuming that the coefficient of diffusion in velocity space is uniform over the whole energy axis, so that $D_v(\varepsilon,t) \equiv D_v(t)\ \forall\,\varepsilon$. In fact, the power per unit volume $[\mathrm{W/m^3}]$ due to RF heating is just the integral over the energy axis of the corresponding particle flux:

$$P_{RF}(t) = \int_0^{\varepsilon_{\max}} J_{RF}(\varepsilon,t)\,d\varepsilon = m_e\int_0^{\varepsilon_{\max}} D_v(\varepsilon,t) f(\varepsilon,t)\,d\varepsilon - 2m_e\int_0^{\varepsilon_{\max}} D_v(\varepsilon,t)\,\varepsilon\,\frac{\partial f(\varepsilon,t)}{\partial \varepsilon}\,d\varepsilon. \tag{5.21}$$

Introducing the hypothesis of uniform $D_v(t)$, the last equation can be simplified to

$$P_{RF}(t) = m_e D_v(t)\left(\int_0^{\varepsilon_{\max}} f(\varepsilon,t)\,d\varepsilon - 2\int_0^{\varepsilon_{\max}} \varepsilon\,\frac{\partial f(\varepsilon,t)}{\partial \varepsilon}\,d\varepsilon\right), \tag{5.22}$$

where the first integral on the r.h.s. simply equals $n_e(t)$, while the second integral can be integrated by parts:

$$\int_0^{\varepsilon_{\max}} f(\varepsilon,t)\,d\varepsilon = n_e(t) \tag{5.23a}$$

$$\int_0^{\varepsilon_{\max}} \varepsilon\,\frac{\partial f(\varepsilon,t)}{\partial \varepsilon}\,d\varepsilon = \Big[\varepsilon f(\varepsilon,t)\Big]_0^{\varepsilon_{\max}} - \int_0^{\varepsilon_{\max}} f(\varepsilon,t)\,d\varepsilon = 0 - n_e(t) = -n_e(t)\,. \tag{5.23b}$$

Substituting Eqs. 5.23 into Eq. 5.22, a very simple expression is obtained for the power per unit volume coupled from the RF antenna to the electrons through the EM fields:

$$P_{RF}(t) = 3m_e D_v(t) n(t) \qquad [\mathrm{W/m^3}]\,. \tag{5.24}$$

Since the total power must be 50 W, it is sufficient to require that $P_{RF}(t)V_S = 50$ W, where V_S is the volume of the plasma source $\left[\mathrm{m}^3\right]$ where electrons are contained: the required value of the diffusion coefficient is then

$$D_v^*(t) = \frac{50\ \mathrm{W}}{3m_e V_S n_e(t)} \qquad \left[\mathrm{m}^2/\mathrm{s}^3\right]\ . \tag{5.25}$$

5.2 Collisional Processes

5.2.1 Electron-Electron Coulomb Collisions

Each electron interacts through a long-range electrostatic field with all the other electrons that are within a region approximately equal to a Debye sphere. The Fokker-Planck theory of e-e interactions [55] postulates that small velocity variations are the most probable, so that the Boltzmann collision integral can be expanded in Taylor series. A second hypothesis is that all but the lowest-order terms of the series contribute negligibly to the collision integral; this leads to a Fokker-Planck equation with two free parameters to be determined.

Another assumption is that changes in velocity result from two-particle interactions, or collisions during which spatial correlation effects (polarization effects or multiple collisions) are unimportant: this hypothesis is usually valid for all under-dense plasmas where the Boltzmann Equation holds in the first place. With this last assumption, the Fokker-Planck collision integral can be completely specified.

An important result of this theory is that ‘grazing’ collisions (i.e. events causing small deflections) have a dominant effect over large-angle collisions, so that one can imagine the target electron being ‘continuously’ accelerated (or decelerated) by the interaction with other electrons, without undergoing ‘jumps’ in energy. As a consequence, even though the Coulomb collision operator is not local in energy-space, its net effect does depend on the local shape of the EEDF. Therefore, it is possible to write the Coulomb collision operator in flux conservative form, but the corresponding flux function will depend on the whole EEDF.

According to the derivation in [54], the flux in energy space due to Coulomb collisions between electrons can be written as

$$J_{e-e}(\varepsilon,t) = \alpha(t)\left[P(\varepsilon,t)\left(\frac{f(\varepsilon,t)}{2\varepsilon} - \frac{\partial f(\varepsilon,t)}{\partial\varepsilon}\right) - Q(\varepsilon,t)\,f(\varepsilon,t)\right] \quad \left[\mathrm{m}^{-3}/\mathrm{s}\right], \tag{5.26}$$

where $P(\varepsilon,t)$ and $Q(\varepsilon,t)$ are integral quantities obtained from $f(\varepsilon,t)$:

$$P(\varepsilon,t) = \frac{2}{\sqrt{\varepsilon}}\int_0^{\varepsilon}\varepsilon' f(\varepsilon',t)d\varepsilon' + 2\varepsilon\int_{\varepsilon}^{\infty}\frac{f(\varepsilon',t)}{\sqrt{\varepsilon'}}d\varepsilon' \qquad [\text{m}^{-3}\,\text{J}^{0.5}], \tag{5.27}$$

$$Q(\varepsilon,t) = \frac{3}{\sqrt{\varepsilon}}\int_0^{\varepsilon} f(\varepsilon',t)d\varepsilon' \qquad [\text{m}^{-3}/\text{J}^{0.5}]. \tag{5.28}$$

$\alpha(t)$ is a parameter that depends weakly on the first two moments of $f(\varepsilon,t)$

$$\alpha(t) = \frac{q_e^4}{24\pi\epsilon_0^2}\sqrt{\frac{2}{m_e}}\ln\Lambda(t) \qquad [\text{J}^{1.5}\text{m}^3/\text{s}] \tag{5.29}$$

where q_e is the electron charge [C], m_e is the electron mass [kg], ϵ_0 is the vacuum permittivity [F/m], and Λ is a non-dimensional parameter defined as

$$\Lambda = \frac{\lambda_D}{b_{\frac{\pi}{2}}}. \tag{5.30}$$

where λ_D is the Debye length [m],

$$\lambda_D = \sqrt{\frac{\epsilon_0 k T_e}{q_e^2 n_e(t)}} = \sqrt{\frac{2}{3n_e(t)}}\sqrt{\frac{\epsilon_0\langle\varepsilon\rangle(t)}{q_e^2}}, \tag{5.31}$$

and $b_{\frac{\pi}{2}}$ is the impact parameter for a 90 deg deviation [m]:

$$b_{\frac{\pi}{2}} = \frac{q_e^2}{4\pi\epsilon_0\frac{1}{2}m_e v_0^2} \simeq \frac{1}{4\pi}\frac{q_e^2}{\epsilon_0\langle\varepsilon\rangle(t)}. \tag{5.32}$$

Finally, the following expression is obtained for Λ:

$$\Lambda(t) = 4\pi\sqrt{\frac{2}{3n_e(t)}}\left[\frac{\epsilon_0\langle\varepsilon\rangle(t)}{q_e^2}\right]^{\frac{3}{2}}. \tag{5.33}$$

5.2.2 Electron Impact Excitation

Describing the excitation of Ground State neutrals by electron impact is rather straightforward, the only complication being the fact of having quite a large number of excited states to take into account. Each excited state p is characterized by a *threshold energy* $\varepsilon_{ex}^{(p)}$ and a cross-section $\sigma_{ex}^{(p)}(\varepsilon)$. An electron with energy $\varepsilon > \varepsilon_{ex}^{(p)}$ has a non-zero probability of exciting a Ground State neutral to level p; if this happens, then the electron loses exactly the threshold energy and its residual kinetic energy drops to $\varepsilon - \varepsilon_{ex}^{(p)}$.

In order to determine the Source term $S_{ex}(\varepsilon,t)$ [m^{-3}/s] that appears in Eq. 5.8, instead of following a single electron, one should focus on a certain energy ε^* and quantify the instantaneous effect of the excitation process on the number density of particles at that energy, i.e. $f(\varepsilon^*)d\varepsilon$. For each energy level p, there are two different contributions:

1. a positive contribution of electrons (previously) having energy $\varepsilon^* + \varepsilon_{ex}^{(p)}$, which lose the energy $\varepsilon_{ex}^{(p)}$ in an excitation event and fall to the energy ε^*;
2. a negative contribution of electrons having energy ε^*, which excite a neutral and fall to the energy $\varepsilon^* - \varepsilon_{ex}^{(p)}$.

Clearly, the positive contribution from higher energy is only present if $\varepsilon^* + \varepsilon_{ex}^{(p)} \le \varepsilon_{max}$. Similarly, the negative contribution towards lower energy is only present if $\varepsilon^* \ge \varepsilon_{ex}^{(p)}$. Since S_{ex} describes the interaction between points in energy space that have a distance $\varepsilon_{ex}^{(p)}$ from each other, it is a *non-local* operator. It can be written as

$$S_{ex}(\varepsilon, t) = \sum_p \Big[H\big(\varepsilon_{max} - \varepsilon_{ex}^{(p)} - \varepsilon\big)\, \nu_{ex}^{(p)}\big(\varepsilon + \varepsilon_{ex}^{(p)}\big)\, f\big(\varepsilon + \varepsilon_{ex}^{(p)}, t\big) - H\big(\varepsilon - \varepsilon_{ex}^{(p)}\big)\, \nu_{ex}^{(p)}\big(\varepsilon\big)\, f\big(\varepsilon, t\big) \Big] \tag{5.34}$$

where $\nu_{ex}^{(p)}(\varepsilon)$ is the excitation collision frequency to level p for electrons having energy ε:

$$\nu_{ex}^{(p)}(\varepsilon) = n_g\, \sigma_{ex}^{(p)}(\varepsilon)\, v(\varepsilon)\ . \tag{5.35}$$

In Eq. 5.35, n_g is the average density of neutral particles in the source [m^{-3}], $\sigma_{ex}^{(p)}(\varepsilon)$ is the cross-section [m^2] for excitation from Ground State to the excited level p, and $v(\varepsilon) = \sqrt{2\varepsilon/m_e}$ is the electron velocity [m/s]. To simplify the notation, the common Heaviside step function is used in Eq. 5.34:

$$H(x) = \begin{cases} 1 & \text{if } x \ge 0\,, \\ 0 & \text{otherwise.} \end{cases} \tag{5.36}$$

Table 5.1 collects the set of energy levels of electronic excitation of Argon (suggested by Hayashi [56]), which are implemented in the numerical model. The corresponding cross-sections are shown in Figs. 5.1-5.5.

Level No.	Energy (eV)	Paschen notation	Racah notation
1	11.55	$1s_5$	$4s[3/2]_2$
2	11.62	$1s_4$	$4s[3/2]_1$
3	11.72	$1s_3$	$4s'[1/2]_0$
4	11.83	$1s_2$	$4s'[1/2]_1$
5	12.91	$2p_{10}$	$4p[1/2]_1$
6	13.08	$2p_9$	$4p[5/2]_3$
7	13.09	$2p_8$	$4p[5/2]_2$
8	13.15	$2p_7$	$4p[3/2]_1$
9	13.17	$2p_6$	$4p[3/2]_2$
10	13.27	$2p_5$, $2p_4$	$4p[1/2]_0$, $4p'[3/2]_1$
11	13.03	$2p_3$	$4p'[3/2]_2$
12	13.33	$2p_2$	$4p'[1/2]_1$
13	13.47	$2p_1$	$4p'[1/2]_0$
14	13.84	$3d_6$, $3d_5$	$3d[1/2]_0$, $3d[1/2]_1$
15	13.90	$3d_3$	$3d[3/2]_2$
16	13.98	$3d'_4$	$3d[7/2]_4$
17	14.01	$3d_4$	$3d[7/2]_3$
18	14.06	$3d''_1$, $2s_5$	$3d[5/2]_2$, $5s[3/2]_2$
19	14.09	$3d'_1$, $2s_4$	$3d[5/2]_3$, $5s[3/2]_1$
20	14.15	$3d_2$	$3d[3/2]_1$
21	14.21	$3s''''_1$	$3d'[5/2]_2$
22	14.23	$3s'''_1$, $3s''_1$, $2s_3$, $2s_2$	$3d'[5/2]_3$, $3d'[3/2]_2$, $5s'[1/2]_0$, $5s'[1/2]_1$
23	14.30	$3s'_1$	$3d'[3/2]_1$
24	14.71	$4d_5$	$4d[1/2]_1$
25	15.20	$4p_2$, $4p_4$, $4p_3$	$6p'[1/2]_1$, $6p'[3/2]_1$, $6p'[3/2]_2$

Table 5.1: Energy levels of electronic excitation for Argon [56]. Levels 1 and 3 are metastable, all other levels are transitory (also called ‘resonant states’), i.e. they can de-excite by spontaneous photon emission. Levels 10, 14, 18, 19, 22 and 25 are the combination of two or more quantum states; since such states have energies very close to each other (the difference being ≤ 0.01 eV), and similar collisional behavior, it is practical to treat them as a unique energy level.

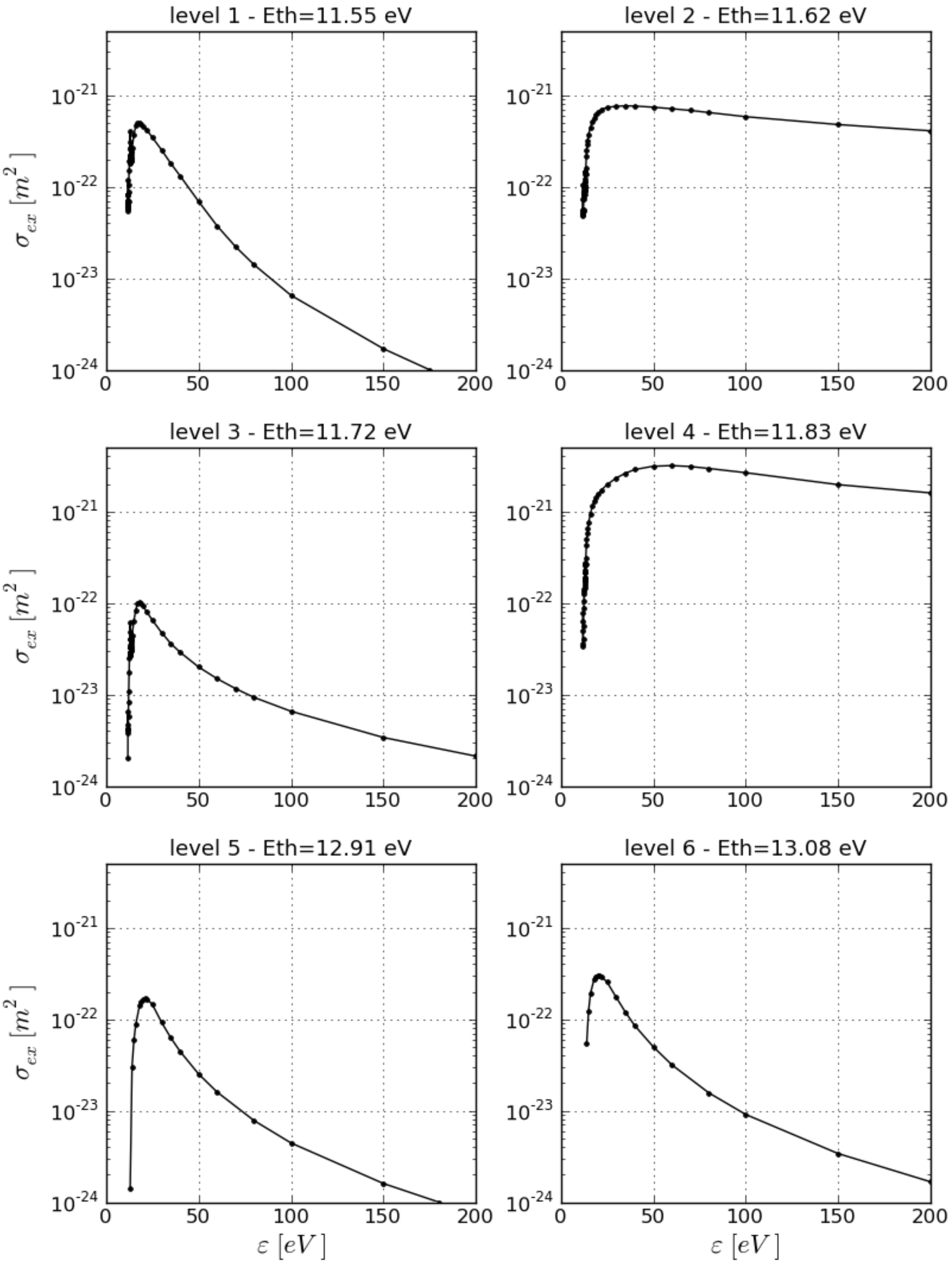

Figure 5.1: Electron impact cross-sections for the excitation of Ground State neutral Argon atoms to the energy levels 1 to 6 (defined in Table 5.1). The kinetic energy ε of the impacting electron (in abscissa) is limited to the range of interest $0 \le \varepsilon \le 200$ eV. The cross-section values (in ordinate) make use of the same logarithmic scale for all energy levels. The cross-sections reported in this figure belong to a consistent dataset suggested by Hayashi [56]; the dots represent the experimental data, while the solid line is the linear piecewise interpolation curve used in the numerical model.

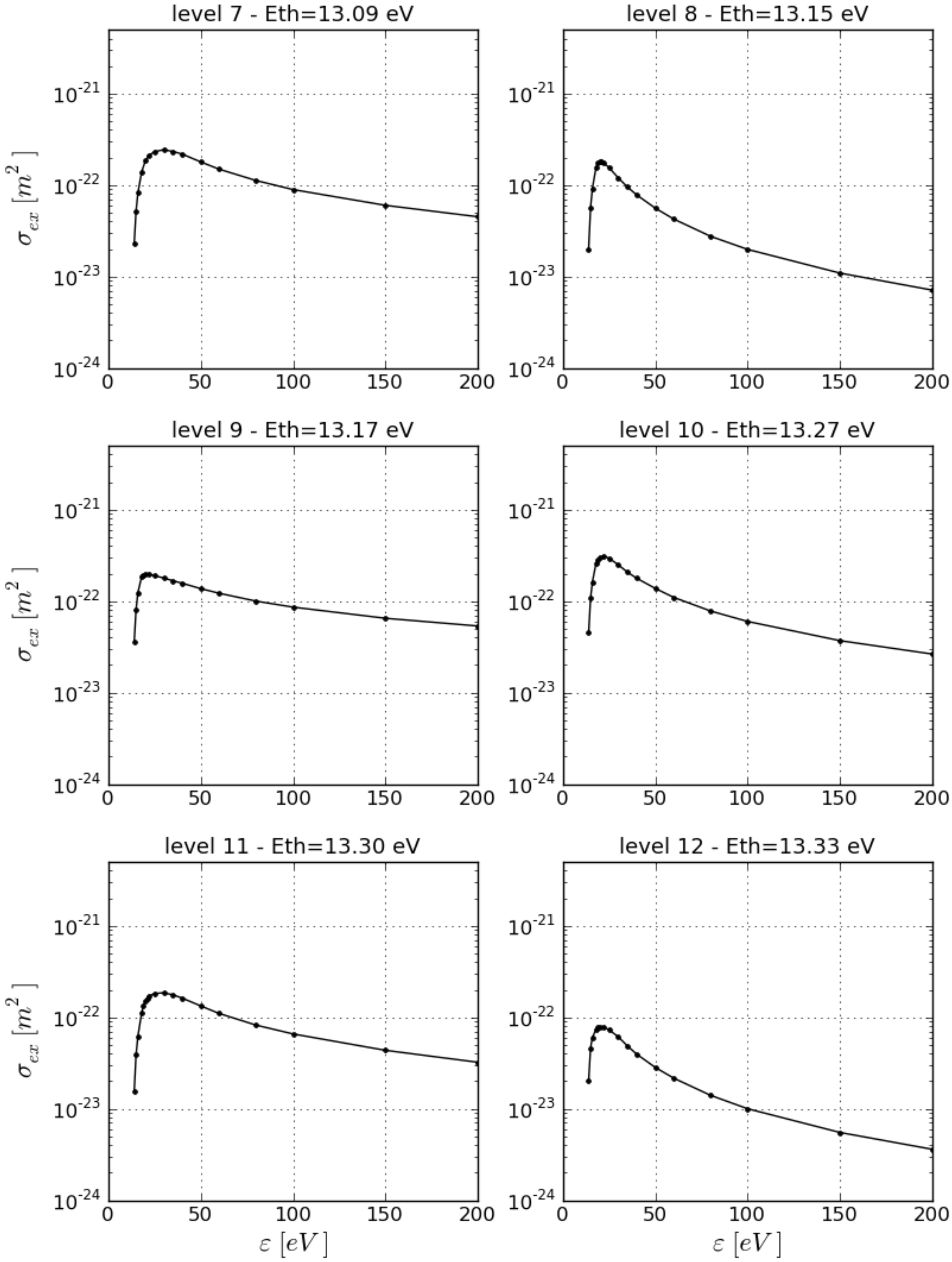

Figure 5.2: Electron impact cross-sections for the excitation of Ground State neutral Argon atoms to the energy levels 7 to 12 (defined in Table 5.1). The kinetic energy ε of the impacting electron (in abscissa) is limited to the range of interest $0 \le \varepsilon \le 200$ eV. The cross-section values (in ordinate) make use of the same logarithmic scale for all energy levels. The cross-sections reported in this figure belong to a consistent dataset suggested by Hayashi [56]; the dots represent the experimental data, while the solid line is the linear piecewise interpolation curve used in the numerical model.

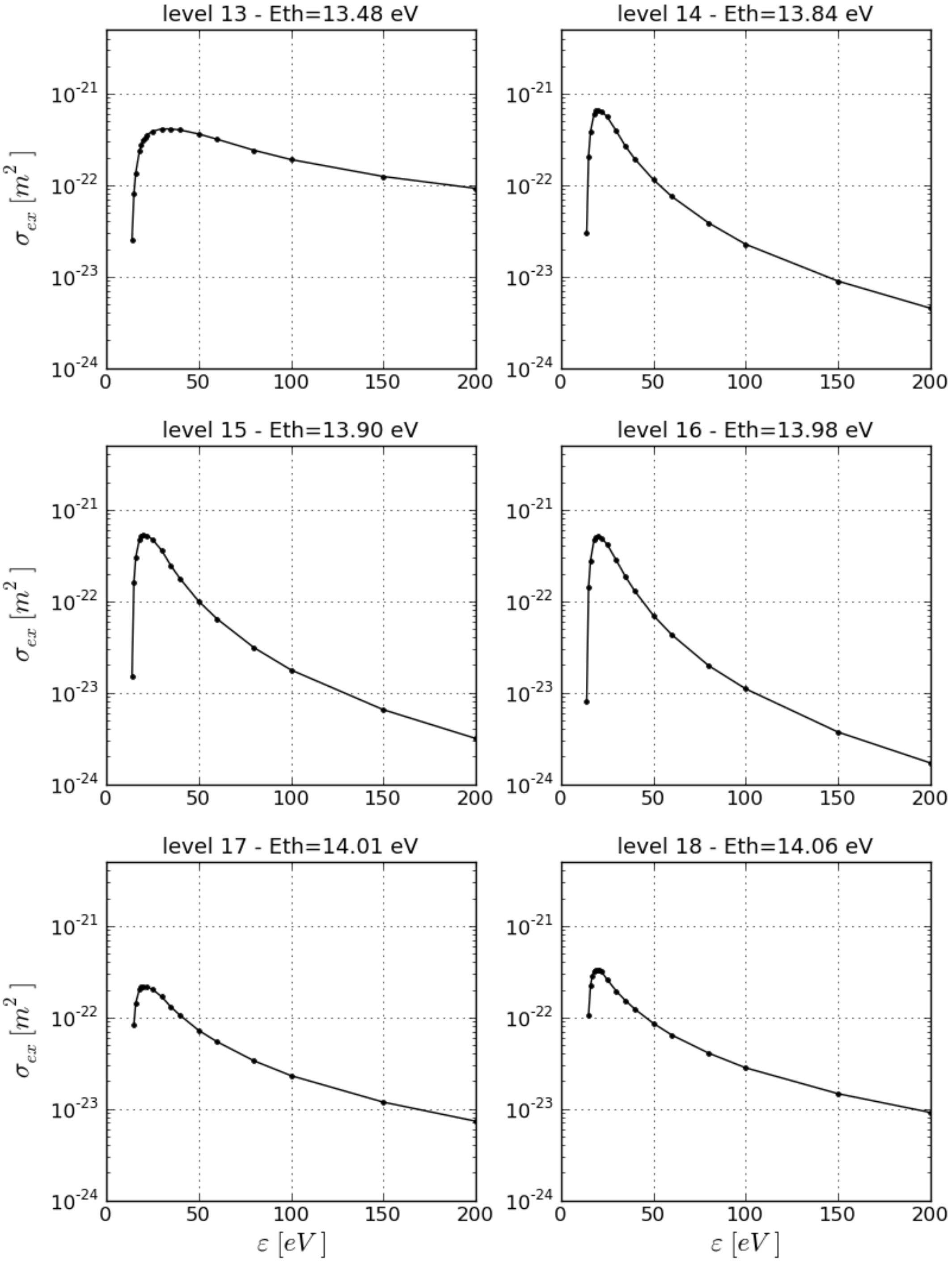

Figure 5.3: Electron impact cross-sections for the excitation of Ground State neutral Argon atoms to the energy levels 13 to 18 (defined in Table 5.1). The kinetic energy ε of the impacting electron (in abscissa) is limited to the range of interest $0 \leq \varepsilon \leq 200$ eV. The cross-section values (in ordinate) make use of the same logarithmic scale for all energy levels. The cross-sections reported in this figure belong to a consistent dataset suggested by Hayashi [56]; the dots represent the experimental data, while the solid line is the linear piecewise interpolation curve used in the numerical model.

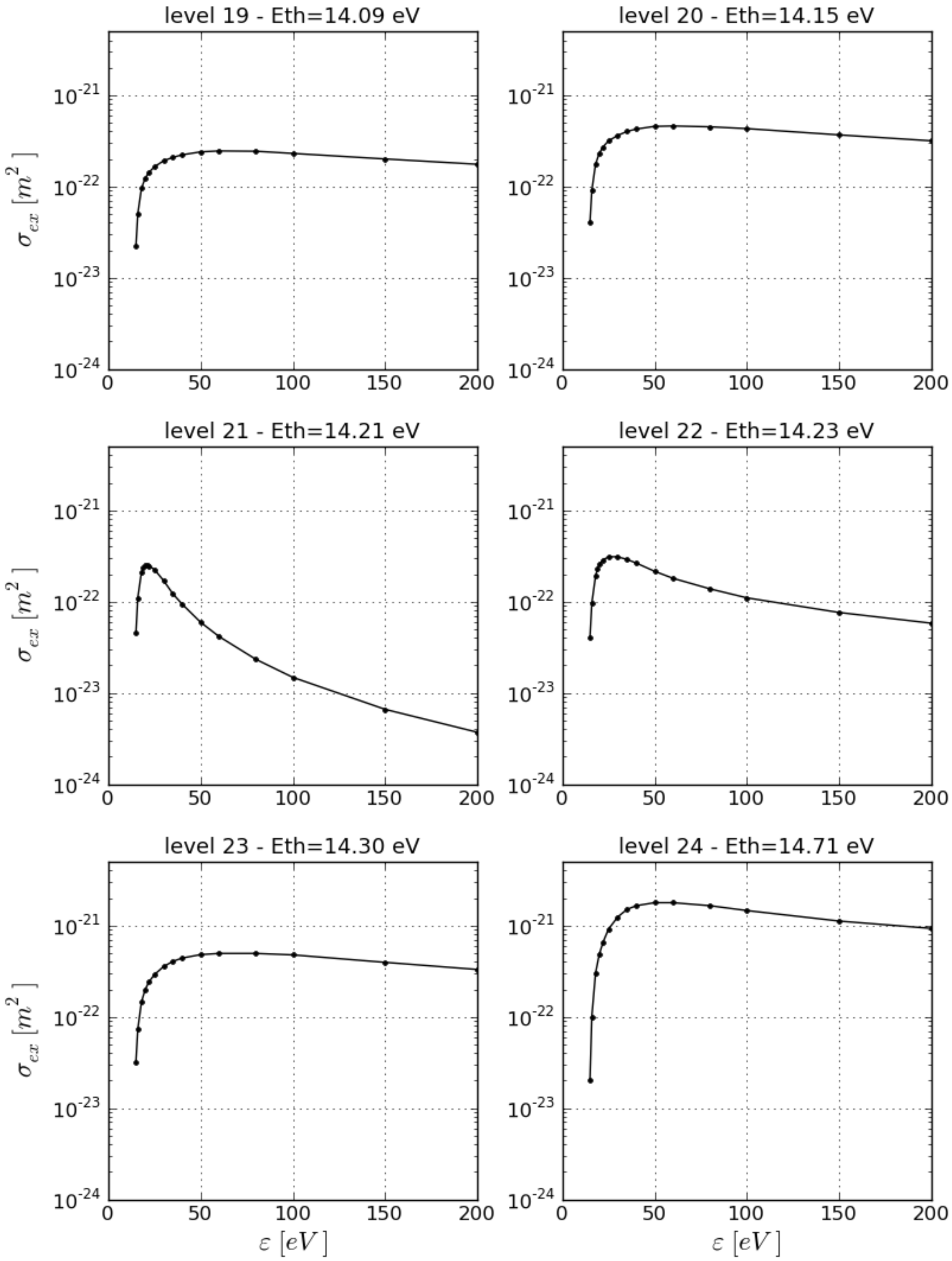

Figure 5.4: Electron impact cross-sections for the excitation of Ground State neutral Argon atoms to the energy levels 19 to 24 (defined in Table 5.1). The kinetic energy ε of the impacting electron (in abscissa) is limited to the range of interest $0 \leq \varepsilon \leq 200$ eV. The cross-section values (in ordinate) make use of the same logarithmic scale for all energy levels. The cross-sections reported in this figure belong to a consistent dataset suggested by Hayashi [56]; the dots represent the experimental data, while the solid line is the linear piecewise interpolation curve used in the numerical model.

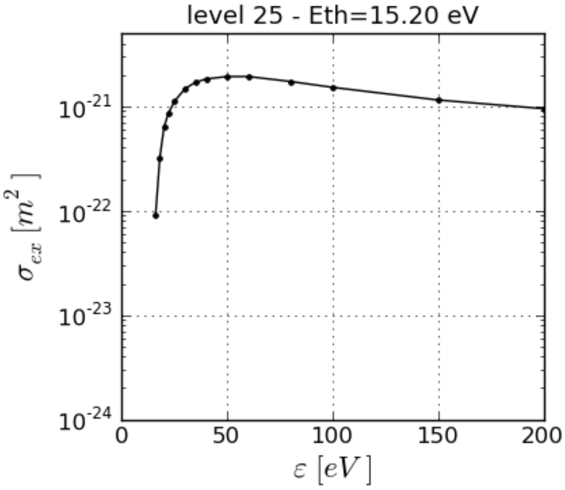

Figure 5.5: Electron impact cross-sections for the excitation of Ground State neutral Argon atoms to energy level 25 (defined in Table 5.1). The kinetic energy ε of the impacting electron (in abscissa) is limited to the range of interest $0 \le \varepsilon \le 200$ eV. The cross-section values (in ordinate) make use of the same logarithmic scale used in Figs. 5.1-5.4. The cross-sections reported in this figure belong to a consistent dataset suggested by Hayashi [56]; the dots represent the experimental data, while the solid line is the linear piecewise interpolation curve used in the numerical model.

5.2.3 Electron Impact Ionization

The ionization of a Ground State neutral particle by electron impact is a process similar to excitation, but it is definitely more complicated to model. An electron with kinetic energy $\varepsilon > \varepsilon_{iz}$, the *ionization energy*, has a non-zero probability of ionizing a Ground State neutral upon collision. If this happens, the impacting electron is called the 'primary' electron, and a new 'secondary' electron is obtained after ionization.

After ionization, it is not practical to distinguish between the primary and the secondary electrons, and such a separation is not even useful for the present modeling purposes; hence, the electron that causes ionization will be called the 'incident electron', and the two electrons obtained after ionization will be called 'ejected electrons' with no distinction.

Similarly to the excitation process, the residual kinetic energy after collision is $\varepsilon - \varepsilon_{iz}$, but this is shared between the two ejected electrons in a non-deterministic way. A common statistical approach in dealing with this problem is to introduce the *energy distribution of ejected electrons* $g(\varepsilon, \varepsilon_s)$, where $\varepsilon > \varepsilon_{iz}$ is the energy of the incident electron and ε_s is the energy of the ejected electrons. $g(\varepsilon, \varepsilon_s)\, d\varepsilon_s$ is the probability of finding ejected electrons with energy between ε_s and $\varepsilon_s + d\varepsilon_s$, produced after an electron impact ionization event with incident energy ε. Clearly, the energy of the ejected electrons is bounded by $0 \le \varepsilon_s \le \varepsilon - \varepsilon_{iz}$. The normalization property of the energy distribution of ejected electrons is

$$\int_0^{\varepsilon - \varepsilon_{iz}} g(\varepsilon, \varepsilon_s)\, d\varepsilon_s = 2, \tag{5.37}$$

because two ejected electrons correspond to one incident electron. Since the sum of the kinetic energy of the two ejected electrons necessarily equals $\varepsilon - \varepsilon_{iz}$, it follows that for each ejected electron at energy ε_s^* there is exactly one ejected electron at energy $(\varepsilon - \varepsilon_{iz}) - \varepsilon_s^*$. As a consequence, the energy distribution of ejected electrons is *symmetrical* with respect to $(\varepsilon - \varepsilon_{iz})/2$.

Following the same procedure described in Sec. 5.2.2, one should focus on a certain energy ε^* on the energy axis in order to quantify the instantaneous effect of ionization on the number density $f(\varepsilon^*)d\varepsilon$. Again, two different contributions can be distinguished:

1. a positive contribution of ejected electrons produced at energy ε^*, due to ionization impacts in the whole range of incident energies between $\varepsilon^* + \varepsilon_{iz}$ and ε_{max};
2. a negative contribution of incident electrons having energy ε^*, which ionize a neutral and produce ejected electrons at lower energies $0 \le \varepsilon_s \le \varepsilon^* - \varepsilon_{iz}$.

Accordingly, the ionization Source term can be written as:

$$S_{iz}(\varepsilon,t) \;=\; H\big(\varepsilon_{max}-\varepsilon_{iz}-\varepsilon\big)\int_{\varepsilon+\varepsilon_{iz}}^{\varepsilon_{max}} \nu_{iz}\left(\varepsilon'\right) f\left(\varepsilon',t\right) g\left(\varepsilon',\varepsilon\right) d\varepsilon' \;-\; H\big(\varepsilon-\varepsilon_{iz}\big)\,\nu_{iz}\big(\varepsilon\big)\, f\big(\varepsilon,t\big) \tag{5.38}$$

where $\nu_{iz}(\varepsilon)$ is the ionization collision frequency for electrons having energy ε:

$$\nu_{iz}(\varepsilon) \;=\; n_g\,\sigma_{iz}(\varepsilon)\, v(\varepsilon)\;. \tag{5.39}$$

As in Eq. 5.35, n_g is the average density of neutral particles in the source [m^{-3}], and $v(\varepsilon) = \sqrt{2\varepsilon/m_e}$ is the velocity of the incident electron [m/s]. $\sigma_{iz}(\varepsilon)$ is the ionization cross-section [m^2] from Ground State. In Eq. 5.38, $H(\cdot)$ is the Heaviside step function defined by Eq. 5.36. Fig. 5.6 reports the cross-section data for $\sigma_{iz}(\varepsilon)$ used in the model, as collected by Hayashi [56].

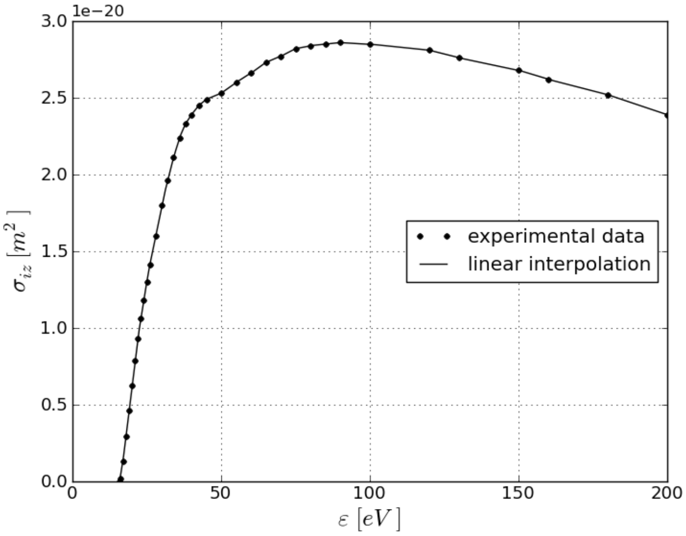

Figure 5.6: Cross-section data for electron impact ionization of Ground State neutral Argon atoms; experimental data are shown [56], together with the piecewise linear interpolation curve used in the model. The Argon ionization energy used in the model is ε_{iz} = 15.76 eV.

It is rare to find in the literature an explicit expression for the ejected energy distribution $g\left(\varepsilon,\varepsilon_s\right)$; instead, experimentalists usually measure the energy of ejected electrons in order to provide the *energy differential cross-section* $\sigma_{iz}\left(\varepsilon,\varepsilon_s\right)$ for electron impact ionization [m^2/J], which results in the usual ionization cross section upon integration over the half-range of ejected energies:

$$\int_0^{\frac{\varepsilon-\varepsilon_{iz}}{2}} \sigma_{iz}\left(\varepsilon,\varepsilon_s\right) d\varepsilon_s \;=\; \sigma_{iz}(\varepsilon)\;. \tag{5.40}$$

The following identity holds,

$$\sigma_{iz}(\varepsilon,\varepsilon_s) \;=\; \sigma_{iz}(\varepsilon)\, g(\varepsilon,\varepsilon_s)\ , \tag{5.41}$$

which can be used as a definition for obtaining $g(\varepsilon,\varepsilon_s)$ from the available energy differential cross-section data available in the literature.

Eq. 5.41 shows how the energy differential cross-section $\sigma_{iz}(\varepsilon,\varepsilon_s)$ retains information about the probability of causing ionization, and about the energy distribution of the ejected electrons, at the same time. Since reliable data for energy differential cross-sections are quite difficult to find, and they are usually given for a small set of values of the incident energy ε, in this thesis work the energy differential cross-sections for Argon are only used to construct the function $g(\varepsilon,\varepsilon_s)$. Consistently, the calculation of the ionization frequency (Eq. 5.39) makes use of the data shown in Fig. 5.6 for the Argon total ionization cross-section $\sigma_{iz}(\varepsilon)$.

It is worth pointing out that most often the energy differential cross-section is given as a function of two non-dimensional variables [57]: the *reduced incident energy*

$$u \;=\; \frac{\varepsilon}{\varepsilon_{iz}}, \tag{5.42}$$

which must be > 1 for ionization to occur, and the *reduced ejected energy*

$$x \;=\; \frac{\varepsilon_s}{\varepsilon-\varepsilon_{iz}} \qquad (0 \le x \le 1)\,, \tag{5.43}$$

which is usually limited to values in $[0, 0.5]$, taking advantage of the symmetry property. Using the two new variables, $\sigma_{iz}(u,x)$ is now the quantity of interest, which can be found plotted as a function of x, parametric in u. Fang et al. [57] suggest the use of the Gaussian fit

$$\sigma_{iz}(u,x) \;\simeq\; a\, e^{b(x-0.5)^2}, \tag{5.44}$$

where the two parameters $a(u)$ and $b(u)$ are related to the size and shape of the energy differential cross-section, respectively. Accordingly, the non-dimensional parameter $b(u)$ uniquely defines the normalized $G(u,x)$ as

$$G(u,x) \;:=\; (\varepsilon-\varepsilon_{iz})\cdot g(u\varepsilon_{iz}, x(\varepsilon-\varepsilon_{iz})) \simeq\; c_0\, e^{b(u)\cdot(x-0.5)^2}, \tag{5.45}$$

where c_0 is just a normalization constant that ensures $\int_0^{0.5} G(u,x)dx = 1$.

Table 5.2 contains the parameter $b(u)$ for Argon, as reported in [57]; the corresponding Gaussian fits are displayed in Fig. 5.7.

u	1.125	1.50	2.25	3.00	5.00	7.50	10.00
b	0.118	1.10	3.64	5.83	10.00	13.35	15.51

Table 5.2: Parameter $b(u)$ for the Gaussian fit of the (normalized) energy distribution function of ejected electrons; data for Argon from [57].

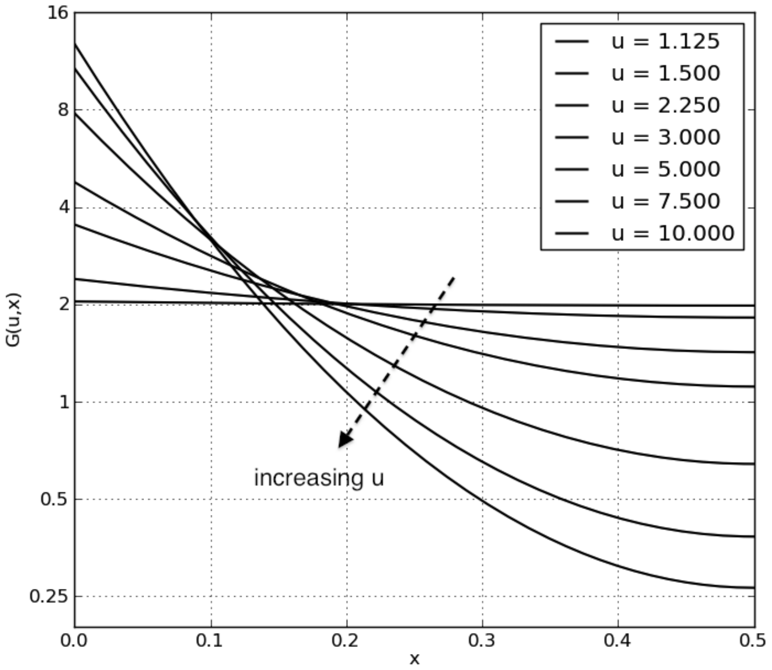

Figure 5.7: Non-dimensional energy distribution function of ejected electrons after an ionizing collision with an Argon neutral atom (Eq. 5.45), as a function of the reduced incident energy u (Eq. 5.42) and of the reduced ejected energy x (Eq. 5.43). Curves are obtained using the Gaussian fit in Eq. 5.45 with $b(u)$ given in Table 5.2, according to [57].

5.3 Semi-Discrete Formulation

5.3.1 Integral Formulation: Method of Lines

Several numerical methods exist that permit one to find an approximate solution to the PDE given by Eq. 5.8. In order to ensure a correct implementation of conservation of the number of particles, an *integral formulation* is employed. As a first step, the energy axis is discretized into N cells C_j ($j \in [0, N-1]$) having central energy ε_j and extension $\Delta\varepsilon_j$; each cell C_j coincides with the energy interval $\left[\varepsilon_{j-\frac{1}{2}}, \varepsilon_{j+\frac{1}{2}}\right]$. (Since the time variable is not discretized instead, this method is called 'semi-discrete'.) Then, one should note that the integral of $f(\varepsilon, t)$ over one cell is just the particle number density in that cell:

$$\int_{C_j} f(\varepsilon, t)\, d\varepsilon \;=\; n_j(t)\,. \tag{5.46}$$

Hence, the integration of Eq. 5.8 over each cell gives a system of N balance equations for the number densities in each cell:

$$\begin{aligned} \frac{d\,n_j(t)}{dt} \;=\; &-\left[J_{RF}\left(\varepsilon_{j+\frac{1}{2}}, t\right) - J_{RF}\left(\varepsilon_{j-\frac{1}{2}}, t\right)\right] \;-\; \left[J_{e-e}\left(\varepsilon_{j+\frac{1}{2}}, t\right) - J_{e-e}\left(\varepsilon_{j-\frac{1}{2}}, t\right)\right] \\ &+ \int_{\varepsilon_{j-\frac{1}{2}}}^{\varepsilon_{j+\frac{1}{2}}} S_{ex}(\varepsilon, t)\, d\varepsilon \;+ \int_{\varepsilon_{j-\frac{1}{2}}}^{\varepsilon_{j+\frac{1}{2}}} S_{iz}(\varepsilon, t)\, d\varepsilon \qquad (j \in [0, N-1]) \end{aligned} \tag{5.47}$$

It should be pointed out that no approximation was introduced in deriving Eq. 5.47, which is in fact exact.

In order to proceed with a numerical solution, the terms on the right hand side must be approximated as functions of the N values $n_j(t)$. A simple procedure is to assume that the energy axis is *discrete*, i.e. the kinetic energy of an electron can only assume one of the set of N values ε_j, which correspond to the center of (or another pre-determined location in) the mesh cells earlier described. As another way to look at it, one can think of the electron energy distribution function as a sum of N Dirac deltas of amplitude $n_j(t)$:

$$f(\varepsilon, t) \;\simeq\; \sum_{j=0}^{N-1} \delta(\varepsilon - \varepsilon_j)\, n_j(t)\,. \tag{5.48}$$

Accordingly, the source terms can be rewritten as

$$\int_{\varepsilon_{j-\frac{1}{2}}}^{\varepsilon_{j+\frac{1}{2}}} S_{ex}(\varepsilon, t)\, d\varepsilon \;=\; S_{ex,j}(t)\,\Delta\varepsilon_j \tag{5.49a}$$

$$\int_{\varepsilon_{j-\frac{1}{2}}}^{\varepsilon_{j+\frac{1}{2}}} S_{iz}(\varepsilon, t)\, d\varepsilon \;=\; S_{iz,j}(t)\,\Delta\varepsilon_j\,. \tag{5.49b}$$

As described in Section 5.1.4, J_{RF} is a linear operator.

If we assume that the flux J at the interface between two neighboring cells depends linearly on the values of $f(\varepsilon)$ in those cells, then it is possible to write

$$\begin{aligned} J(\varepsilon_{j+\frac{1}{2}}) &= a_j n_j - b_{j+1} n_{j+1} \\ J(\varepsilon_{j-\frac{1}{2}}) &= a_{j-1} n_{j-1} - b_j n_j \end{aligned} \tag{5.50}$$

where a_j and b_j are coefficients having dimension of $\left[\mathrm{s}^{-1}\right]$. a_j may be interpreted as the frequency with which electrons having energy ε_j are accelerated to ε_{j+1}; similarly, b_j is the frequency of deceleration for electrons from ε_j to ε_{j-1}. The difference between the right and left fluxes in Eq. 5.50 gives the following net contribution to cell j:

$$-\left[J(\varepsilon_{j+\frac{1}{2}}) - J(\varepsilon_{j-\frac{1}{2}})\right] = a_{j-1} n_{j-1} - \left(a_j + b_j\right) n_j + b_{j+1} n_{j+1} \,. \tag{5.51}$$

Denoting by $\vec{n}(t)$ the vector of N values $n_j(t)$, Eq. 5.47 can be rewritten in matrix form as

$$\frac{d\vec{n}}{dt} = \mathrm{M}\,\vec{n} \,. \tag{5.52}$$

Eq. 5.52 is a system of ODEs, which can be integrated in time using the most appropriate time integrator, chosen among a great variety of options: semi-analytic or discrete, explicit or implicit, single-step or multi-step, fixed-step or adaptive-step, etc. Indeed, the widespread use of this method, the so-called *Method of Lines* (MOL), is mostly due to its ample set of possible choices for the time integration, which makes it a flexible tool for the solution of complex PDEs.

In the present case, the semi-discrete model given by Eq. 5.52 was obtained using an integral approach; as a consequence, the discrete variables n_js are not point values as in a standard finite-difference scheme, but they represent integral quantities on the cell: they are in fact particle numbers per unit volume in physical space. The main advantage of this fact is that integral properties of the original PDE, like particle and energy conservations, can be easily enforced on the semi-discrete model, at the time when the matrix M in Eq. 5.52 is constructed. To achieve this, matrix M is written as the sum of the separate contributions from EM heating, electron-electron Coulomb collisions, and electron-neutral excitation and ionization,

$$\mathrm{M} = \mathrm{M}_{RF} + \mathrm{M}_{e-e} + \mathrm{M}_{ex} + \mathrm{M}_{iz} \,, \tag{5.53}$$

so that each matrix on the r.h.s. of Eq. 5.53 can be constructed to satisfy the aforementioned integral conservations. The matrices M_{RF} and M_{e-e} are tri-diagonal, and according to Eq. 5.51 they have the form given in the following 5x5 example:

$$\mathrm{M}_J^{(N=5)} = \begin{pmatrix} -a_0 & b_1 & 0 & 0 & 0 \\ a_0 & -(a_1+b_1) & b_2 & 0 & 0 \\ 0 & a_1 & -(a_2+b_2) & b_3 & 0 \\ 0 & 0 & a_2 & -(a_3+b_3) & b_4 \\ 0 & 0 & 0 & a_3 & -(a_4+b_4) \end{pmatrix} . \tag{5.54}$$

In Eq. 5.54 the sum of the terms on each column (apart from the last column) equals zero, meaning that the rate of variation of n_j is correctly balanced by the rates of variation of n_{j-1} and n_{j+1}; that is, electrons are neither created nor destroyed by the EM fields or the e-e Coulomb collisions, but they can only move from one cell to a neighbor cell. The matrix in Eq. 5.54 implicitly contains two Boundary Conditions (BCs):

- a homogeneous Neumann BC at $\varepsilon = 0$, i.e. no-flux at zero energy (because $b_0 = 0$);
- a homogeneous Dirichlet BC at $\varepsilon = \varepsilon_{\max}$, i.e. $f(\varepsilon_{\max}) = 0$.

The sum of the terms in the last column in Eq. 5.54 is not zero because electrons flow out of the system whenever they ‘jump’ to an energy higher than $\varepsilon_{\max}$. This is one of the major differences with respect to the model described in [54].

In general, the flux matrices M_{RF} and M_{e-e} are completely defined by their vectors of coefficients $\vec{a}$ and $\vec{b}$; in the case of electron-electron Coulomb collision, each coefficient depends on $\vec{n}$ (it is a non-linear operator).

5.3.2 RF Heating Matrix

On a discrete energy mesh, the flux function $J_{RF}(\varepsilon, t)$ given by Eq. 5.20 needs to be evaluated at the cell interfaces (see Eq. 5.47). The functional dependence of $J_{RF}\left(\varepsilon_{j+\frac{1}{2}}, t\right)$ on the vector $\vec{n}(t)$ can be obtained from Eq. 5.20, by introducing suitable numerical approximations to the terms that appear on the r.h.s.

The value $f\left(\varepsilon_{j+\frac{1}{2}}, t\right)$ of the distribution function at the interface between cell C_j and cell C_{j+1} can be obtained by linear interpolation of the adjacent cell center values, so that

$$\begin{aligned} f\left(\varepsilon_{j+\frac{1}{2}}, t\right) &\approx \left(\frac{\varepsilon_{j+1} - \varepsilon_{j+\frac{1}{2}}}{\varepsilon_{j+1} - \varepsilon_j}\right) f(\varepsilon_j, t) + \left(\frac{\varepsilon_{j+\frac{1}{2}} - \varepsilon_j}{\varepsilon_{j+1} - \varepsilon_j}\right) f(\varepsilon_{j+1}, t) \\ &\approx \left(\frac{\varepsilon_{j+1} - \varepsilon_{j+\frac{1}{2}}}{\varepsilon_{j+1} - \varepsilon_j}\right) \frac{n_j(t)}{\Delta\varepsilon_j} + \left(\frac{\varepsilon_{j+\frac{1}{2}} - \varepsilon_j}{\varepsilon_{j+1} - \varepsilon_j}\right) \frac{n_{j+1}(t)}{\Delta\varepsilon_{j+1}} . \end{aligned} \tag{5.55}$$

Consistently with the linear interpolation above, the partial derivative of the EEDF with respect to energy, evaluated at the same cell interface $\varepsilon_{j+\frac{1}{2}}$, is

$$\frac{\partial f}{\partial \varepsilon}\left(\varepsilon_{j+\frac{1}{2}}, t\right) \approx \frac{f(\varepsilon_{j+1}, t) - f(\varepsilon_j, t)}{\varepsilon_{j+1} - \varepsilon_j} \approx \frac{1}{\varepsilon_{j+1} - \varepsilon_j}\left(\frac{n_{j+1}(t)}{\Delta\varepsilon_{j+1}} - \frac{n_j(t)}{\Delta\varepsilon_j}\right). \tag{5.56}$$

The substitution of Eqs. 5.55 and 5.56 into Eq. 5.20 yields a finite-difference approximation to the flux $J_{RF}\left(\varepsilon_{j+\frac{1}{2}}, t\right)$, as

$$J_{RF}\left(\varepsilon_{j+\frac{1}{2}}, t\right) \approx m_e D_v^*(t)\left[\frac{1}{\Delta\varepsilon_j}\left(\frac{\varepsilon_{j+1} + \varepsilon_{j+\frac{1}{2}}}{\varepsilon_{j+1} - \varepsilon_j}\right) n_j(t) - \frac{1}{\Delta\varepsilon_{j+1}}\left(\frac{\varepsilon_{j+\frac{1}{2}} + \varepsilon_j}{\varepsilon_{j+1} - \varepsilon_j}\right) n_{j+1}(t)\right]. \tag{5.57}$$

Eq. 5.57 can be written in the form $J\left(\varepsilon_{j+\frac{1}{2}}\right) = a_j n_j - b_{j+1} n_{j+1}$ (see Eq. 5.50), with

$$a_j^{RF}(t) = D_v^*(t)\left(\frac{m_e}{\Delta\varepsilon_j}\,\frac{\varepsilon_{j+1} + \varepsilon_{j+\frac{1}{2}}}{\varepsilon_{j+1} - \varepsilon_j}\right), \tag{5.58a}$$

$$b_{j+1}^{RF}(t) = D_v^*(t)\left(\frac{m_e}{\Delta\varepsilon_{j+1}}\,\frac{\varepsilon_{j+\frac{1}{2}} + \varepsilon_j}{\varepsilon_{j+1} - \varepsilon_j}\right). \tag{5.58b}$$

It remains to verify whether the discrete formulation above ensures that 50 W are coupled to the electrons. The total EM power coupled to electrons in the discrete model is

$$\begin{aligned} P_{RF}(t) &= \sum_{j=0}^{N-1} J_{RF}\left(\varepsilon_{j+\frac{1}{2}}, t\right)\left(\varepsilon_{j+1} - \varepsilon_j\right) = \sum_{j=0}^{N-1}\left(a_j^{RF} n_j - b_{j+1}^{RF} n_{j+1}\right)\left(\varepsilon_{j+1} - \varepsilon_j\right) = \\ &= D_v^*(t) m_e \sum_{j=0}^{N-1}\left(\bar{a}_j^{RF} n_j - \bar{b}_{j+1}^{RF} n_{j+1}\right) = D_v^*(t) m_e\left[\bar{a}_0^{RF} n_0 + \sum_{j=1}^{N-1}\left(\bar{a}_j^{RF} - \bar{b}_j^{RF}\right) n_j + \bar{b}_N^{RF} n_N\right] \end{aligned} \tag{5.59}$$

where

$$\bar{a}_j^{RF} = \frac{\varepsilon_{j+1} + \varepsilon_{j+\frac{1}{2}}}{\Delta\varepsilon_j}, \qquad \bar{b}_{j+1}^{RF} = \frac{\varepsilon_{j+\frac{1}{2}} + \varepsilon_j}{\Delta\varepsilon_{j+1}}. \tag{5.60}$$

Substituting the formula for $D_v^*(t)$ (Eq. 5.25) into Eq. 5.59, and noticing that $n_N = 0$ because homogeneous Dirichlet BCs are applied at $\varepsilon_N = \varepsilon_{\max}$, one gets

$$P_{RF}(t) = \frac{50\ \mathrm{W}/V_S}{3 n_e(t)}\left[\bar{a}_0^{RF} n_0 + \sum_{j=1}^{N-1}\left(\bar{a}_j^{RF} - \bar{b}_j^{RF}\right) n_j\right], \tag{5.61}$$

so that, in order to ensure that $P_{RF}(t) V_s = 50$ W, the terms within the square brackets must sum up to exactly $3 n_e(t)$. It is easy to demonstrate that such a requirement is satisfied only if:

1. the energy mesh has uniform spacing $\Delta\varepsilon$,

2. the first cell C_0 has central energy $\varepsilon_0 = 0$ and an extension $\Delta\varepsilon_0 = \Delta\varepsilon/2$.

In fact, in such a case

$$\begin{aligned} \bar{a}_0^{RF} &= \frac{\varepsilon_1 + \varepsilon_{0.5}}{\Delta\varepsilon_0} = \frac{1.5\,\Delta\varepsilon}{0.5\,\Delta\varepsilon} = 3, \\ \bar{a}_j^{RF} - \bar{b}_j^{RF} &= \frac{\left(\varepsilon_{j+1} - \varepsilon_{j-1}\right) + \left(\varepsilon_{j+\frac{1}{2}} - \varepsilon_{j-\frac{1}{2}}\right)}{\Delta\varepsilon} = \frac{2\,\Delta\varepsilon + \Delta\varepsilon}{\Delta\varepsilon} = 3, \end{aligned} \tag{5.62}$$

so that

$$\left[\bar{a}_0^{RF}\, n_0 + \sum_{j=1}^{N-1}\left(\bar{a}_j^{RF} - \bar{b}_j^{RF}\right) n_j\right] = 3n_0 + \sum_{j=1}^{N-1} 3n_j = 3\sum_{j=0}^{N-1} n_j = 3n_e(t). \tag{5.63}$$

Q.E.D.

5.3.3 e-e Coulomb Matrix

Making use of Eqs. 5.55 and 5.56, Eq. 5.26 can be expressed as

$$\begin{aligned} J_{e-e}\left(\varepsilon_{j+\frac{1}{2}}, t\right) \approx \alpha(t)\Big\{&\left(s^+_{j+\frac{1}{2}} \big/ \Delta\varepsilon_j\right) \cdot \left[P\left(\varepsilon_{j+\frac{1}{2}}, t\right) u^+_{j+\frac{1}{2}} - Q\left(\varepsilon_{j+\frac{1}{2}}, t\right)\right] \cdot n_j(t) - \\ &- \left(s^-_{j+\frac{1}{2}} \big/ \Delta\varepsilon_{j+1}\right) \cdot \left[P\left(\varepsilon_{j+\frac{1}{2}}, t\right) u^-_{j+\frac{1}{2}} + Q\left(\varepsilon_{j+\frac{1}{2}}, t\right)\right] \cdot n_{j+1}(t)\Big\}, \end{aligned} \tag{5.64}$$

where $\alpha(t)$ is a parameter that depends weakly on $\vec{n}(t)$ according to Eq. 5.29. In Eq. 5.64, the following notation was introduced:

$$s^+_{j+\frac{1}{2}} = \frac{\varepsilon_{j+1} - \varepsilon_{j+\frac{1}{2}}}{\varepsilon_{j+1} - \varepsilon_j}, \qquad s^-_{j+\frac{1}{2}} = \frac{\varepsilon_{j+\frac{1}{2}} - \varepsilon_j}{\varepsilon_{j+1} - \varepsilon_j}, \tag{5.65}$$

and

$$u^+_{j+\frac{1}{2}} = \frac{1}{\varepsilon_{j+1} - \varepsilon_{j+\frac{1}{2}}} + \frac{0.5}{\varepsilon_{j+\frac{1}{2}}}, \qquad u^-_{j+\frac{1}{2}} = \frac{1}{\varepsilon_{j+\frac{1}{2}} - \varepsilon_j} - \frac{0.5}{\varepsilon_{j+\frac{1}{2}}}. \tag{5.66}$$

Eq. 5.64 can be written in the form $J_{e-e}(\varepsilon_{j+\frac{1}{2}}) = a_j n_j - b_{j+1} n_{j+1}$ (see Eq. 5.50), with

$$a_j(t) = \alpha(t) \cdot \left(s^+_{j+\frac{1}{2}} \big/ \Delta\varepsilon_j\right) \cdot \left[P\left(\varepsilon_{j+\frac{1}{2}}, t\right) u^+_{j+\frac{1}{2}} - Q\left(\varepsilon_{j+\frac{1}{2}}, t\right)\right], \tag{5.67a}$$

$$b_{j+1}(t) = \alpha(t) \cdot \left(s^-_{j+\frac{1}{2}} \big/ \Delta\varepsilon_{j+1}\right) \cdot \left[P\left(\varepsilon_{j+\frac{1}{2}}, t\right) u^-_{j+\frac{1}{2}} + Q\left(\varepsilon_{j+\frac{1}{2}}, t\right)\right]. \tag{5.67b}$$

It is possible to evaluate all the coefficients $\vec{a}(t)$ and $\vec{b}(t)$ defined by Eq. 5.67 by a simple matrix-vector multiplication. To achieve this, the integrals in Eq. 5.67 should be written as a function of the values $\vec{n}(t)$; this is easily obtained by making use of Eq. 5.48, so that

$$P\left(\varepsilon_{j+\frac{1}{2}}, t\right) \approx \frac{2}{\sqrt{\varepsilon_{j+\frac{1}{2}}}} \sum_{k=0}^{j} \varepsilon_k \, n_k(t) + 2\varepsilon_{j+\frac{1}{2}} \sum_{k=j+1}^{N-1} \frac{n_k(t)}{\sqrt{\varepsilon_k}}, \tag{5.68a}$$

$$Q\left(\varepsilon_{j+\frac{1}{2}}, t\right) \approx \frac{3}{\sqrt{\varepsilon_{j+\frac{1}{2}}}} \sum_{k=0}^{j} n_k(t). \tag{5.68b}$$

At this stage it is useful to introduce the *discrete* Heaviside step function

$$H_{jk} = \begin{cases} 0 & \text{if } j < k \text{ (i.e. } k > j) \\ 1 & \text{if } j \geq k \text{ (i.e. } k \leq j) \end{cases}, \tag{5.69}$$

so that the sums in Eqs. 5.68 can run over the whole range of mesh cells:

$$P\left(\varepsilon_{j+\frac{1}{2}}, t\right) \approx \sum_{k=0}^{N-1} \left(H_{jk} \frac{2\varepsilon_k}{\sqrt{\varepsilon_{j+\frac{1}{2}}}} + \left(1 - H_{jk}\right) \frac{2\varepsilon_{j+\frac{1}{2}}}{\sqrt{\varepsilon_k}} \right) n_k(t), \tag{5.70a}$$

$$Q\left(\varepsilon_{j+\frac{1}{2}}, t\right) \approx \sum_{k=0}^{N-1} \left(H_{jk} \frac{3}{\sqrt{\varepsilon_{j+\frac{1}{2}}}} \right) n_k(t). \tag{5.70b}$$

Substituting Eqs. 5.70 into Eqs. 5.67, one can finally obtain a matrix expression for the coefficients:

$$\vec{a}(t) = \alpha(t) \cdot \mathrm{A} \vec{n}(t) \tag{5.71a}$$

$$\vec{b}(t) = \alpha(t) \cdot \mathrm{B} \vec{n}(t) \tag{5.71b}$$

where the constant matrices A and B are defined as

$$A_{j,k} = \left(s^{+}_{j+\frac{1}{2}} \Big/ \Delta\varepsilon_j \right) \left[H_{jk} \varepsilon^{-\frac{1}{2}}_{j+\frac{1}{2}} \left(2u^{+}_{j+\frac{1}{2}} \varepsilon_k - 3 \right) + \left(1 - H_{jk}\right) \varepsilon_{j+\frac{1}{2}} \left(2u^{+}_{j+\frac{1}{2}} \varepsilon_k^{-\frac{1}{2}} \right) \right], \tag{5.72a}$$

$$B_{j+1,k} = \left(s^{-}_{j+\frac{1}{2}} \Big/ \Delta\varepsilon_{j+1} \right) \left[H_{jk} \varepsilon^{-\frac{1}{2}}_{j+\frac{1}{2}} \left(2u^{-}_{j+\frac{1}{2}} \varepsilon_k + 3 \right) + \left(1 - H_{jk}\right) \varepsilon_{j+\frac{1}{2}} \left(2u^{-}_{j+\frac{1}{2}} \varepsilon_k^{-\frac{1}{2}} \right) \right]. \tag{5.72b}$$

Now that the coefficients $\vec{a}(t)$ and $\vec{b}(t)$ can be obtained from Eqs. 5.71 together with Eqs. 5.72, one can evaluate the matrix M_{e-e} in the form given by Eq. 5.54. At each time-step, though, the matrix M_{e-e} has to be updated by reevaluating $\alpha(t)$ and performing the matrix-vector multiplications in Eqs. 5.71 that lead to the new values of $\vec{a}(t)$ and $\vec{b}(t)$.

According to Rockwood [54], the matrix elements A_{jk} (in this case, multiplied by $\alpha(t)$) may be interpreted as the rate [m^3/s] for acceleration of electrons from ε_j to ε_{j+1} while electrons at ε_k go to ε_{k-1}. Similarly, B_{jk} represents the rate of deceleration from ε_j to ε_{j-1} while electrons at ε_k go to ε_{k+1}. Since electrons cannot be decelerated below ε_0, it follows that $A_{j0} = 0 \, \forall j$, and $B_{0k} = 0 \, \forall k$.

The considerations above are consistent with the fact that electron-electron Coulomb collisions make electrons exchange energy between each other, so that the EEDF relaxes towards its 'most probable' configuration, i.e. a (truncated) Maxwellian distribution. It is extremely important to point out that this process conserves the total energy of the colliding electrons, unless one takes into consideration the *radiation cooling* due to the Bremsstrahlung phenomenon, which can be safely neglected for the range of electron density and temperature under study (in fact, the Bremsstrahlung power per unit volume flowing out of the system is $P_{Br} \propto n_e^2 T_e^{0.5}$).

In order to ensure the correct numerical implementation of e-e Coulomb collisions, it helps to consider an *idealized system* where e-e Coulomb collisions are the only process that affects the time evolution of the EEDF. If such a system is *closed*, i.e. all electrons are confined, e-e Coulomb collisions do not change the total kinetic energy, sum of the kinetic energy of all the electrons in the system; this is an important property that must be retained by the discrete formulation.

It is more interesting to consider an idealized system that is *open* instead, as in the numerical model under study: those electrons that reach an energy $\varepsilon > \varepsilon_{max}$ are not confined by the electrostatic potential well, and are assumed to flow out of the system almost instantaneously. In this situation, e-e Coulomb collisions cause energy to be *transported* out of the system by the flux J_{e-e}^{out} of escaping electrons, which are assumed to have exactly the confinement energy $\varepsilon_N = \varepsilon_{\text{max}}$: the corresponding power flux per unit volume is

$$P_{e-e}^{\text{out}} = -J_{e-e}^{\text{out}} \cdot \varepsilon_{\text{max}} \qquad \left[\text{W/m}^3\right]. \tag{5.73}$$

By global energy balance, the escaping power above must equal the time derivative of the total electron energy in the system, $E(t)$ $\left[\text{J/m}^3\right]$:

$$\frac{dE}{dt} = \frac{d}{dt}\left(\sum_{j=0}^{N-1} \varepsilon_j n_j\right) = \sum_{j=0}^{N-1} \varepsilon_j \dot{n}_j \, . \tag{5.74}$$

There is no reason to believe that the power balance $P_{e-e}^{\text{out}} = dE/dt$ is exactly satisfied by the discrete expressions derived so far. Nevertheless, it is quite easy to modify the definitions given by Eq. 5.72 in order to enforce energy conservation. In fact, the physical interpretation of the elements of the matrices A and B as rate coefficients suggests a detailed energy balance: when electrons are accelerated from ε_j to ε_{j+1} by means of decelerating electrons from ε_k to ε_{k-1}, the rate of acceleration is

$$\nu_{\mathrm{acc}} = \alpha(t) A_{jk}\, n_k \qquad \left[\mathrm{s}^{-1}\right], \tag{5.75}$$

while the rate of deceleration is

$$\nu_{\mathrm{dec}} = \alpha(t) B_{kj}\, n_j \qquad \left[\mathrm{s}^{-1}\right]. \tag{5.76}$$

In a unit time, the energy gained by the n_j accelerating electrons must equal the energy lost by the n_k decelerating electrons,

$$n_j \cdot \nu_{\mathrm{acc}} \cdot \left(\varepsilon_{j+1} - \varepsilon_j\right) = n_k \cdot \nu_{\mathrm{dec}} \cdot \left(\varepsilon_k - \varepsilon_{k-1}\right) \qquad \left[\mathrm{J\,m^{-3}s^{-1}}\right], \tag{5.77}$$

which gives the condition that must be satisfied for energy conservation:

$$A_{jk}\left(\varepsilon_{j+1} - \varepsilon_j\right) = B_{kj}\left(\varepsilon_k - \varepsilon_{k-1}\right) . \tag{5.78}$$

After having calculated the A matrix by means of Eq. 5.72a, Eq. 5.78 should be used in place of Eq. 5.72b in order to correctly implement energy conservation for electron-electron Coulomb collisions.

5.3.4 Excitation Matrix

Fig. 5.8 shows how the excitation process is modeled on a discrete energy mesh: a fraction of the electrons having energy ε undergo an excitation collision, i.e. they excite neutral particles from Ground State to energy level p. From energy conservation, those electrons lose an amount of kinetic energy $\varepsilon_{ex}^{(p)}$, and their residual energy is $\varepsilon_r = \varepsilon - \varepsilon_{ex}^{(p)}$, but this does not correspond to one of the allowed values ε_j on the mesh. In order to conserve energy, it is necessary to share the just-collided electrons among two or more cells, some with an energy higher than ε_r, and some with an energy lower than ε_r. The simplest choice, which causes the minimum numerical diffusion, is to share the just-collided electrons between two neighbor cells, as shown in Fig. 5.8. The fractions α and β of electrons going to the lower energy and to the higher energy cell, respectively, are determined by imposing the simultaneous conservation of number and energy:

$$\begin{cases} \alpha + \beta = 1 \\ \alpha\,\varepsilon_a + \beta\,\varepsilon_b = \varepsilon - \varepsilon_{ex}^{(p)} . \end{cases} \tag{5.79}$$

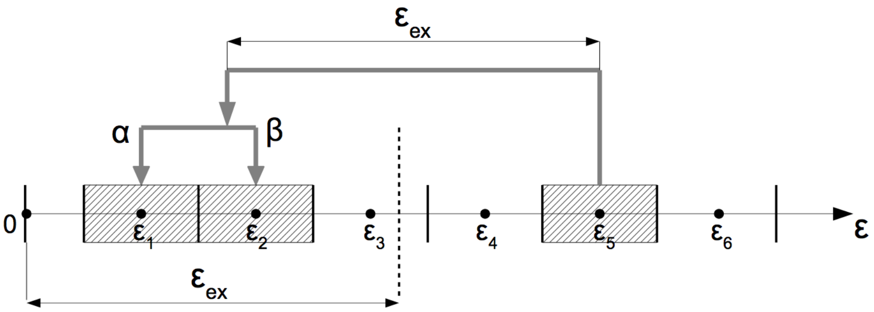

Figure 5.8: Excitation process on a discrete energy mesh.

The structure of the 'excitation matrix' for the energy level p, in the case of a mesh with 7 energy cells and $\varepsilon_{ex}^{(p)}$ lying between ε_2 and ε_3, is

$$\mathrm{M}_{ex}^{(p)\,(N=7)} = \left(\begin{array}{ccc|cccc} 0 & 0 & 0 & \alpha_3 \nu_3 & 0 & 0 & 0 \\ 0 & 0 & 0 & \beta_3 \nu_3 & \alpha_4 \nu_4 & 0 & 0 \\ 0 & 0 & 0 & 0 & \beta_4 \nu_4 & \alpha_5 \nu_5 & 0 \\ 0 & 0 & 0 & -\nu_3 & 0 & \beta_5 \nu_5 & \alpha_6 \nu_6 \\ 0 & 0 & 0 & 0 & -\nu_4 & 0 & \beta_6 \nu_6 \\ 0 & 0 & 0 & 0 & 0 & -\nu_5 & 0 \\ 0 & 0 & 0 & 0 & 0 & 0 & -\nu_6 \end{array}\right), \tag{5.80}$$

where $\nu_j = \nu_{ex}^{(p)}(\varepsilon_j)$ is defined by Eq. 5.35. The total excitation matrix M_{ex} is the sum of the single excitation matrices:

$$\mathrm{M}_{ex} = \sum_p \mathrm{M}_{ex}^{(p)} \,. \tag{5.81}$$

5.3.5 Ionization Matrix

When an electron having energy $\varepsilon^* > \varepsilon_{iz}$ undergoes an ionization collision with a (Ground State) neutral Argon atom, it extracts a secondary electron from the neutral. In this process the impacting electron supplies the secondary electron with an amount of energy equal to the *bound energy* ε_{iz} (the ionization energy), plus some kinetic energy. From energy conservation, the sum of the kinetic energies of the two ejected electrons (primary + secondary) is equal to the residual impact energy $\varepsilon_r = \varepsilon^* - \varepsilon_{iz}$. The energy of the two ejected electrons can assume any value $\varepsilon \in [0, \varepsilon_r]$, and it is statistically described by the *energy distribution function of the ejected electrons* $g(\varepsilon^*, \varepsilon)$. But for a fixed ε^*, $g(\varepsilon^*, \varepsilon)$ is still a continuous function of the ejected energy ε, while the energy mesh is discrete in the numerical model: as shown in Fig. 5.9, only a finite set of energy values ε_j are available to the ejected electrons.

In general, the available energies are the center values of those cells that are at least partially allowed to the ejected electrons.

In order to describe the ionization process on an energy mesh, the quantity of interest is γ_j, that is the average number of ejected electrons reaching energy ε_j, *per impacting electron*. The evaluation of the coefficients γ_j is a delicate issue, as one should exactly conserve the particle number and the kinetic energy, which results in the two following constraints:

$$\begin{cases} \sum_{j=0}^{j_{max}} \gamma_j &= 2 \\ \sum_{j=0}^{j_{max}} \gamma_j \varepsilon_j &= \varepsilon^* - \varepsilon_{iz} \, . \end{cases} \tag{5.82}$$

In order to satisfy Eq. 5.82, at least two allowed energies are necessary. Therefore, if only ε_0 is available, then ε_1 should be considered allowed too. With two available energies, the conservation of particles and energy can be easily enforced, in the same fashion as for the excitation case (see Eq. 5.79), by solving the linear system

$$\begin{cases} \gamma_0 + \gamma_1 &= 2 \\ \gamma_0 \varepsilon_0 + \gamma_1 \varepsilon_1 &= \varepsilon^* - \varepsilon_{iz} \, . \end{cases} \tag{5.83}$$

When three or more energies are available, one can use the information given by $g(\varepsilon^*, \varepsilon)$, but a careful procedure should be applied in order to ensure particle and energy conservation. There is no unique solution of course, but a simple procedure recommended for numerical implementation is the following:

1. evaluate the γ_js by estimating the shaded areas in Fig. 5.9 (a numerical quadrature algorithm like the trapezoidal rule is sufficient), so that

$$\gamma_j \simeq \int_{C_j} g(\varepsilon^*, \varepsilon) d\varepsilon; \tag{5.84}$$

2. rescale the γ_js in order to ensure that particles are conserved, i.e. $\sum_j \gamma_j = 2$; this is accomplished by multiplying all γ_js by the same constant factor:

$$\gamma_j = \gamma_j \left(\frac{2}{\sum_j \gamma_j} \right); \tag{5.85}$$

3. reduce γ_0 and increase $\gamma_{j_{max}}$ by the same amount $\Delta\gamma$ (with sign), in order to ensure that energy is conserved, i.e. $\sum_j \gamma_j \varepsilon_j = \varepsilon^* - \varepsilon_{iz}$; this correction is just

$$\Delta\gamma = \frac{1}{\varepsilon_{j_{max}}} \left[\left(\varepsilon^* - \varepsilon_{iz} \right) - \sum_j \gamma_j \varepsilon_j \right], \tag{5.86}$$

and accordingly:

$$\begin{aligned} \gamma_0 &= \gamma_0 - \Delta\gamma \\ \gamma_{j_{max}} &= \gamma_{j_{max}} + \Delta\gamma\,. \end{aligned} \tag{5.87}$$

Points 2 and 3 in the procedure above are ‘small corrections’, which become smaller as the energy mesh is progressively refined.

Finally, the structure of the ‘ionization matrix’ in the case of a uniform mesh with 7 energy cells and ε_{iz} lying between ε_2 and ε_3, is

$$\mathrm{M}_{iz} = \left(\begin{array}{ccc|cccc} 0 & 0 & 0 & \gamma_3^0 \nu_3 & \gamma_4^0 \nu_4 & \gamma_5^0 \nu_5 & \gamma_6^0 \nu_6 \\ 0 & 0 & 0 & \gamma_3^1 \nu_3 & \gamma_4^1 \nu_4 & \gamma_5^1 \nu_5 & \gamma_6^1 \nu_6 \\ 0 & 0 & 0 & 0 & 0 & \gamma_5^2 \nu_5 & \gamma_6^2 \nu_6 \\ 0 & 0 & 0 & -\nu_3 & 0 & 0 & \gamma_6^3 \nu_6 \\ 0 & 0 & 0 & 0 & -\nu_4 & 0 & 0 \\ 0 & 0 & 0 & 0 & 0 & -\nu_5 & 0 \\ 0 & 0 & 0 & 0 & 0 & 0 & -\nu_6 \end{array} \right), \tag{5.88}$$

where $\nu_j = \nu_{iz}(\varepsilon_j)$ is defined by Eq. 5.39. In Eq. 5.88, the notation γ_m^n is used, where m is the energy index of the impacting electron, and n is the energy index of the ejected electrons.

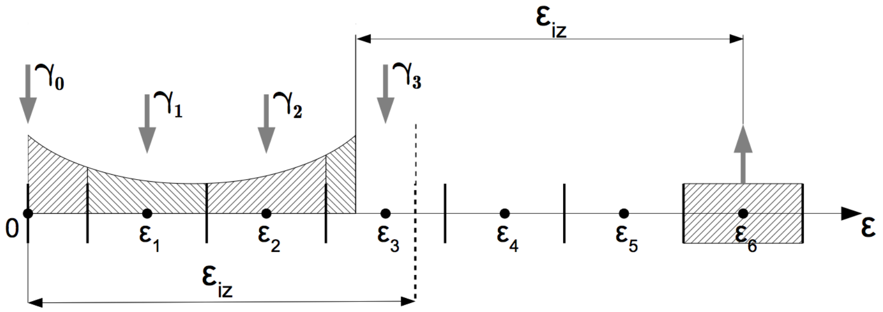

Figure 5.9: Example of ionization process on a discrete energy mesh. For each electron at energy ε_6 that undergoes an ionizing collision, a secondary electron is produced. The energy of the primary and secondary electrons after the collision is treated statistically: the energy distribution of the ejected electrons is $g(\varepsilon_6, \varepsilon)$, which is depicted by the shaded area on the low energy side of the energy axis. On the given mesh, only a discrete set of energies ε_0, ε_1, ε_2, and ε_3 are available to the ejected electrons; for each impacting electron, γ_0, γ_1, γ_2 and γ_3 are the average number of electrons that reach the aforementioned energies.

5.4 Integration in Time

5.4.1 An ODE system for the normalized EEDF

Eq. 5.12 describes the time evolution of the normalized EEDF, $F(\varepsilon)$; a discrete formulation can be obtained as a system of ODEs for the unknowns F_js, defined as the average values of $F(\varepsilon)$ in each cell C_j:

$$F_j = \frac{1}{\Delta\varepsilon_j}\int_{C_j} F(\varepsilon)\,d\varepsilon. \tag{5.89}$$

Recalling that $n_j = \int_{C_j} f(\varepsilon)\,d\varepsilon$ and $F(\varepsilon) = f(\varepsilon)/n_e$, one gets the simple relation

$$n_j = n_e \Delta\varepsilon_j F_j, \tag{5.90}$$

which can be put in matrix form as

$$\vec{n} = n_e \mathrm{D}\vec{F}, \tag{5.91}$$

where D is a diagonal matrix having the array of cell sizes $\overrightarrow{\Delta\varepsilon}$ on the main diagonal:

$$\mathrm{D}_{ij} = \delta_{ij}\Delta\varepsilon_j. \tag{5.92}$$

With common notation, the symbol δ_{ij} in Eq. 5.92 is the Kronecker operator:

$$\delta_{ij} = \begin{cases} 1 & \text{if } i = j, \\ 0 & \text{otherwise.} \end{cases} \tag{5.93}$$

Substituting Eq. 5.91 into Eq. 5.52, one gets

$$\frac{d\vec{F}}{dt} = \left(\mathrm{D}^{-1}\mathrm{M}\mathrm{D} - \frac{1}{n_e}\frac{dn_e}{dt}\mathrm{I}\right)\vec{F} \tag{5.94}$$

where I is just the identity matrix ($\mathrm{I}_{ij} = \delta_{ij}$). In order to numerically integrate the system of ODEs defined by the last equation, the term $1/n_e\, dn_e/dt$ should be expressed in terms of the solution vector $\vec{F}$. In fact, this can be done by means of a simple algebraic reformulation:

$$\frac{dn_e}{dt} = \frac{d}{dt}\left(\sum_j n_j\right) = \frac{d}{dt}\|\vec{n}\|_1 = \left\|\frac{d\vec{n}}{dt}\right\|_1 = \|\mathrm{M}\vec{n}\|_1 = n_e\left\|\mathrm{M}\mathrm{D}\vec{F}\right\|_1, \tag{5.95}$$

where the notation $\|\cdot\|_1$ represents the L1-norm in $\mathbb{R}^N$ space; the linearity property of such a norm, when applied to a positive-valued vector, was used. If Eq. 5.95 is substituted into Eq. 5.94, one gets

$$\frac{d\vec{F}}{dt} = \left[\mathrm{D}^{-1}\mathrm{M}\mathrm{D} - \left\|\mathrm{M}\mathrm{D}\vec{F}\right\|_1 \mathrm{I}\right]\vec{F}. \tag{5.96}$$

At this stage it is useful to define the matrix

$$\mathrm{C} = \mathrm{D}^{-1}\mathrm{MD}, \tag{5.97}$$

so that

$$\left\|\mathrm{MD}\vec{F}\right\|_1 = \left\|\mathrm{DC}\vec{F}\right\|_1 = \vec{\Delta\varepsilon}^T\mathrm{C}\vec{F}, \tag{5.98}$$

where $\vec{x}^T\vec{y} = c \in \mathbb{R}$ is the inner (scalar) product between vectors in $\mathbb{R}^N$. Finally, a compact matrix expression for the time evolution of the (discrete) normalized EEDF is given by the following first-order system of ODEs:

$$\frac{d\vec{F}}{dt} = \left[\mathrm{C} - \left(\vec{\Delta\varepsilon}^T\mathrm{C}\vec{F}\right)\mathrm{I}\right]\vec{F}. \tag{5.99}$$

It should be pointed out that Eq. 5.99 above still depends on n_e, but only indirectly, through matrix $\mathrm{C} = \mathrm{D}^{-1}\mathrm{MD}$. In fact, according to Eq. 5.53, matrix M is the sum of the matrices for each contribution (EM heating, electron-electron Coulomb collisions, electron-neutral excitation and ionization), which explicitly depend on n_e or n_g; in turn, n_g depends on n_e through the average ionization collision frequency for neutrals, and through the ionization efficiency of the plasma source (see Eq. 4.28).

It is useful to rewrite the various matrices in order to show the dependence on n_e and n_g. The EM heating matrix may be rewritten as

$$\mathrm{M}_{RF}(t) = \frac{1}{n_e(t)}\mathrm{M}^*_{RF} \tag{5.100}$$

where M^*_{RF} is a constant coefficient matrix with units $\left[\mathrm{m}^{-3}\mathrm{s}^{-1}\right]$. The e-e Coulomb matrix may be rewritten as

$$\mathrm{M}_{e-e}(t) = \alpha(t)\, n_e(t)\, \mathrm{M}^*_{e-e}(t) \tag{5.101}$$

where $\mathrm{M}^*_{e-e}(t)$ is a tri-diagonal square matrix with diagonals $\left[\vec{a}^*, -(\vec{a}^* + \vec{b}^*), \vec{b}^*\right]$. The arrays $\vec{a}^*$ and $\vec{b}^*$ are related by a matrix-vector multiplication to the discrete normalized EEDF:

$$\begin{cases} \vec{a}^*(t) = \mathrm{AD}\vec{F}(t) \\ \vec{b}^*(t) = \mathrm{BD}\vec{F}(t) \end{cases} \qquad \left[\mathrm{J}^{-1.5}\right] \tag{5.102}$$

where A and B are the constant matrices given by Eqs. 5.72. Both the excitation and ionization matrices are directly proportional to the neutral density:

$$\mathrm{M}_{ex}(t) = n_g(t)\mathrm{M}^*_{ex}\,, \qquad \mathrm{M}_{iz}(t) = n_g(t)\mathrm{M}^*_{iz}\,, \tag{5.103}$$

where M^*_{ex} and M^*_{iz} are constant matrices with units $\left[\mathrm{m}^3\mathrm{s}^{-1}\right]$. Finally, one gets

$$\mathrm{M}(t) \;=\; \frac{1}{n_e(t)}\mathrm{M}^*_{RF} \;+\; \alpha(t)\,n_e(t)\,\mathrm{M}^*_{e-e}(t) \;+\; n_g(t)\left(\mathrm{M}^*_{ex}+\mathrm{M}^*_{iz}\right), \tag{5.104}$$

where the constant matrices M^*_{RF}, M^*_{ex}, M^*_{iz}, A, B and D need only be evaluated once, in preprocessing.

5.4.2 Time-Scale Separation for Accelerated Convergence to Steady State

The 0D-1V kinetic model for a Helicon plasma source describes the average state of the system with a state vector

$$\vec{U} \;=\; \left\{n_e,\; n_g,\; \Phi_w,\; \vec{F}\right\}, \tag{5.105}$$

where all quantities depend on time, and the actual dimension of the array $\vec{F}$ depends on the energy resolution $\Delta\varepsilon$ (chosen in preprocessing and constant throughout the simulation) and on the confinement potential Φ_w.

The purpose of the model is to properly evolve $\vec{U}(t)$, starting from given Initial Conditions $\vec{U}_0$, to a self-consistent steady state solution $\vec{U}_{ss}$. The method of solution proposed here is based on *time-scale separation*: $n_e(t)$ and $n_g(t)$ have the largest characteristic time scales and they are therefore integrated together in time, while $\vec{F}(t)$ has a very short time scale and hence it is assumed that during this evolution the normalized EEDF is always in equilibrium, together with $\Phi_w(t)$.

The complete iterative procedure, capable of accelerating the convergence to steady-state, is the following:

1. Given the coupled analytical solution $\left\{\langle n_g\rangle, \langle n_e\rangle, T_e\right\}$ calculated in Section 4.1.2, the initial state vector is obtained as follows:

$$\begin{bmatrix} n_g \\ n_e \\ \Phi_w \\ F(\varepsilon) \end{bmatrix}_0 \;=\; \begin{bmatrix} \langle n_g\rangle \\ \langle n_e\rangle \\ \frac{k_B T_e}{2q_e}\left[1+\ln\left(\frac{M_{Ar}}{2\pi m_e}\right)\right] \\ \frac{2}{\sqrt{\pi}}\sqrt{\frac{\varepsilon}{k_B T_e}}\exp\left(-\frac{\varepsilon}{k_B T_e}\right) \end{bmatrix}, \tag{5.106}$$

   where the discrete $\vec{F}$ is obtained from its continuous counterpart $F(\varepsilon)$ by truncating it at $\varepsilon_{\max} = q_e\Phi_w$, by sampling it at the discrete energies ε_j, and by renormalizing in order to ensure that $\sum_j F_j = 1$.

2. While keeping n_g and n_e frozen, cycling to find the discrete EEDF $\vec{F}$ and the corresponding potential confinement Φ_w that ensure the balance of the electron and ion losses (i.e. quasineutrality):
   (a) given Φ_w, finding the steady-state EEDF by means of a pseudo-transient time integration; calculating the electron flux $\Gamma_e = J(\varepsilon_{\max})$ at steady-state;
   (b) given the steady-state EEDF, calculating the ion flux $\Gamma_i = n_S\, u_B$ according to the kinetic Bohm criterion and planar sheath theory (Section 4.1.3);
   (c) comparing Γ_e to Γ_i:

```
if ($|\Gamma_e - \Gamma_i| <$ TOL) then
    STORE $\vec{F}$ and $\Phi_w$
    EXIT from the cycle
else if ($\Gamma_e < \Gamma_i$) then
    DECREASE $\Phi_w$
else if ($\Gamma_e > \Gamma_i$) then
    INCREASE $\Phi_w$
end if
```

   the feedback mechanism controlling Φ_w ensures fast convergence;
   (d) calculating the new initial conditions $\vec{F}_0$ as a discrete Maxwellian having the same mean energy of the 'old' EEDF, but truncated at the new value of Φ_w; iterating from point (a).

3. Given the self-consistent coupled solution for the EEDF and the confinement potential, calculating the integral quantities required to evolve the densities:

$$\langle\varepsilon\rangle = \int_0^{\varepsilon_{\max}} \varepsilon\, F(\varepsilon)\, d\varepsilon \qquad [\mathrm{J}] \tag{5.107a}$$

$$K_{iz} = \int_{\varepsilon_{iz}}^{\varepsilon_{\max}} \sigma_{iz}(\varepsilon)\, v(\varepsilon)\, F(\varepsilon)\, d\varepsilon \qquad [\mathrm{m^3/s}] \tag{5.107b}$$

$$K_{ex}^{(p)} = \int_{\varepsilon_{ex}^{(p)}}^{\varepsilon_{\max}} \sigma_{ex}^{(p)}(\varepsilon)\, v(\varepsilon)\, F(\varepsilon)\, d\varepsilon \qquad [\mathrm{m^3/s}] \tag{5.107c}$$

$$u_B = \sqrt{\frac{2}{3}\frac{\langle\varepsilon\rangle}{M_{Ar}}} \qquad [\mathrm{m/s}] \tag{5.107d}$$

$$\delta_S = \frac{n_S}{n_e} = \int_{\langle\varepsilon\rangle/3}^{\varepsilon_{\max}} \sqrt{1-\frac{\langle\varepsilon\rangle}{3\varepsilon}}\, F(\varepsilon)\, d\varepsilon \tag{5.107e}$$

4. Evolving $n_e(t)$ and $n_g(t)$ while keeping $\overrightarrow{F}$ and Φ_w constant (hence, all the quantities above are kept constant); the 0D balance equation for the total kinetic energy in the system is used,

$$\frac{dn_e}{dt} = \frac{1}{\langle\varepsilon\rangle}\left[\frac{P_a}{V} - \left(K_{iz}\varepsilon_{iz} + \sum_p K_{ex}^{(p)}\varepsilon_{ex}^{(p)}\right)n_g n_e - \frac{A}{V}\left(u_B\,\varepsilon_{\max}\,\delta_S\right)n_e\right], \tag{5.108}$$

   together with the 1D analytic solution for the average neutral density,

$$n_g = \frac{[\dot{N}_g]}{K_{iz}n_eV}\eta_{iz}(\xi,\zeta). \tag{5.109}$$

   When n_e (or n_g) has changed by more than a prescribed relative margin (e.g. 10%), storing the new values of n_e and n_g and going back to the EEDF solver (point 2); iterating until steady-state is reached $\frac{dn_e}{dt} \simeq 0$.

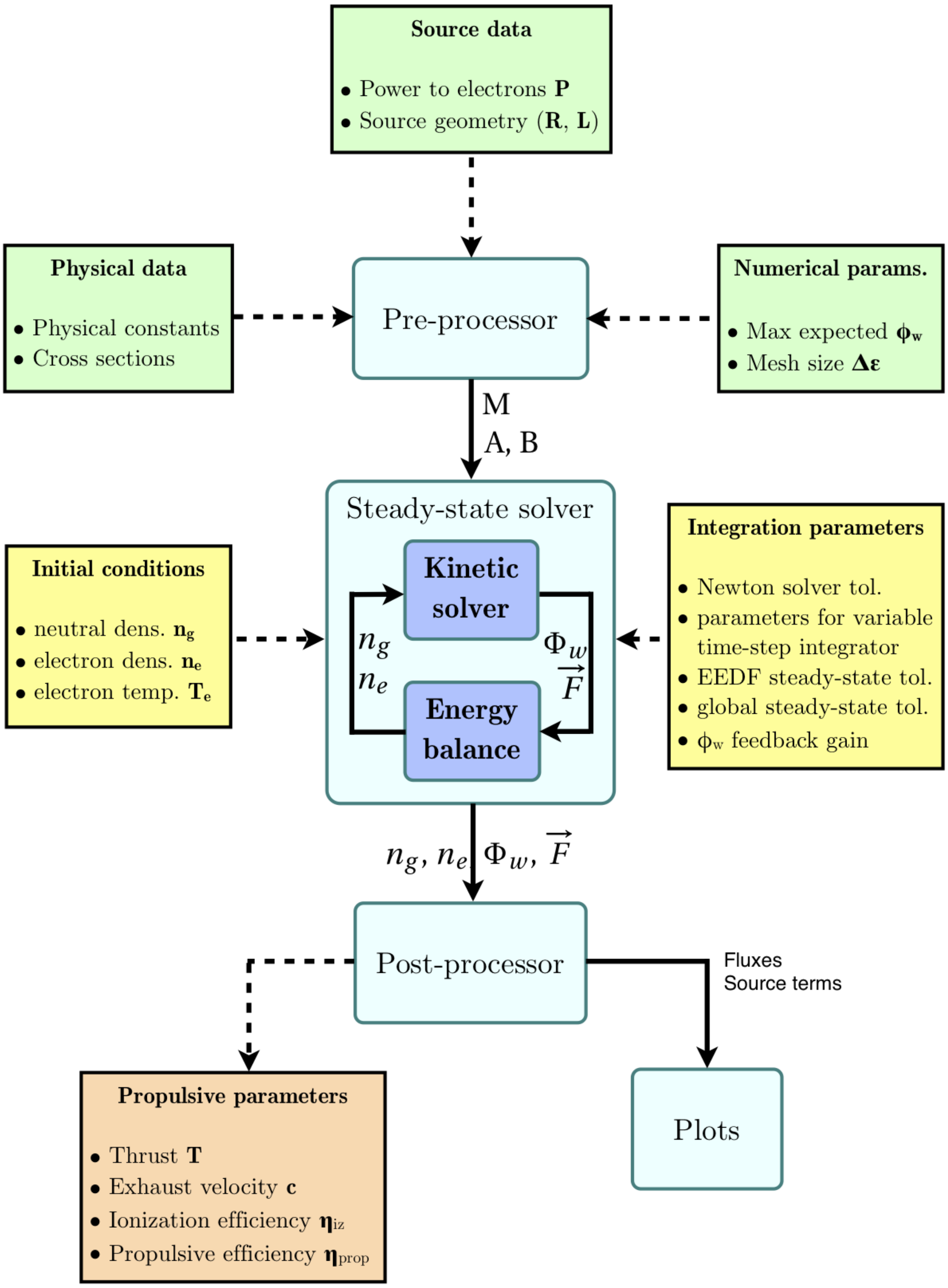

Figure 5.10: Schematic of the global architecture of the 0D1V electron kinetic model.

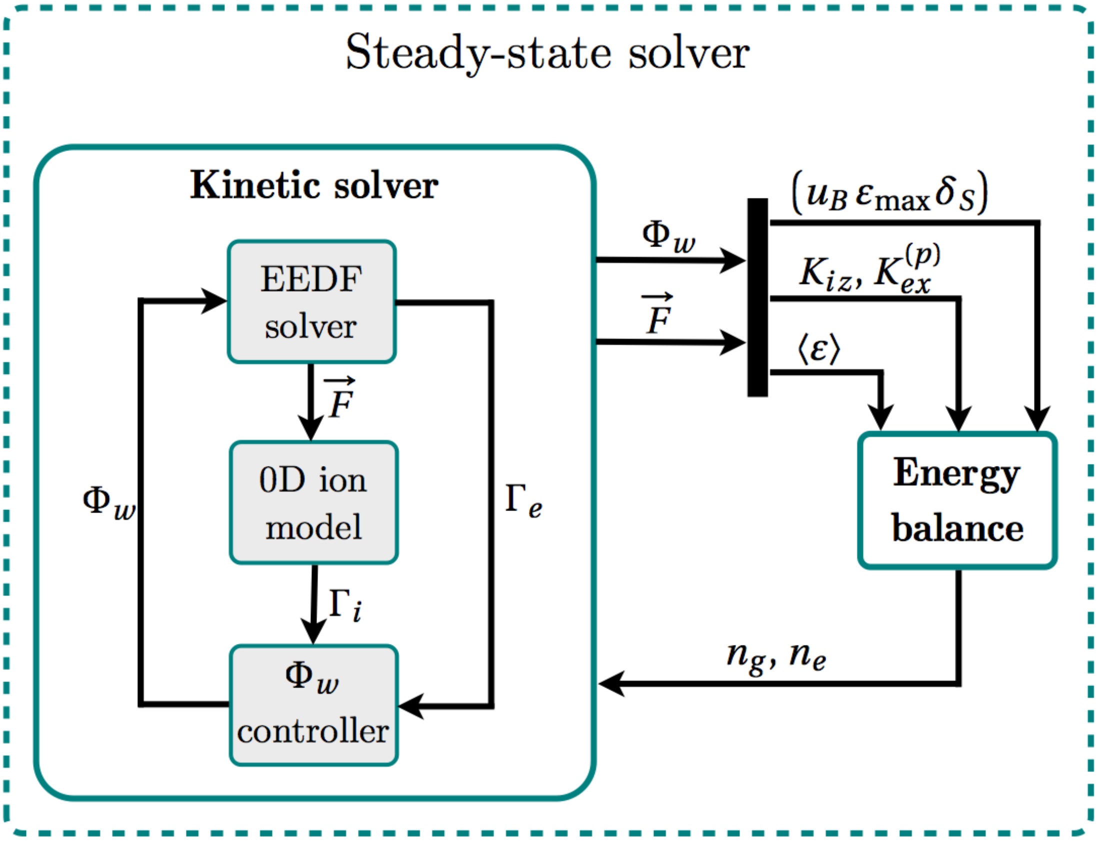

Figure 5.11: Schematic of the iterative procedure used to find the self-consistent steady-state solution $\vec{U}_{ss} = \left\{n_g, n_e, \Phi_w, \vec{F}\right\}_{ss}$.

5.5 Simulations

Fig. 5.12 shows the fluxes of electrons in energy space due to RF heating and electron-electron Coulomb collisions. At a given energy ε^*, the flux is the difference between the number of electrons that increase their energy above ε^* (coming from lower energies), and the number of electrons that decrease their energy below ε^* (coming from higher energies), in the unit time. Since those values are calculated from the normalized EEDF, which retains no information about the electron density (and hence the electron number), the fluxes shown are normalized with respect to the total number of electrons in the system, and they are in $\left[\mathrm{s}^{-1}\right]$.

The integral in energy of a flux in energy (which coincides with the total signed area under the curve) is the average energy given to the electrons by the corresponding process, per unit time and unit density; i.e., it is the *power coupled per electron*. In the case of e-e Coulomb collisions, this area is nearly zero, but it is slightly negative: in fact, on average the electrons are cooling, because of the flux of the high energy electrons that are escaping from the source at $\varepsilon = \varepsilon_{\max}$. In the case of RF heating, the area is definitively positive; in fact, it was show in Sec. 4.2.2 that the power coupled per electron is known a-priori when a constant velocity diffusion coefficient is used (see Eq. 4.54).

Since the velocity diffusion coefficient is chosen according to Eq. 5.25, 50 W are coupled to the electrons in the source. This power goes into 3 main processes:

1. plasma creation (i.e. ionization collisions);
2. excitation collisions;
3. ion beam acceleration.

The third point may seem obscure, but it can be easily explained. Those electrons that jump out of the potential well where they were previously confined are assumed to have a kinetic energy equal to $\varepsilon_{\max}$; in physical reality, they will have a kinetic energy just slightly larger than $\varepsilon_{\max}$, which permits them to escape from the source with a non-zero velocity, but for all practical purposes this can be neglected. Hence, the electrons exit the system with virtually no kinetic energy, while the ions are accelerated by the same potential profile that was confining the electrons: this is a statement of energy conservation, because when an electron-ion couple is created, the electron has a negative potential (electrostatic) energy, while the ion has a positive potential energy. As a conclusion, it is correct to state that some of the power coupled to the electrons goes into accelerating the ions; and in fact, in a Helicon plasma thruster it is desirable that *most* of that power goes to the ion beam.

The various processes sum up to 50 W only when steady-state is reached. If their sum is less than 50 W, power goes into increasing the electron density; if it is more than 50 W, the electron density decreases. Accordingly, a simple global balance equation is used, in order to evolve the electron density (see Eq. 5.108).

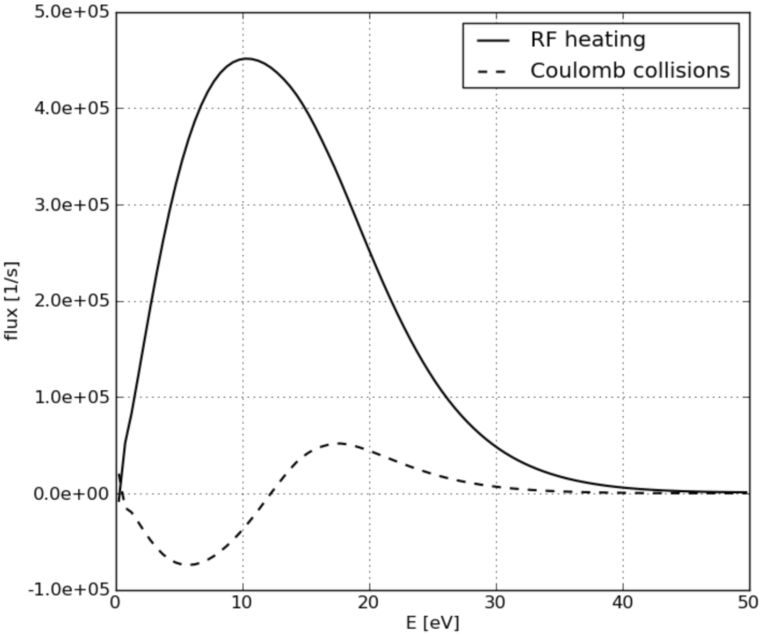

Figure 5.12: Fluxes of electrons in energy space due to RF heating (solid line) and electron-electron Coulomb collisions (dashed line). The energy axis is in [eV]; the fluxes are in $\left[s^{-1}\right]$, as they represent the net number of electrons crossing a given energy, per unit time, divided by the total number of electrons in the system.

Fig. 5.13 shows the (signed) source terms due to ionization and excitation. At a given energy, the net effect of such collisional processes is calculated as the difference between the positive contribution (in green) and the negative contribution (in red). Clearly, the contribution from excitation is zero, as the green and red areas coincide. The contribution from ionization is positive, as two electrons are put back onto the mesh for each electron that undergoes ionization; in fact, the positive area is twice the negative area. At the 'correct' steady state, the electron production rate exactly balances the electron loss rate due to the outgoing flux at $\varepsilon_{\max} = q_e \Phi_w$.

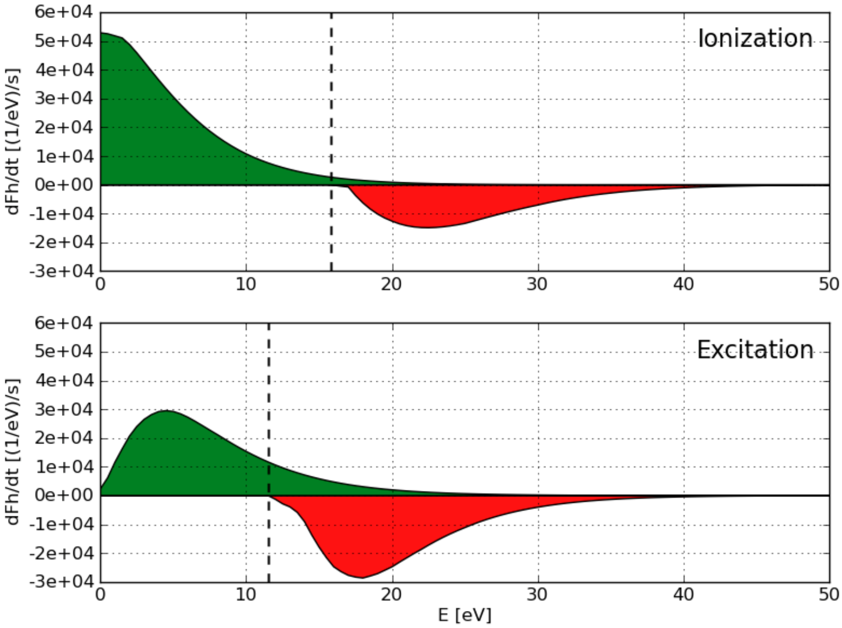

Figure 5.13: Sources (in green) and sinks (in red) of electrons in energy space, due to ionization collisions (top) and excitation collisions (bottom). The signed integral of the source terms gives the net number of electrons produced per second, divided by the total number of electrons in the system. Accordingly, since the energy axis is in [eV], the source terms have dimensions of $\left[\mathrm{eV}^{-1}\mathrm{s}^{-1}\right]$. The vertical dashed lines identify the ionization energy (15.76 eV) and the first excitation energy (11.55 eV).

For a specific operating point $\{n_e, n_g\}$, the normalized EEDF must be calculated self-consistently with the confinement potential Φ_w, which defines the maximum energy allowed to electrons, as $\varepsilon_{\max} = q_e \Phi_w$. Hence, the confinement potential defines the limit of the energy axis itself, i.e. the domain on which the normalized EEDF is computed. To find the value of Φ_w, the energy axis is truncated at $\varepsilon_{\max} = q_e \Phi_w$, and the normalized EEDF is run to steady-state on the given domain; then a new Φ_w is calculated and the process is repeated, until the loss rates for electrons and ions differ by less than a prescribed tolerance.

If a constant mesh spacing is used, than $\varepsilon_{\max}$ can be chosen between the allowed discrete energy values, the energy axis remains the same (it is just shortened), and there is no need to recompute the constant matrices M^*_{RF}, M^*_{ex}, M^*_{iz}, A, B and D at each iteration (see Sec. 5.4.1): it is sufficient to use a reduced number of rows and columns.

The self-consistent confinement potential Φ_w is obtained by matching the (normalized)

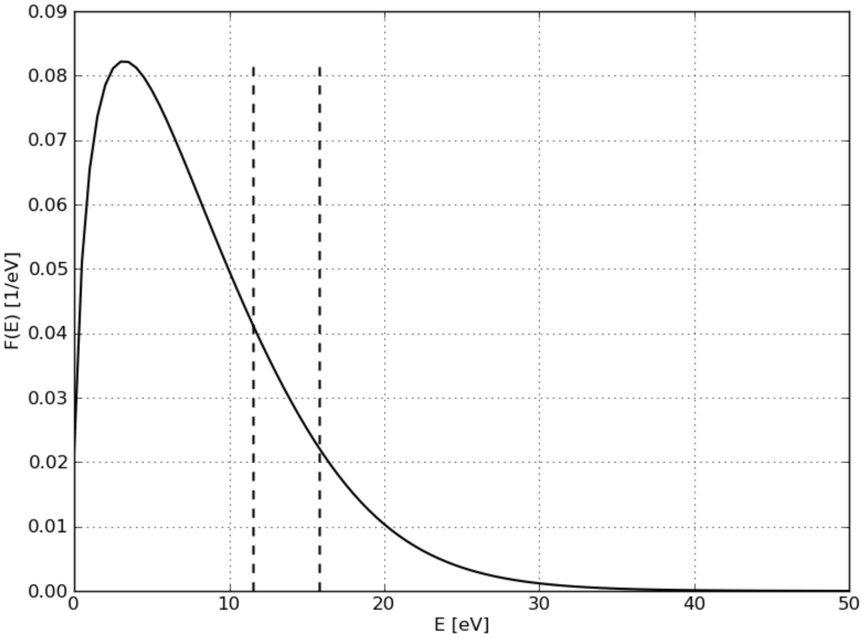

Figure 5.14: Example of a steady-state normalized EEDF, obtained for a given operating point $\{n_e, n_g\}$, and for a tentative value of the confinement potential Φ_w. The energy axis is in [eV], while the normalized EEDF is in $\left[\text{eV}^{-1}\right]$; due to normalization, the area under the curve is strictly equal to one. The vertical dashed lines identify the first excitation energy (11.55 eV) and the ionization energy (15.76 eV).

outgoing fluxes of electrons and ions $\left[\text{s}^{-1}\right]$, also called *loss rates*, which are obtained as

$$\begin{aligned}\Gamma_e^* &= \frac{1}{n_e}\left[J_{RF}\left(\varepsilon_{\max}\right) + J_{e-e}\left(\varepsilon_{\max}\right)\right],\\ \Gamma_i^* &= \frac{n_S u_B A}{n_e V} = \frac{\delta_s u_B A}{V},\end{aligned} \tag{5.110}$$

where A is the area of the exit section, and V is the volume of the plasma source. In Eq. 5.110, $\delta_s = n_S/n_e$ is the ratio of the density at the sheath boundary to the average electron density (Eq. 5.107e), while u_B is the Bohm velocity (Eq. 5.107d). Many of the quantities above (i.e. J_{RF}, J_{e-e}, δ_s an u_B) depend on the steady-state normalized EEDF, which in turn depends on the imposed value of Φ_w.

As an example, Fig. 5.15 shows the profile of $\Gamma_e^*(\Phi_w)$ and $\Gamma_i^*(\Phi_w)$ for a given operating point $\{n_e, n_g\}$: since the two fluxes are decreasingly and increasingly monotonic, respectively, an intersection point is easily found, which defines the value Φ_w^* which is consistent with the hypothesis of quasi-neutrality in the plasma source.

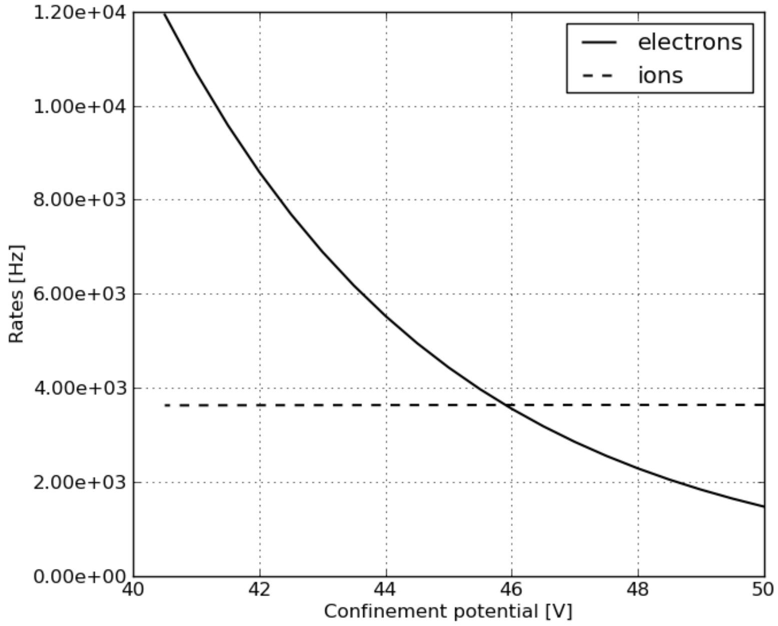

Figure 5.15: Loss rates for electrons (solid lines) and ions (dashed lines), at a given operating point $\{n_e, n_g\}$, as a function of the confinement potential Φ_w.

6

Detailed Neutral Model

The neutral dynamics strongly influences the spatial distribution and strength of the source term for ions, which in turn affects the plasma density and potential, and hence the kinetic energy available to the confined electrons for ionization of the neutral particles. For the purpose of hybrid modeling, this strongly coupled system needs to be tackled one piece at a time: so far, the models presented were spatially averaged or purely analytic, so the next logical step is to resolve at least one spatial dimension, and possibly two.

To allow for the large average mean-free-path expected in the source for neutral-neutral collisions, a 1D analytic model based on a random walk argument was proposed earlier in Chapter 4. Such a model had three main limitations: first, in the experiment there is no barrier to the neutral motion in the axial direction except drag from the sidewalls, and so it is legitimate to suspect that the gas may maintain a considerable mean axial velocity after injection into the source, while the analytic model does not include a mean velocity; second, the neutral density in front of the injector can still be sufficiently high to have a mean-free-path much smaller than the source radius or than the mean-free-path elsewhere, while the model assumes a constant mean-free-path; and third, the gas expansion upon injection into the source is definitely two dimensional.

In this Chapter, a novel code dedicated to the neutral dynamics is presented, which is kinetic, in the sense that it evolves in time the velocity distribution function of the neutral particles on a phase-space domain. Such a model is 3D-3V, i.e. it resolves three dimensions in space, and three components in velocity. **Section 6.1** gives a detailed argument in favor of this six-dimensional kinetic model, explaining why it is regarded as necessary for the better understanding of the dynamics of the rarefied neutral gas in the source.

Section 6.2 reviews past research on the Convected Scheme for the kinetic simulation of cold plasmas and rarefied gases. Several versions of the Convected Scheme are discussed, and the advantages and downsides of the different approaches are assessed, on the basis of the accumulated experience of use at UW Madison.

In **Section 6.3**, computational considerations motivate the selection of a cell-centered semi-Lagrangian (CCSL) version of the Convected Scheme, in which the Moving-Cells (MCs) are remapped back to the fixed mesh at the end of each time-step. To compensate for the conspicuous and anisotropic numerical diffusion inherent in this particular method, a novel high-order remapping procedure is developed, which is based on the application of small corrections to the final position of the MC upon remapping. The new 'ballistic operator' maintains the desirable properties of the original scheme (i.e. global and local mass conservation, and positivity preservation), while drastically reducing the undesired numerical diffusion. A few non-oscillatory variations on the new scheme are also given, which may be particularly useful in the presence of sharp density gradients.

In **Section 6.4**, the computational domain is shown to be subdivided into a 'physical domain', where the velocity distribution function of the neutral gas is calculated on a phase-space mesh and evolved at each time-step, and a 'ghost region' that lies beyond the boundaries and is used for implementing the various types of boundary conditions. The geometry under consideration is simply a cylinder open to vacuum to one end and with a small circular hole (the injector) to the other end, which is otherwise closed. The phase-space mesh is also discussed: this is obtained as the Cartesian product of the spatial and velocity meshes, which are separately described.

The effect of collisions between like particles on the velocity distribution function is described by the Collision Operator, which is discussed in **Section 6.5**; the current implementation is an integral formulation of the Bhatanagar-Gross-Krook relaxation model. The exact conservation by the Collision Operator of local integral quantities, like the particle number, momentum and kinetic energy, is explicitly enforced on the discrete mesh by applying 'small corrections' to the nominal distribution function of the just collided particles.

Section 6.6 describes the Boundary Conditions (BCs) employed in the model, which are of different kinds. *Periodic planes* permit one to simulate only half the domain, taking advantage of the symmetry of the phase-space mesh. All the *physical walls* are assumed adiabatic and diffusely reflecting, so that there is no heat exchange between the gas and the wall, but there is friction due to the transfer of parallel momentum. The *injector* is assumed to be sonic with a given temperature and mass-flow, and its implementation enforces the exact nominal quantity of particles and kinetic energy to be injected in a time-step. *Free-space* BCs are simulated by the use of a layer of perfectly absorbing ghost cells.

Finally, **Section 6.7** shows the results of a campaign of 3D-3V simulations, which have mainly test and validation purposes.

6.1 Motivation for a 3D-3V Kinetic Simulation

The choice of a 3D-3V model was made because the geometry of the thruster requires at least 2D (cylindrical) geometry in space. When using two spatial dimensions, the corresponding components of velocity are needed to describe particle motion, and the third component of velocity must also be taken into account since it acts as a reservoir for energy. That energy is transferred into the other directions when collisions occur. Thus 2D-3V was necessary.

For the purposes of this thesis work, a 3D-3V model was developed instead, because it is more general and slightly easier to code, although it uses more memory and is somewhat slower to run.

Kinetic in this context means that the system is described at a level where the distribution of the particles with respect to independent variables including both space and velocity is obtained: the scalar field $f(t, \mathbf{x}, \mathbf{v})$ is solved for, which is the particle number density in phase space and has dimensions of $[m^{-6}s^{3}]$. The kinetic description is necessary because the hypothesis of local thermal equilibrium is not applicable, and hence the form of $f(t, \mathbf{x}, \mathbf{v})$ for any point in space cannot be obtained from local integral properties of the fluid, like density, mean velocity and temperature. Local thermal equilibrium is not reached because the mean free path is comparable with the system dimensions; or, as another way to put it, the collision time is comparable with the time needed to traverse the system.

The time evolution of the distribution function $f(t, \mathbf{x}, \mathbf{v})$ of a set of identical particles is described by Boltzmann's equation, whose general form is:

$$\frac{\partial f}{\partial t} + \mathbf{v} \cdot \frac{\partial f}{\partial \mathbf{x}} + \frac{\mathbf{F}}{m} \cdot \frac{\partial f}{\partial \mathbf{v}} = \left[\frac{\partial f}{\partial t}\right]_{coll} \tag{6.1}$$

where $\mathbf{F}(t, \mathbf{x}, \mathbf{v})$ is the force field acting on each particle, and the term on the right-hand side is the *Boltzmann collision integral*, which describes the effect of collisions among particles. Equation (6.1) is expressed in an Eulerian form, and 7 scalar independent variables are present. Equivalently, one can focus on a Lagrangian trajectory $(\mathbf{x}(t), \mathbf{v}(t))$ in phase space, defined as:

$$\begin{cases} \dfrac{d\mathbf{x}}{dt} = \mathbf{v}(t) \\ \dfrac{d\mathbf{v}}{dt} = \dfrac{1}{m}\mathbf{F}(t, \mathbf{x}, \mathbf{v}) \end{cases} \tag{6.2}$$

with initial conditions $(\mathbf{x}_0, \mathbf{v}_0)$ at $t = t_0$. Substituting (6.2) into (6.1), the $l.h.s.$ can be identified as the total derivative of f, and (6.1) is rewritten as

$$\frac{Df}{Dt} = \left[\frac{\partial f}{\partial t}\right]_{coll}, \tag{6.3}$$

which states that the time rate of change of the distribution function along the trajectory (6.2) is only determined by the collision operator. Hence, in the absence of collisions f is constant along each phase-space trajectory. This is equivalent to saying that the fluid motion in phase-space is *incompressible*.

For the simulation of neutral Argon gas expansion inside the thruster, the force field $\mathbf{F}(t, \mathbf{x}, \mathbf{v})$ can be safely set to zero: the domain is small enough to permit neglect of the gravitational force, and the frame of reference is considered to be inertial. Accordingly, Boltzmann's equation can be simplified as

$$\frac{\partial f}{\partial t} + \mathbf{v} \cdot \frac{\partial f}{\partial \mathbf{x}} = \left[\frac{\partial f}{\partial t}\right]_{\text{coll}}, \tag{6.4}$$

where the Boltzmann collision integral on the right hand side of the equation takes into account two-body short-range interactions between like particles. Additionally, the effect of electron impact ionization can be easily taken into account, as it is a negative source term proportional to the local phase-space density $f(t, \mathbf{x}, \mathbf{v})$.

6.2 The Convected Scheme: a Review

The neutral model employs a straightforward and easily implemented scheme for solution of the Boltzmann equation (6.1) (or similar kinetic equations) with a number of desirable properties. The starting point is a solution of the kinetic equation in integral form, which uses the method of characteristics to take an initial cell and propagate it forward in time until it is remapped onto the phase space mesh. Such a scheme is called 'Convected Scheme' (CS) to reflect the fact that it focusses on describing the convective motion of the fluid [58]. More recently a terminology has arisen that would call this a 'forward semi-Lagrangian' scheme.

Semi-Lagrangian schemes (as well as fully-Lagrangian schemes) do not suffer of time-step restrictions based on the mesh size (i.e., the well known Courant-Friedrichs-Levy limit that affects explicit Eulerian methods). Hence, such schemes are particularly well suited to kinetic simulations, where the highest and lowest speed on the grid may be different by some orders of magnitude. Accordingly, in the CS the selection of the time-step size is based on physical considerations (usually Δt is a small fraction of the *collision time*), and the mesh size can be chosen to match the required spatial resolution.

The benefit of moving the initial cell forward in time, compared to tracing back a trajectory starting from the successive time-step (as most Semi-Lagrangian schemes do), is essentially that it allows one to focus on the conservation of various quantities associated with a single initial cell (number, energy, momentum) when the contents of that cell are remapped to the phase space mesh. Particular attention was paid in plasma simulations to handling the ballistic motion near the points at which particles bounce, and in the vicinity of the zero energy cell, which turns out to be a little difficult to handle while conserving energy [59, 60].

The Convected Scheme solves Boltzmann's equation (6.1) using a natural time-splitting procedure:

1. first, the distribution function is evolved for one time step according to the collision operator only
$$\frac{\partial f}{\partial t} = \left[\frac{\partial f}{\partial t}\right]_{coll} \tag{6.5a}$$
2. then, the updated distribution function is advected for one time step along the characteristic trajectories, according to the collisionless equation
$$\frac{Df}{Dt} = 0\,. \tag{6.5b}$$

Whether to execute the steps above in this order or not is really an arbitrary choice, since it only depends on the definition of time-step. The collision operator invariably involves the flux of particles in velocity space, but it is usually totally local in physical space. As such, step 1 is naturally solved on the phase-space mesh. As concerns step 2, the Convected Scheme really uses the integral form of (6.5b), with a single phase-space cell as the control-volume at $t = t_0$:

$$\iint_{C(t)} f\,(t,\mathbf{x},\mathbf{v})\;d\mathbf{x}\,d\mathbf{v} \;=\; \iint_{C_0} f\,(t_0,\mathbf{x}_0,\mathbf{v}_0)\;d\mathbf{x}_0 d\mathbf{v}_0 \tag{6.6}$$

where the *r.h.s.* is just the total number of particles contained in cell C_0 at instant t_0, and $C(t)$ is the control-volume that evolves from C_0 by means of the map defined by (6.2). For obvious reasons, $C(t)$ is called a Moving Cell (MC). The meaning of (6.6) is clear: it is merely a statement of mass conservation for a MC, during the ballistic motion. But to understand the practical utility of (6.6), a suitable discretization of the variables must be introduced. The total number of particles in the initial phase-space cell C_0 is

$$N_0 = f_{ij}(t_0)\,\Gamma_{ij} = N_{ij}(t_0) \tag{6.7}$$

where $f_{ij}(t)$ is the average value of the distribution function in the phase-space cell centered at point $(\mathbf{x}_i, \mathbf{v}_j)$, and Γ_{ij} is the corresponding volume in phase-space of the cell. It is evident from the last expression that the Eulerian phase-space mesh is needed not only to solve the collisional step, but also to give proper initial conditions to the ballistic operator:

$$N_{ij}^{MC}(t) \;\equiv\; N_{ij}(t_0) \qquad\qquad t \geq t_0\,. \tag{6.8}$$

At the end of the time step, the particles in the MC are remapped back onto the Eulerian mesh, where the collision operator is applied next.

Alternatively, it is possible to evaluate the fraction of particles in the MC that have undergone a collision, and this permits one to remap to the mesh only those particles. In such cases, one can let the MC move for more than one time step, until the number of particles contained is a tiny fraction of the initial number, or until the geometrical distortion of the MC will require remapping to preserve accuracy. The application of the aforementioned ideas led to the Long-Lived Moving Cell (LLMC) version of the CS [61, 62]. The LLMC option considerably reduces the numerical diffusion of the scheme, and hence it is particularly suited to the simulation of low-collisional systems. But in order to follow the same trajectories for multiple time-steps, it is necessary to store the position and velocity of each MC, together with the number of particles they contain. Hence, the memory requirements of the LLMC-CS can be prohibitive for multi-dimensional simulations.

In any case, the exact time evolution of the MC can be evaluated analytically only in a few situations, and important approximations must be introduced regarding the following points:

1. parametrization of the profile of the distribution function f in the MC,

2. parametrization of the shape of the MC in phase-space,

3. definition of the Lagrangian trajectories that are to be traced for each MC.

Evidently, the choices made about the points above must be compatible with each other.
As concerns point 1, while the MC is always assumed to have a uniform density profile in physical space, it is usually considered to be a Dirac delta in velocity space.
As concerns point 2, the MC is usually obtained from the Cartesian product of a convex polyhedron in physical space and a convex polyhedron in velocity space. This is always the case when dealing with more than one dimension in physical space. Moreover, the MC is usually not deformable in velocity space, but it can usually undergo expansion/contraction and distortion in physical space. Remembering that the flow is incompressible in phase-space, the MC must have a phase-space volume constant in time.
As concerns point 3, there are three ways of handling the motion of the cell, that have been employed: first, one can move the cell center and assume the cell shape does not change; second, one can move the centers of cell faces and assume that each face does not change its orientation; third, one can move vertices of cells. In any case, a single initial velocity, equal to the central velocity $\mathbf{v}_j$, is given to the trajectories.

At the end of the ballistic move, particles must be placed back on the phase-space mesh according to the Convective Scheme remapping rule; for a domain in $\mathbb{R}^m$, this consists in depositing the particles from the Moving Cell onto the overlapped fixed cells C_i, according to the m-dimensional integral over C_i:

$$N_i \;=\; N_i + \oint_{C_i} n_{MC}(\mathbf{x})\; d\mathbf{x} \;=\; N_i + \oint_{C_i \cap MC} n_{MC}(\mathbf{x})\; d\mathbf{x} \tag{6.9}$$

where $n_{MC}(\mathbf{x})$ is the m-dimensional density in the Moving Cell (MC). Since n_{MC} is assumed uniform in the MC, the above rule can be simplified to

$$\begin{aligned} N_i \mathrel{+}= \; n_{MC} \oint_{C_i \cap MC} d\mathbf{x} \;&=\; n_{MC}\, V_{C_i \cap MC} \;= \\ =\; n_{MC}\, V_{MC} \frac{V_{C_i \cap MC}}{V_{MC}} \;&=\; N_{MC}\, F_i \end{aligned} \tag{6.10}$$

where the symbol V is used to denote the volumes in $\mathbb{R}^m$, and F_i is called the "overlapping fraction". The notation $N_i + = (\ldots)$ means $N_i = N_i + (\ldots)$; hence, (6.10) denotes the contribution to N_i due to a given MC. Obviously, the sum of all the overlapping fractions is one:

$$\sum_i F_i \;=\; \sum_i \left(\frac{V_{C_i \cap MC}}{V_{MC}} \right) \;=\; \frac{V_{MC}}{V_{MC}} \;=\; 1 \tag{6.11}$$

In its application to rarefied neutral gas simulations, the Convected Scheme solves the integral form of (6.4) using a time-splitting procedure, i.e. by successively applying a *ballistic operator* and a *collision operator*. Such a mesh-based method has important advantages over particle approaches like the Direct Simulation Monte-Carlo [63], e.g. the absence of statistical noise, a more uniform resolution in velocity space, and reduced memory requirements for a given accuracy level. As a downside, the application of the Convective Scheme to neutral simulations poses a number of challenges:

1. reducing the numerical diffusion in space introduced by the ballistic operator,
2. approximating the Boltzmann collision integral with an efficient collision operator,
3. treating generic boundary conditions in a semi-Lagrangian framework,
4. reducing spurious coupling effects between spatial and velocity meshes (e.g. the ‘ray effect’ in the presence of sharp gradients).

The reduction of numerical diffusion (point 1) is treated in detail in Section 6.3, where a third-order remapping procedure is derived, and the results are compared to the standard first-order version. The successive Sections 6.4.1 and 6.4.2 describe the computational domain, the spatial mesh and the velocity mesh employed. Points 2 and 3 are treated afterwards (in Sections 6.5 and 6.6, respectively), since they are strictly related to the velocity mesh set-up. Point 4 has not been thoroughly investigated yet, and it is a major topic for future research (but see also [64] where particles were allowed to travel within rays of finite angular extent).

6.3 Development of a High Order Remapping Rule

Due to the high dimensionality (3D-3V) required by the neutral gas model, computational efficiency is of paramount importance. Therefore, the simplest version of a Convected Scheme was selected for implementation, where the MCs are rigidly translated according to the motion of their center, and hence the density in each MC is uniform and constant during the time step. In the semi-Lagrangian version at hand, the MCs are fully remapped onto the mesh at the end of each time-step. This scheme will be referred to as the *Cell-Centered Semi-Lagrangian Convected Scheme* (CCSL-CS).

The CCSL-CS has many desirable properties: it is fast and efficient, it is conservative, it preserves positivity, and it has very low phase-error (usually negligible). On the other hand, the accuracy of the scheme is only 1^{st} order in space, the leading error being a strong numerical diffusion term which has a non-linear dependence on the Courant parameter. In a 3D simulation, this means that diffusion is *anisotropic*, and hence the ballistic operator can introduce unphysical geometrical distortion wherever the density gradient is not aligned with the mesh axes.

In the earlier work on the Convected Scheme, the order of the scheme was not considered to be of great concern, since the methods were integral methods and the number of remappings per collision time (which is often the critical physical time period) or even during the entire simulation was small. The remapping errors were thus believed to be modest. Unfortunately, the system at hand presents very low gas collisionality and very high density gradients, conditions in which numerical diffusion can be a serious problem. Hence, if the desirable properties of the scheme can be retained in a higher order version, this would represent a major improvement.

In order to increase the accuracy of the scheme, two different approaches can be used:

1. allowing for a non-uniform density in the MC;
2. given an a priori estimate of the remapping error, applying a small correction to the final position of the MC to compensate for it.

The former option complicates significantly the evaluation of the integral in Eq. 6.9, since Eq. 6.10 is not applicable. Seeking a more numerically efficient method, the latter option is investigated hereafter.

The remainder of this section reports a simple set of modifications (essentially a small correction to the final position of the MC upon remapping) which changes the order of the spatial move from first to third. (While a similar procedure can certainly be applied to the energy/velocity move, its effects on energy conservation mean that its desirability is less clear cut. In this work the focus is on neutral particle kinetics, where the velocity is constant.) The basic CS is unchanged by this modification, in that conservation laws can be built into the scheme as before. The ease of implementation is similarly basically unaffected.

6.3.1 The Convected Scheme as an advection equation solver

In this section attention is focused on the ballistic move. It is shown that for a neutral kinetic simulation the CCSL-CS is an advection equation solver, and a simple 1D version with 'small steps' is recast as a finite-difference scheme. The modified equation analysis (MEA) is introduced as a tool to demonstrate the first-order accuracy of the original CCSL-CS, and to analyze the form of the local truncation error (LTE). Important analogies to the Donor-cell scheme are pointed out, and the MPDATA algorithm is considered for the compensation of the first and second order terms of the LTE. Subtle differences between the two methods are discussed in detail, which cause the aforementioned approach to fail. (In the following section this analysis is extended to a general velocity field, and it is shown how the CS can be made third order accurate.)

For a neutral gas simulation, if the physical coordinates are fixed in an inertial reference frame and the gravitational force is neglected, then $\mathbf{F} = 0$ in Boltzmann's equation (6.1), and the particles move in straight trajectories. In this situation, the velocity of the MC does not change during the time-step, and no remapping is needed in velocity space. Hence, for each velocity one passive advection equation with uniform velocity is solved.

For the sake of clarity, a one-dimensional domain with uniform spatial mesh spacing Δx is considered. On this domain, the 1D density function $n(x,t)$ is convected with a uniform velocity u. Hence the simple advection equation

$$\frac{\partial n}{\partial t} + u\frac{\partial n}{\partial x} = 0 \tag{6.12}$$

is to be solved over the domain. In order to be able to compare the analysis here with the more common finite-difference schemes, a small Δt is chosen, so that a MC cannot travel more than one cell before being remapped. (We would point out, however, that these choices are for ease of explanation, since in fact we prefer to think we are solving a method of characteristics in an integral form, rather than a PDE; and that no CFL criterion actually applies to the methods we shall employ.) As another way to put it, Δt will temporarily be said to satisfy the relation

$$-1 < \left(U = \frac{u\Delta t}{\Delta x}\right) < +1 \tag{6.13}$$

which is the Courant-Friedrichs Limit for finite-difference schemes.

If the following notation is introduced:

$$U^{+} = \frac{1}{2}\left(U + |U|\right) \geq 0 \tag{6.14}$$

$$U^{-} = \frac{1}{2}\left(U - |U|\right) \leq 0 \tag{6.15}$$

the 1D CCSL-CS algorithm can be recast as a simple finite-difference single-step scheme with a 3-point stencil:

$$n_i^{k+1} = n_{i-1}^{k} U^{+} + n_i^{k}(1 - |U|) - n_{i+1}^{k} U^{-} \tag{6.16}$$

where i is the index over space, and k is the index over time. The last expression is equivalent to a Donor-cell scheme, but with the important difference that *the velocity here is not defined at the cell edges, but at the cell centers.* This consideration will be most important when high-order corrections are applied to the scheme.

A detailed Modified Equation Analysis (MEA) of (6.16) for a generic velocity field will be performed in the next section. This will provide a means to make the CS third order accurate. Instead, at this stage it is instructive to consider the velocity to be uniform over the domain: in such a situation (6.16) retains no information about the location of the velocity on the grid, and the local truncation error (LTE) of the 1D CCSL-CS is identical to the 1D Donor-cell scheme. According to the analysis performed in [65], the expansion of all terms in (6.16) to 3^{rd} order in Taylor series about the point $n_i^k = n(x_i, t^k)$ gives a second order expression for the *Modified Equation* of the scheme:

$$\frac{\partial n}{\partial t} + u\frac{\partial n}{\partial x} = \frac{\Delta x^2}{2\Delta t}\left(|U| - U^2\right)\frac{\partial^2 n}{\partial x^2} + \frac{\Delta x^3}{6\Delta t}\left(-U + 3|U|U - 2U^3\right)\frac{\partial^3 n}{\partial x^3} + H.O.T.\,, \tag{6.17}$$

which holds for the Donor-cell, and hence for the CCSL-CS, given the hypothesis that $u = const$. The expression in Eq. 6.17 is the Modified Equation that is solved by the scheme, *whenever the density is a smooth function that can be differentiated at least three times* with respect to space. The $r.h.s.$ of 6.17, which would be zero if the advection equation was solved exactly, is the local truncation error of the scheme. The first term on the $r.h.s.$ is a 1^{st} order error linearly proportional to the second derivative of $n(x)$, and it has the form of a Numerical Diffusion:

$$\mathscr{E}_1 = \frac{\partial}{\partial x}\left(D\frac{\partial n}{\partial x}\right) \qquad D = \frac{\Delta x^2}{2\Delta t}\left(|U| - U^2\right) \tag{6.18}$$

The second term on the $r.h.s.$ is a 2^{nd} order error linearly proportional to the third derivative of $n(x)$, and it has the form of a Numerical Dispersion:

$$\mathscr{E}_2 = \frac{\partial}{\partial x}\left(K\frac{\partial^2 n}{\partial x^2}\right) \qquad K = \frac{\Delta x^3}{6\Delta t}\left(-U + 3|U|U - 2U^3\right) \tag{6.19}$$

It should be noted that in this particular 1D case with uniform velocity u, the local truncation error of the CCSL-CS as given by Eq. 6.17 is exactly identical to the error of the Donor-cell scheme. Nevertheless, as is common for semi-Lagrangian schemes, the CCSL-CS is by no means limited by the Courant-Friedrichs-Lewy condition. In fact, when

$$\left|\frac{u\Delta t}{\Delta x}\right| > 1, \tag{6.20}$$

the displacement of the MC is split into two parts: the first part is an integer multiple of Δx, and the second part is a fractional step $< \Delta x$:

$$S_x \; = \; u\Delta t \; = \; l\,\Delta x + S'_x \qquad l \in \mathbb{I}. \tag{6.21}$$

It is to this latter fractional step that the truncation analysis above can be applied, by changing the definition of U:

$$U = \frac{S'_x}{\Delta x} \qquad -1 < U < 1 \tag{6.22}$$

To construct a 3^{rd} order version of the CCSL-CS algorithm, the first two terms ($\mathscr{E}_1$ and $\mathscr{E}_2$) of the local truncation error must be compensated. Of course, now that the form of these terms is known, the "compensation" issue consists of two points:

1. finding a suitable estimate of $\mathscr{E}_1$ and $\mathscr{E}_2$;
2. using an efficient strategy to compensate for the two terms.

It is important to note that the two points above will introduce new numerical errors, which will be different in nature and magnitude depending on the choices that are made. In particular, the desirable properties that are common to the Donor-cell scheme and the CCSL-CS should not be altered:

- exact mass conservation;
- preservation of positivity;
- low phase error;

- monotonic behavior for uniform u.

Of the above requirements, only the monotonicity can be sacrificed at this stage, since many strategies exist to deal with that problem alone. In any case, the task implied by the other requirements is not trivial.

The correct way to solve this problem for the Donor-cell scheme (which is, up to this point, completely equivalent to the CCSL-CS) was explained by Smolarkiewicz in 1984 [66]. There he demonstrated that the compensation stage should use the same Donor-cell scheme, and he suggested an iterative procedure to achieve this. In fact, the errors $\mathscr{E}_1$ and $\mathscr{E}_2$ can be rewritten as the first spatial derivatives of convective fluxes:

$$\mathscr{E}_1 = \frac{\partial}{\partial x}\left(u_1^* n\right) \qquad u_1^* = \frac{D}{n}\frac{\partial n}{\partial x} \tag{6.23a}$$

$$\mathscr{E}_2 = \frac{\partial}{\partial x}\left(u_2^* n\right) \qquad u_2^* = \frac{K}{n}\frac{\partial^2 n}{\partial x^2} \tag{6.23b}$$

where u_1^* and u_2^* are the *effective diffusive velocity* and *effective dispersive velocity*, respectively. As a consequence, the equation solved by the 1D CCSL-CS and Donor-cell schemes can be recast as:

$$\frac{\partial n}{\partial t} = -\frac{\partial}{\partial x}(u n) + \frac{\partial}{\partial x}\left(u_1^* n\right) + \frac{\partial}{\partial x}\left(u_2^* n\right) + H.O.T. \tag{6.24}$$

In [66], the error terms are not compensated directly, but an iterative algorithm is advised instead. Such an algorithm, called "MPDATA" [67], consists of doing a first Donor-cell step with the physical velocity u, followed by some corrective Donor-cell steps that use the numerical velocities u_1^* and u_2^*. The iterative method is shown to converge to the full compensation of the $\mathscr{E}_1+\mathscr{E}_2$ errors after $N > 3$ steps. In [65] the sum of the successive approximations is computed analytically to find a single numerical velocity that represents the effects of an arbitrary number of passes; this procedure permits a 50 % computational saving for a third order scheme.

It is important to note that the equivalence between the 1D Donor-cell scheme and the 1D CCSL-CS does not hold when the velocity is not uniform. This is simply because of the different location of the velocity on the grid for the two schemes. Now, even if u is uniform over the domain, Eq. 6.23 shows that the numerical velocities u_1^* and u_2^* are not uniform for a generic density function $n(x)$. Hence, *the two schemes are equivalent only to first order.* As a confirmation of the difference between the two schemes, the application of the MPDATA procedure to the CCSL-CS has turned out to be unstable.

6.3.2 Modified Equation Analysis

The last section emphasized that the 1D versions of the CCSL-CS and Donor-cell scheme are not equivalent because of the different location of the velocity on the grid. Nevertheless, when a uniform velocity field is considered, the two methods have the identical LTE, and this fact suggested that a high-order version of the CCSL-CS could be obtained using multi-pass corrections, as was done in MPDATA. But such a strategy fails since the two schemes have a different behavior during the anti-diffusive step.

Starting from the aforementioned considerations, in this section the analogy with the Donor-cell scheme is dropped, and a detailed third order MEA is performed for a general velocity field. As a starting point, the equation to be solved is now the 1D continuity equation

$$\partial_t n + \partial_x (u\, n) = 0 \tag{6.25}$$

where the velocity $u(x,t)$ is not constrained to be constant in time or uniform in space. Nevertheless, for the sake of clarity, it will be assumed that $u > 0$ unless otherwise stated. In this situation, the 1D CCSL-CS is

$$n_i^{k+1} \ = \ U_{i-1}^k\, n_{i-1}^k + \left(1 - U_i^k\right) n_i^k \tag{6.26}$$

which is, after substitution of the 3^{rd} order Taylor expansions about the point $\left(x_i, t^k\right)$,

$$\begin{aligned} &\left(\Delta t\,\partial_t + \frac{\Delta t^2}{2}\partial_{tt}^2 + \frac{\Delta t^3}{6}\partial_{ttt}^3\right) n + O\left(\Delta t^4\right) = \\ -&\left(\Delta x\,\partial_x - \frac{\Delta x^2}{2}\partial_{xx}^2 + \frac{\Delta x^3}{6}\partial_{xxx}^3\right)(Un) + O\left(\Delta x^4\right) \end{aligned} \tag{6.27}$$

where $n \equiv n_i^k$ and $U \equiv U_i^k$. As a first step, the time derivatives of n are eliminated by means of the substitution:

$$n_t\,\Delta t = -\,(Un)_x\,\Delta x + \mathscr{E}\,\Delta t \tag{6.28}$$

where $\mathscr{E}$ is the (1^{st} order) local truncation error (LTE) of the scheme. An expression for n_{tt} can be obtained by differentiating the above with respect to time, multiplying by Δt, and using (6.28) wherever the n_t term appears:

$$n_{tt}\,\Delta t^2 = \ U\,(Un)_{xx}\,\Delta x^2 + U_x\,(Un)_x\,\Delta x^2 - (U_t\, n)_x\,\Delta x\,\Delta t - (U\mathscr{E})_x\,\Delta x\,\Delta t + \mathscr{E}_t\,\Delta t^2 \tag{6.29}$$

where the last two terms on the *r.h.s* are third order since they contain the LTE itself. The same procedure can be repeated to get an expression for the third time derivative:

$$\begin{aligned} n_{ttt}\,\Delta t^3 = &- U^2\,(Un)_{xxx}\,\Delta x^3 + \left(2U_t\frac{\Delta t}{\Delta x} - 3UU_x\right)(Un)_{xx}\,\Delta x^3 \\ &+ \left(2U_{xt}\frac{\Delta t}{\Delta x} - U_x^2 - UU_{xx}\right)(Un)_x\,\Delta x^3 \\ &+ U\,(U_t\,n)_{xx}\,\Delta x^2 \Delta t + U_x\,(U_t\,n)_x\,\Delta x^2 \Delta t - (U_{tt}\,n)_x\,\Delta x\,\Delta t^2 + H.O.T. \end{aligned} \tag{6.30}$$

where the $H.O.T.$ come from the terms containing the LTE, which are now fourth order. Substituting (6.28), (6.29) and (6.30) into (6.26), one gets:

$$\begin{aligned} n_t + (un)_x \;=\; & \frac{\Delta x^2}{2\,\Delta t}\left[(1-U)\,(Un)_{xx} - U_x\,(Un)_x + (U_t\,n)_x\,\frac{\Delta t}{\Delta x}\right] \\ &+ \frac{\Delta x^3}{6\,\Delta t}\left[\left(U^2-1\right)(Un)_{xxx} + \left(3UU_x - 2U_t\frac{\Delta t}{\Delta x}\right)(Un)_{xx}\right. \\ &\quad + \left(U_x^2 + 2U_{xx} - 2U_{xt}\frac{\Delta t}{\Delta x}\right)(Un)_x - U\,(U_t\,n)_{xx}\,\frac{\Delta t}{\Delta x} \\ &\quad \left. - U_x\,(U_t\,n)_x\,\frac{\Delta t}{\Delta x} + (U_{tt}\,n)_x\left(\frac{\Delta t}{\Delta x}\right)^2\right] \\ &+ \frac{1}{2}\left[(U\mathcal{E})_x\,\Delta x - \mathcal{E}_t\,\Delta t\right] + O\left(\Delta x^3\right) \end{aligned} \tag{6.31}$$

where the *r.h.s.* is the truncation error. The fact that the expression for the LTE is formally implicit does not mean the problem is insoluble. In fact, since the LTE is first order, the last term in brackets on the *r.h.s.* is second order. This implies that the leading-term (first order) of the LTE is already known at this stage, and it is just the first term on the *r.h.s.* of (6.31):

$$\mathcal{E}_1 = \frac{\Delta x^2}{2\,\Delta t}\left[(1-U)\,(Un)_{xx} - U_x\,(Un)_x + (U_t\,n)_x\,\frac{\Delta t}{\Delta x}\right]. \tag{6.32}$$

The second order term of the LTE can be obtained by substituting $\mathcal{E} \approx \mathcal{E}_1$ into (6.31). Accordingly, the space and time derivatives of the LTE are approximated as

$$\mathcal{E}_x \approx \frac{\Delta x^2}{2\,\Delta t}\left[(1-U)\,(Un)_{xxx} - 2U_x\,(Un)_{xx} - U_{xx}\,(Un)_x + (U_t\,n)_{xx}\,\frac{\Delta t}{\Delta x}\right] \tag{6.33}$$

and

$$\begin{aligned} \mathcal{E}_t \approx \frac{\Delta x^3}{2\,\Delta t^2}&\left[\left(U^2-U\right)(Un)_{xxx} + \left((3U-2)\,U_x - 2U_t\frac{\Delta t}{\Delta x}\right)(Un)_{xx}\right. \\ &+ \left((U-1)\,U_{xx} + U_x^2 - 2U_{xt}\frac{\Delta t}{\Delta x}\right)(Un)_x \\ &\left. + (1-U)\,(U_t\,n)_{xx}\,\frac{\Delta t}{\Delta x} - U_x\,(U_t\,n)_x\,\frac{\Delta t}{\Delta x} + (U_{tt}\,n)_x\left(\frac{\Delta t}{\Delta x}\right)^2\right] \end{aligned} \tag{6.34}$$

where the approximation $n_t \Delta t \approx -(Un)_x \Delta x$ was used instead of the full (6.28). The modified equation of the 1D CCSL-CS, subject to the hypothesis $u > 0$, is obtained by substituting (6.32) for $\mathscr{E}$, (6.33) for $\mathscr{E}_x$, and (6.34) for $\mathscr{E}_t$ into (6.31):

$$\begin{aligned} n_t + (un)_x \;=\; & \frac{\Delta x^2}{2\Delta t}\left[(1-U)\,(Un)_{xx} - U_x\,(Un)_x + (U_t\,n)_x\,\frac{\Delta t}{\Delta x}\right] \\ & + \frac{\Delta x^3}{6\Delta t}\left[\left(3U - 2U^2 - 1\right)(Un)_{xxx} + \left(\frac{9}{2}U_x - 6UU_x + U_t\frac{\Delta t}{\Delta x}\right)(Un)_{xx}\right. \\ & \quad + \left(\frac{3}{2}U_{xx} - 2UU_x - 2U_x^2 + U_{xt}\frac{\Delta t}{\Delta x}\right)(Un)_x + \left(2U - \frac{3}{2}\right)(U_t\,n)_{xx}\,\frac{\Delta t}{\Delta x} \\ & \quad \left. + 2U_x\,(U_t\,n)_x\,\frac{\Delta t}{\Delta x} - \frac{1}{2}\,(U_{tt}\,n)_x\left(\frac{\Delta t}{\Delta x}\right)^2\right] \; + \; O\!\left(\Delta x^3\right) . \end{aligned} \tag{6.35}$$

Eq. (6.35) shows that, for a given velocity field $u\,(x,t)$, the PDE that is really solved by the scheme (6.26) approximates the continuity equation $n_t + (un)_x = 0$ only to first order. In fact, (6.35) contains the spurious terms $\mathscr{E}_1 = O(\Delta x)$ and $\mathscr{E}_2 = O(\Delta x^2)$.

6.3.3 Third order remapping method

In the following treatment a novel approach is used in order to devise a third order version of the CCSL-CS. From a Lagrangian view-point, the basic idea is to *apply a correction to the position of the Moving-Cell before it is remapped.* Since a correction to the position is $\delta x = \delta u\,\Delta t$, one can think of a correction to the velocity as well.

It is important to consider that the velocity field $u\,(x,t)$ need not be the physical velocity field, which is called $u_0\,(x,t)$ from now on. In fact, it is assumed that

$$u = u_0 + u_1 + u_2 \qquad \text{or} \qquad U = U_0 + U_1 + U_2 \tag{6.36}$$

where $U_1 \propto \Delta x$ and $U_2 \propto \Delta x^2$ will be evaluated by requiring (6.35) be a third order approximation to the ‘physical’ continuity equation:

$$n_t + (u_0 n)_x = O\!\left(\Delta x^3\right). \tag{6.37}$$

In other words, without changing the remapping rule on which the CS is based, a third order scheme can be obtained by applying first and second order corrections (u_1 and u_2) to the physical velocity field u_0. Such a method is direct (i.e. non iterative), and guarantees the compensation of both $\mathscr{E}_1$ and $\mathscr{E}_2$ for sufficiently smooth density profiles. After some algebra, the substitution of (6.36) into (6.35) gives (6.37) only if

$$U_1 \;=\; \frac{\Delta x}{2}\left[(1-U_0)\,\frac{1}{n}\,(U_0\,n)_x + U_{0\,t}\,\frac{\Delta t}{\Delta x}\right], \tag{6.38}$$

and

$$\begin{aligned} U_2 = \frac{\Delta x^2}{12} \Bigg[& \left(1 - 3U_0 + 2U_0^2\right) \frac{1}{n} (U_0\, n)_{xx} + \left(2U_0 U_{0\,x} - 3U_{0\,x} - 4U_{0\,t} \frac{\Delta t}{\Delta x}\right) \frac{1}{n} (U_0\, n)_x \\ & + (6 - 5U_0) \frac{1}{n} (U_{0\,t}\, n)_x \frac{\Delta t}{\Delta x} + 2U_{0\,tt} \left(\frac{\Delta t}{\Delta x}\right)^2 \Bigg]. \end{aligned} \tag{6.39}$$

The expressions 6.38 and 6.39 formally contain the *exact* space and time derivatives of U_0 and n, but for any practical situation, such derivatives will be evaluated numerically. For (6.37) to hold, both U_1 and U_2 must be estimated with third order accuracy; accordingly, the finite difference schemes must be second order accurate in (6.38), and first order in (6.39).

With the proper approximations for U_1 and U_2, the scheme that results from using the velocity expansion (6.36) in the 1D CCSL-CS remapping rule (6.26) is third order accurate, conservative, sign preserving, and it has an extremely low phase error. When the velocity u_0 is constant and uniform, formulas (6.38) and (6.39) are further simplified: in such a situation, Cartesian 2D and 3D versions of the algorithm are obtained straightforwardly by applying independent corrections to each component of the velocity vector, resulting in a very compact and numerically efficient method. In fact, all these properties make this approach particularly suitable for application to neutral gas kinetic simulations.

6.3.4 3D analysis

One might wonder whether the above procedure could be used to obtain a third order scheme for the advection equation in three dimensions, for a generic flow field. In fact, that would open the possibility to apply the CCSL-CS to the multi-dimensional solution of generic hyperbolic conservation equations (for example, Navier-Stokes). Such an application is beyond the scope of this work, and it is opinion of the authors that a complete third order analysis in 3D can be carried on only with a considerable amount of algebra. Nevertheless, for completeness, a brief outline of the procedure to obtain a second-order scheme in 3D is given hereafter.

The equation to be solved is now the 3D continuity equation

$$\partial_t n + \partial_x (u\, n) + \partial_y (v\, n) + \partial_z (w\, n) = 0, \tag{6.40}$$

where u, v, and w are respectively the x, y, and z components of the velocity vector. For the sake of clarity, it will be assumed that u, v, and w are all > 0, and that

$$U = \frac{u\Delta t}{\Delta x} < 1, \qquad V = \frac{v\Delta t}{\Delta y} < 1, \qquad W = \frac{w\Delta t}{\Delta z} < 1. \tag{6.41}$$

Under the hypothesis above, if a Cartesian grid with uniform spacing over each direction is considered, the 3D CCSL-CS can be written as a finite-difference scheme,

$$\begin{aligned} n_{i,j,k}^{m+1} = & \; n_{i,j,k}^{m}\left(1-U_{i,j,k}^{m}\right)\left(1-V_{i,j,k}^{m}\right)\left(1-W_{i,j,k}^{m}\right) \\ & + n_{i-1,j,k}^{m}\, U_{i-1,j,k}^{m}\left(1-V_{i-1,j,k}^{m}\right)\left(1-W_{i-1,j,k}^{m}\right) \\ & + n_{i,j-1,k}^{m}\left(1-U_{i,j-1,k}^{m}\right) V_{i,j-1,k}^{m}\left(1-W_{i,j-1,k}^{m}\right) \\ & + n_{i,j,k-1}^{m}\left(1-U_{i,j,k-1}^{m}\right)\left(1-V_{i,j,k-1}^{m}\right) W_{i,j,k-1}^{m} \\ & + n_{i-1,j-1,k}^{m}\, U_{i-1,j-1,k}^{m}\, V_{i-1,j-1,k}^{m}\left(1-W_{i-1,j-1,k}^{m}\right) \\ & + n_{i,j-1,k-1}^{m}\left(1-U_{i,j-1,k-1}^{m}\right) V_{i,j-1,k-1}^{m}\, W_{i,j-1,k-1}^{m} \\ & + n_{i-1,j,k-1}^{m}\, U_{i-1,j,k-1}^{m}\left(1-V_{i-1,j,k-1}^{m}\right) W_{i-1,j,k-1}^{m} \\ & + n_{i-1,j-1,k-1}^{m}\, U_{i-1,j-1,k-1}^{m}\, V_{i-1,j-1,k-1}^{m}\, W_{i-1,j-1,k-1}^{m}, \end{aligned} \tag{6.42}$$

where i, j, and k are the indices over the three spatial directions, and m is the index over time. A 2^{nd} order Taylor series expansion about the point $\left(x_i, y_j, z_k, t^m\right)$ gives:

$$\begin{aligned} & n_t\,\Delta t + (nU)_x\,\Delta x + (nV)_y\,\Delta y + (nW)_z\,\Delta z = \\ & - n_{tt}\frac{\Delta t^2}{2} + O\left(\Delta t^3\right) + (nU)_{xx}\frac{\Delta x^2}{2} + (nV)_{yy}\frac{\Delta y^2}{2} + (nW)_{zz}\frac{\Delta z^2}{2} \\ & + (nUV)_{xy}\,\Delta x\,\Delta y + (nVW)_{yz}\,\Delta y\,\Delta z + (nWU)_{zx}\,\Delta z\,\Delta x + O\left(\Delta s^3\right), \end{aligned} \tag{6.43}$$

where $\Delta s = \sqrt{\Delta x^2 + \Delta y^2 + \Delta z^2}$.

As usual, an expression for n_{tt} is obtained by differentiating the equality

$$n_t\,\Delta t = -(nU)_x\,\Delta x - (nV)_y\,\Delta y - (nW)_z\,\Delta z + \mathscr{E}\,\Delta t \tag{6.44}$$

with respect to time. Seeking a second order scheme, the term containing the local truncation error $\mathscr{E}$ can be neglected, since it contributes to higher order terms only. After some algebraic manipulations, this gives:

$$\begin{aligned} n_{tt}\,\Delta t^2 \simeq & \left[U\,(nU)_x\,\Delta x + nVU_y\,\Delta y + nWU_z\,\Delta z - nU_t\,\Delta t\right]_x \Delta x \\ & + \left[V\,(nV)_y\,\Delta y + nWV_z\,\Delta z + nUV_x\,\Delta x - nV_t\,\Delta t\right]_y \Delta y \\ & + \left[W\,(nW)_z\,\Delta z + nUV_x\,\Delta x + nVW_y\,\Delta y - nW_t\,\Delta t\right]_z \Delta z \\ & + 2\,(nUV)_{xy}\,\Delta x\,\Delta y + 2\,(nVW)_{yz}\,\Delta y\,\Delta z + 2\,(nWU)_{zx}\,\Delta z\,\Delta x\,. \end{aligned} \tag{6.45}$$

The substitution of (6.45) into (6.43) leads to the modified equation (to 2^{nd} order) for the 3D CCSL-CS:

$$\begin{aligned} n_t + (un)_x + (vn)_x + (wn)_z \; = \; & \frac{\Delta x}{2\Delta t}\left[(1-U)\,(nU)_x\,\Delta x + nVU_y\,\Delta y + nWU_z\,\Delta z + nU_t\,\Delta t\right]_x \\ & + \frac{\Delta y}{2\Delta t}\left[(1-V)\,(nV)_y\,\Delta y + nWV_z\,\Delta z + nUV_x\,\Delta x + nV_t\,\Delta t\right]_y \\ & + \frac{\Delta z}{2\Delta t}\left[(1-W)\,(nW)_z\,\Delta z + nUW_x\,\Delta x + nVW_y\,\Delta y + nW_t\,\Delta t\right]_z \\ & + \; H.O.T. \end{aligned} \tag{6.46}$$

At this point it can assumed that u, v and w are obtained by a first order perturbation to the physical velocity:

$$\begin{cases} u = u_0 + u_1 \\ v = v_0 + v_1 \\ w = w_0 + w_1 \end{cases} \qquad \text{or} \qquad \begin{cases} U = U_0 + U_1 \\ V = V_0 + V_1 \\ W = W_0 + W_1 \end{cases} \tag{6.47}$$

so that, after substitution into (6.46), the corrections are obtained by imposing the compensation of the first order errors. For the general case with no restriction on the sign of the velocity components, one gets:

$$U_1 = \left[\left(|U_0| - U_0^2\right)\frac{(nU_0)_x}{nU_0}\right]\frac{\Delta x}{2} + \left[V_0 U_{0y}\right]\frac{\Delta y}{2} + \left[W_0 U_{0z}\right]\frac{\Delta z}{2} + \left[U_{0t}\right]\frac{\Delta t}{2} \tag{6.48a}$$

$$V_1 = \left[\left(|V_0| - V_0^2\right)\frac{(nV_0)_y}{nV_0}\right]\frac{\Delta y}{2} + \left[W_0 V_{0z}\right]\frac{\Delta z}{2} + \left[U_0 V_{0x}\right]\frac{\Delta x}{2} + \left[V_{0t}\right]\frac{\Delta t}{2} \tag{6.48b}$$

$$W_1 = \left[\left(|W_0| - W_0^2\right)\frac{(nW_0)_z}{nW_0}\right]\frac{\Delta z}{2} + \left[U_0 W_{0x}\right]\frac{\Delta x}{2} + \left[V_0 W_{0y}\right]\frac{\Delta y}{2} + \left[W_{0t}\right]\frac{\Delta t}{2} \tag{6.48c}$$

and the correction to be applied to the final position of the MC is simply

$$\delta\mathbf{r} \; = \; \begin{pmatrix} \delta x \\ \delta y \\ \delta z \end{pmatrix} \; = \; \begin{pmatrix} U_1 \Delta x \\ V_1 \Delta y \\ W_1 \Delta z \end{pmatrix} \; . \tag{6.49}$$

When the velocity field and the density are smooth functions of space and time, the corrections above lead to a simple and efficient 2^{nd} order version of the 3D CCSL-CS, for a generic velocity field. As usual, the scheme is conservative and positivity preserving.

6.3.5 Monotonic variations

For a constant velocity field u_0, the first order version of the 1D CCSL-CS guarantees the solution $n(x,t)$ will conserve the monotonicity of the initial conditions. Unfortunately, this is not true for the third order version. In fact, wherever the advected function $n(x)$ happens not to be differentiable in space, the finite difference approximations in (6.38) and (6.39) become meaningless and the estimates for U_1 and U_2 are incorrect. At best, the accuracy of the scheme drops to first order; more likely, U_1 and U_2 are overestimated and $O(1)$. As a consequence, Gibbs' oscillations would appear, with an amplitude that does not decrease on refining the mesh. In such a situation the scheme would probably retain a first-order accuracy in the L_2 norm, but *it cannot converge to the correct solution* in the L_∞ norm.

Limiters In order to make the third order CCSL-CS monotonic, i.e. non-oscillating, it should be noticed that the spurious oscillations are due to the corrections U_1 and U_2. Hence, a natural approach is to reduce the magnitude of these corrections with a *limiter function* wherever the conditions are favorable for spurious oscillations to arise. Basically, in order to preserve monotonicity, the limiter function is supposed to reduce the scheme to first order in the proximity of a discontinuity in n_x. In practice, it happens that U_1 and U_2 are reduced also in regions where no such limiting is needed: a typical long-time effect is the artificial flattening of smooth local maxima and minima. Several limiter functions were obtained by adapting the flux limiters commonly used in high order Total Variation Diminishing (TVD) schemes [68–71]. Here, the general implementation is based on the slight modification of (6.36) into

$$U = U_0 + \phi(r)\,[U_1 + U_2] \tag{6.50}$$

where $\phi(r)$ is the limiter function and r is the ratio of successive gradients on the solution mesh, with a slightly modified definition in order to assure that $-1 \le r \le 1$:

$$r = \min\left[\frac{n_i - n_{i-1}}{n_{i+1} - n_i}, \frac{n_{i+1} - n_i}{n_i - n_{i-1}}\right]. \tag{6.51}$$

In the tests performed so far, the best results were obtained using the Superbee limiter designed by Roe [72] in 1986

$$\phi(r) = \max\left[0, \min(2r, 1)\right], \tag{6.52}$$

where the original simple formula is further simplified here because $r \le 1$.

Non-oscillating reconstructions Taking a slightly different point of view, the finite difference approximations in (6.38) and (6.39) are evaluated from a local quadratic polynomial interpolation of the discrete function $\{n_i\}$ between three equally spaced grid points: once that the reconstructed polynomial is obtained, it is analytically differentiated in order to give an approximation for the first and second derivatives of $n(x)$ at the center point. In general, it is well-known that polynomial interpolations are not suited to reconstruct ‘non-smooth’ functions on a uniform grid, and hence there is no surprise that spurious oscillations are triggered whenever there is a discontinuity in the solution.

Following naturally from these considerations is the idea of using non-polynomial functions for local interpolation. In [73] a third order non-oscillating reconstruction technique is outlined, which uses only three grid points (resulting in an ideally compact stencil), and that does not need limiters. Such a method is based on a *Local Double Logarithmic Reconstruction* (LDLR) of the form

$$r_0(x) \simeq A + B\log(x+C) + D\log(x+E)\,, \tag{6.53}$$

within cell C_0. As described is more detail later on, the five parameters in last equation are obtained by imposing conservation, formal third order accuracy, symmetry, and Local Variation Boundedness (LVB). The complete form of the reconstructing function is

$$r_0(x) = \overline{n}_0 + \phi_0(x) - \frac{1}{\Delta x}\int_{C_0} \phi_0(\xi)\, d\xi \tag{6.54}$$

where $\overline{n}_0$ is the average value of $n(x)$ within cell C_0, and $\frac{1}{\Delta x}\int_{C_0}\phi_0(\xi)\,d\xi$ represents the mean value of the function $\phi_0(x)$, which is defined as:

$$\phi_0(x) = -\frac{c\,\Delta x}{a}\log\left[(x-x_0) - \frac{\Delta x}{2}\left(\frac{2}{a}-1\right)\right] - \frac{d\,\Delta x}{b}\log\left[(x-x_0) - \frac{\Delta x}{2}\left(\frac{2}{b}-1\right)\right]. \tag{6.55}$$

For any choice of the coefficients a, b, c and d, the reconstruction (6.54) is conservative, since

$$\frac{1}{\Delta x}\int_{C_0} r_0(x)\, dx \equiv \overline{n}_0\,. \tag{6.56}$$

The requirement of third order accuracy requires the reconstruction to match the second order finite difference approximations to the derivative $u'(x)$ at the cell faces:

$$r_0'\left(x_0 - \frac{\Delta x}{2}\right) = \frac{\overline{u}_0 - \overline{u}_{-1}}{\Delta x} = \delta_L\,, \tag{6.57a}$$

$$r_0'\left(x_0 + \frac{\Delta x}{2}\right) = \frac{\overline{u}_1 - \overline{u}_0}{\Delta x} = \delta_R\,, \tag{6.57b}$$

which permits to solve for the parameters c and d as functions of a, b, δ_L and δ_R:

$$c = \frac{(a-1)\,[\delta_2(1-b) - \delta_1]}{b-a}\,, \tag{6.58}$$

$$d = \delta_1 - c\,. \tag{6.59}$$

The reconstruction should be symmetric, in the sense that if $r_0'(x_0 - \Delta x/2) = -r_0'(x_0 + \Delta x/2)$, then $r_0'(x_0)$ should be zero. This permits to find b as a function of a,

$$b = \frac{a}{a-1}\,, \tag{6.60}$$

and hence all the 3 parameters b, c and d that show up in (6.55) are univocally determined once that a is known. To construct a reconstruction procedure of sufficiently low variation Marquina's concept of *Local Variation Boundedness* is used:

Definition 6.3.1 (Local Variation Bounded [74])**.** The local variation of a function $f(x)$ in a cell C_i is given by $LV\left(f_i\right) = TV\left(f\right)|_{C_i}$. The function is Local Variation Bounded (LVB) in C_i if $LV\left(f_i\right) = O(\Delta x)$, where Δx is the cell size.

An expression for $a(\delta_1, \delta_2)$ which ensures that the reconstruction (6.55) be a well defined smooth LVB function is [73]

$$a(\delta_1,\delta_2) = (1-\mathrm{TOL})\left(1+\mathrm{TOL}-\frac{2|\delta_1|^q|\delta_2|^q+\mathrm{TOL}}{|\delta_1|^{2q}+|\delta_2|^{2q}+\mathrm{TOL}}\right)\,, \tag{6.61}$$

where $\mathrm{TOL} = 0.1\Delta x^q$ and $q = 1.4$. Once that a is determined from (6.61), b, c and d are obtained from (6.60), (6.58) and (6.59), respectively. For the purposes of the third-order CCSL-CS, the first and second derivatives of the reconstruction (6.54) are needed,

$$r_0'(x) = \phi_0'(x) = -\frac{c\,\Delta x/a}{(x-x_0)-\dfrac{\Delta x}{2}\left(\dfrac{2}{a}-1\right)} - \frac{d\,\Delta x/b}{(x-x_0)-\dfrac{\Delta x}{2}\left(\dfrac{2}{b}-1\right)}\,, \tag{6.62a}$$

$$r_0''(x) = \phi_0''(x) = \frac{c\,\Delta x/a}{\left[(x-x_0)-\dfrac{\Delta x}{2}\left(\dfrac{2}{a}-1\right)\right]^2} + \frac{d\,\Delta x/b}{\left[(x-x_0)-\dfrac{\Delta x}{2}\left(\dfrac{2}{b}-1\right)\right]^2} \tag{6.62b}$$

which only need to be evaluated for $x = x_0$, giving the following compact formulas:

$$r_0'(x_0) = \frac{2c}{2-a} + \frac{2d}{2-b}\,, \tag{6.63a}$$

$$r_0''(x_0) = -\frac{1}{\Delta x}\left[\frac{4ac}{(2-a)^2} + \frac{4bd}{(2-b)^2}\right]\,. \tag{6.63b}$$

The most demanding part of the algorithm is the evaluation of the coefficient a by means of (6.61), since it requires the exponentiation of $|\delta_1|$ and $|\delta_1|$ by the real power q, operation which is usually much slower than taking the natural logarithm or exponential. The number of exponentiations can be reduced to one if the *smoothness parameter* θ is used,

$$\theta_0 = \frac{\Delta x \min(|\delta_1|,|\delta_2|)+\mathrm{TOL}}{\Delta x \max(|\delta_1|,|\delta_2|)+\mathrm{TOL}} \tag{6.64}$$

where TOL is in this case a small number that depends on the machine precision ϵ. In the numerical simulations run for this thesis, $\mathrm{TOL} = \epsilon^{3/4}$. The expression for a can be reformulated as a function of θ_0 alone,

$$a\left(\theta_0\right) = \left(1 - \mathrm{TOL}\right)\left(1 + \mathrm{TOL} - \frac{2\left(\theta_0\right)^q}{1 + \left(\theta_0\right)^{2q}}\right), \tag{6.65}$$

so that only one exponentiation to real power is required. In the kinetic code for neutrals, considerable speedup is obtained by creating a look-up table for $a\left(\theta_0\right)$ in preprocessing.

6.3.6 1D and 2D numerical tests

The Modified Equation Analysis that was carried out in the preceding sections was based exclusively on the Local Truncation Error (LTE), which is the difference between the model equation and the modified equation of the scheme. Accordingly, a scheme is labeled as ‘first order’ or ‘third order’ depending on the form of the LTE. This can be misleading, because it is important to approximate to high order not just the model equation, but the solution itself. In fact, the Modified Equation that is solved by the numerical scheme is a *singular perturbation* to the model equation, and as such it may lead to ‘spurious’ features that were not present before. Whether or not such features are triggered depends mainly on the initial density profile and on the boundary conditions.

Following from the above considerations, the primary purpose of this section is to assess the Global Error (GE) of the scheme, which is the actual difference between the *exact solution* and the *approximated solution*. The GE is quantified a-posteriori in the L_∞, L_2 or L_1 norm, depending on what is more appropriate, and convergence analyses are performed by successively decreasing the mesh size. A limited number of test-cases are considered, both in 1D and 2D.

1D advection equation As the simplest test case, the third order CCSL-CS is applied to the solution of the equation

$$n_t + u\, n_x = 0\,, \tag{6.66}$$

where the velocity u is uniform in space and constant in time. The solution $n\left(x,t\right) > 0$ is sought over the domain $\left(x,t\right) \in \left[0,L\right] \times \left[0,T\right]$ with periodic boundary conditions in space $n\left(0,t\right) \equiv n\left(L,t\right)$, and initial conditions $n\left(x,0\right) = n_0\left(x\right)$. As a consequence, $n\left(x,t\right) \equiv n\left(x - kL, t\right)$, with $k \in \mathbb{Q}$, and the analytic solution to (6.66) is $n\left(x,t\right) = n_0\left(x - ut\right)$.

For the sake of generality, the independent variables are normalized with respect to L and T, introducing $\xi = x/L$ and $\tau = t/T$. Moreover, the simulation time is chosen to be $T = L/u$ so that the final solution coincides with the initial conditions: $n(x, T) = n_0(x - L) = n_0(x)$. Under these assumptions, the normalized equation

$$n_\tau + n_\xi = 0 \tag{6.67}$$

will be numerically solved on the domain $(\xi, \tau) \in [0,1] \times [0,1]$. The analytic solution to (6.67) is $n(\xi, \tau) = n_0(\xi - \tau)$.

The application of the third order CCSL-CS to (6.67) comes from the usual CS remapping rule, which is used after moving the cell a distance $U\Delta\xi$, where $U = U_0 + U_1 + U_2$. With the new variables, now $U_0 = u\Delta t/\Delta x = \Delta\tau/\Delta\xi$, and it will be imposed here that $|U_0| < 1$. The first and second order corrections in the case of uniform and constant (but not necessarily positive) U_0 are:

$$U_1 = \frac{\Delta\xi}{2}\left(|U_0| - U_0^2\right)\frac{n_\xi}{n} \tag{6.68a}$$

$$U_2 = \frac{\Delta\xi^2}{12}\left(U_0 - 3|U_0|U_0 + 2U_0^3\right)\frac{n_{\xi\xi}}{n} \tag{6.68b}$$

which will be approximated using the finite difference expressions

$$\left.\frac{1}{n}\frac{\partial n}{\partial \xi}\right|_{\xi=\xi_i} = \left.\frac{\partial\left(\log n\right)}{\partial\xi}\right|_{\xi=\xi_i} = \frac{1}{\Delta\xi}\log\left(\frac{n_{i+1}}{n_{i-1}}\right) + O\left(\Delta\xi^2\right) \tag{6.69a}$$

$$\left.\frac{1}{n}\frac{\partial^2 n}{\partial \xi^2}\right|_{\xi=\xi_i} = \frac{4}{\Delta\xi^2}\,\frac{n_{i+1} - 2n_i + n_{i-1}}{n_{i+1} + 2n_i + n_{i-1}} + O\left(\Delta\xi^2\right) \tag{6.69b}$$

but different choices can be made, as long as a second order approximation is used for (6.69a) and a first order approximation is used for (6.69b).

As a first test case, a Gaussian profile centered at $\xi = 0.5$ is given as initial condition,

$$n(\xi, 0) = 0.1 + \exp\left(-\frac{\xi - 0.5}{0.1}\right)^2 \tag{6.70}$$

and then evolved in time for $\tau \in [0,1]$. A Courant parameter $U_0 = 0.3$ is chosen. The final solution obtained with the third order CCSL-CS is compared qualitatively with the original first order version in Fig. 6.1, for different numbers N of subdivisions in space ($\Delta\xi = 1/N$). The L_2 and L_∞ norms of the error for the third order scheme are also computed by doubling the number of subdivisions up to 3200 cells. The results are summarized by Fig. 6.2, which confirms that the error of the scheme decreases as $(\Delta\xi)^3$ in both the norms; it is most noticeable that the asymptotic convergence behavior of the scheme is reached very soon, starting from $N \approx 30$.

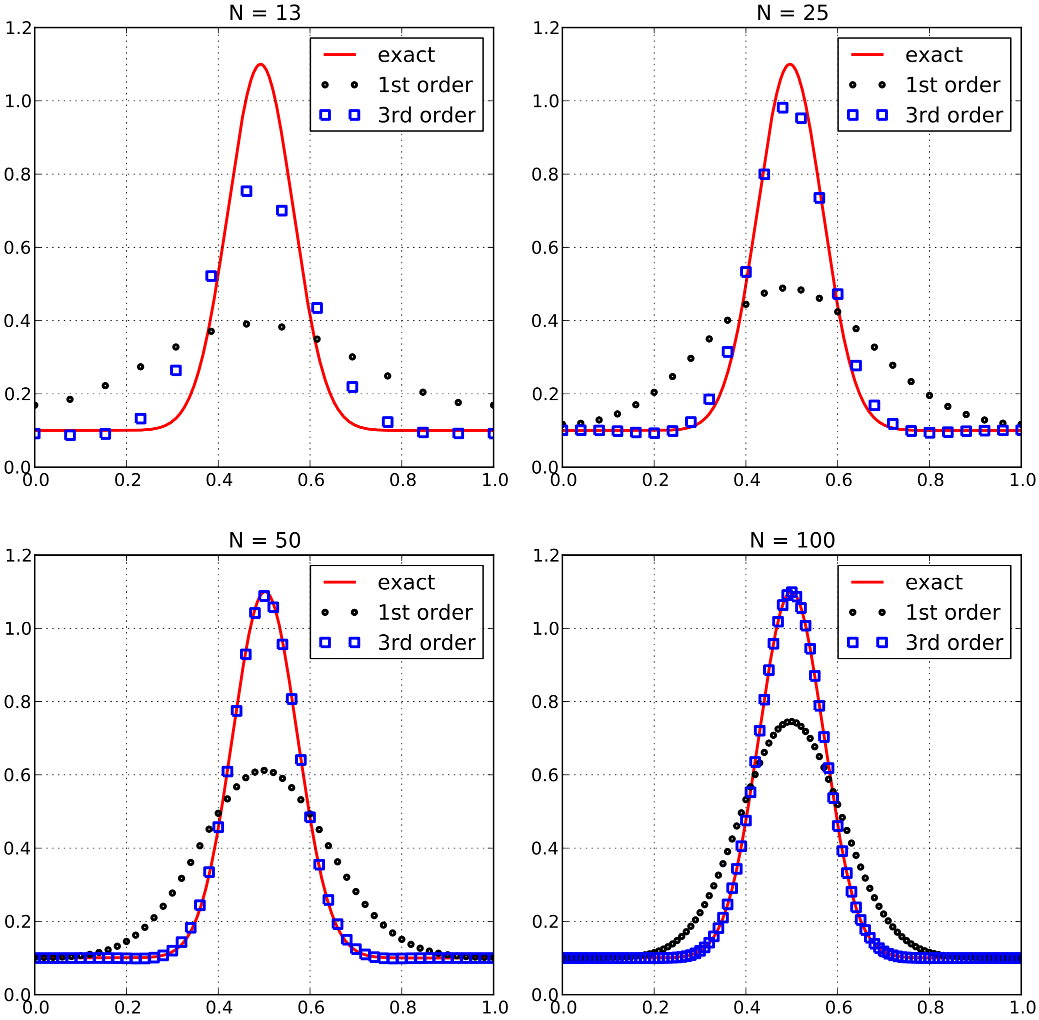

Figure 6.1: 1D advection with Gaussian initial profile: final solution at time $\tau = 1.0$ for increasing number of spatial subdivisions.

As a second test case, a rectangular profile is given as initial condition:

$$n(\xi,0) = \begin{cases} 1.1 & \text{if } 0.25 < \xi < 0.75, \\ 0.1 & \text{otherwise.} \end{cases} \tag{6.71}$$

As before, $\tau \in [0,1]$ and $U_0 = 0.3$, and a series of identical simulations is performed using

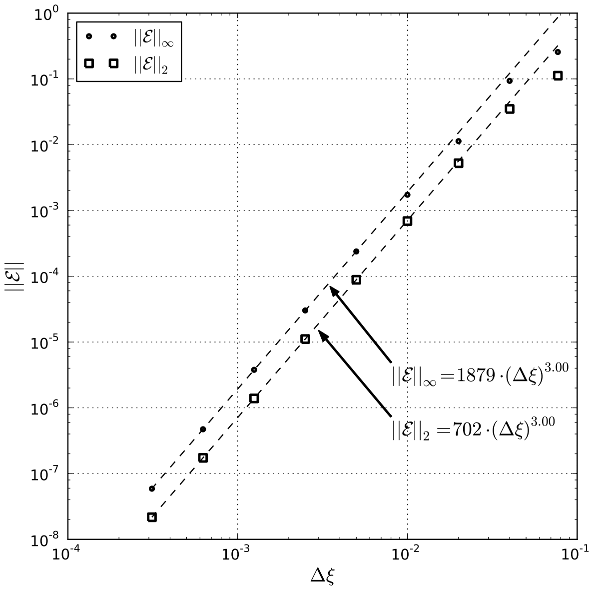

Figure 6.2: Convergence analysis for 1D advection with Gaussian initial profile.

an increasingly fine mesh. Since the initial density profile is not ‘smooth’, the 3^{rd} order CCSL-CS undergoes non-physical oscillations in the regions close to the discontinuities. This effect does not compromise the positive-definiteness of the scheme, which is inherited from the CS remapping rule, but it considerably deteriorates the solution. Hence, the non-oscillatory option described in Section 6.3.5 is implemented here, and Fig. 6.3 gives a qualitative picture of the improvement upon the standard 1^{st} order scheme. As is common practice in the case of discontinuous solutions, a convergence analysis based on the L_1 norm of the error is presented in Fig. 6.4: as expected, both schemes exhibit sub-linear convergence [75].

The GE of the (nominally) 1^{st} order scheme goes as $(\Delta\xi)^{0.5}$, a result obtained a-priori in [76] (pg. 121). The GE of the (nominally) 3^{rd} order scheme is proportional to $(\Delta\xi)^{0.8}$, which is slightly better than the expected $(\Delta\xi)^{0.75}$ for the non-limited case: in fact, in [75] the order of convergence for unlimited stable schemes is established as $(\Delta\xi)^{p/(p+1)}$ where p is the order of the approximation for smooth flows.

2D continuity equation with rotating velocity field As a test case with non-uniform velocity, the continuity equation is solved on a square domain with a given rotating velocity

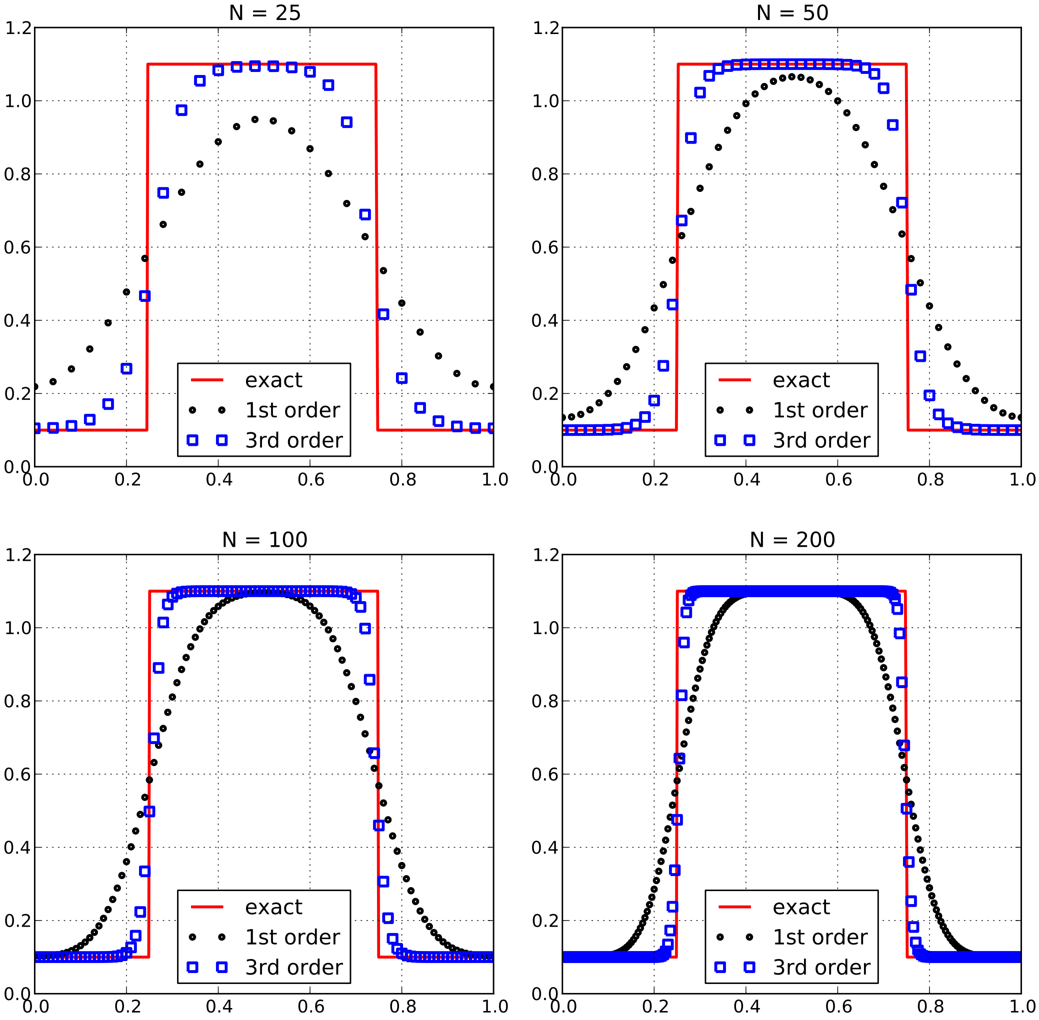

Figure 6.3: 1D advection with rectangular initial profile: final solution at time $\tau = 1.0$ for increasing number of spatial subdivisions.

field. The equation to be solved is:

$$\partial_t n + \partial_x (u\, n) + \partial_y (v\, n) = 0 \tag{6.72}$$

on the square domain $(x, y) \in [0, L] \times [0, L]$ and in the time interval $t \in [0, T]$. The two components of the velocity vector are

$$u = -\omega \left(y - L/2\right) \tag{6.73a}$$

$$v = +\omega \left(x - L/2\right) \,, \tag{6.73b}$$

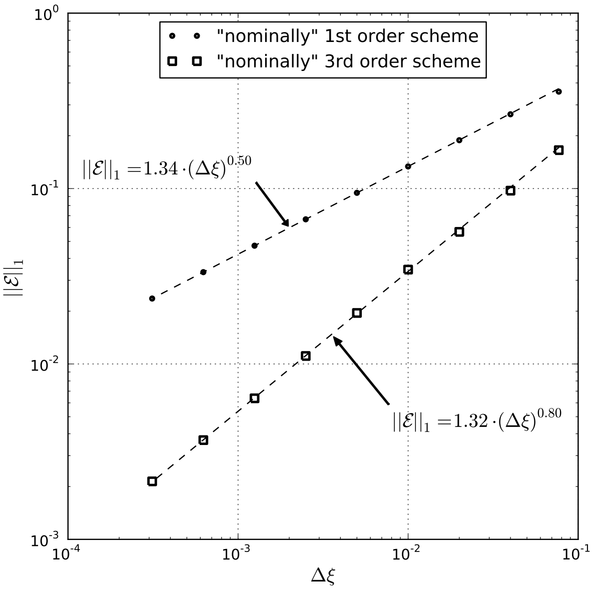

Figure 6.4: Convergence analysis for 1D advection with rectangular initial profile.

where $\omega = 2\pi/T$ [rad/s] is the angular frequency of the rotating field. After normalization of the spatial and temporal variables with respect to L and T, one gets:

$$\partial_\tau n + \partial_\xi \left(\overline{u}\, n\right) + \partial_\eta \left(\overline{v}\, n\right) = 0 \tag{6.74}$$

where $\left(\xi, \eta\right) \in [0,1] \times [0,1]$, $\tau \in [0,1]$, and the normalized velocities were introduced:

$$\overline{u} = u\,T/L = -2\pi \left(\eta - 0.5\right) \tag{6.75a}$$

$$\overline{v} = v\,T/L = +2\pi \left(\xi - 0.5\right)\ . \tag{6.75b}$$

The application of the second order CCSL-CS to (6.74) comes from the usual CS remapping rule, which is used after moving the cell a distance $\Delta\mathbf{r} = \left[U\Delta\xi, V\Delta\eta\right]$, where $U = U_0 + U_1$ and $V = V_0 + V_1$. With the new variables, now $U_0 = u\,\Delta t/\Delta x = \overline{u}\,\Delta\tau/\Delta\xi$ and $V_0 = v\,\Delta t/\Delta y = \overline{v}\,\Delta\tau/\Delta\eta$. The same number of subdivisions is employed along both the x and y axes, so that $\Delta\eta = \Delta\xi$. The corrections U_1 and V_1 are evaluated using second order finite difference approximations to (6.48):

$$(U_1)_{i,j} = \frac{1}{2}\left[\operatorname{sign}(U_0)_{i,j} - (U_0)_{i,j}\right]\frac{(n\,U_0)_{i+1,j} - (n\,U_0)_{i-1,j}}{n_{i+1,j} + n_{i-1,j}} + \frac{1}{4}(V_0)_{i,j}\left[(U_0)_{i,j+1} - (U_0)_{i,j-1}\right] \tag{6.76a}$$

$$(V_1)_{i,j} = \frac{1}{2}\left[\operatorname{sign}(V_0)_{i,j} - (V_0)_{i,j}\right]\frac{(n\,V_0)_{i,j+1} - (n\,V_0)_{i,j-1}}{n_{i,j+1} + n_{i,j-1}} + \frac{1}{4}(U_0)_{i,j}\left[(V_0)_{i+1,j} - (V_0)_{i-1,j}\right] \tag{6.76b}$$

The maximum Courant parameter in the domain is fixed at 0.8, i.e. $|U_0|_{\max} = \left|\overline{u}_{\max}\Delta\tau/\Delta\xi\right| = 0.8$, and $|V_0|_{\max} = \left|\overline{v}_{\max}\Delta\tau/\Delta\eta\right| = 0.8$. According to (6.75), the time step is also fixed:

$$\Delta\tau = \frac{0.8}{\pi}\Delta\xi\ . \tag{6.77}$$

The system is evolved for a time $\tau \in [0, 0.25]$, which means that the bell performs one quarter ($\pi/2$) of a full rotation (2π), during the whole simulation. A ‘compressed’ Gaussian bell profile is given as initial condition:

$$n\left(\xi,\eta,0\right) = \begin{cases} \exp\left[-\tan^2\left(\frac{\pi}{2}\frac{r}{R}\right)\right] & \text{if } r < R \\ 0 & \text{otherwise} \end{cases} \tag{6.78}$$

where $r = \sqrt{(\xi-\xi_c)^2 + \left(\eta-\eta_c\right)^2}$ is the distance from the center $\left(\xi_c, \eta_c\right)$ of the bell, and R is the ‘radius’ of the bell. The density profile given by (6.78) is preferable over the more common cosine bell because it is ∞-many times differentiable over the whole domain, and it is thus a perfectly ‘smooth’ function suitable for convergence analysis. In the following simulations, the center is chosen at the point $\left(\xi_c, \eta_c\right) = (0.5, 0.75)$, and a radius $R = 0.2$ is used. The results are shown in Figure 6.5, where it appears difficult to determine an asymptotic order of convergence; nevertheless, the use of the 2^{nd} order scheme considerably improves the solution upon the original 1^{st} order method.

6.4 Computational Domain

The computational domain is subdivided into a ‘physical domain’, where the velocity distribution function of the neutral gas is calculated on a phase-space mesh and evolved at each time-step, and a ‘ghost region’ that lies beyond the boundaries and is used for implementing the various types of boundary conditions.

The phase-space mesh is obtained as the Cartesian product of the spatial mesh (Sec. 6.4.1) and the velocity mesh (Sec. 6.4.2).

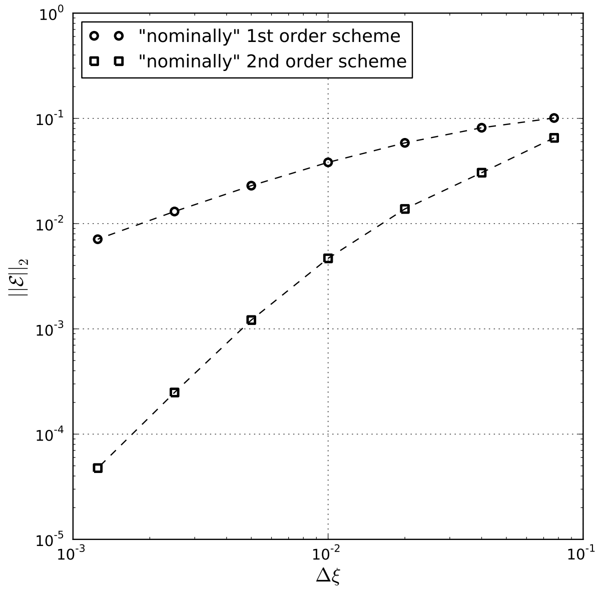

Figure 6.5: Convergence analysis for 2D advection with rotating velocity field. A 'compressed' Gaussian bell is given as the initial density profile. The L2 norm of the error at the end of the simulation ($\tau = 0.25$) is shown for an increasing number of subdivisions in x and y.

6.4.1 Spatial Mesh

The geometry under consideration is simply a cylinder open to vacuum on one end and with a small circular hole (the injector) on the other end, which is otherwise closed.

A uniform Cartesian mesh is employed in space, with the z axis aligned with the cylinder axis of symmetry; the mesh spacing is $\Delta x \equiv \Delta y \neq \Delta z$. The curved boundaries are approximated with a staircase approach, which is believed to give satisfactory results due to the integral formulation of the BCs (see Section 6.6).

6.4.2 Velocity Mesh

The velocity mesh is the Cartesian product of a uniform mesh in speed and a mesh in the solid angle; accordingly, the velocity grid is a double-indexed list of discrete velocity vectors, $\mathbf{v}_{ij} = \hat{\mathbf{n}}_i\, v_j$, where i is the index labeling directions, and j is the index labeling speeds.

The unit vectors $\hat{\mathbf{n}}_i$ must be chosen carefully in order to maximize the uniformity of their angular spacing; in order to accomplish this, the surface of a unit sphere is first subdi-

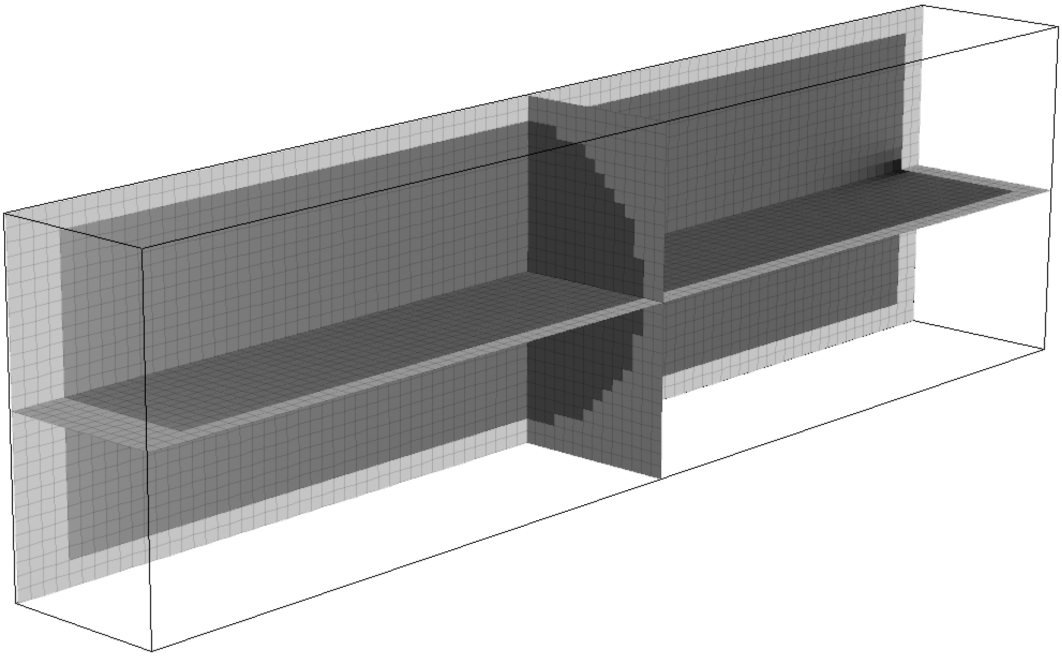

Figure 6.6: Three-slice projection showing the salient features of the spatial mesh used in the 3D-3V kinetic model for neutrals: a uniform Cartesian grid is employed, the computational domain is surrounded by a ghost region, and the curved surface is approximated with a 'staircase' approach. The open end of the cylinder is on the left, the closed end (with the injector) is on the right.

vided into 20 identical triangles (spherical icosahedron), then each triangle is refined into 4 smaller triangles by connecting the midpoints of their sides by great circles. This refinement is repeated recursively, until the required angular resolution is obtained: each vertex on the unit sphere identifies a unit vector $\hat{\mathbf{n}}_i$, with a solid angle $\Delta\Omega_i$ associated with it (Fig. 6.7).

The calculation of $\Delta\Omega_i$ requires the creation of the dual mesh of the given triangular mesh: such a dual mesh is composed of hexagons, plus 20 pentagons, and the areas of those spherical polygons numerically coincide with the solid angles required (Fig. 6.7d).

The speed axis v is discretized in concentric spherical shells of uniform thickness Δv_j, and we let v_j be the center radius of the shell. The volume of the cell (i, j) in velocity space [$\mathrm{m}^3\mathrm{s}^{-3}$] can be evaluated as

$$V_{ij} = \frac{\Delta\Omega_i}{4\pi}\left[\frac{4\pi}{3}\left(v_j+\frac{\Delta v_j}{2}\right)^3-\frac{4\pi}{3}\left(v_j-\frac{\Delta v_j}{2}\right)^3\right] = \Delta\Omega_i\,\Delta v_j\left(v_j^2+\frac{\Delta v_j^2}{12}\right). \tag{6.79}$$

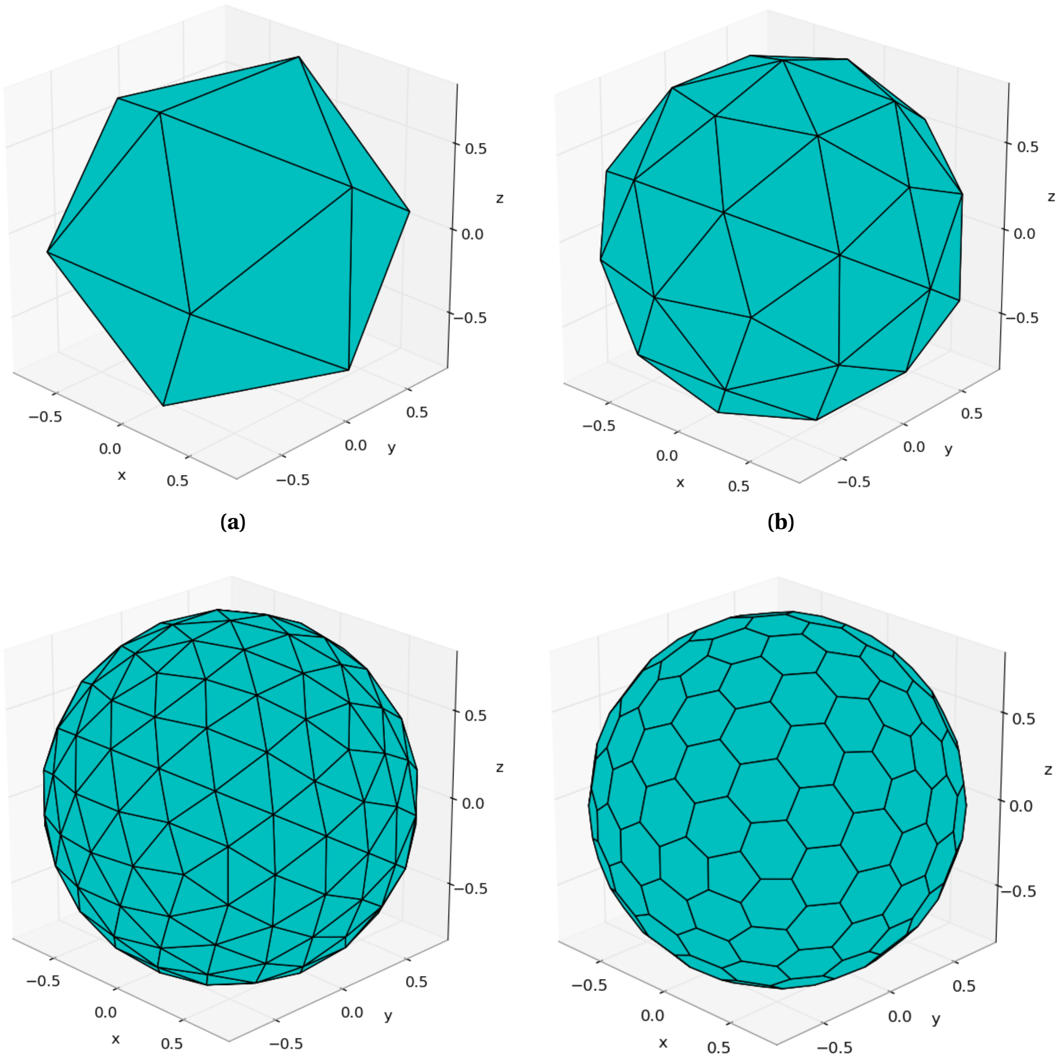

(a) (b) (c) (d)

Figure 6.7: Procedure for the construction of the angular mesh. Each face of the icosahedron (a) is subdivided into 4 triangles by connecting the midpoints of each arc, to obtain a refined mesh (b); the procedure is repeated to the required level of refinement, where the coordinates of the vertices of the spherical polyhedron (c) identify the unit vectors $\hat{\mathbf{n}}_i$; the corresponding solid angles $\Delta\Omega_i$ coincide with the areas of the spherical polygons obtained from the dual mesh (d).

6.5 Collision Operator

In an ‘operator split’ environment, the Collision Operator evolves the distribution function for one time-step Δt according to (6.5a). The effect of the Boltzmann Collision Integral on the R.H.S. is approximated using an integral formulation of the Bhatnagar-Gross-Krook (BGK) model [77], which is implemented in two steps, both local in space:

1. the number of particles that scatter out of each phase-space cell during the time-step Δt, due to collisions against the background gas, is:

   $$\Delta N_{\text{out}} = N_0 \left[1 - \exp\left(-\nu \, \Delta t\right)\right] \,, \tag{6.80}$$

   where N_0 is the number of particles inside the phase-space cell at the beginning of the time-step, and $\nu\left(\mathbf{v}_c\right)$ is the total collision frequency;

2. all the particles that have undergone a collision in the same spatial cell are put into a drift-Maxwellian distribution $\mathscr{M}\left(\mathbf{v}\right)$, which gives the number of particles that scatter into each phase-space cell:

   $$\Delta N_{\text{in}} = \mathscr{M}\left(\mathbf{v}_c\right) \cdot V_c \,, \tag{6.81}$$

   where V_c is the volume of the cell in phase-space $[m^6 s^{-3}]$.

Both the aforementioned steps give rise to numerical problems. As a first issue, the formula for $\nu\left(\mathbf{v}_c\right)$ is a three-dimensional integral over velocity-space:

$$\nu\left(\mathbf{v}_c\right) = \int_{\mathbb{R}^3} \|\mathbf{v}_c - \mathbf{v}\| \, \sigma\left(\|\mathbf{v}_c - \mathbf{v}\|\right) \, f\left(\mathbf{v}\right) \, d^3\mathbf{v} \,, \tag{6.82}$$

where $\sigma\left(\|\mathbf{v}_c - \mathbf{v}\|\right)$ is the cross-section $[m^2]$ for elastic collisions between like particles. In the context of the BGK approximation, (6.82) is a waste of computational effort. In order to approximate the integral on the RHS, an average value $\langle\sigma\rangle$ is used (justified because the cross section for elastic collisions of non-excited Ar does not change appreciably in the range of velocities of interest). Moreover, the real distribution $f\left(\mathbf{v}\right)$ is approximated by a suitable analytic distribution function $f^*\left(\mathbf{v}\right)$:

$$f\left(\mathbf{v}\right) \approx f^*\left(\mathbf{v}\right) = \frac{n}{4\pi \, v_T^2} \, \delta_D\big(\|\mathbf{v} - \mathbf{u}\| - v_T\big) \,, \tag{6.83}$$

where n, $\mathbf{u}$ and v_T are the density, mean velocity and thermal velocity of the original $f\left(\mathbf{v}\right)$, respectively, and δ_D is the Dirac delta function. Substituting (6.83) into (6.82), introducing the random velocity $\mathbf{v}' = \mathbf{v} - \mathbf{u}$, and using the identity $d^3\mathbf{v}' = (v')^2 d\Omega \, dv'$, one gets:

$$\nu\left(\mathbf{v}_c\right) \approx \frac{n\,\langle\sigma\rangle}{4\pi} \oint_{\mathbb{S}} \sqrt{(v_c')^2 + v_T^2 - 2\, v_c' \, v_T \cos\theta \; d\Omega} \,, \tag{6.84}$$

which is solvable using $d\Omega = \cos\theta \, d\theta \, d\phi$. Consistently with the approximations already introduced, (6.84) can be further simplified by neglecting the $\cos\theta$ dependence inside the square root, leading to a very easily manageable formula for the total collision frequency:

$$\nu(\mathbf{v}_c) \approx n \langle\sigma\rangle \sqrt{(v_0')^2 + v_T^2}\,. \tag{6.85}$$

A second issue is that (6.81) does not ensure mass, momentum and energy conservation on a finite grid: to satisfy such a requirement, one should compute *exactly*

$$\Delta N_{\text{in}} = \int_c \mathcal{M}(\mathbf{v})\, d^3\mathbf{x}\, d^3\mathbf{v} = \langle\mathcal{M}\rangle_c V_c \neq \mathcal{M}(\mathbf{v}_c)\, V_c\,, \tag{6.86}$$

but this is extremely difficult, due to the complicated shape of the domain in velocity space. As an efficient alternative to computing the exact integral of the exact Nominal Maxwellian (NM) distribution function $\mathcal{M}(\mathbf{v})$, one can still use (6.81), but substituting the NM with a Discrete Conservation-Corrected Maxwellian (DCCM), $\mathcal{M}^*(\mathbf{v})$. The DCCM is constructed by applying small corrections to the NM that ensure explicitly all the aforementioned conservation rules on the grid. Among other possible choices, we write $\Delta f(\mathbf{v})$ as a first-order correction to the original Maxwellian: each value of the sampled Nominal Maxwellian is written as a function of the parameters to be conserved,

$$f_\alpha\left(n, \mathbf{u}, \varepsilon'\right) = n\left(\frac{3}{4\pi\varepsilon'}\right)^{\frac{3}{2}} \exp\left[-\frac{\|\mathbf{v}_\alpha - \mathbf{u}\|^2}{4\varepsilon'/3}\right]\,, \tag{6.87}$$

and Δf_α is the first order term of the Taylor series of f_α,

$$\Delta f_\alpha = \frac{\partial f_\alpha}{\partial n}\Delta n + \frac{\partial f_\alpha}{\partial u_x}\Delta u_x + \frac{\partial f_\alpha}{\partial u_y}\Delta u_y + \frac{\partial f_\alpha}{\partial u_z}\Delta u_z + \frac{\partial f_\alpha}{\partial \varepsilon'}\Delta\varepsilon'\,. \tag{6.88}$$

What we have obtained is a 5-term expansion in the basis functions $\frac{\partial f_\alpha}{\partial(\cdot)}$, with unknown coefficients $[\Delta n, \Delta u_x, \Delta u_y, \Delta u_z, \Delta\varepsilon']$. These 5 coefficients are uniquely determined by requiring the combination of all the Δf_α s to satisfy the 5 scalar conservation equations.

6.6 Boundary Conditions

For a semi-Lagrangian scheme such as the Convected Scheme, boundary conditions (BCs) are applied to the *characteristics* that come off the wall, and no modification is made due to the wall on the characteristics that go towards the wall. As a consequence, BCs must be handled in a way that satisfies causality, and this is a considerable advantage when compared to Eulerian schemes. On the other hand, the outgoing characteristics must be correlated with the incoming characteristics, explicitly for each case, and this may be a non-trivial problem where quantities like mass or energy are to be exactly conserved.

6.6.1 Periodic Planes

The use of periodic planes enables the simulation of an axially-symmetric geometry using only half (or one quarter) of the computational domain. Implementing periodic planes is straightforward: when a part of a MC crosses the plane, its position and velocity are transformed by a rotation about the symmetry axis. Issues concerning this procedure take place wherever the transformed velocity does not coincide with one of the discrete values of the velocity mesh: in such cases, it is necessary to remap the velocity vector onto two or more vectors, and this fact introduces numerical diffusion in velocity space (although only in direction, and not in energy). Another possible side-effect is the late-time creation of non-physical density bumps in the region close to the axis, which take place essentially because of the asymmetries in the particle fluxes. The angular mesh used in the current version of the code is symmetric with respect to each of the three principal planes, and this property permits one to simulate only one half of the cylinder without incurring the above drawbacks.

6.6.2 Diffusely reflecting adiabatic walls

Since in the CS no random numbers are generated, diffuse adiabatic reflection is implemented in an *integral* fashion, which permits us to model any geometry of the wall (a staircase approach is used here) by using a thick layer of ghost-cells:

1. the MCs coming from the domain pass seamlessly through the boundary wall, and they remap onto the ghost-cells by applying the same *volume-rule* that is used inside the domain;

2. the ghost-cells gather the incoming particles on an energy basis, so that the information about the angular direction is lost, but mass and kinetic energy can be exactly conserved;

3. for every ghost cell and for each speed, a list of the spatial cells in the domain which are ‘visible’ from that cell is constructed. Equal densities are launched into equal solid angles, for those cells in the list. This rule guarantees that an initially uniform isotropic distribution retains those properties after bouncing off the wall.

For any finite mesh-size, the implementation above guarantees that mass and total kinetic energy of the colliding particles are exactly conserved, while their average parallel momentum is transferred to the wall. Moreover, such an algorithm isotropizes the distribution function without introducing any diffusion in energy space, and it has the overall effect of converting directional kinetic energy into random kinetic energy: as a consequence of the friction against the wall (no-slip condition), the temperature of the gas locally increases in an irreversible thermodynamic process.

6.6.3 Injector

This section treats the issues related to the modeling of an injector in a kinetic simulation, with a particular focus on the realization of the nominal mass and energy fluxes going into the system (at least, as far as roundoff errors permit in a finite precision calculation). In a semi-Lagrangian framework, a satisfactory implementation of this kind of boundary condition needs particular care; henceforth a discussion on the problem is given, and an elegant and versatile solution is developed thereafter.

There is no unique way to model an injector. Here the injector is modeled as a device capable of imposing the *flux* of the particles across the inlet section, which is a portion of the 2D boundary surface. According to this point of view, in a fluid simulation the injector would impose the fluxes of mass, momentum and energy. In the kinetic simulation at hand, instead, the injector imposes the *flux function* $\Gamma(\mathbf{x},\mathbf{v})$, which is defined as

$$\Gamma(\mathbf{x},\mathbf{v}) = f(\mathbf{x},\mathbf{v})\,(\mathbf{v}\cdot\mathbf{k}) \ , \tag{6.89}$$

where $\mathbf{k}$ is the unit vector normal to the surface, and $\mathbf{x}$ must lay on the surface itself. It should be noticed that the flux function $\Gamma(\mathbf{x},\mathbf{v})$ is signed, according to the *normal velocity* $\mathbf{v}\cdot\mathbf{k} = v\cos\theta$: assuming that $\mathbf{k}$ points toward the system, $\Gamma > 0$ for particles that are flowing into the system, and $\Gamma < 0$ for particles that are going out.

The form of Eq. 6.89 suggests that the required flux function can be obtained by imposing Dirichlet BCs on the distribution function.

Since the flow upstream of the inlet section is highly collisional, one can safely assume that local thermal equilibrium is reached; moreover, due to the low pressure in the source, the flow is assumed to be sonic at the inlet section. (A supersonic injector could also be designed, but such a case is not considered here.) Hence, the distribution function at the inlet section is a drift-Maxwellian $\mathscr{M}(\mathbf{v})$ (having density n, mean velocity $\mathbf{u}$ and temperature T evaluated a priori) in sonic flow conditions (i.e. $\|\mathbf{u}\| = \sqrt{5/3K_BT/M}$).

Unfortunately, Eq. 6.89 cannot be directly used in this regard, because $f(\mathbf{x},\mathbf{v})$ is defined at the cell centers, while $\Gamma(\mathbf{x},\mathbf{v})$ must be imposed on the cell faces. Related to this problem is the question: what happens if $f(\mathbf{x},\mathbf{v})$ is not smooth across the plane? In such a situation, the flux function will depend on the values of $f(\mathbf{v})$ on the two opposite sides of the plane, $f^-(\mathbf{v})$ and $f^+(\mathbf{v})$. Moreover, the flux function can be decomposed in two contributions of opposite sign, which depend on only one of the two values:

$$\Gamma = \Gamma\left(f^-, f^+\right) = \Gamma^+\left(f^-\right) + \Gamma^-\left(f^+\right) , \tag{6.90}$$

where the positive flux is due to particles that cross the plane in the direction of $\mathbf{k}$ (i.e. $\mathbf{v}\cdot\mathbf{k} > 0$), while the negative flux is due to particles that cross the plane in the opposite direction ($\mathbf{v}\cdot\mathbf{k} < 0$):

$$\begin{aligned} \Gamma^+(\mathbf{v}) &= f^-(\mathbf{v})\, v^+ > 0 \\ \Gamma^-(\mathbf{v}) &= f^+(\mathbf{v})\, v^- < 0 \,. \end{aligned} \tag{6.91}$$

In Eq. 6.91 the following notation was introduced:

$$v^+ = \begin{cases} \mathbf{v}\cdot\mathbf{k} & \text{if } \mathbf{v}\cdot\mathbf{k} > 0, \\ 0 & \text{otherwise.} \end{cases} \qquad v^- = \begin{cases} \mathbf{v}\cdot\mathbf{k} & \text{if } \mathbf{v}\cdot\mathbf{k} < 0, \\ 0 & \text{otherwise.} \end{cases} \tag{6.92}$$

If a numerical test-case is set up with Riemann initial conditions, (i.e. $f(\mathbf{x},\mathbf{v})$ is uniform in each of the two semi-spaces defined by the plane $\mathscr{S}$), where the discontinuity plane $\mathscr{S}$ is aligned with the cartesian mesh and does not cut through the cells, then it can be shown that after one time-step the first-order CCSL-CS will have moved the correct amount of particles through the plane, with the correct velocity. This is to say that if Riemann initial conditions are given to the first-order CCSL-CS, this will compute the *exact* flux function at the plane.

Hence, a possible solution for controlling the flux through the inlet section is to solve the corresponding Riemann problem in preprocessing, in order to construct a 'map' (to be used during the simulation), which would take into account the effect of the injector. Basically, the map would tell how many particles should be added or removed from a certain phase-space cell, at each time-step. Unfortunately, such a map should contain *absolute* values, and hence it may ask to remove, say, 10 particles from a phase-space cell that only contains 9 particles. As a consequence, this 'map' implementation of the Injector could not ensure positivity of the solution. As an aside, using the map would have another drawback: it would be much more difficult to implement a time-varying flux.

An alternative procedure was used instead, which ensures positivity and permits a greater flexibility in the time profile of the flux. The basic idea is to control only the positive flux Γ^+ while letting $\Gamma^- = 0$: the number and velocity of the particles flowing into the system through the injector are imposed explicitly, while no particle is allowed to flow upstream. This is implemented by loading the ghost cells immediately behind the inlet section uniformly with a certain distribution function, and launching the particles into the domain using the usual ballistic mover. From the point of view of the gas contained in the cylinder, the injector behaves like a wall, i.e. the back wall of the cylinder does not contain any 'holes' at all. As a result, such an injector model is also consistent with the fact that information carried by pressure waves is not supposed to travel upstream through the sonic injector.

The distribution function to be loaded in the injector (ghost) region is found by requiring that the mass and energy fluxes going into the system exactly match the fluxes from the sonic drift-Maxwellian $\mathcal{M}(\mathbf{v})$. For the mass flux, this means

$$\iiint \Gamma^{+}\left(f^{-}\right) d\mathbf{v} = \iiint \Gamma(\mathcal{M})\, d\mathbf{v}\,. \tag{6.93}$$

The integral on the RHS is

$$\oint \mathcal{M}(\mathbf{v})\, v_z\, d^3\mathbf{v} = \int_{-\infty}^{+\infty} dv_x \int_{-\infty}^{+\infty} dv_y \left[\int_{-\infty}^{0} \mathcal{M}(\mathbf{v})\, v_z\, dv_z + \int_{0}^{\infty} \mathcal{M}(\mathbf{v})\, v_z\, dv_z\right], \tag{6.94}$$

where the first integral in brackets can be rewritten by making a substitution of variable $v_z' = -v_z$. Using the basic properties of integrals one gets:

$$\begin{aligned}&\oint \mathcal{M}(\mathbf{v})\, v_z\, d^3\mathbf{v} = \\ &\int_{-\infty}^{+\infty} dv_x \int_{-\infty}^{+\infty} dv_y \int_{0}^{\infty} \left[\mathcal{M}\left(v_x, v_y, v_z\right) - \mathcal{M}\left(v_x, v_y, -v_z\right)\right] v_z\, dv_z\end{aligned} \tag{6.95}$$

and as long as the term in square brackets is > 0 (which is always the case for a drift-Maxwellian distribution having mean velocity $\mathbf{u} = u_z\hat{\mathbf{z}}$ with $u_z > 0$), the *Unilateral Maxwellian* (UM) distribution function to be loaded on the upstream side of the injector is:

$$f^{-}\left(v_x, v_y, v_z\right) = \begin{cases} \mathcal{M}\left(v_x, v_y, v_z\right) - \mathcal{M}\left(v_x, v_y, -v_z\right) & \text{if } v_z > 0, \\ 0 & \text{otherwise.} \end{cases} \tag{6.96}$$

It should be remarked that the application of the same procedure to exact matching of the energy flux would have led to the same form of $f^{-}(\mathbf{v})$ as defined in Eq. 6.96. In fact, such a distribution function ensures that the fluxes of all its even-power moments are exactly identical to the drift-Maxwellian counterparts.

As regards the odd-power moments, the Unilateral Maxwellian underestimates the exact values by less than 3% in the simulations (due to the fact that $\|\Gamma^{+}\| \gg \|\Gamma^{-}\|$ for a sonic drift-Maxwellian). Such an error is partially compensated by the reflection of the particles inside the domain: this effect gives a net positive flux for all odd-power moments.

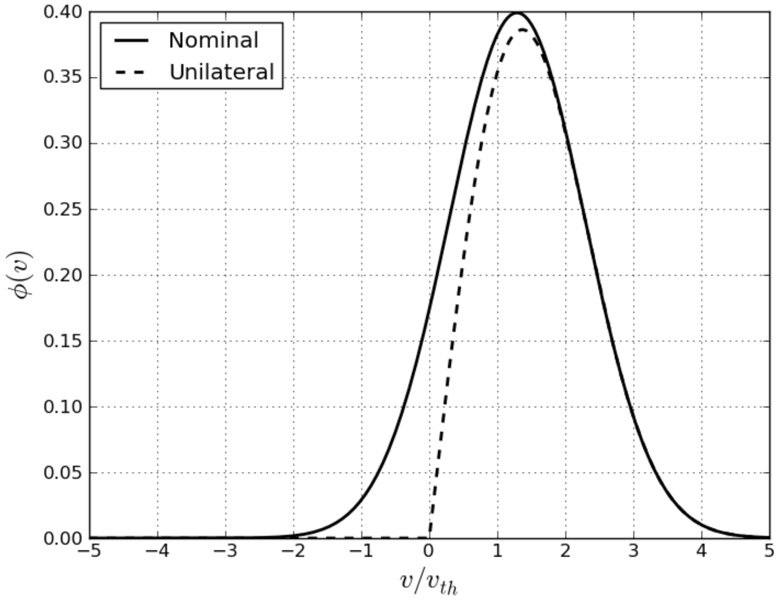

Figure 6.8: Normalized 1D distributions $\phi(v)$. Solid line: nominal sonic drift-Maxwellian. Dashed line: unilateral distribution loaded in the injector ghost region.

As explained in Section 6.5, once a Nominal Maxwellian (NM) is loaded onto the mesh, its moments over phase-space do not coincide anymore with the nominal values, because:

1. the velocity axes do not extend to $\pm\infty$,
2. particles in a phase-space cell are given the central velocity $\mathbf{v}_c$.

For this reason, a Discrete Conservation-Corrected Maxwellian (DCCM) $\mathscr{M}^*(\mathbf{v})$ should be used in place of the NM in Eq. 6.96.

It should be stressed here that, due to the uniform Cartesian spatial mesh employed in the simulations, the injector is modeled in a very simplified way, using just a few cells. A detailed analysis of the region close to the injector would require a high local resolution, using an unstructured grid as in [78], or an adaptive multi-grid approach.

6.6.4 Free Space

At the open end of the cylinder, perfect absorption is implemented: all particles that cross the exit section are simply absorbed. This approximation is believed to give quite reason-

Mach	ε_1	ε_3	ε_5	ε_7	ε_9
0.25	5.3e-01	4.0e-01	3.2e-01	2.6e-01	2.2e-01
0.50	2.2e-01	1.2e-01	7.1e-02	4.5e-02	3.0e-02
0.75	8.3e-02	3.1e-02	1.4e-02	6.9e-03	3.7e-03
1.00	2.9e-02	7.6e-03	2.6e-03	1.0e-03	4.6e-04
1.25	9.4e-03	1.8e-03	4.7e-04	1.5e-04	5.5e-05
1.50	2.9e-03	4.1e-04	8.3e-05	2.1e-05	6.6e-06

Table 6.1: Relative errors on the net fluxes of the odd-power moments of the Unilateral Maxwellian, with respect to the nominal values. The errors depend on the Mach number only; ε_1 corresponds to the error on the momentum flux. For $M = 1$ (sonic injector) the errors are smaller than 3%.

able results, based on geometrical considerations: because of the high Knudsen number, it is quite improbable that a particle leaving from the exit section will undergo a series of collisions that will direct it back into the domain.

The implementation first checks whether, at its final position, the Moving Cell (MC) is beyond the exit plane (at least partially). If so, the MC trajectory in the last time step is reconstructed in order to understand if the cell center has actually crossed the exit section (a circle) or if it has crossed the lateral wall. In the former case, the MC (or the part of it outside the cylinder) is just ‘forgot’ and no remapping is necessary; in the latter case, the MC (or a part of it) is remapped onto the ghost cells so that diffuse reflection at the wall can be applied.

6.7 Simulations

A 3D-3V kinetic simulation of neutral gas expansion is shown hereafter, as part of the hybrid simulation of a Helicon Plasma Thruster. Argon gas at ambient temperature is injected through a small injector into a slender quartz tube; on the other end, the tube is open to vacuum.

In the following test-cases no plasma is present, and only Ar-Ar hard-sphere elastic collisions are considered. Accordingly, there is no negative source term due to ionization, and hence the gas density along the axis of the cylinder decreases less steeply than it does in the nominal operational regime of the thruster. In order to test the behavior of the scheme for high Knudsen numbers ($Kn > 1$), an additional simulation with reduced injected mass-flow is run. A 3D version of the third-order CCSL-CS (see Sec. 6.3) is used as the ballistic operator of the scheme, and the results are compared to the standard first-order version.

The simulation domain is a half cylinder (cut on the meridian plane) of diameter $d = 20$ mm and length $L = 80$ mm, open on one end to vacuum (perfectly absorbing boundary), and closed on the other end by a plane wall with a small orifice (the injector) at the center. All material walls are assumed adiabatic. The spatial mesh is a uniform Cartesian grid with the z coordinate aligned along the symmetry axis of the cylinder. The cell size is $\Delta x = \Delta y = 0.833$ mm and $\Delta z = 1.000$ mm; a total of 17920 spatial cells is used. The curvature of the external wall of the cylinder is approximated with a 'staircase' approach. The velocity mesh is obtained by the independent discretization of the magnitude and the direction of the velocity vector: the speed axis $\|\mathbf{v}\|$ extends from 0 to 1200 m/s, with 15 subdivisions; the unit vector $\mathbf{v}/\|\mathbf{v}\|$ can assume 642 different directions, which are obtained by a hierarchical subdivision of the unit sphere (see Appendix for more details). Accordingly, the whole velocity space is discretized into 9630 cells. The phase-space mesh is obtained by the Cartesian product of the spatial mesh and the velocity mesh, for a total of approximately 173 million phase-space cells. Since two double-precision values of the distribution function are stored for each phase-space cell, the simulation requires about 2.6 GB of RAM.

Different kinds of boundary conditions are employed in the model, as described in Sec. 6.6: adiabatic diffuse reflection at the material walls, periodic boundary conditions at the meridian plane yz (so that only half of the cylinder is simulated), perfect absorption at the open end of the cylinder, and critical (sonic) flow at the injector (mass-flow and gas properties are imposed).

The distribution function at the inlet section is assumed to be a drifting Maxwellian. As such, its free parameters are the density n, the mean velocity $\mathbf{u}$ and the temperature T, which are uniquely determined from the total temperature $T_0 = 300$ K, mass-flow $\dot{n} = 3 \cdot 10^{18}$ part/s, section area $A = 3.33\,\mathrm{mm}^2$, and Mach number $Ma = 1$. The collision operator is based on a simplified Bhatnagar-Gross-Krook (BGK) model [77], as described in Sec. 6.5.

Figures 6.9-6.12 show the steady-state results for the simulations that use the nominal inlet mass-flow $\dot{n} = 3 \cdot 10^{18}$ part/s: due to the low values of the Knudsen number realized in the domain (see Figure 6.11), such a situation is labeled as a 'low-Kn' test case. Figures 6.13-6.16 show the steady-state results for the simulations that use a reduced inlet mass-flow $\dot{n} = 1 \cdot 10^{18}$ part/s ('high-Kn' test case, see Figure 6.15). Two different simulations are run for each test case: one uses the standard first-order ballistic operator, and the other uses the new third-order algorithm. The results are compared in each figure and, as expected, the third order algorithm gives the sharpest results.

Most noticeable are the differences in the region close to the injector, where the high density gradients enhance the effects of numerical diffusion: in both regimes most of the density drop between the injector and the exit section is concentrated just in front of the injector, and this effect is better captured by the third order algorithm (see Figures 6.9 and 6.13). As a result of the higher average density obtained in both regimes, the first-order scheme appears to overestimate the temperature by 10-20 K over the whole domain (Figures 6.10 and 6.14). Moreover, in the low-Kn regime, an annular recirculation region appears just next to the injector, and such a phenomenon is much better resolved by the third order scheme (see Figure 6.12).

In the high-Kn test case the recirculation region vanishes as expected, and the low numerical diffusion of the third order scheme makes it possible to observe the spurious 'ray-effect' due to the combination of highly divergent flow field, Dirac-delta velocity mesh, and low collisionality (bottom of Figure 6.16); such an effect can be mitigated by increasing the number of directions in the angular mesh (but memory requirements are prohibitive for such a run). In the same conditions, the standard first order algorithm gives artificially smooth results instead (top of Figure 6.16), due to the numerical diffusion.

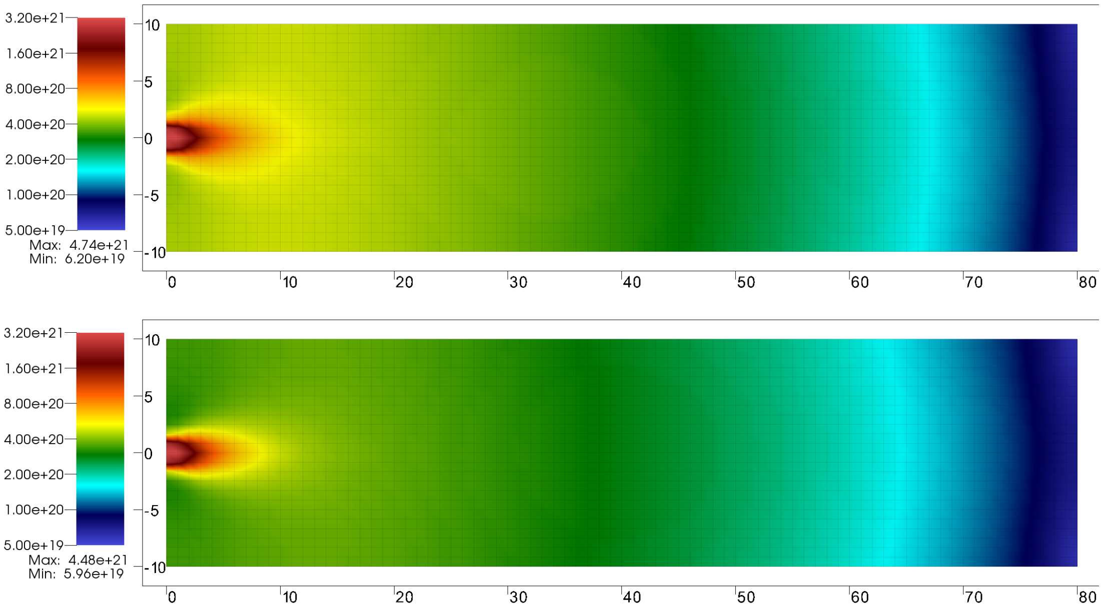

Figure 6.9: Steady state density distribution for the low-Kn test case: comparison between the 1^{st} order result (top), and the 3^{rd} order result (bottom). Axis scales are in [mm], density is in [m^{-3}].

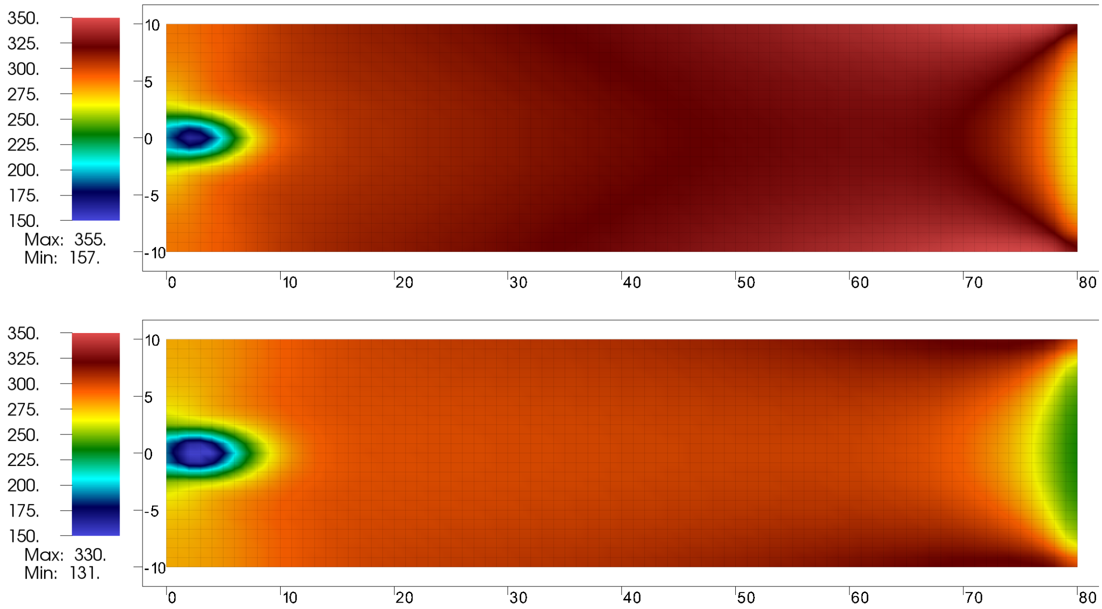

Figure 6.10: Steady state temperature distribution for the low-Kn test case: comparison between the 1^{st} order result (top), and the 3^{rd} order result (bottom). Axis scales are in [mm], temperature is in [K].

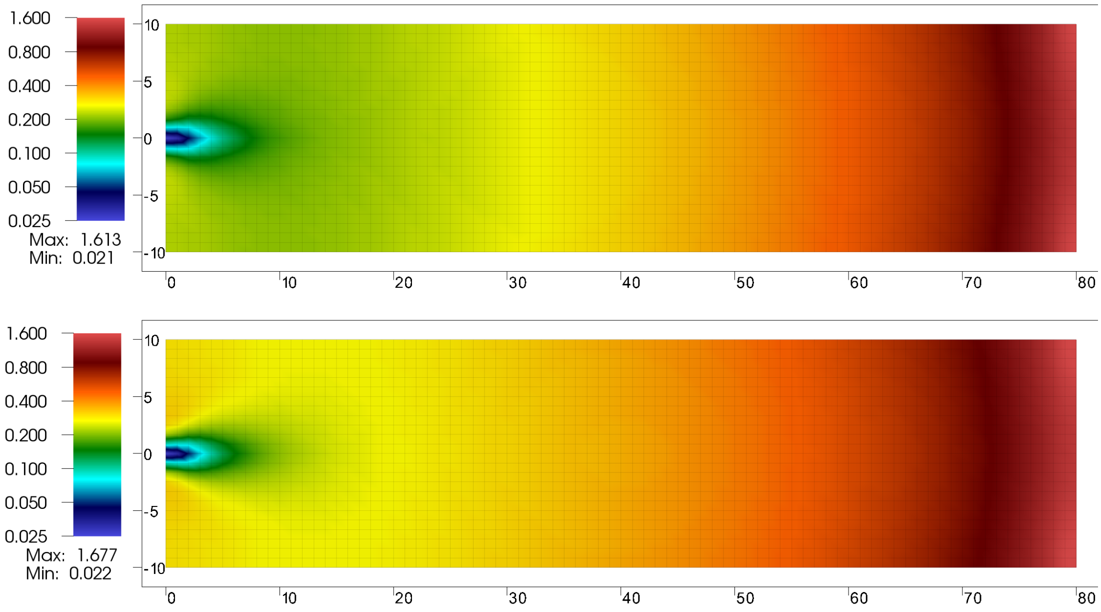

Figure 6.11: Steady state Knudsen number distribution for the low-Kn test case: comparison between the 1^{st} order result (top), and the 3^{rd} order result (bottom). Axis scales are in [mm], Kn is dimensionless.

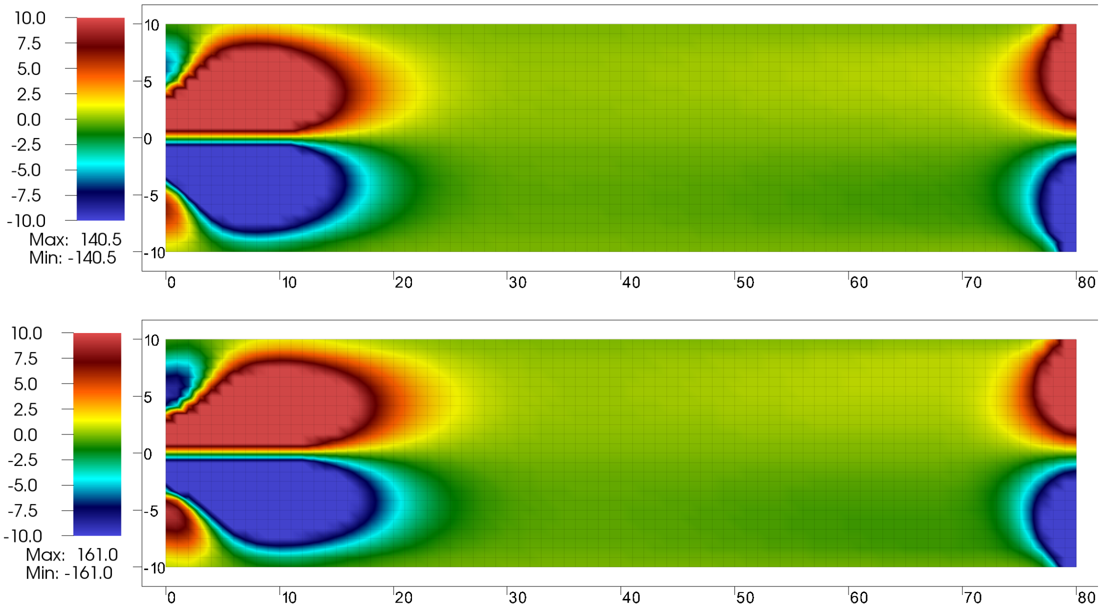

Figure 6.12: Steady state distribution of the y component of the velocity vector for the low-Kn test case: comparison between the 1^{st} order result (top), and the 3^{rd} order result (bottom). Axis scales are in [mm], velocity is in [m/s].

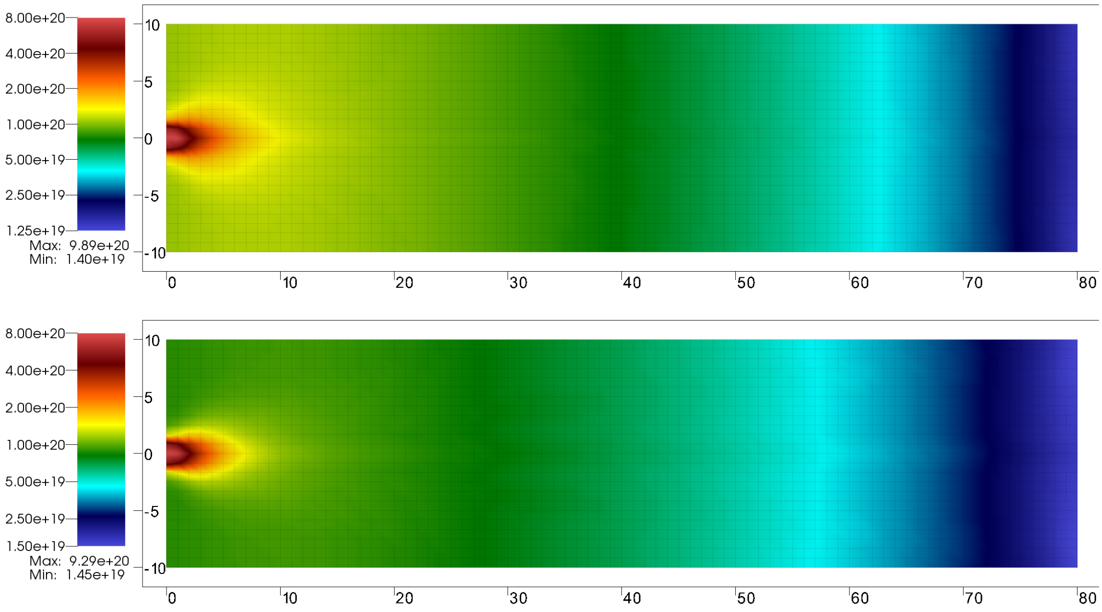

Figure 6.13: Steady state density distribution for the high-Kn test case: comparison between the 1^{st} order result (top), and the 3^{rd} order result (bottom). Axis scales are in [mm], density is in [m^{-3}].

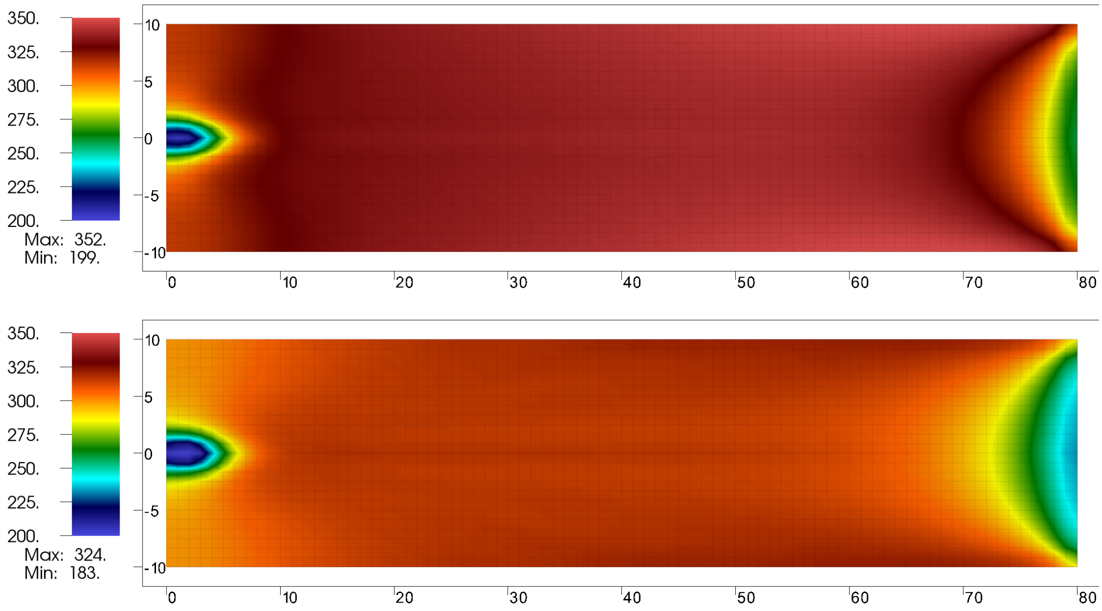

Figure 6.14: Steady state temperature distribution for the high-Kn test case: comparison between the 1^{st} order result (top), and the 3^{rd} order result (bottom). Axis scales are in [mm], temperature is in [K].

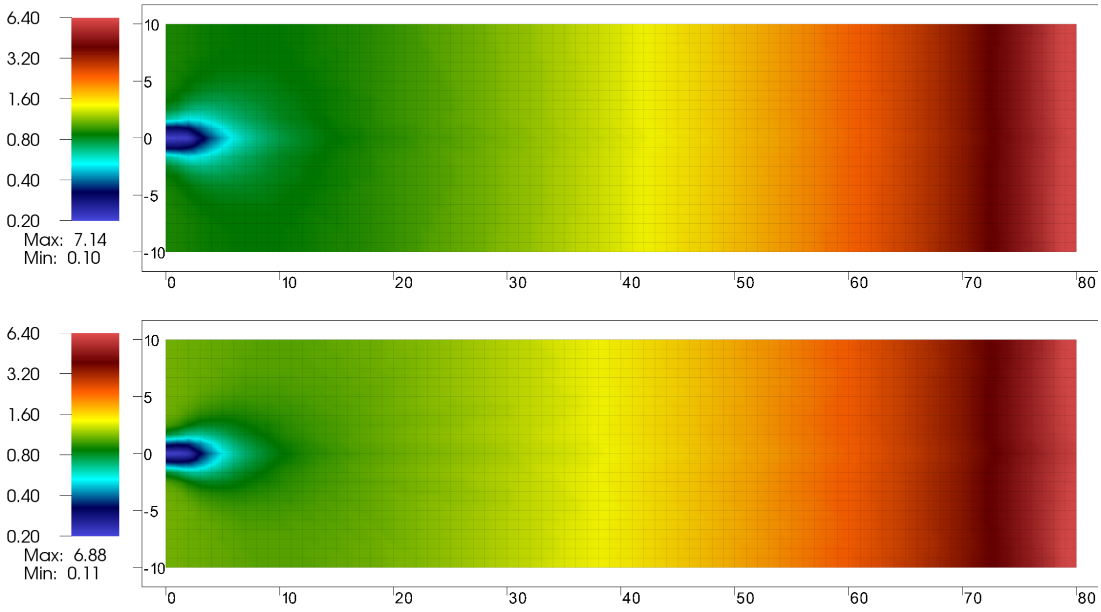

Figure 6.15: Steady state Knudsen number distribution for the high-Kn test case: comparison between the 1^{st} order result (top), and the 3^{rd} order result (bottom). Axis scales are in [mm], Kn is dimensionless.

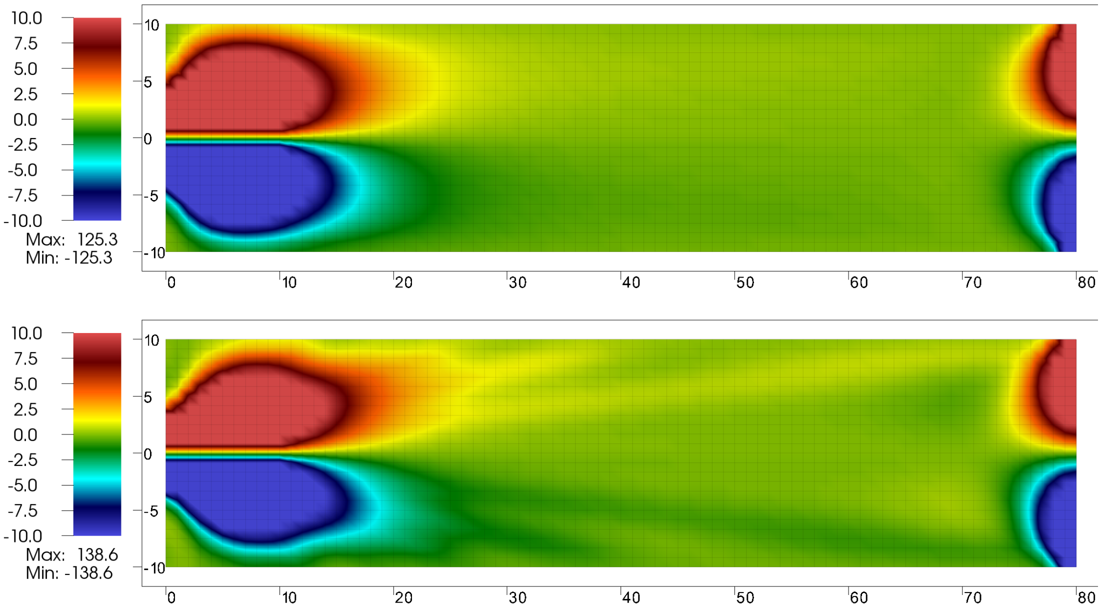

Figure 6.16: Steady state distribution of the y component of the velocity vector for the high-Kn test case: comparison between the 1^{st} order result (top), and the 3^{rd} order result (bottom). Axis scales are in [mm], velocity is in [m/s].

7

Conclusions and Outlook

7.1 Rationale

A novel hybrid approach to the simulation of a Helicon plasma source has been investigated, which is based on the use of multi-LOD (Level-Of-Detail) submodels.

In what can be defined as the ‘standard’ hybrid approach, a computational grid is defined a priori and the various submodels exchange data directly on the grid. The interfaces between the submodels are defined by the quantities that lie on the mesh, and the required spatial resolution is determined by the mesh size Δx. Most often, even for steady-state problems, the solution is sought by time-marching, and the time-step size Δt is determined by the fastest of the phenomena (usually a CFL criterion must be satisfied, so that $\Delta t \propto \Delta x$).

For the above reasons, ‘standard’ hybrid models can be very computationally demanding, unless a set of speedup strategies are applied, including subcycling, multigrid, and implicit time-stepping. While interfacing the different submodels on the same grid, such speedup procedures may introduce errors that are difficult to spot, and that may propagate and grow unpredictably, as no extensive theory exists. Accordingly, ‘standard’ hybrid models may be very difficult to build, test, and run, and this negatively affects their practical usefulness.

The multi-LOD hybrid approach aims at addressing this operative shortcoming specifically, and it is based on the idea that, whenever possible, one should avoid exchanging point-data between the submodels; instead, ‘more efficient’ interfaces should be investigated. Possibly, if each high-LOD submodel exchanged data to a reduced model (low-LOD), the low-LOD models would be easier to couple together, they would run faster, and they might permit one to easily assess a sensitivity matrix of the whole hybrid model. Broadly speaking, submodels may pass to each other a fitted curve, an analytic expression, a set of coefficients, and so on. This approach is natural, and it is believed to provide flexibility, robustness and physical insight.

The multi-LOD approach is first of all a ‘philosophy’, and a collection of quite generic guidelines; it may become a concrete methodology only through accumulated experience. This thesis work is intended to be the first step in that direction, and the simulation of a Helicon plasma source is a challenging test-bed.

7.2 Summary

According to the ideas above, a series of increasingly complicated models have been developed. Since the detailed and self-consistent simulation of the whole plasma source falls way beyond the scope of a single PhD thesis, most of the effort has been put into understanding the *coupled dynamics of electrons and neutrals*, which has not been throughly investigated yet.

In order to assess the ionization efficiency of the source, 0D and 1D analytic models of the neutral depletion process are presented. The comparison of the two models show the regimes where a higher level of detail is necessary, and the conditions under which the 1D model asymptotically recovers the 0D solution.

Subsequently, the neutral dynamics is coupled to the electron dynamics, by means of a semi-analytic 0D model which assumes Maxwellian electrons. The solution obtained gives a first estimate of the plasma parameters in the source, so that proper ranges for the characteristic lengths and time-scales of the various physical processes are calculated. Those results are essential to the preliminary design of a *bounce averaged* electron kinetic model, which is still 0D in space, but which calculates the electron energy distribution function self-consistently with the various processes.

After that, the 0D-1V electron kinetic model is designed in detail, including the effect of electromagnetic heating and various collisional processes. Accelerated convergence to the self-consistent steady-state is obtained by means of time-scale separation, fixed-point iteration, implicit time integration with Newton’s solver and variable time-step, and a reduced auxiliary model. The neutral density in the source is obtained from the aforementioned 1D analytic model.

When the necessity for a detailed kinetic model for neutrals was realized, a 3D-3V semi-Lagrangian Convected Scheme was developed, which solves the Boltzmann equation in six-dimensional phase-space, plus time. Being the first implementation of the Convected Scheme to be 3D in space, several computational problems arose, and new solutions had to be found. For this reason, a considerable part of this thesis work had to deal with a new method for implementing diffuse boundary conditions, a new injector model, a new mass-, momentum- and energy-conserving collision operator for the Bhatnagar-Gross-Krook model, and a new angular mesh. Moreover, a novel third-order positivity-preserving remapping method with low numerical diffusion was developed.

7.3 Status of the Numerical Implementation

While this dissertation is being printed, the models described are undergoing tests and further development. As new results are obtained and insight is gained in the physics and the numerical methods used, it is natural to constantly improve the modular numerical environment.

As concerns the 0D-1V kinetic electron model, the solver for the normalized EEDF is fully operational and mostly validated, and the self-consistent confinement potential is calculated in a few iterations. The numerical integrator for the energy balance equation, which describes the evolution of the electron density in the source, is under completion. The design of the interface mechanism between the normalized EEDF solver and the density solver is complete; implementation and testing is under way. The 0D-1V kinetic electron model is expected be fully operational soon, so that it will be possible to conduct an extended simulation campaign.

As concerns the 3D-3V kinetic model for the neutrals, it has been tested in the final configuration, that includes elastic and ionization collisions. Currently, the best method to interface this neutral kinetic model to the kinetic electron model is under investigation. A method for performing a re-start of the simulation, so that the quantities are allowed to evolve smoothly, is being addressed as well.

7.4 Recommendations for Future Work

In future work, it is planned that a higher level electron model will be developed, which incorporates at least one spatial dimension and two velocity dimensions. The results from this model will be compared with those from the 0D-1V electron model. The use of both of these in conjunction with each of the different neutral models will be explored, with a view to finding the optimal strategy for hybrid modeling of the helicon thruster system. This is intended to form a worked example of how to optimize a general hybrid model. When combined with other models such as the detailed EM models and PIC models of ions being developed at CISAS, this should provide the capability to model the thruster in detail and to obtain results while having a high degree of confidence in their validity. That confidence will be based in part on testing using models with a lower level of detail, which provide physical understanding of how the thruster system functions.

References

[1] C. Charles. **Plasmas for spacecraft propulsion**. *Journal of Physics D: Applied Physics*, **42**(16):163001, 2009.

[2] C. Charles. **Hydrogen ion beam generated by a current-free double layer in a helicon plasma**. *Applied Physics Letters*, **84**(3):332–334, 2004.

[3] C. Charles and R. W. Boswell. **Laboratory evidence of a supersonic ion beam generated by a current-free "helicon" double-layer**. *Physics of Plasmas*, **11**(4):1706–1714, 2004.

[4] F. F. Chen. **Helicon Plasma Sources**. In Oleg A. Popov, editor, *High Density Plasma Sources*, chapter 1, pages 1–75. Noyes Publications, Park Ridge, NJ, 1995.

[5] R. W. Boswell. **Electrostatic and electromagnetic eigenmodes near the electron and ion gyrofrequencies in a cylindrical plasma**. *Journal of Plasma Physics*, **31**:197, 1984.

[6] R. W. Boswell. **Very efficient plasma generation by whistler waves near the lower hybrid frequency**. *Plasma Physics and Controlled Fusion*, **26**(10):1147, 1984.

[7] F. F. Chen. **Plasma ionization by helicon waves**. *Plasma Physics and Controlled Fusion*, **33**:339–364, 1991.

[8] K. P. Shamrai and V. B. Taranov. **Resonances and anti-resonances of a plasma column in a helicon plasma source**. *Physics Letters A*, **204**(2):139–145, 1995.

[9] K. P. Shamrai, V. P. Pavlenko, and V. B. Taranov. **Excitation, conversion and damping of waves in a helicon plasma source driven by an m=0 antenna.** *Plasma Physics and Controlled Fusion*, **39**:505–529, 1997.

[10] K. P. Shamrai and V. B. Taranov. **Volume and surface rf power absorption in a helicon plasma source**. *Plasma Sources Science and Technology*, **5**(3):474–491, 1996.

[11] A. W. Degeling, G. G. Borg, and R. W. Boswell. **Transitions from electrostatic to electromagnetic whistler wave excitation**. *Physics of Plasmas*, **11**(5):2144–2155, 2004.

[12] F. F. Chen and D. Arnush. **Generalized theory of helicon waves. I. Normal modes**. *Physics of Plasmas*, **4**(9), 1997.

[13] D. Arnush and F. F. Chen. **Generalized theory of helicon waves. II. Excitation and absorption**. *Physics of Plasmas*, **5**(5), 1998.

[14] S. Cho. **The field and power absorption profiles in helicon plasma resonators**. *Physics of Plasmas*, **3**:4268, 1996.

[15] S. Cho and M. A. Lieberman. **Self-consistent discharge characteristics of collisional helicon plasmas**. *Physics of Plasmas*, **10**(3):882–890, 2003.

[16] S. Cho. **Helicon and Trivelpiece-Gould Eigenmodes in Helicon Plasmas**. *Journal of the Korean Physical Society*, **52**(6):1809–1813, 2008.

[17] K. P. Shamrai and V. B. Taranov. **Resonance wave discharge and collisional energy absorption in helicon plasma source**. *Plasma Physics and Controlled Fusion*, **36**:1719, 1994.

[18] Y. M. Aliev and M. Krämer. **Parametric instabilities in helicon-produced plasmas**. *Physics of Plasmas*, **12**(7):072305, 2005.

[19] M. Krämer, Y. M. Aliev, A. B. Altukhov, A. D. Gurchenko, E. Z. Gusakov, and K. Niemi. **Anomalous helicon wave absorption and parametric excitation of electrostatic fluctuations in a helicon-produced plasma**. *Plasma Physics and Controlled Fusion*, **49**(5A):A167, 2007.

[20] G. G. Borg and I. V. Kamenski. **Collisionless energy coupling to electrons by helicon waves in the near field of an antenna**. *Physics of Plasmas*, **4**(3):529–536, 1997.

[21] H. Gui and J. Scharer. **Nonlinear trapping simulations for helicon plasma sources**. In *Plasma Science, 1999. ICOPS '99. IEEE Conference Record - Abstracts. 1999 IEEE International Conference on*, page 141, 1999.

[22] A. Degeling, J. Scharer, and R. W. Boswell. **Evidence of electron trapping in a helicon discharge**. In *Plasma Science, 2000. ICOPS 2000. IEEE Conference Record - Abstracts. The 27th IEEE International Conference on*, page 226, 2000.

[23] F. F. Chen and D. D. Blackwell. **Upper limit to Landau damping in helicon discharges**. *Physical Review Letters*, **82**:2677, 1999.

[24] Y. Mouzouris, J. Scharer, and M. Bettenhausen. **Antenna coupling and absorption mechanisms in a helicon source operation**. In *Plasma Science, 1996. IEEE Conference Record - Abstracts., 1996 IEEE International Conference on*, page 158, 1996.

[25] A. Fruchtman, G. Makrinich, and J. Ashkenazy. **Two-dimensional equilibrium of a low temperature magnetized plasma**. *Plasma Sources Science and Technology*, **14**(1):152, 2005.

[26] M. Denning, M. Wiebold, and J. Scharer. **Observations of neutral depletion and plasma acceleration in a flowing high-power argon helicon plasma**. *Physics of Plasmas*, **15**(7), 2008.

[27] E. Ahedo. **Cylindrical model of a helicon-generated plasma**. *International Electric Propulsion Conference*, 2009.

[28] E. Ahedo and M. Merino. **Acceleration of a focused plasma jet in a divergent magnetic nozzle**. *International Electric Propulsion Conference*, 2009.

[29] E. Ahedo and M. M. Sánchez. **The Role Of Current Free Double Layers In Plasma Propulsion**. *44th AIAA/ASME/SAE/ASEE Joint Propulsion Conference and Exhibit*, 2008.

[30] E. Ahedo and M. M. Sánchez. **Theory of a Stationary Current-Free Double Layer in a Collisionless Plasma**. *Phys. Rev. Lett.*, **103**(13):135002, 2009.

[31] E. Ahedo. **Double-layer formation and propulsive assessment for a three-species plasma expanding in a magnetic nozzle**. *Physics of Plasmas*, **18**(3):033510, 2011.

[32] K. Sato and F. Miyawaki. **Formation of presheath and current-free double layer in a two-electron-temperature plasma**. *Physics of Fluids B: Plasma Physics*, **4**(5):1247–1254, 1992.

[33] J. G. Andrews and J. E. Allen. **Theory of a Double Sheath between Two Plasmas**. *Proceedings of the Royal Society of London. Series A, Mathematical and Physical Sciences*, **320**(1543):pp. 459–472, 1971.

[34] G. Hairapetian and R. L. Stenzel. **Particle dynamics and current-free double layers in an expanding, collisionless, two-electron-population plasma**. *Physics of Fluids B: Plasma Physics*, **3**(4):899–914, 1991.

[35] F. F. Chen. **Physical mechanism of current-free double layers**. *Physics of Plasmas*, **13**(3), 2006.

[36] R. Winglee, T. Ziemba, L. Giersch, J. Prager, J. Carscadden, and B. R. Roberson. **Simulation and laboratory validation of magnetic nozzle effects for the high power helicon thruster**. *Physics of Plasmas*, **14**(6):063501, 2007.

[37] A. Meige, R. W. Boswell, C. Charles, and M. M. Turner. **One-dimensional particle-in-cell simulation of a current-free double layer in an expanding plasma**. *Physics of Plasmas*, **12**(5):052317, 2005.

[38] M. A. Lieberman, C. Charles, and R. W. Boswell. **A theory for formation of a low pressure, current-free double layer**. *Journal of Physics D: Applied Physics*, **39**(15):3294–3304, 2006.

[39] F. W. Perkins and Y. C. Sun. **Double Layers without Current**. *Phys. Rev. Lett.*, **46**(2):115–118, 1981.

[40] J. Carlsson, M. Manente, and D. Pavarin. **Implicitly charge-conserving solver for Boltzmann electrons**. *Physics of Plasmas*, **16**(6):062310, 2009.

[41] S. Gallian. *Helicon Thruster Simulation with a Quasi Two-Dimensional Boltzmann Electron Model*. Master's thesis, Universitá di Padova, 2008-2009.

[42] D. Bose, T. R. Govindan, and M. Meyyappan. **Modelling of magnetic field profile effects in a helicon source**. *Plasma Sources Science and Technology*, **13**(4):553, 2004.

[43] D. Bose, T. R. Govindan, and M. Meyyappan. **A coupled plasma and sheath model for high density reactors**. *Plasma Science, IEEE Transactions on*, **30**(2):653 – 659, 2002.

[44] M. J. Kushner. **Hybrid modelling of low temperature plasmas for fundamental investigations and equipment design**. *Journal of Physics D: Applied Physics*, **42**(19):194013, 2009.

[45] R. L. Kinder and M. J. Kushner. **Noncollisional heating and electron energy distributions in magnetically enhanced inductively coupled and helicon plasma sources**. *Journal of Applied Physics*, **90**(8):3699–3712, 2001.

[46] R. L. Kinder and M. J. Kushner. **Wave propagation and power deposition in magnetically enhanced inductively coupled and helicon plasma sources**. *Journal of Vacuum Science and Technology A*, **19**(1):76–86, 2001.

[47] R. L. Kinder, A. R. Ellingboe, and M. J. Kushner. **H- to W-mode transitions and properties of a multimode helicon plasma reactor**. *Plasma Sources Science and Technology*, **12**(4):561, 2003.

[48] M. A. Lieberman and A. J. Lichtenberg. *Principles of Plasma Discharges and Materials Processing*. Wiley-Interscience, 2nd edition, 2005.

[49] P. M. Bellan. *Fundamentals of Plasma Physics*. Cambridge University Press, 1st edition, 2008.

[50] R. P. Brinkmann. **The plasma-sheath transition in low temperature plasmas: on the existence of a collisionally modified Bohm criterion**. *Journal of Physics D: Applied Physics*, **44**(4):042002, 2011.

[51] S. D. Baalrud and C. C. Hegna. **Kinetic theory of the presheath and the Bohm criterion**. *Plasma Sources Science and Technology*, **20**(2):025013, 2011.

[52] H. Amemiya. **Sheath Formation Criterion and Ion Flux for Non-Maxwellian Plasma**. *Journal of the Physical Society of Japan*, **66**(5):1335–1338, 1997.

[53] V. I. Kolobov and V. A. Godyak. **Nonlocal electron kinetics in collisional gas discharge plasmas**. *Plasma Science, IEEE Transactions on*, **23**(4):503 –531, 1995.

[54] S. D. Rockwood. **Elastic and Inelastic Cross Sections for Electron-Hg Scattering from Hg Transport Data**. *Physical Review A*, **8**(5):2348–2358, 1973.

[55] M. N. Rosenbluth, W. M. MacDonald, and D. L. Judd. **Fokker-Planck Equation for an Inverse-Square Force**. *Phys. Rev.*, **107**(1):1–6, 1957.

[56] M. Hayashi. **Bibliography of Electron and Photon Cross Sections with Atoms and Molecules Published in the 20th Century - Argon**. Technical Report NIFS-DATA-72, National Institute for Fusion Science (NIFS) of Japan, 2003.

[57] D. Fang, W. Hu, J. Tang, Y. Wang, and F. Yang. **Energy distribution of secondary electrons in electron-impact ionization of hydrogenic and heliumlike ions**. *Phys. Rev. A*, **47**(3):1861–1865, 1993.

[58] W. N. G. Hitchon. *Plasma Processes for Semiconductor Fabrication*. Cambridge University Press, 1999.

[59] W. N. G. Hitchon, G. J. Parker, and J. E. Lawler. **Physical and numerical verification of discharge calculations**. *IEEE Transactions on Plasma Science*, **21**(2):228 –238, 1993.

[60] W. N. G. Hitchon, G. J. Parker, and J. E. Lawler. **Accurate models of collisions in glow discharge simulations**. *IEEE Transactions on Plasma Science*, **22**(3):267 –274, 1994.

[61] J. Feng and W. N. G. Hitchon. **Self-consistent kinetic simulation of plasmas**. *Phys. Rev. E*, **61**(3):3160–3173, 2000.

[62] A. J. Christlieb, W. N. G. Hitchon, and E. R. Keiter. **A computational investigation of the effects of varying discharge geometry for an inductively coupled plasma**. *IEEE Transactions on Plasma Science*, **28**(6):2214–2231, 2000.

[63] G. A. Bird. *Molecular Gas Dynamics and the Direct Simulation of Gas Flows*. Oxford University Press, 2nd edition, 1994.

[64] A. J. Christlieb, W. N. G. Hitchon, I. D. Boyd, and Q. Sun. **Kinetic description of flow past a micro-plate**. *Journal of Computational Physics*, **195**(2):508 – 527, 2004.

[65] L. Margolin and P. K. Smolarkiewicz. **Antidiffusive Velocities for Multipass Donor Cell Advection**. *SIAM Journal on Scientific Computing*, **20**(3):907–929, 1998.

[66] P. K. Smolarkiewicz. **A fully multidimensional positive definite advection transport algorithm with small implicit diffusion**. *Journal of Computational Physics*, **54**(2):325–362, 1984.

[67] P. K. Smolarkiewicz and W. W. Grabowski. **The multidimensional positive definite advection transport algorithm: nonoscillatory option**. *Journal of Computational Physics*, **86**(2):355–375, 1990.

[68] J. P. Boris and D. L. Book. **Flux-corrected transport. I. SHASTA, a fluid transport algorithm that works**. *Journal of Computational Physics*, **11**(1):38–69, 1973.

[69] B. van Leer. **Towards the ultimate conservative difference scheme. II. Monotonicity and conservation combined in a second-order scheme**. *Journal of Computational Physics*, **14**(4):361–370, 1974.

[70] A. Harten. **High resolution schemes for hyperbolic conservation laws**. *Journal of Computational Physics*, **49**(3):357–393, 1983.

[71] P. K. Sweby. **High Resolution Schemes Using Flux Limiters for Hyperbolic Conservation Laws**. *SIAM Journal on Numerical Analysis*, **21**(5):995–1011, 1984.

[72] P. L. ROE. **Characteristic-based schemes for the Euler equations**. *Annual Review of Fluid Mechanics*, **18**:337–365, 1986.

[73] R. ARTEBRANT AND H. J. SCHROLL. **Limiter-Free Third Order Logarithmic Reconstruction**. *SIAM Journal on Scientific Computing*, **28**(1):359–381, 2006.

[74] A. MARQUINA. **Local Piecewise Hyperbolic Reconstruction of Numerical Fluxes for Nonlinear Scalar Conservation Laws**. *SIAM Journal on Scientific Computing*, **15**(4):892–915, 1994.

[75] J. W. BANKS, T. ASLAM, AND W. J. RIDER. **On sub-linear convergence for linearly degenerate waves in capturing schemes**. *Journal of Computational Physics*, **227**(14):6985 – 7002, 2008.

[76] R. J. LEVEQUE. *Numerical Methods for Conservation Laws*. B. Verlag, 1992.

[77] P. L. BHATNAGAR, E. P. GROSS, AND M. KROOK. **A Model for Collision Processes in Gases. I. Small Amplitude Processes in Charged and Neutral One-Component Systems**. *Phys. Rev.*, **94**(3):511–525, 1954.

[78] D. A. FIXEL AND W. N. G. HITCHON. **Convective scheme solution of the Boltzmann transport equation for nanoscale semiconductor devices**. *Journal of Computational Physics*, **227**(2):1387 – 1410, 2007.